Wang, Fan (2012) Functional neuroimaging of the somatosensory system with Ultra-high-field fMRI and MEG. PhD thesis, University of Nottingham.

Functional Neuroimaging of the Somatosensory System with Ultra-high-field fMRI and MEG

Fan Wang, BSci.

Thesis submitted to the University of Nottingham for the degree of Doctor of Philosophy

November 2011

Abstract:

Multimodal neuroimaging using a combination of Magnetoencephalography (MEG) and ultra-high-field fMRI are used in order to gain further insight into the neural oscillations and haemodynamic responses in the somatosensory cortex.

Single pulse electrical median nerve stimulation (MNS) with regular and jittered intervals is used in MEG. A preliminary study is used to determine acceptable trial number and length, and highlights points to be considered in paradigm optimization. Time-frequency analysis shows that the largest activities are beta event-related desynchronization (ERD) and event-related synchronization (ERS) between 13Hz and 30Hz. No significant difference in both the induced oscillations and evoked responses are found. Paired pulse MNS with varying ISIs are studied using MEG and 7T fMRI. The beta ERD is suggested to have a gating role with a magnitude irrespective of the starting point of stimulus. Non-linearity effects both in beta ERD/ERS and P35m are shown for ISIs of up to 2s, implying that the non-linear neural responses to the stimulus may still contribute to the BOLD non-linearity even when the evoked response has returned to baseline. Multiple pulse MNS with varying pulse train length and frequency are also investigated using MEG and MEG-fMRI. The gating role of beta ERD is further confirmed and the N160m is suggested to be modulated under this role. No accumulative effect is seen in the ERS with increasing pulse number but the amplitude of the ERS is modulated by the frequency. This can be explained by a Cortical Activation Model (CAM).

Efforts to spatially separate the beta ERD and ERS are shown for all three studies. Group averaged SAM images suggest a separation of activation areas along the central gyrus. Significant difference are found in the z MNI coordinate between beta ERD and ERS peak locations, suggesting that these two effects could arise from different generators. In the multiple pulse frequency study, by including the temporal signature of beta ERD and ERS as a regressor in BOLD fMRI analysis, delayed BOLD responses are located posterior to the standard BOLD response. However, the exact nature of the relationship between this delayed BOLD response and the ERS effects requires further work.

Acknowledgements:

Firstly, I would like to thank my supervisor Prof Peter Morris for his great support and high quality expertise for this thesis. Not only in this particular work, but his patience, kindness and encouragement has guided me during all my PhD studies and directed me towards future work and research.

I would also like to give my thanks to the people at the SPMMRC who have helped me a lot and made great contributions to this work, in particular for the people in MEG groups, Dr Claire Stevenson, Dr Matt Brooks, Dr Johanna Zummer who taught me a lot about MEG and Prof Penny Gowland, Dr Sue Francis and Dr Paul Glover who helped me a lot with MRI.

Many thanks to all members in the MR centre who have give me great help and suggestions from different backgrounds for both my research and life, making my study here very happy.

Finally, all my achievement is impossible without the support from my friends and the love of my family. I would like to dedicate this work to my Dad Xinyong Wang and my Mum Wenxia Li, your unreserved love is my greatest motivation.

Contents

Chapter 1

Introduction

Overview:

This chapter introduces the area of interest in this thesis. In section 1.1, a brief overview of the nervous system and the purpose of the studies in this thesis are introduced. In section 1.2, different kinds of neuroimaging techniques are introduced with focus on Magnetoencephalography (MEG) and functional MRI, which are combined in the multimodal functional studies discussed in this thesis. Finally in section 1.3, a brief overview of each chapter is given.

1.1 *The nervous system*

How the nervous system works remains one of the most challenging areas of science. It includes some questions such as the nature of the sensory signal process, motor behaviour and control, and learning and memory. It also poses the fundamental challenge of understanding the basis of consciousness and cognition. Nowadays, the study of the nervous system has become an interdisciplinary field including biological science, physics, mathematics, computer science and other disciplines.

Anatomically, the nervous system of human is divided into the central nervous system (CNS) and peripheral nervous system (PNS). The CNS, which includes the brain and spinal cord, forms the majority of the nervous system. It receives and processes the information from the

PNS. The PNS can be further divided into the somatic and automatic nervous system. Functionally, the nervous system can be divided into the visual system, somatosensory system, auditory systems etc. These sub-systems enable organisms to process different types of information and to control different types of behaviours.

Neural oscillations are rhythmic neuronal activity in the brain. Although it was reported as early as 1930 [1], that the ongoing alpha (8-13Hz) activity can be blocked by certain events, for example, opening one's eyes, the event-related changes in neural oscillations were not defined, confirmed and quantified until recent decades. In 1977, the quantification of event related changes of oscillatory activity was introduced by Pfurtscheller and Aranibar [2]. Since then, a new field has been opened in brain research which has grown rapidly. In this thesis, the neural oscillatory changes in the somatosensory cortex, including their roles; how they are generated and under what model they can be interpreted, is investigated. The relationship between oscillatory neural activity and haemodynamic responses is also studied. As neural oscillations are thought to play important roles in neural information processing, the investigation of oscillatory effects in thesomatosensory cortex can help us gain deeper insight into the mechanisms underlying sensory information processing. These effects include feedback neural connections between cortical areas and sub-cortical organizations. Thus the study of these effects helps define the relationship between the modulation of neural oscillations and cortical activation states. Since the oscillatory activity in somatosensory cortex has been observed to be associated with brain disorders, the in-vivo studies on healthy health volunteers undertaken in the work described in this thesis may eventually also contribute to clinical applications.

Neuroimaging techniques are powerful tools to study the neural oscillations. In recent years, with the development of in-vivo non-invasive techniques, the level of understanding of functional brain activity has rapidly advanced. In this thesis, parallel MEG/fMRI

experiments are carried out to study the oscillatory activity and their contributions to haemodynamic responses.

1.2 *Neuroimaging techniques*

A number of different techniques are applied to image the structure or function of the brain. Functional imaging measures the dynamic changes of the brain during sensory, motor or cognitive tasks directly (measuring neuroelectrical activity) or indirectly (measuring associated metabolic changes). These methods are compared in terms of their temporal resolution, spatial resolution and invasiveness in Figure 1-1.
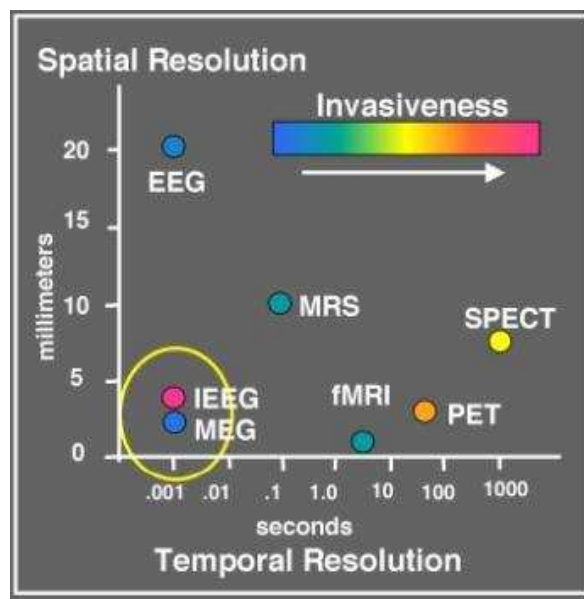
Figure 1-1: The spatial, temporal resolution and invasiveness of different neuroimaging techniques. The figure is from [3].

In this thesis, the non-invasive MEG and fMRI methods are used. MEG is a non-invasive direct imaging method which measures the magnetic field associated with the neuroelectrical activity. The MEG signal arises from the postsynaptic currents from cortex parallel to skull surface. The high sampling rate (600Hz) of MEG offers a good temporal resolution. fMRI is

a non-invasive indirect imaging method which measures the haemodynamic Blood Oxygenation Level Dependent (BOLD) changes which is influenced by the metabolic of oxygen during neural activity. Ultra-high-field fMRI used in this thesis has a good spatial resolution ($2\times2\times2mm^3$). The different physiological processes measured by MEG and fMRI measures are illustrated in Figure 1-2. Hence, parallel MEG-fMRI experiments are carried out in order to investigate the neuroelectircal and haemodynamic activity during signal process in the somatosensory system.
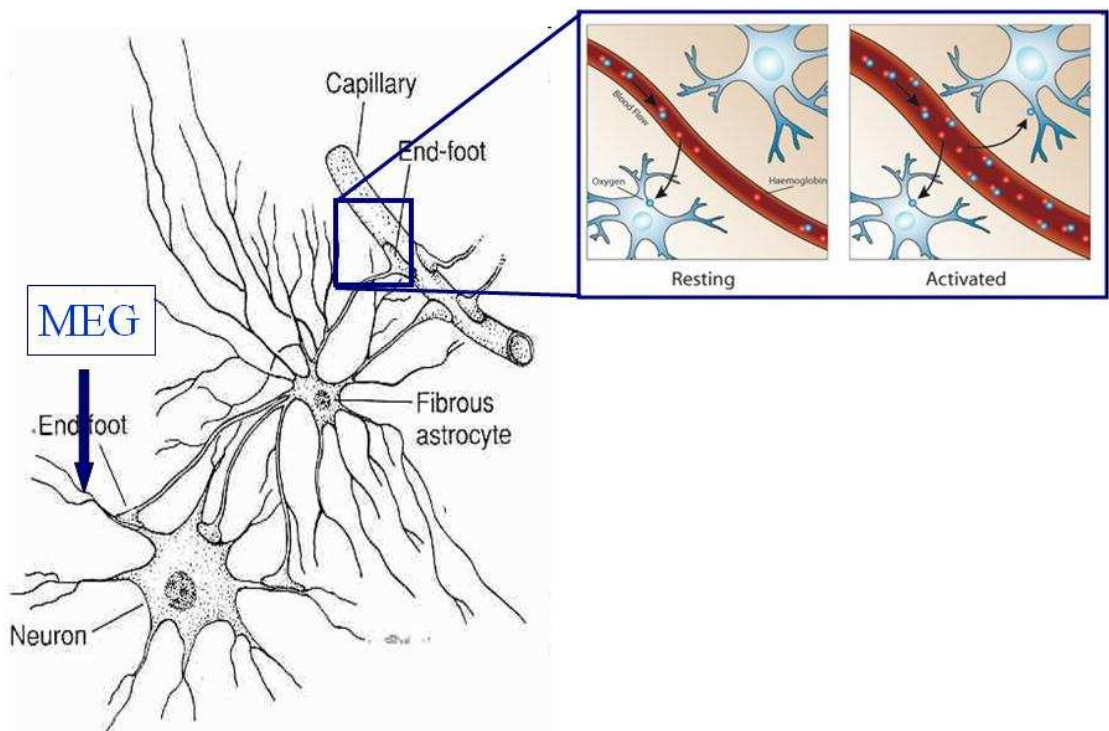
Figure 1-2: The MEG (left) and fMRI (right) have different sources

1.3 *Thesis aim and overview*

The work in this thesis explores in detail the way in which MEG and fMRI can be combined to investigate the somatosensory signal process and to understand the relationship between

neuromagnetic and haemodynamic effects in the somatosensory cortex. A series of experiments with single, paired and multiple median nerve stimulation (MNS) are carried out to find the modulating roles and the associations between MEG and fMRI. The structure of the rest of the thesis is as follows:

Chapter 2 introduces the basic physics underlying nuclear magnetic resonance and the methods used to measure the relaxation effects.

Chapter 3 introduces the basic principles and strategies of magnetic resonance imaging, Echo Planar Imaging, the physical and physiological basis of BOLD, MRI hardwire and MR safety issues.

Chapter 4 introduces the neurophysiological basis of the MEG signal, the hardware for MEG data recording and noise reduction and beamformer data analysis methods used in the experimental chapters including both the mathematical basis and application strategies.

Chapter 5 introduces the background of the following experiments including details about the somatosensory system, somatosensory neuroelectrical activity, the cortical activation model (CAM) and somatosensory fMRI.

Chapter 6 contains the experiments of single pulse MNS in regular and jittered conditions to test the influence of temporal regularity on the neuroelectircal activity in the somatosensory cortex using MEG. A testing study used to optimise the paradigms is also taken.

Chapter 7 contains the experiments of paired pulse MNS with varying inter stimulus intervals (ISIs). Both fMRI and MEG are combined to find the modulation of neuroelectircal

activity under varying ISIs and its contribution to the BOLD response. A gating role is found in this study.

Chapter 8 contains the experiments of multiple pulse MNS with varying train length and link pulses MNS with varying frequencies. The gating role found in Chapter 7 is further tested and the model introduced in Chapter 5 is also tested and used to interpret the results.

Chapter 9 summarizes the conclusions of all this work and gives some suggestions for future work.

1.4 *References*

[1]   Berger, H., Electroencephalogram of humans. Journal Fur Psychologie Und Neurologie, 1930. **40**: p. 160-179.
[2]   Pfurtscheller, G. and Aranibar, A., Event-Related Cortical Desynchronization Detected By Power Measurements Of Scalp Eeg. Electroencephalography and Clinical Neurophysiology, 1977. **42**(6): p. 817-826.
[3]   4D-Neuroimaging, http://web.mit.edu/kitmitmeg/whatis.html.

Chapter 2

Nuclear Magnetic Resonance

Introduction: In this chapter, a basic overview of nuclear magnetic resonance (NMR) theory is described. First, in Section 2.1, basic properties of nuclear magnetism are introduced, including the spin angular momentum, Zeeman splitting and bulk magnetisation. In Section 2.2, a classical description of Larmor precession and the application of radio frequency (RF) field are discussed. In Section 2.3, the theory underlying relaxation effects is introduced and the Bloch equation is derived. Finally in section 2.4, the free induced decay and the experimental methods used to measure both spin-lattice relaxation and spin-spin relaxation are discussed. However, a complete description of NMR requires a full quantum mechanical derivation to which the reader is referred elsewhere [1-7].

2.1 *Basic properties of nuclear magnetism*

2.1.1 Properties of nuclei

The basic unit of matter is the atom, which consists of a dense, central nucleus surrounded by a cloud of negatively charged electrons. The nucleus has four important physical properties: mass, electric charge, magnetism and spin. Spin can be thought of classically as a nucleus rotating around its central axis, like a planet. Spin is quite intangible in that it has almost no effect on the chemical and physical character of the substance. But by applying a

strong magnetic field and radio frequency pulses, the spin offers an opportunity to explore

the microscopic and internal structure of matter without disturbing it.

2.1.2 Spin angular momentum

In the classical condition, angular momentum is a vector quantity that is useful in describing

the rotational state of a physical system. The angular moment **L** of a particle about a given

origin is defined as:

$$\mathbf{L} = \mathbf{r} \times \mathbf{P} \qquad \text{[2-1]}$$

where **r** is the position vector from origin to particle and **P** is the linear momentum of the

particle and $\times$ signifies a cross-product. The relationship between **L**, **r** and **P** is shown in

Figure 2-1. However, to describe spin angular momentum properly, we need to introduce

quantum mechanics.
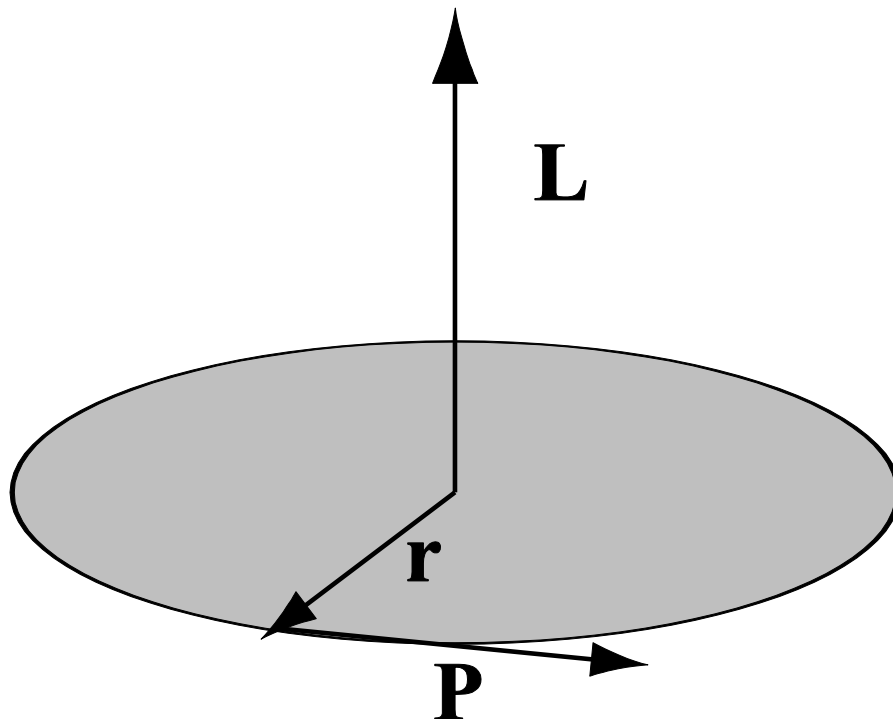
Figure 2-1: Classical angular momentum. The relationship between linear momentum (**P**),

position (**r**) and angular momentum (**L**) is shown.

In quantum mechanics, the angular momentum is quantized, which means the spin can only exist in some discrete stable state. The total angular momentum P is given by:

$$P = \hbar\sqrt{I(I+1)} \quad \text{[2-2]}$$

where $\hbar = h/2\pi$, h is Planck's constant and I is the spin quantum number, which can be either integral, half integral or zero. Each elementary particle has an associated spin quantum number. Spin angular momentum should not be thought of as produced by rotation; rather it is an intrinsic property of the particle. Even at a temperature of absolute zero, the particle retains spin. In classical mechanics, the angular momentum which is a vector has both magnitude and orientation. In quantum mechanics, the spin angular momentum also has information about direction. In the projection onto the z-axis, it has 2I+1 sublevels:

$$P_z = \hbar m_I \qquad m_I = -I, -(I-1), \ldots (I-1), I \quad \text{[2-3]}$$

These levels are degenerate in the absence of an external field. If an electrical or magnetic field is applied, the degeneracy is lifted and they have different energy. The quantisation of the spin angular moment for a spin with I= 1/2 and 3/2 is shown schematically in Figure 2-2.
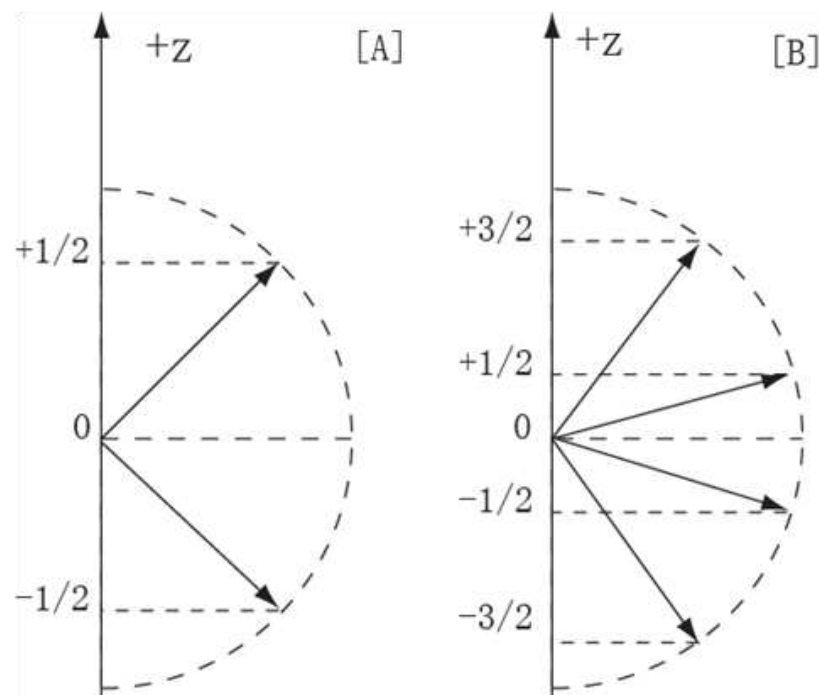
Figure 2-2: The quantisation of the spin angular moment for spin I= 1/2 [A] and spin I= 3/2 [B].

Particles with integer spin quantum number are bosons and those with half integer spins are fermions. In 1924, Wolfgang Pauli stated the Pauli Exclusion Principle, which means no two identical fermions may occupy the same quantum state simultaneously. [8] A more rigorous statement of this principle is that, for two identical fermions, the total wave function is anti-symmetric. In 1928, Paul Dirac offered a description called the Dirac equation which explains the half-integer quantum number which matches both quantum mechanics and special relativity. Details will not be discussed here. [9]

The spin can be thought of as a circulating electrical current, which generates magnetic moment. But as with angular momentum we have previously described, this magnetic moment **μ** is also an intrinsic property of particles and proportional to the total angular momentum:

$$\boldsymbol{\mu} = \gamma \mathbf{P} \qquad [2\text{-}4]$$

μ is a vector quality and γ is scalar quality called the gyromagnetic ratio. The value of γ depends on the nucleus and can be positive or negative. A positive value is defined such that the magnetic moment is parallel to the angular moment. In the international system of units, the unit is radians per second per tesla (rad·s^{-1}T^{-1}). It can also be given as MHz/T dividing by $2\pi \times 10^6$. For protons, the magnetic moment unit is the Bohr magneton:

$$\mu_{\mathrm{N}} = \frac{e\hbar}{2m_{\mathrm{p}}} = 5.05 \times 10^{-27}\,\mathrm{J} \cdot \mathrm{T}^{-1} \qquad [2\text{-}5]$$

where e is the elementary charge and m_{p} is the proton rest mass. All values are defined in SI units. The gyromagnetic ratio can be written as:

$$\gamma = g\,\frac{e}{2m_{\mathrm{p}}} = g\mu_{\mathrm{N}}\,/\,\hbar \qquad [2\text{-}6]$$

where g is the g-factor and is constant for a particular nucleus. Thus we can see that the gyromagnetic ratio is related to the charges and mass of the nucleus. Table 2-1 lists selected properties of some isotopes.

Table 2-1: A selection of isotopes and their properties [7]

Nucleus	Intrinsic spin	Nature abundance	Gyromagnetic ratio (MHz/T)
^{1}H	1/2	~100%	45.58
^{2}H	1	0.015%	6.54
^{13}C	1/2	1.1%	10.71
^{14}N	1	99.6%	3.08
^{15}N	1/2	0.37%	-4.32
^{17}O	5/2	0.04%	-5.77
^{23}Na	3/2	~100%	11.26
^{31}P	1/2	~100%	17.24
^{129}Xe	1/2	24.4%	-11.78

2.1.3 Zeeman splitting

When an external magnetic field is applied, the degeneracy of spin states m_I is broken. The energy of spin, E, within a magnetic field **B** is:

$$E = -\boldsymbol{\mu} \cdot \mathbf{B} \qquad [2\text{-}7]$$

Conventionally, it is assumed that the magnetic field applied parallel to the z-axis, B_0, is uniform and static. From Equation[2-3],[2-4] and [2-7]:

$$E = -\mu B_0 = -\gamma m_I \hbar B_0 \quad [2\text{-}8]$$

Each of the 2I+1 states of m_I now has a different energy. Consider the simplest condition of a proton for which the spin quantum number is 1/2, there are two spin states with the m_I =-1/2 and +1/2. As illustrated in Figure 2-3, the splitting of spin states with the application of

an external magnetic field is the Zeeman splitting. [10] The energy difference between these two sublevels is:

$$\Delta E = \gamma \hbar B_0 = \frac{\gamma h B_0}{2\pi} \qquad [2\text{-}9]$$

As the energy could also be written as:

$$\Delta E = h\nu \quad [2\text{-}10]$$

Then we can get:

$$\nu = \frac{\gamma B_0}{2\pi} \quad [2\text{-}11]$$
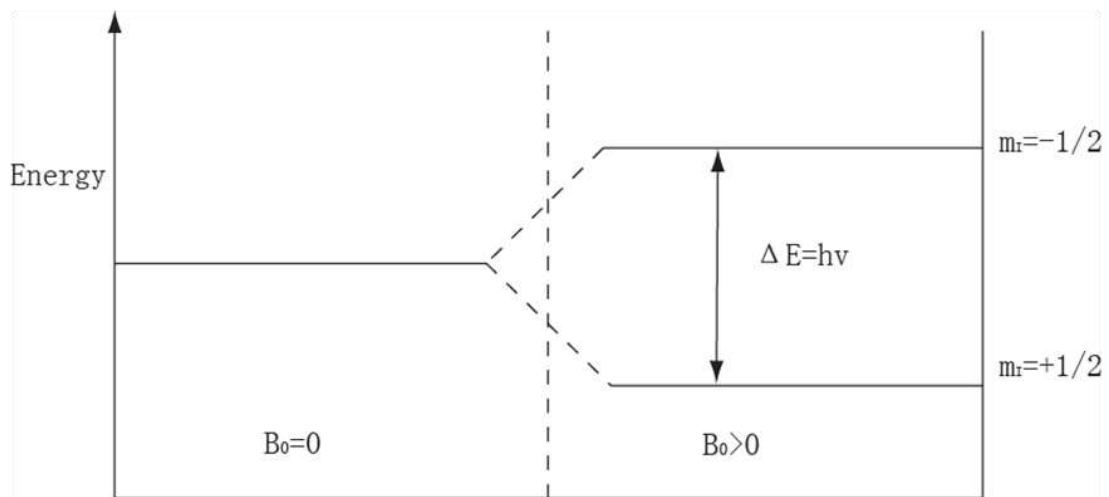
Figure 2-3: Zeeman splitting effects. The right half shows different energy levels for a nucleus (I=1/2) in a magnetic field B_0.

Transition from the lower to the higher states could be induced by external RF pulses with frequency ν and transition from higher to lower states generates photons, which could be detected as the resonance signal. In this way, the Larmor frequency of a nucleus in an external magnetic field is expressed in angular frequency as:

$$\omega_0 = \gamma B_0 \qquad [2\text{-}12]$$

2.1.4 Bulk magnetisation

Theoretically, the spin has a tendency to get to the state with lower energy. However, in real objects with a large number of spins, the dynamic of spins is described by the Boltzmann distribution. Only at T=0K, (absolute zero), are they all in ground state. In thermal equilibrium, which keeps spins in both states, the kinetic energy is of the order of kT, where k is Boltzmann constant and T is absolute temperature. The ratio of the populations of states is described by the Boltzmann distribution:

$$P(E) \propto e^{-E/kT} \quad [2\text{-}13]$$

Combine this equation with Equation [2-8], we can find the ratio of parallel (N_+) spins which are in the lower energy state to anti-parallel(N_-) spins which are in the higher energy state:

$$\frac{N_+}{N_-} = \frac{e^{m_{I+}E}}{e^{m_{I-}E}} = \frac{e^{\gamma\hbar B_0/2kT}}{e^{-\gamma\hbar B_0/2kT}} = e^{\gamma\hbar B_0/kT} \quad [2\text{-}14]$$

where m_I labels states of spins at sublevels with different energy. If $\gamma\hbar B_0 \ll kT$, Equation [2-14] can be simplified as:

$$\frac{N_+}{N_-} = e^{\gamma\hbar B_0/kT} \approx 1 + \frac{\gamma\hbar B_0}{kT} \quad [2\text{-}15]$$

And:

$$\frac{N_+ - N_-}{N_+ + N_-} \approx \frac{\gamma\hbar B_0}{2kT} \quad [2\text{-}16]$$

For protons with I=1/2, the magnetisation at thermal equilibrium is:

$$M_0 \approx \frac{1}{4} \frac{{}^2\hbar^2}{kT} B_0 \quad [2\text{-}17]$$

M_0 is the longitudinal magnetisation along the z-axis and ρ is the density of spins per unit volume. The transverse magnetisation in the plane perpendicular to the z axis depends on the phase coherence of the spin precession. In a static field, each spin precesses individually

with random phase. The bulk magnetisation within the transverse plane is zero. So the total magnetisation in the z direction is $\mathbf{M} = M_0 \mathbf{k}$. This net magnetisation, $\mathbf{M}$, is the vector sum of the magnetic moments of the individual spins. It is the bulk magnetisation due to excess spins in the lower energy state that leads to the NMR signal.

2.2 *The Classical description*

2.2.1 Larmor precession

The classical description, which is a useful way of thinking about the macroscopic spin system, is introduced. To understand how the spins interact with external environments, the simplest condition is considered: the response of an ensemble of protons in a static magnetic field, ignoring any interactions between them and with surrounding spins. The bulk magnetic moment vector of these spins is $\mathbf{M}$. The torque $\mathbf{T}$ of this magnetic moment vector due to the magnetic field $\mathbf{B}$ is:

$$\mathbf{T} = \mathbf{M} \times \mathbf{B} \quad [2\text{-}18]$$

where $\mathbf{B}$ is the external magnetic field applied in the z direction, $\mathbf{B} = B_0 \mathbf{k}$. This torque is equal to the change of total angular momentum:

$$\frac{d\mathbf{P}}{dt} = \mathbf{T} \quad [2\text{-}19]$$

By combing Equation[2-18], [2-19] and[2-4], the response of the spin magnetic moment to the magnetic field is:

$$\frac{d\mathbf{M}}{dt} = \gamma \frac{d\mathbf{P}}{dt} = \gamma \mathbf{T} = \gamma [\mathbf{M} \times \mathbf{B}] \quad [2\text{-}20]$$

The precession of $\mathbf{M}$ around $\mathbf{B}$ and the resultant change of magnetisation, $\Delta\mathbf{M}$ are illustrated in Figure 2-4.
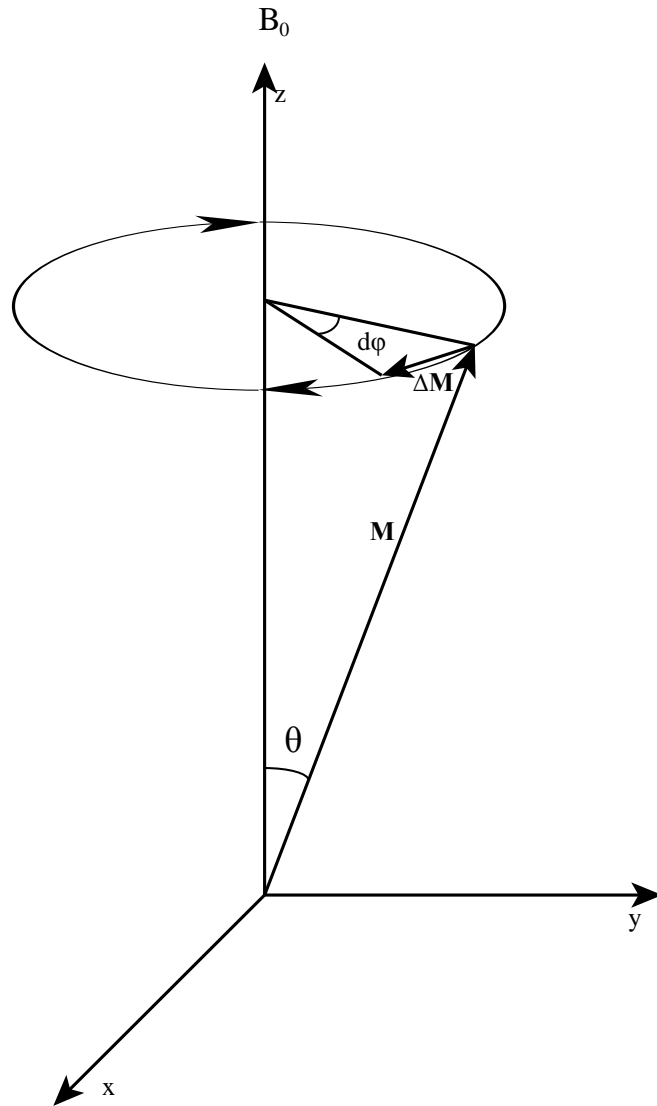
Figure 2-4: Precession of bulk magnetic moment vector **M** around the applied external magnetic field   **B**=B$_0$**k**.

As illustrated in Figure 2-4, after a short time period, dt, the change of magnetic moment vector Δ**M** is in the direction perpendicular to the plane defined by **M** and **B**. The angular change of **M** in the plane that is perpendicular to **B** is defined as dφ and the angle between **M** and **B** is θ. Hence, by using Equation[2-20]:

$$\left|\mathrm{d}\mathbf{M}\right| = \mathrm{M}_0 \sin\theta \left|\mathrm{d}\varphi\right|$$
$$\left|\mathrm{d}\mathbf{M}\right| = \gamma \left|\mathbf{M}\times\mathbf{B}\right|\mathrm{dt} = \gamma\mathrm{M}_0\mathrm{B}_0 \sin\theta\mathrm{dt} \quad [2\text{-}21]$$
$$\mathbf{M_0}\sin\theta\left|\mathrm{d}\varphi\right| = \gamma\mathrm{M}_0\mathrm{B}_0 \sin\theta\mathrm{dt}$$

The frequency of precession is thus:

$$\omega_0 = \left|\frac{\mathrm{d}\varphi}{\mathrm{dt}}\right| = \gamma\mathrm{B}_0 \quad [2\text{-}22]$$

It is the same as we generated from quantum mechanical arguments before, which means we can use this classical model to simplify our description of spin precession. The spin in static magnetic field rotates around the z direction at the Larmor frequency. As ω_0 is constant, we can calculate the integral of Equation[2-22]:

$$\varphi = -\omega_0 t + \varphi_0 \quad [2\text{-}23]$$

Where φ_0 is the angle at t=0. In the Cartesian Representation:

$$\mathbf{M(t)} = \mathrm{M}_x(t)\mathbf{i} + \mathrm{M}_y(t)\mathbf{j} + \mathrm{M}_z(t)\mathbf{k}$$
$$\begin{cases} \mathrm{M}_x(t) = \mathrm{M}_x(0)\cos\omega_0 t + \mathrm{M}_y(0)\sin\omega_0 t \\ \mathrm{M}_y(t) = \mathrm{M}_y(0)\cos\omega_0 t - \mathrm{M}_x(0)\sin\omega_0 t \\ \mathrm{M}_z(t) = \mathrm{M}_z(0) \end{cases} \quad [2\text{-}24]$$

2.2.2 Rotating reference frame

If we apply RF pulses to this spin angular moment, the description will be quite complex in the laboratory frame as both the original moment and the applied field from RF pulses are rotating. Hence we introduce the rotating reference frame, which is denoted by primed quantities (x', y', z') [11]. Viewed from the origin direction of z axis, the frame is rotating anticlockwise at the Larmor frequency, which is illustrated in Figure 2-6. The transformation from the laboratory reference frame to this rotating frame is:

$$\mathbf{i}' = \mathbf{i}\cos\omega_0 t - \mathbf{j}\sin\omega_0 t$$
$$\mathbf{j}' = \mathbf{i}\sin\omega_0 t + \mathbf{j}\cos\omega_0 t \qquad [2\text{-}25]$$
$$\mathbf{k}' = \mathbf{k}$$
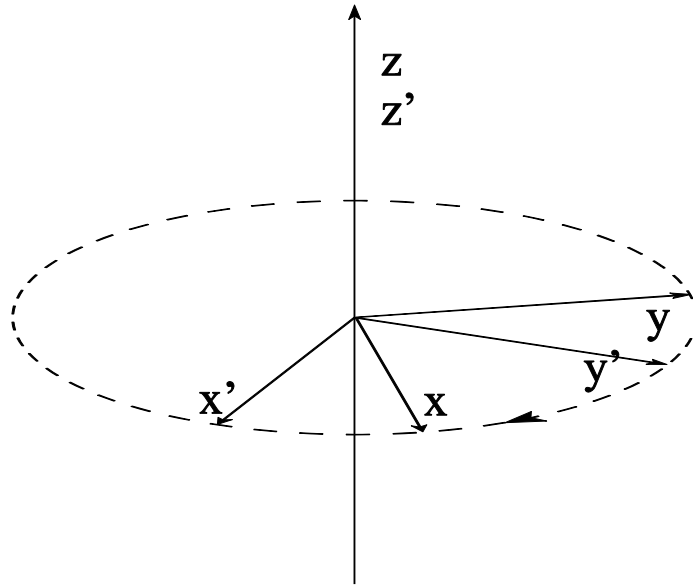
Figure 2-5: The rotating reference frame. The primed frame rotates around the z=z' axis and the rotation frequency is the Larmor Frequency.

The spin undergoing Larmor precession is stationary in this rotating frame. In the laboratory reference frame, a time dependent vector $\mathbf{V}(t)$ could be written in terms of its components along the x y and z axis as:

$$\mathbf{V} = V_x(t)\mathbf{i} + V_y(t)\mathbf{j} + V_z(t)\mathbf{k} \quad [2\text{-}26]$$

$V_x(t)$, $V_y(t)$ and $V_z(t)$ is components of $V(t)$. As the primed frame is rotating, we define the rotational angular velocity vector as $\mathbf{\Omega}$, hence these unit vectors are also rotating with $\mathbf{\Omega}$.

$$\frac{d\mathbf{i}'}{dt} = \mathbf{\Omega} \times \mathbf{i}' \quad [2\text{-}27]$$

The time derivate of $\mathbf{V}$ is

$$\frac{d\mathbf{V}}{dt} = \frac{dV_x}{dt}\mathbf{i}' + \frac{dV_y}{dt}\mathbf{j}' + \frac{dV_z}{dt}\mathbf{k}' + V_x\frac{d\mathbf{i}'}{dt} + V_y\frac{d\mathbf{j}'}{dt} + V_z\frac{d\mathbf{k}'}{dt}$$

$$= \frac{dV_x}{dt}\mathbf{i}' + \frac{dV_y}{dt}\mathbf{j}' + \frac{dV_z}{dt}\mathbf{k}' + \mathbf{\Omega}\times(V_x\mathbf{i}' + V_y\mathbf{j}' + V_z\mathbf{k}') \qquad [2\text{-}28]$$

$$= \left(\frac{d\mathbf{V}}{dt}\right)' + \mathbf{\Omega}\times\mathbf{V}$$

If we put the magnetic moment **M** as vector **V** into Equation[2-28], we have:

$$\frac{d\mathbf{M}}{dt} = \left(\frac{d\mathbf{M}}{dt}\right)' + \mathbf{\Omega}\times\mathbf{M} \quad [2\text{-}29]$$

Combining this equation with Equation[2-20], we can generate:

$$\left(\frac{d\mathbf{M}}{dt}\right)' = \mathbf{M}\times(\gamma\mathbf{B}+\Omega) = \gamma\mathbf{M}\times\mathbf{B}_{eff} \quad [2\text{-}30]$$

where $\mathbf{B}_{eff}$ is effective magnetic field in the rotating frame. Thus, the magnetic moment in this rotating frame acts as though it is in a static field of $\mathbf{B}_{eff.}$

2.2.3 RF pulses and flip angle

In the magnetic resonance experiment, the spins are perturbed by a magnetic field generated by RF pulses applied perpendicular to the static field B_0. We assume this time dependent field is along the x axis. Then the total field is:

$$\mathbf{B}_{total}(\mathbf{t}) = B_0\mathbf{k} + \mathbf{B_1}(\mathbf{t}) \quad [2\text{-}31]$$

Here $\mathbf{B_1}(\mathbf{t})$ is:

$$\mathbf{B_1}(\mathbf{t}) = 2\mathbf{i}B_1\cos\omega t \quad [2\text{-}32]$$

The linearly polarized field $\mathbf{B_1}$ along the x axis, can be broken down into two counter-rotating components with the same amplitude of B_1 but rotating in clockwise and anticlockwise directions:

$$\mathbf{B_A} = B_1(\mathbf{i}\cos\omega t + \mathbf{j}\sin\omega t)$$
$$\mathbf{B_C} = B_1(\mathbf{i}\cos\omega t - \mathbf{j}\sin\omega t)$$

[2-33]

where $\mathbf{B_A}$ is magnetic field component rotating in anticlockwise direction and $\mathbf{B_C}$ is the

component rotating in clockwise direction, as illustrated in Figure 2-6.
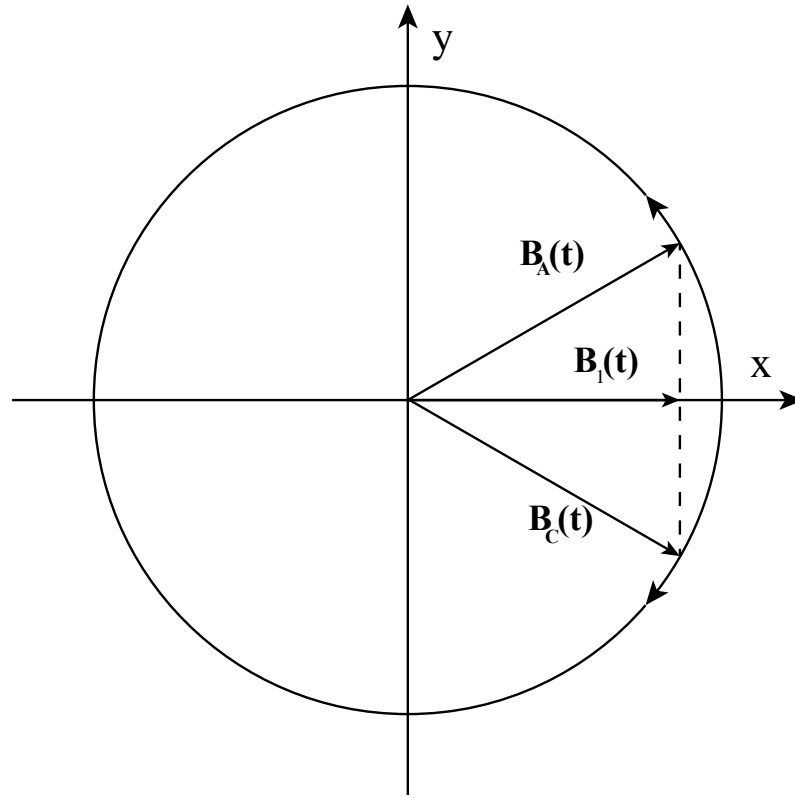
Figure 2-6: The two counter-rotating circular components of the oscillating $\mathbf{B_1}$ field.

Near resonance, when the frequency of the RF field is near the Larmor frequency, only the

clockwise component which is rotating in the same direction as the magnetic moment affects

the spin. The anticlockwise component can be neglected. Using this approximation:

$$\mathbf{B_1}(t) = \mathbf{B_c} = B_1(\mathbf{i}\cos\omega t - \mathbf{j}\sin\omega t) \quad [2\text{-}34]$$

From Equation[2-25], in the reference frame rotating at angular velocity $\mathbf{\Omega} = \omega \cdot \mathbf{k}$, $\mathbf{B_1}(t)$ can be

described as:

$$\mathbf{B_1}(t) = B_1\mathbf{i}' \quad [2\text{-}35]$$

In the presence of an RF field, the precession of the magnetic moment is:

$$\frac{d\mathbf{M}}{dt} = \gamma \mathbf{M} \times \mathbf{B}_{total} = \gamma \mathbf{M} \times (B_0 \mathbf{k} + B_1 \mathbf{i}') \quad [2\text{-}36]$$

Combine this equation with Equation[2-29] and consider the rotating frame is turning at ω around the z axis, we get:

$$\left(\frac{d\mathbf{M}}{dt}\right)' = \frac{d\mathbf{M}}{dt} - \Omega \times \mathbf{M} = \gamma \mathbf{M} \times \left[\left(B_0 - \frac{\omega}{\gamma}\right)\mathbf{k} + B_1 \mathbf{i}'\right] \quad [2\text{-}37]$$

The effective magnetic field in this frame is:

$$\mathbf{B}_{eff} = \left(B_0 - \frac{\omega}{\gamma}\right)\mathbf{k} + B_1 \mathbf{i}' \quad [2\text{-}38]$$

When the frequency of the RF field is exactly the same as the Larmor frequency, $\omega = \omega_0$, the magnetic moment in a rotating reference frame only precesses about the x' axis. The B_1 field tips the magnetic moment to the x-y plane. This is called the on-resonance condition and occurs when:

$$\omega = \gamma B_0 \quad [2\text{-}39]$$

When the on-resonance condition is fulfilled, the RF field applied for a while as an RF pulse will tip the magnetic moment away from the z direction. The spin rotates through an angle θ, which is:

$$\theta = \gamma B_1 \tau \quad [2\text{-}40]$$

θ is called the flip angle and τ is the duration of the RF field. Using this equation we can calculate the amplitude of RF pulses and the duration for the flip angle to be 90° or any other special angles. Figure 2-7 shows a 90° flip viewed in both rotating and laboratory reference frame.
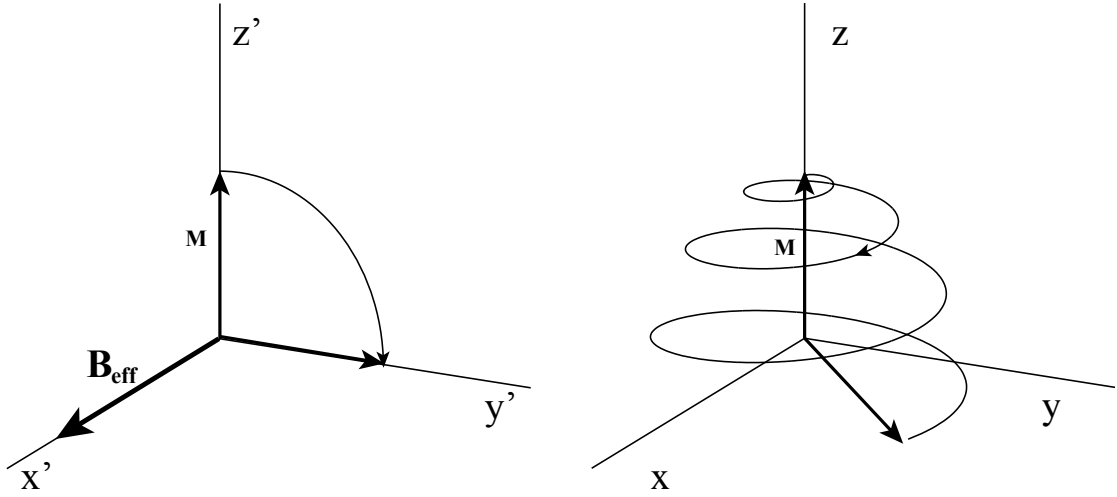
Figure 2-7: An on resonance 90° spin flip viewed in rotating reference frame (left) and laboratory reference frame (right).

When the frequency of the RF field is slightly different from the Larmor frequency, $\omega \neq \omega_0$, the behaviour of the magnetic moment will be more complex. Returning to Equation [2-37], $\mathbf{B_{eff}}$ will not be equal to $B_1\mathbf{i'}$, it will have an angle which is not 90° to the z' direction and the magnetic moment will precess in a tilted rotating reference frame. This precession is illustrated in Figure 2-8. In the case that ω is near ω_0, there is a small angle θ' between the precession axis and $\mathbf{z'}$ such that:

$$\cos\theta' = \frac{B_0 - \omega/\gamma}{B_{eff}}$$

$$\sin\theta' = \frac{B_1}{B_{eff}}$$

[2-41]

From this equation, the angular velocity of the magnetic moment around $\mathbf{B_{eff}}$ is:

$$\omega_{eff} = \gamma B_{eff} = \gamma\sqrt{(B_0 - \omega/\gamma)^2 + B_1^2}$$ [2-42]

This precession viewed in the rotating reference frame, in which $\mathbf{B_1}$ is stationary as described in Equation[2-35], is illustrated in Figure 2-8.
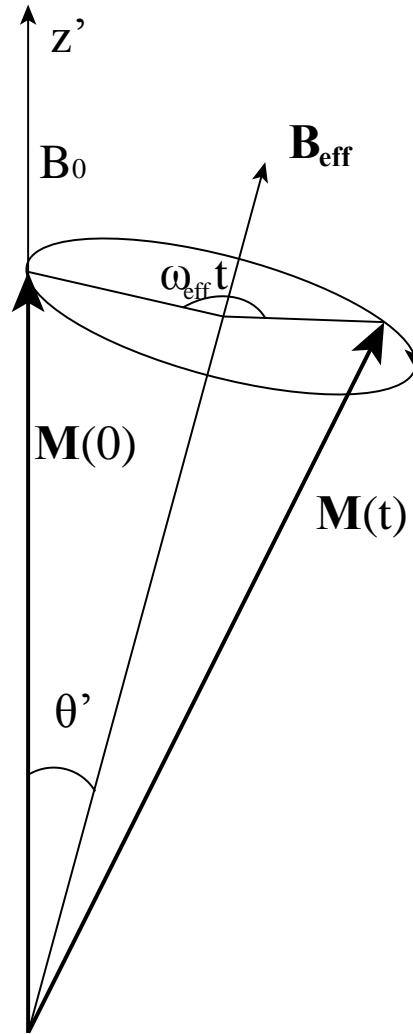
Figure 2-8: In the condition of $\omega \neq \omega_0$, the magnetic moment is processing around $\mathbf{B_{eff}}$ with angular velocity ω_{eff}.

2.3 *Relaxation Effects*

2.3.1 Spin-lattice relaxation

The interaction of spins with other spins plays an important role in the behaviour of macroscopic magnetisation. The spins exchange energy with surrounding spins and their

precession is also influenced by local magnetic fields. When an RF pulse is applied and the magnetisation is flipped away from the z axis, it has a natural tendency to return to the condition with the lower energy, which is parallel to the field. During this process, the spins exchange energy with the thermal motions of the molecules in the system called the lattice. This process of energy diffusion is called relaxation. T_1 is introduced to describe this process, and it can be thought of as a characteristic time for this energy exchange. It has been proven to be a first order process:

$$\frac{dM_z}{dt} = \frac{M_0 - M_z}{T_1} \quad [2\text{-}43]$$

M_z is the component of magnetisation along the static field and M_0 is the equilibrium value of magnetisation. T_1 is the time constant for this Spin-Lattice interaction. Liquid systems and tissues have T_1 in the range of $0.1 - 10$s whilst solids could have much longer ones. The solution for Equation[2-43] is:

$$M_z(t) = M_z(0)e^{-t/T_1} + M_0(1 - e^{-t/T_1}) \quad [2\text{-}44]$$

$M_z(0)$ is the initial magnetisation at t=0 and $M_z(t)$ is the function which describes the relaxation of the longitudinal component of magnetisation. When the flip angle of the RF pulse is θ, $M_z(0) = M_0\cos\theta$ and Equation [2-44] can be written as:

$$M_z(t) = M_0[(\cos\theta - 1)e^{-t/T_1} + 1] \quad [2\text{-}45]$$

2.3.2 Spin-spin relaxation

After being flipped to the x-y plane, the transverse component of magnetisation decays. In the sample, nuclei are tumbling randomly and the effective magnetic field for each spin is affected by its neighbouring nuclei. As the surrounding local field is fluctuating, the spins will precess at a slightly different frequency to each other. Over a while, spins will dephase

with respect to each other and this leads to a loss of bulk transverse magnetisation. This relaxation can be described as:

$$\frac{dM_{xy}}{dt} = -\frac{M_{xy}}{T_2} \quad [2\text{-}46]$$

where M_{xy} is the transverse component of magnetisation and T_2 is the constant for spin-spin relaxation. The integral of Equation [2-46] is:

$$M_{xy}(t) = M_{xy}(0)e^{-t/T_2} \quad [2\text{-}47]$$

Unlike T_1, T_2 is is less dependent on the static magnetic field. There is an additional dephasing that results from large scale inhomogeneities of the applied static magnetic field. It comes from both the imperfection of the magnet itself and the effect of geometry and composition of the sample which affects the local field. This is different from the random fluctuations of nearby nuclei; the field is inhomogeneous but not time dependant. Variance in the local fields leads to different local precession frequencies. Individual spins precessing with different frequencies tend to dephase, reducing the net magnetisation vector. This dephasing is usually referred to as 'fan out'. Thus the overall relaxation time of transverse component, T_2^*, could be written as:

$$\frac{1}{T_2^*} = \frac{1}{T_2} + \frac{1}{T_2'} \quad [2\text{-}48]$$

T_2' is the relaxation time of the "fan out" component, which is recoverable and will be discussed in Section 2.4.3. T_2 which is the loss of the transverse component due to random thermal processes cannot be recovered. Table 2-2 shows the T_1 T_2 and T_2^* values of grey matter and white matter measured at different magnetic field strengths.

Table 2-2: T_1 T_2 and T_2* values of brain tissues measured at 1.5T 3T and 7T [12-14]

Grey Matter			
Field strength	T_1(ms)	T_2(ms)	T_2*(ms)
1.5T	1197	96	84
3T	1607	72	66
7T	1939	48	32
White matter			
Field strength	T_1(ms)	T_2(ms)	T_2*(ms)
1.5T	646	94	66
3T	838	77	53
7T	1126	50	26

2.3.3 Bloch Equation

From Equations[2-20], [2-43] and[2-46], we can generate a combined equation which describes the flipping and relaxation of magnetisation:

$$\frac{d\mathbf{M}}{dt} = \gamma \mathbf{M} \times \mathbf{B_{eff}} + \frac{1}{T_1}(M_0 - M_z)\mathbf{k} - \frac{1}{T_2}(M_x\mathbf{i} + M_y\mathbf{j}) \quad [2\text{-}49]$$

This is referred to as the Bloch Equation [15-16]. For the simplest condition in which a static magnetic field is applied along the z direction, after an RF pulse is applied, the evolution of magnetisation can be described as:

$$\frac{dM_x}{dt} = \gamma B_0 M_y - \frac{M_x}{T_2}$$

$$\frac{dM_y}{dt} = -\gamma B_0 M_x - \frac{M_y}{T_2} \quad [2\text{-}50]$$

$$\frac{dM_z}{dt} = \frac{M_0 - M_z}{T_1}$$

The solution of these equations is:

$$M_x(t) = e^{-t/T_2}[M_x(0)\cos\gamma B_0 t + M_y(0)\sin\gamma B_0 t]$$

$$M_y(t) = e^{-t/T_2}[M_y(0)\cos\gamma B_0 t - M_x(0)\sin\gamma B_0 t] \qquad [2\text{-}51]$$

$$M_z(t) = M_z(0)e^{-t/T_1} + M_0(1 - e^{-t/T_1})$$

2.4 NMR Experiments

2.4.1 Free induced decay

In a NMR experiment, an RF pulse is applied in x direction to tip the spins to an angle of θ. During the recovery of the magnetisation, the total time-varying coherent magnetic field, which comes from the sum of the magnetic fields from all spins, is detected by a pickup coil placed along the x or y axis in the laboratory frame. The induced electromotive force (emf) is small and oscillating at the Larmor frequency. This signal is known as the free induced decay (FID), shown in Figure 2-9.
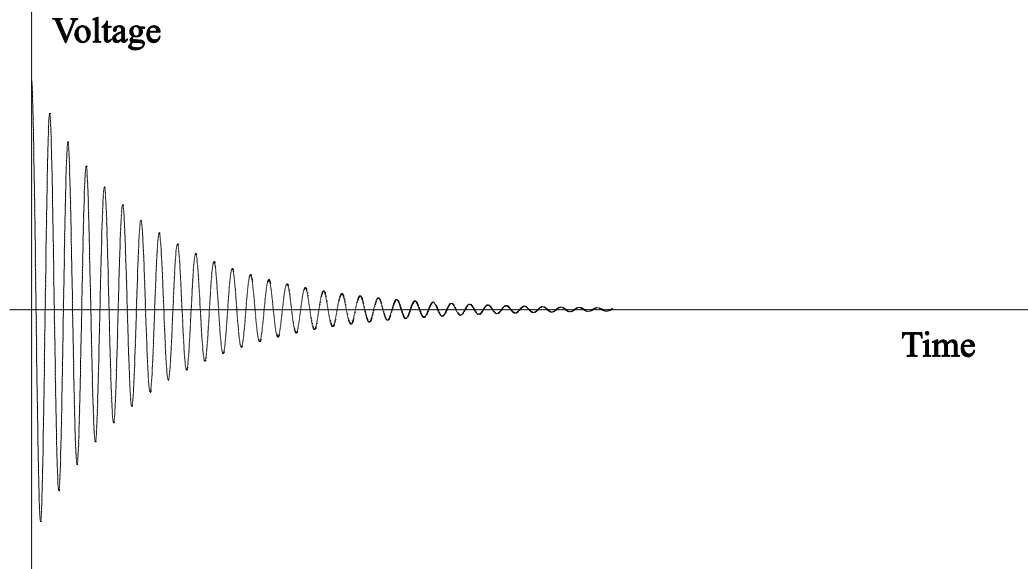
Figure 2-9: The FID detected by the pickup coil placed along the x direction.

The signal is described by:

$$S(t) = M_0 b \sin\theta \cos(\omega_0 t) e^{-t/T_2^*} \quad [2\text{-}52]$$

where b is a constant and a property of the detector. In the simplest condition, only one component is measured, but nowadays by applying quadrature detection with two detectors 90° out of phase to each other, a complex signal is generated.

2.4.2 The measurements of T_1 by inversion recovery:

An inversion recovery pulse sequence consists of a 180° RF pulse followed by a 90° pulse with an interval between them of TI.
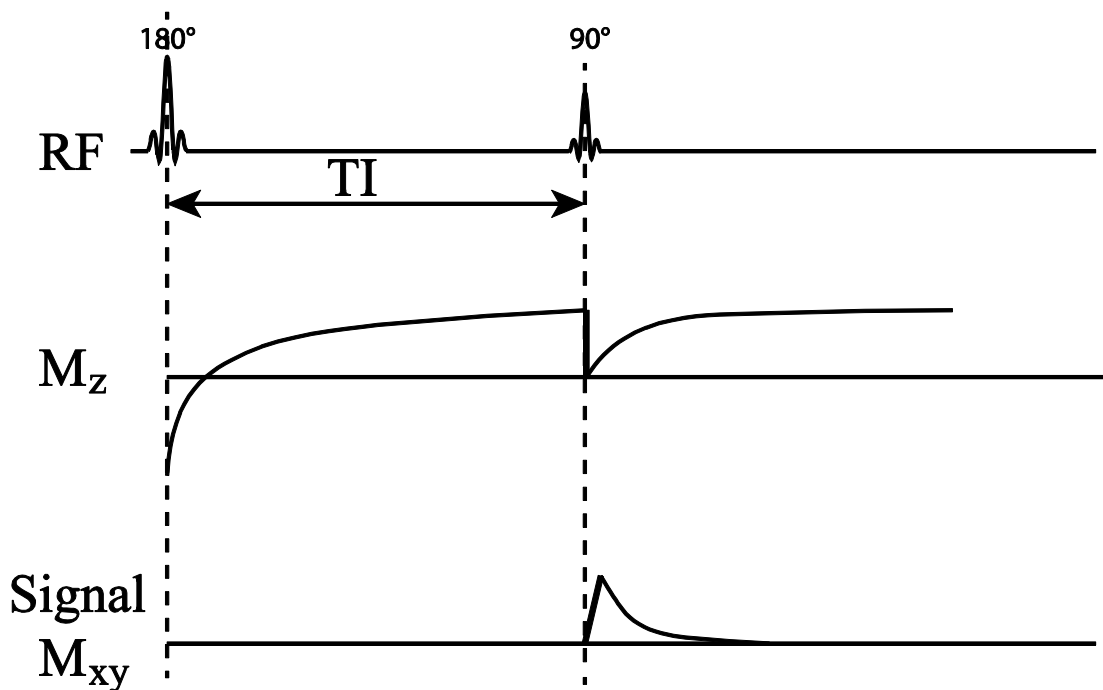
Figure 2-10: Schematic of inversion recovery sequence and signal. The longitudinal magnetisation, M_z, is flipped to the negative direction of the z axis by the 180° RF pulse. Following a delay of time TI, the recovered component of M_z is then flipped to the transverse plane by the 90° pulse, generating the FID signal.

At the start of the sequence, the equilibrium magnetisation M_0 is flipped through 180° such that:

$$M_z(0) = -M_0 \qquad [2\text{-}53]$$

After a time TI, the longitudinal component has recovered according to the equation:

$$M_z(t) = -M_0 e^{-t/T_1} + M_0(1 - e^{-t/T_1}) = M_0(1 - 2e^{-t/T_1}) \quad (0 < t < TI) \qquad [2\text{-}54]$$

The second pulse flips the longitudinal magnetisation into the transverse plane to generate the FID signal:

$$M_{xy} = \left| M_0(1 - 2e^{-TI/T_1}) \right| e^{TI-t/T_2^*} \quad (t > TI) \quad [2\text{-}55]$$

In this equation, M_{xy} is measured as a function of TI. By implementing the above sequence with varying TI, the curve of the magnitude of relaxation signal against TI can be generated. By fitting this curve to Equation[2-55], T_1 can be calculated.

2.4.3 The determination of T_2 using a spin echo sequence

The decay of the transverse magnetisation has different components. One comes from dephasing due to the inhomogeneous static field, which is T_2' and is recoverable; the other comes from loss of the transverse component due to thermal processes which is T_2 and is non-recoverable. The spin echo method was developed to measure T_2. Figure 2-11shows the sequence and signal for spin echo.
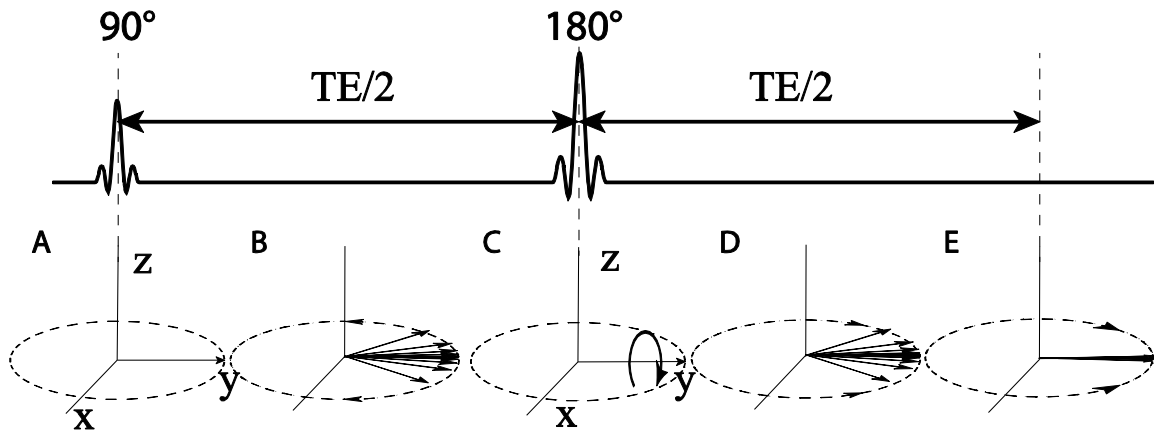
Figure 2-11: Schematic of spin echo pulse sequence. After the application of a 90° pulse, the magnetisation is flipped to the transverse plane [A]. The spin dephasing effect attributed to static inhomogeneities is shown in [B]. A 180° pulse is applied at time TE/2 to flip the spins around y axis. The rephasing effect is shown in [D] and at the time TE, the phase coherence is re-established, generating the echo [E].

Assume that at the beginning (t=0), magnetisation is flipped into the transverse plane along the y' axis in the rotating reference frame. Then the spins with different local magnetic field begin to dephase with respect to each other, generating an FID signal decaying with a time constant T_2^* as shown in Figure 2-9. After a time TE/2, a 180° pulse is applied to flip the magnetisation through 180° around the y'-axis in the transverse plane. The spins precessing slower are now 'ahead' of the Larmor frequency whereas the spins precessing faster are 'behind' it now. Progressively, the fast spins catch up with the main magnetisation and the slow spins drift back toward the main magnetisation. After a time of TE/2, the spins is refocused and the relaxation due to the T_2' effect are recovered, generating an echo signal which represents the T_2 effect. The signal recorded at the time of the echo is:

$$S = S_0 e^{-TE/T_2} \qquad [2\text{-}56]$$

By fitting the amplitude of the echo to Equation[2-56], T_2 can be calculated.

2.5 *References*

[1]   Bovey, F.A., Jelinski, L., Mirau, P.A., American, T. and Telegraph, C., Nuclear magnetic resonance spectroscopy. 1969: Academic Press.

[2]   Schumacher, R.T., Introduction to magnetic resonance: principles and applications. 1970: W.A. Benjamin.

[3]   Mansfield, P. and Morris, P.G., NMR imaging in biomedicine. 1982: Academic Press.

[4]   Morris, P.G., Nuclear magnetic resonance imaging in medicine and biology. 1986: Oxford.

[5]   Abraham, R.J., Fisher, J. and Loftus, P., Introduction to NMR spectroscopy. 1988: Wiley.

[6]   Slichter, C.P., Principles of magnetic resonance. 1990: Springer.

[7]   Levitt, M.H., Spin dynamics: basics of nuclear magnetic resonance. 2001: Wiley.

[8]   Pauli, W., The theoretical significance of the satellites of some spectrum lines and the effect on them of magnetic fields. Naturwissenschaften, 1924. **12**: p. 741-743.

[9]   Dirac, P.A.M., The quantum theory of the electron. Proceedings of the Royal Society of London, 1928. **117**(778): p. 610-624.

[10]   Zeeman, P., The effect of magnetisation on the nature of light emitted by a substance. Nature, 1897. **55**(1424): p. 347-347.

[11]   Rabi, II, Ramsey, N.F. and Schwinger, J., Use of rotating coordinates in magnetic resonance problems. Reviews of Modern Physics, 1954. **26**(2): p. 167-171.

[12]   Peters, A.M., Brookes, M.J., Hoogenraad, F.G., Gowland, P.A., Francis, S.T., Morris, P.G. and Bowtell, R., T2* measurements in human brain at 1.5, 3 and 7T. Magnetic Resonance Imaging, 2007. **25**(6): p. 748-753.

[13]   Cox, E.F. and Gowland, P.A. Measuring T2 and T2* in the brain at 1.5T, 3T and 7T using a hybrid gradient echo-spin echo sequence and EPI. Proceedings in ISMRM. Toronto 2008: p. 1411.

[14]   Wright, P.J., Mougin, O.E., Totman, J.J., Peters, A.M., Brookes, M.J., Coxon, R., Morris, P.E., Clemence, M., Francis, S.T. and Bowtell, R.W., Water proton T1 measurements in brain tissue at 7, 3, and 1.5T using IR-EPI, IR-TSE, and MPRAGE: results and optimization. Magnetic Resonance Materials in Physics, Biology and Medicine, 2008. **21**(1): p. 121-130.

[15]   Bloch, F., Hansen, W.W. and Packard, M., Nuclear induction. Physical Review, 1946. **70**(7-8): p. 460-474.

[16]   Bloch, F., Hansen, W.W. and Packard, M., The nuclear induction experiment. Physical Review, 1946. **70**(7-8): p. 474-485.

Chapter 3

MR imaging and functional MRI

Overview: In this chapter, the basic principles, strategies and hardware for Magnetic Resonance Imaging (MRI) are introduced. Firstly, in Section 3.1 the process of image formation based on spatial localization of the NMR signal and spin-warp imaging are described. In Section 3.2, image contrast and SNR are discussed. Next, in Section 3.3, the fast imaging method Echo Planar Imaging (EPI) required for functional MRI is detailed, including imaging artefacts and parallel imaging. An overview of MRI hardware, with particular reference to the 3T and 7T scanners in the Sir Peter Mansfield MR Centre, and a discussion of MR safety issues constitute Sections 3.4 and 3.5 of this chapter. Finally, an introduction to the BOLD response and its physical and physiological basis constituted Section 3.6.

3.1 *Magnetic resonance imaging methods*

3.1.1 Gradients

To create an image of a subject, it is necessary to determine the spatial distribution of spins within the subject. In Chapter 2, it was shown that spins in the presence of a static magnetic field, B_0, precess at the Larmor frequency, $\omega = \gamma B_0$, where γ is the gyromagnetic ratio. To spatially encode the signal, spatially varying (usually linearly) magnetic field gradients are superimposed onto the static field B_0. The field gradient (**G**) can be described generally as:

$$\mathbf{G} = \frac{\partial B_z}{\partial x}\mathbf{i} + \frac{\partial B_z}{\partial y}\mathbf{j} + \frac{\partial B_z}{\partial z}\mathbf{k} = G_x\mathbf{i} + G_y\mathbf{j} + G_z\mathbf{k} \quad [3\text{-}1]$$

In the magnetic field resulting from the combination of the applied filed gradient and static B_0, the spins at location **r** will precess at a frequency given by:

$$\omega(\mathbf{r}, t) = \gamma[B_0 + \mathbf{G}(t)\square\mathbf{r}] \qquad [3\text{-}2]$$

The detected MR signal contains a variety of frequencies, thus the spatial distribution of spins can be determined by using Fourier transform techniques. The following sections describe methods for signal localization using field gradients.

3.1.2 Frequency encoding

Following the application of an RF pulse, spins will immediately precess at the Larmor frequency. A field gradient is applied along the x direction (G_x), which will make the precession frequency position dependent, therefore this is called the frequency encoding or read-out gradient. Consider a 1D method for simplicity, the signal received from a phase sensitive system in quadrature to the x direction can be described as in Equation[3-3].

$$s(t) = \int \rho(x) e^{i\omega(x,t)} dx \qquad [3\text{-}3]$$

Here $\rho(x)$ is the spin density function along the x direction, and $\omega(x,t)$ is the accumulated phase of spins with different Larmor frequencies. A vector **k** can be defined to represent this

phase accumulation due to frequency coding. If the gradient field is assumed to be constant during signal readout, the x component of **k**, k_x, is given by:

$$k_x = \gamma \int_0^t G_x(t')dt' = \gamma G_x t \qquad [3\text{-}4]$$

Then Equation [3-3] can be written as:

$$s(k_x) = \int \rho(x)e^{ik_x x}dx \qquad [3\text{-}5]$$

It is clear from Equation[3-5] that the signal is the Fourier transform of the spin density $\rho(x)$ and therefore the spin density distribution within the subject can be generated by using an inverse Fourier transform as shown in Equation[3-6]:

$$\rho(x) = \frac{1}{2\pi} \int s(k_x)e^{-ik_x x}dx \qquad [3\text{-}6]$$

The vector, **k**, which contains the spatial frequency and phase information, is usually represented in k-space [1]. k-space is a matrix, in which data from MR signals are stored during data acquisition. The signals covering a single data line of k-space are sampled within the application of a single read gradient. As read gradient is usually constant, simply sampling the signals at a constant rate generates a uniform distribution of value points in k-space. The MR image is reconstructed from k-space. If gradients are applied in multiple directions, a 2D or 3D Fourier Transform is used to yield a 2-dimensional or 3-dimensional image. In 2D-imaging, a slice-selective method [2] is used to form a 2D image of a selected slice.

3.1.3 Phase encoding

2D images can be obtained using frequency encoding in a method known as projection reconstruction method. However, this method is not widely used in MRI nowadays. Frequency encoding is generally applied in one dimension and another method, phase encoding, is used to encode the spins in the second k-space direction. In addition to the frequency encoding gradient in the x direction (G_x), another gradient, G_y, is applied in the y direction, as shown in Figure 3-1 [3]. This is called a phase encoding gradient [4]. If the gradient G_y is applied for a time length of T_{pe}, spins at different locations along the y direction will precess at different frequencies and accumulate a phase difference with respect to each other. Once this gradient is turned off, the spins will precess at the same frequency again but with a permanent phase shift, which varies along the y direction. Hence the spatial position along the y axis has been encoded in the phase shift. The phase of spins at location y can be described as:

$$\omega(y)T_{pe} = k_y y \qquad [3\text{-}7]$$

Where $\omega(y)$ is the frequency of precession at location y which is γG_y and k_y is defined as for k_x as:

$$k_y = \gamma \int_0^{T_{pe}} G_y dt = \gamma G_y T_{pe} \qquad [3\text{-}8]$$

The phase encoding gradient is applied multiple times, each time with different amplitude, in order to cover k-space in the y direction. Using a combination of frequency encoding along the x direction and phase encoding in the y direction, it is possible to fill a 2D k-space, which is the Fourier transform of the spin density projection in the plane. Similarly, if a second phase encoding gradient, G_z, is applied in the z-direction, a 3D k-space can be filled and a 3D image of the subject is generated with a single 3D-Fourier transform.
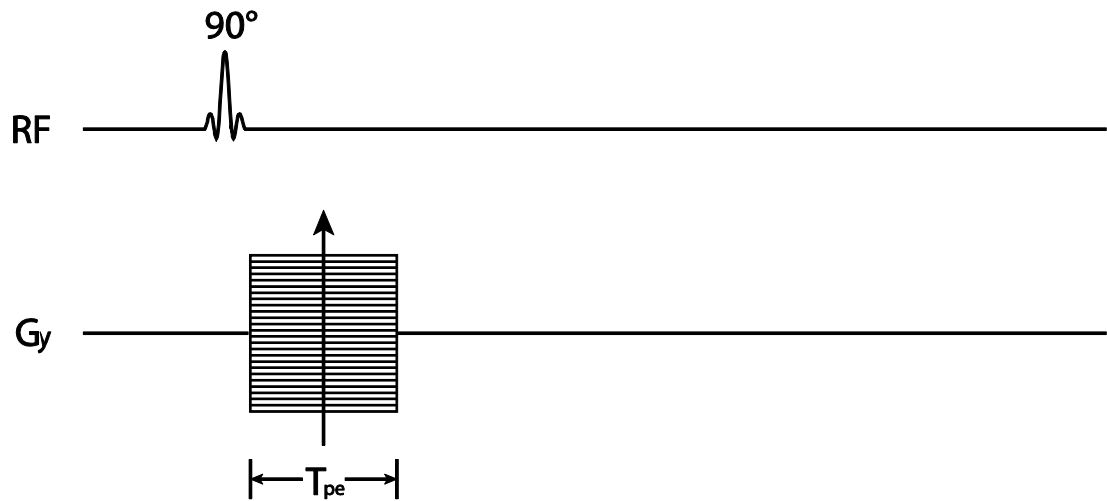
Figure 3-1: The phase encoding method. The phase encoding gradient along the y–axis is applied multiple times to encode different lines in k-space.

3.1.4 Slice selection

In general, MR imaging requires the excitation of spins within a finite spatial range by using the combination of a gradient field and spatially selective RF pulses [5-6]. The slice selective gradient is typically constant during the excitation and is assumed to be in the z-direction here. During the application of this gradient, an RF pulse that has a finite frequency range is applied. As spins along the z-direction have different Larmor frequencies, only the spins precessing within the bandwidth of the RF pulse frequency are excited whilst the other spins are not affected.

Consider a linear gradient applied along the z-direction, G_z, as shown in Figure 3-2. As before, the frequencies of precession are given by:

$$\omega = \gamma(B_0 + G_z z) \quad \text{[3-9]}$$

In order to excite the spins within a range from $z_0 - \Delta z/2$ to $z_0 + \Delta z/2$, where Δz is the slice thickness, the spatially selective RF pulse is required to have a frequency domain centred at $\omega_0 = \gamma B_0$ whilst the range is:

$$\Delta \omega = \gamma(B_0 + G_z \Delta z/2) - \gamma(B_0 - G_z \Delta z/2) = \gamma G_z \Delta z$$
$$\Delta z = \frac{\Delta \omega}{G_z \gamma} \quad \text{[3-10]}$$

It is clear that the slice thickness is proportional to the bandwidth of the RF pulse, and inversely proportional to the amplitude of the gradient. As both parameters influence Δz, different gradients with appropriate RF pulses can be used to excite the slice. In practice, however, with the limitations of hardware, a high gradient together with a RF pulse having large bandwidth is preferred. This increases the frequency difference between slices and reduces the effects of inhomogeneities in the field and of imperfect RF pulses.
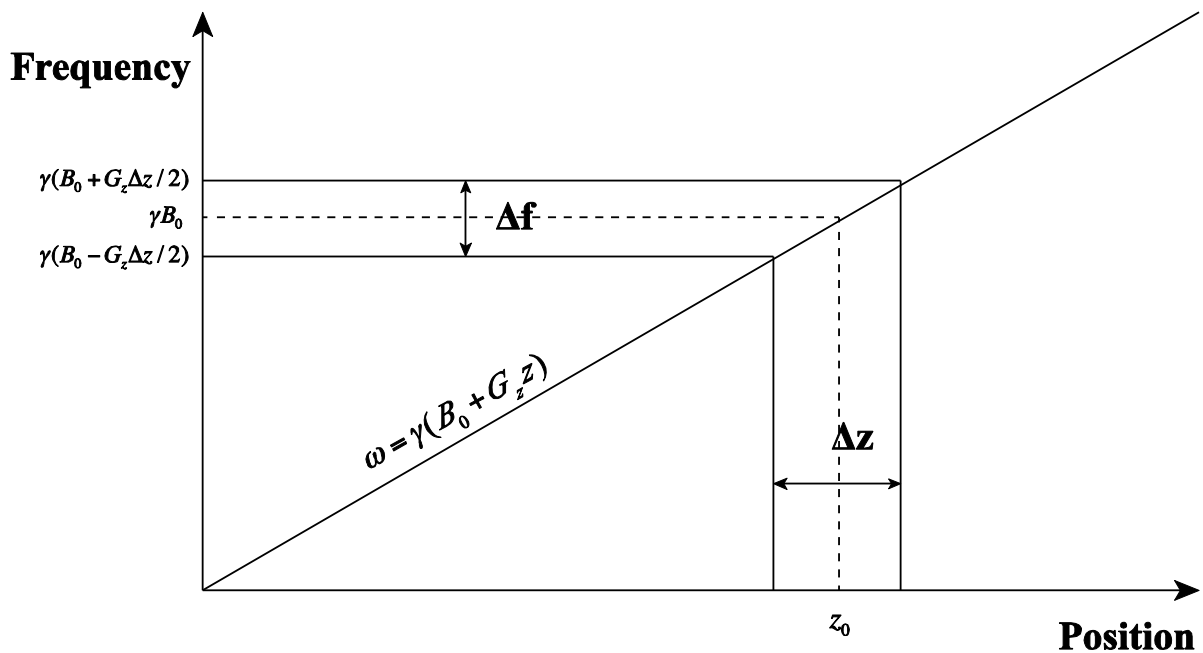
Figure 3-2: The slice selection method and the relationship between slice thickness and gradient amplitude.

Since a magnetic field gradient of duration Δt is applied, a degree of phase dispersion will occur along the direction of the gradient (z). To eliminate possible signal loss due to dephasing, a slice rephasing gradient is applied to refocus the spins. To simplify the problem, it is assumed that the RF pulse instantly tips the spins to the transverse plane at the centre point of RF pulse, so that spins dephase only during the second half of the selective gradient. The phase dispersion across a slice can be described as:

$$\phi(z) = \gamma G_z z \Delta t \qquad \text{[3-11]}$$

In order to unwind the dephasing of the spins, a slice rephasing gradient lobe of reverse polarity, the same amplitude ($-G_z$) and duration $\Delta t/2$ is played following the selective gradient lobe. This reverses the precession rates and unwinds the phase completely.

There are various kinds of RF pulses that can be used for slice selective excitation; the most commonly used is a SINC pulse, which has a top hat distribution in the frequency domain [7]. Both the SINC function and slice selection gradients are illustrated in Figure 3-3. As the SINC function is infinite in extent, and cannot reasonably be achieved in practice, the region between two or three zero crossing points on each side of the primary peak is usually selected. In addition, to optimize the shape of the frequency envelope, some window function filters such as a Hamming window are also applied. However, even using all of the methods above, imperfections in the RF pulses still exist. For example, the immediate neighbourhood of the selected slice could be partly excited. In multiple slice imaging, therefore, gaps between slices are left or all the odd-number and even number slices are excited separately.
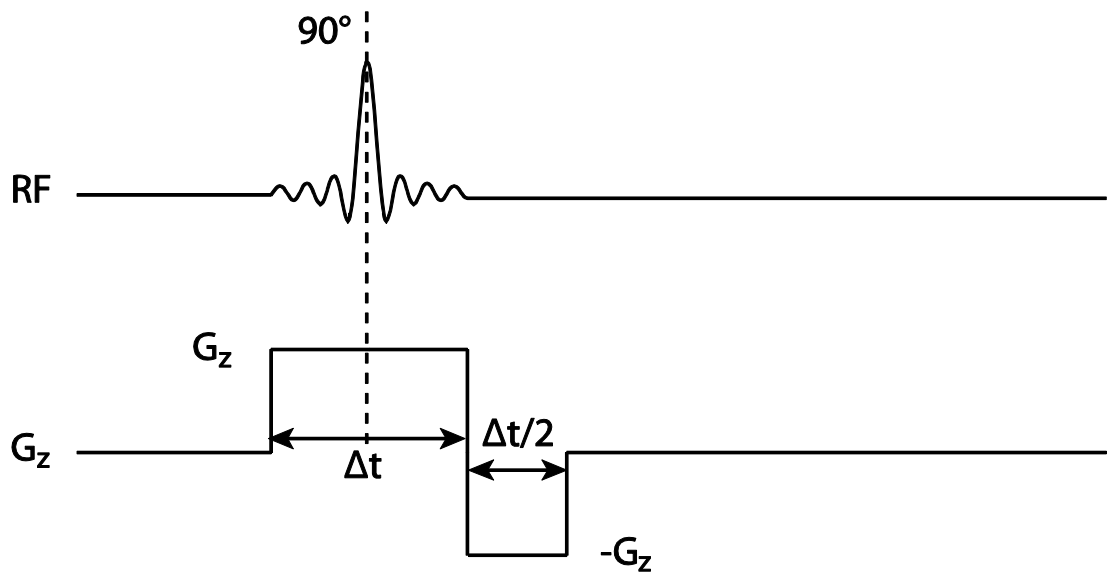
Figure 3-3: The SINC function and slice selection gradient. This gradient is applied along the z-axis and the area of the slice rephasing lobe is half of the original slice selection lobe.

3.1.5 Gradient echo

It was discussed in Chapter 2 that inhomogeneity of the static field results in dephasing of spins and loss of signal. When a gradient field is applied, spins at different locations will precess at different frequencies, also resulting in dephasing. However, this dephasing can be refocused by applying a gradient field of opposite sign. This is illustrated in Figure 3-4, when a positive gradient is applied after the negative one finishes. The amplitude of the positive gradient is the same as the negative one but its duration is doubled. The negative gradient moves the start point to the left of k-space. Signal is acquired during the positive gradient, filling the k-space from left to right. At the centre of the positive gradient, which occurs at Echo Time (TE), the spins are refocused and the echo signal is collected. This method is called Gradient Echo (GE) [8].
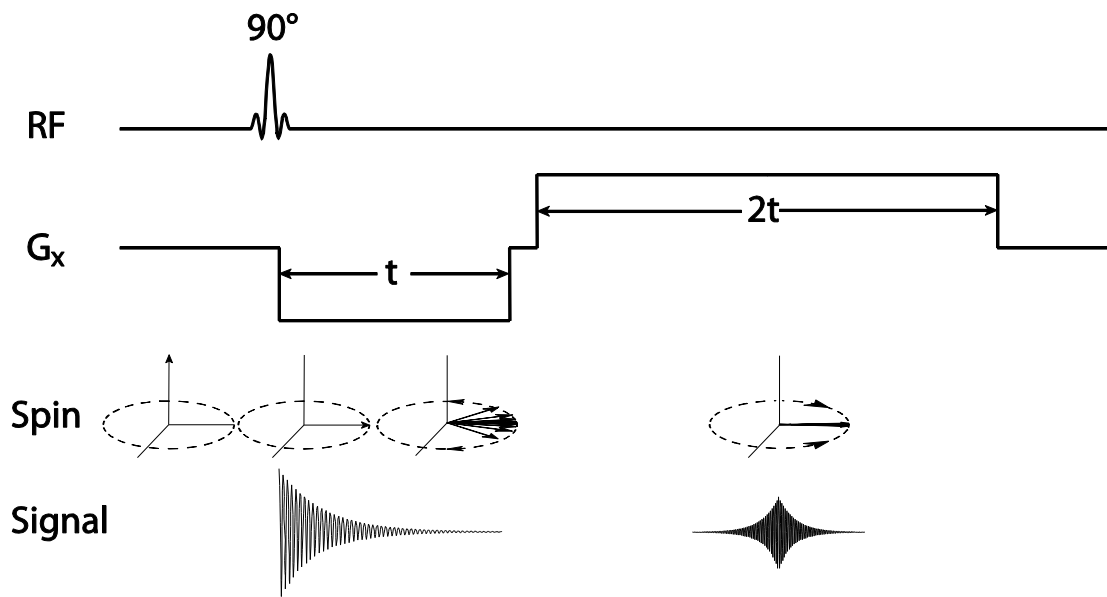
Figure 3-4: Formation of a gradient echo. The area of positive gradient field is twice as large as the negative one. The spins are refocused in the middle of the positive gradient where the dephasing effect from the field gradient is eliminated.

3.1.6 Spin-warp imaging

Spin-warp imaging is a basic method that has been applied in MR imaging since the early 1980s [3]. The pulse scheme of spin-warp imaging is illustrated in Figure 3-5. In this technique, a read-out gradient is applied to collect one line of k-space per excitation, with appropriate delays between the acquisitions to allow the longitudinal magnetisation to recover through T_1 relaxation. The application of different phase encoding gradients before each acquisition ensures that different lines in k-space are sampled so as to fill the whole space, which is then Fourier-transformed to generate an image. In the next paragraph this imaging strategy is discussed in more detail using gradient echo as an example, but spin echo acquisitions are also possible.
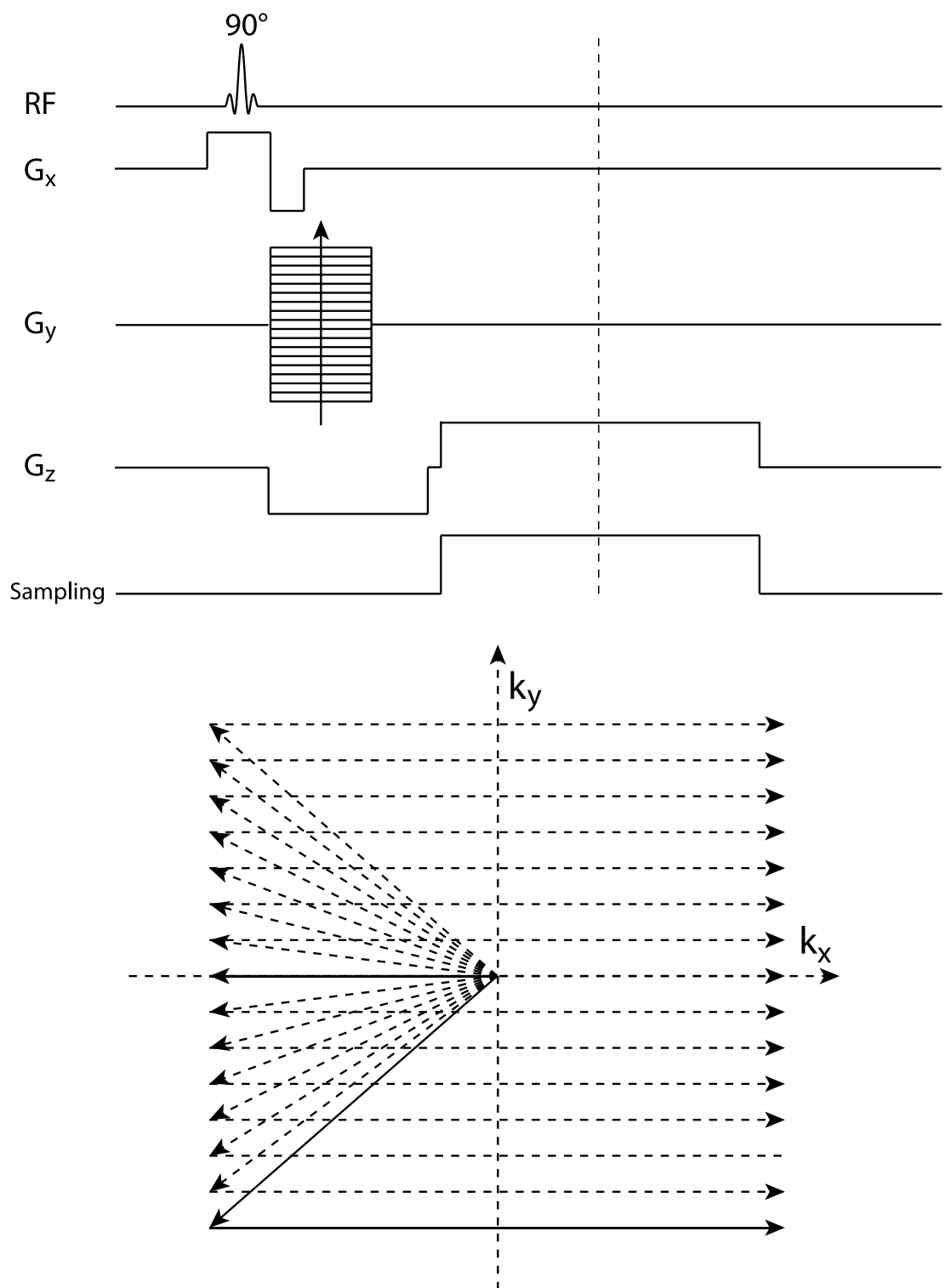
Figure 3-5: Gradient Echo Spin Warp imaging. The pulse sequence is shown in the upper panel whilst the filling of k-space is shown in the lower panel.

The sequence consists of an initial 90° excitation RF pulse applied whilst the slice-selective gradient is turned on along the z-direction to excite spins within a particular slice. Following the RF pulse, a phase encoding gradient is applied along the y-axis. For each acquisition following the excitation pulse, this gradient is applied with different amplitude varying from $-G_y^{max}$ to G_y^{max}. This moves the start point of each line of k-space progressively from bottom to top to cover k-space in the k_y direction, as shown by the dashed arrows in Figure 3-5. The pre-excursion gradient, G_x, which is applied in the x direction with a duration of $t_x/2$, moves the start point of each data line in k-space to the left $(-k_x^{max})$ of the x axis. The frequency encoding gradient is then applied, rephasing the spins and generating a gradient echo in the middle of this gradient lobe. The gradient echo signal is sampled during this read-out gradient, filling the line in k-space, determined by phase encoding, from left to right $(-k_x^{max}$ to $k_x^{max})$ along the x axis. By repeatedly applying excitation RF pulses and different phase encoding gradients, we can sample the whole of k-space as illustrated in Figure 3-5.

The rephasing gradient lobe applied along the z-direction can be combined with the phase encoding lobe to reduce the time for collecting one line in k-space. Similarly, the dephasing gradient before data collection can also be applied simultaneously with the phase encoding lobe. However, during the acquisition time, application of additional gradients would lead to rotation of the data acquisition axis and cause artefacts.

3.2 *Contrast and Signal to Noise Ratio*

3.2.1 Image contrast

The MR signal can be made sensitive to tissue parameters such as T_1, T_2, T_2^* and proton density. In practice, during imaging, more than one 90° excitation RF pulse is applied to each slice during an experiment and the interval between them is called the repetition time (TR). As discussed in Section 2.3.1, T_1 measures the recovery of magnetisation along the z-axis, which can be described as:

$$M_z = M_0(1 - e^{-TR/T_1}) \quad [3\text{-}12]$$

The signal, S, measured at time TE following the 90° RF pulse is therefore:

$$S \propto M_0(1 - e^{-TR/T_1})(e^{-TE/T_2^*}) \quad [3\text{-}13]$$

Figure 3-6 illustrates this relationship between signal intensity, T_1, T_2^*, TR and TE. From Equation[3-13], and Figure 3-6, it is clear that for enhancement of T_1 contrast, a short TR is required, together with a short TE which reduces the effect from T_2^* relaxation. Otherwise if images with enhanced T_2^*-contrast are required, a long TR, which eliminates the influence of T_1, and a long TE are applied. However, if a spin echo method is used instead, which gets rid of the T_2' dephasing effect , T_2-contrast will be obtained. In the case of using long TR and short TE, neither T_1 nor T_2^* influence the contrast of the image; in this case, only the density of spins influences the contrast. This is called Proton Density Weighted (PDW) imaging. [9]
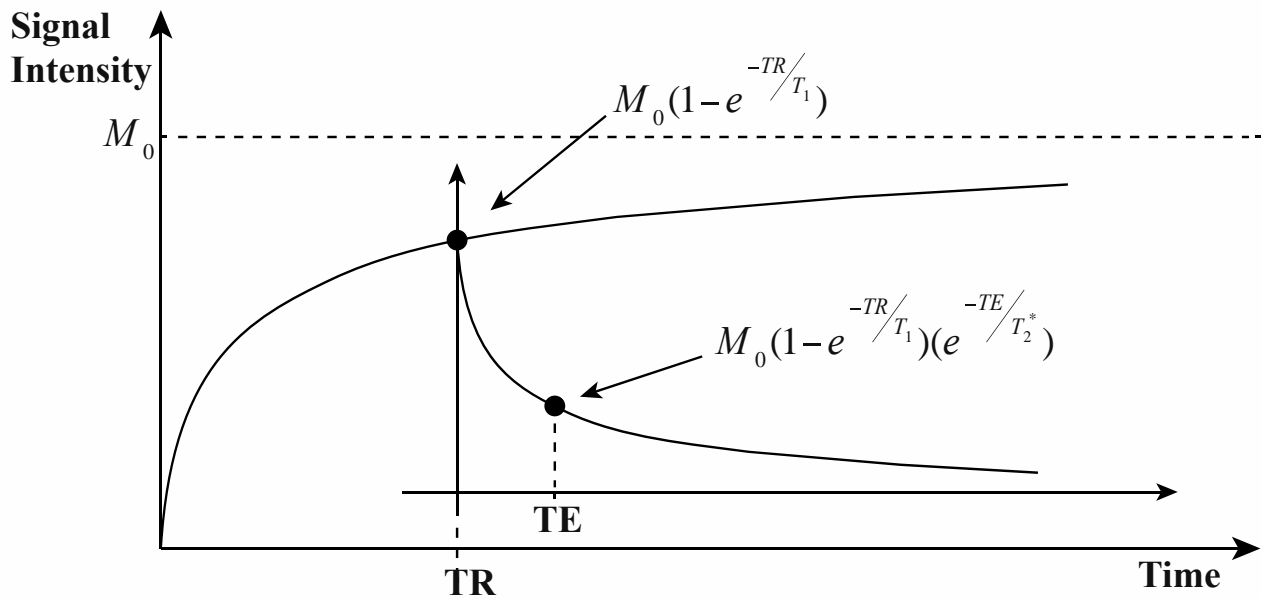
Figure 3-6: The signal intensity decay along the time axis is determined by T_1 and T_2*. It is also determined by the selection of TR and TE. By selecting different combinations of TR and TE, images with different contrast can be generated.

3.2.2 Ernst angle

In the GE Spin Warp sequence discussed above, the RF pulse was assumed to be 90°, which means the magnetisation is fully flipped into the transverse plane. In practice, this angle could be smaller. If a 90° pulse is used to get the maximum signal, we require the z-magnetisation to recover before the next pulse is applied, which means TR should be comparable with or longer than T_1. As T_1 could be as long as several seconds, fast imaging methods (for example Fast Gradient Echo) typically use much shorter TR than T_1. In this case, the magnetisation is flipped through an angle smaller than 90° to prevent saturation. After a given number of TRs, a steady stated is reached for the z-magnetisation:

$$M_{ze} = M_{ze} \cos\theta e^{-TR/T_1} + M_0(1 - e^{-TR/T_1})$$

$$M_{ze} = M_0(\frac{1 - e^{-TR/T_1}}{1 - \cos\theta e^{-TR/T_1}}) \qquad [3\text{-}14]$$

where TR is the time interval between RF pulses, θ is the flip angle and M_{ze} is the steady state equilibrium value of longitudinal magnetisation. The transverse magnetisation, which determines the signal collected at steady state, is:

$$M_{xy}(t) = M_{ze} \sin\theta e^{-t/T_2^*} \qquad [3\text{-}15]$$

Combining Equation [3-15] with Equation [3-14], the signal intensity of the gradient echo sequence is:

$$S_{GRE} = M_0 \sin\theta e^{-TE/T_2^*}(\frac{1 - e^{-TR/T_1}}{1 - \cos\theta e^{-TR/T_1}}) \qquad [3\text{-}16]$$

The flip angle which maximizes the signal is the Ernst Angle [10] and is given by:

$$\theta = \arccos(e^{-TR/T_1}) \qquad [3\text{-}17]$$

The TE and flip angle may also influence the contrast in gradient echo images according to Equation [3-16]. Large flip angles result in strong T_1 weighted images and small flip angles result in spin density (short TE) and T_2^* (long TE) weighted images.

3.2.3 FOV and spatial resolution

The field of view (FOV) is the region of the subject contained within the reconstructed image. Consider the frequency encoding method discussed above (Section 3.1.2), where a linear gradient with amplitude of G_x is applied to the subject. The spins at the centre of the FOV experience a magnetic field of amplitude B_0, whilst the right side experiences a greater

field and the left side a smaller field, as shown in Figure 3-7. From Equation[3-2], the maximum and minimum frequency of signal within k-space is:

$$\omega_{max} = \gamma(B_0 + G_x x_{max}) = \gamma(B_0 + \frac{1}{2}G_x FOV_x)$$

$$\omega_{min} = \gamma(B_0 + G_x x_{min}) = \gamma(B_0 - \frac{1}{2}G_x FOV_x)$$

[3-18]
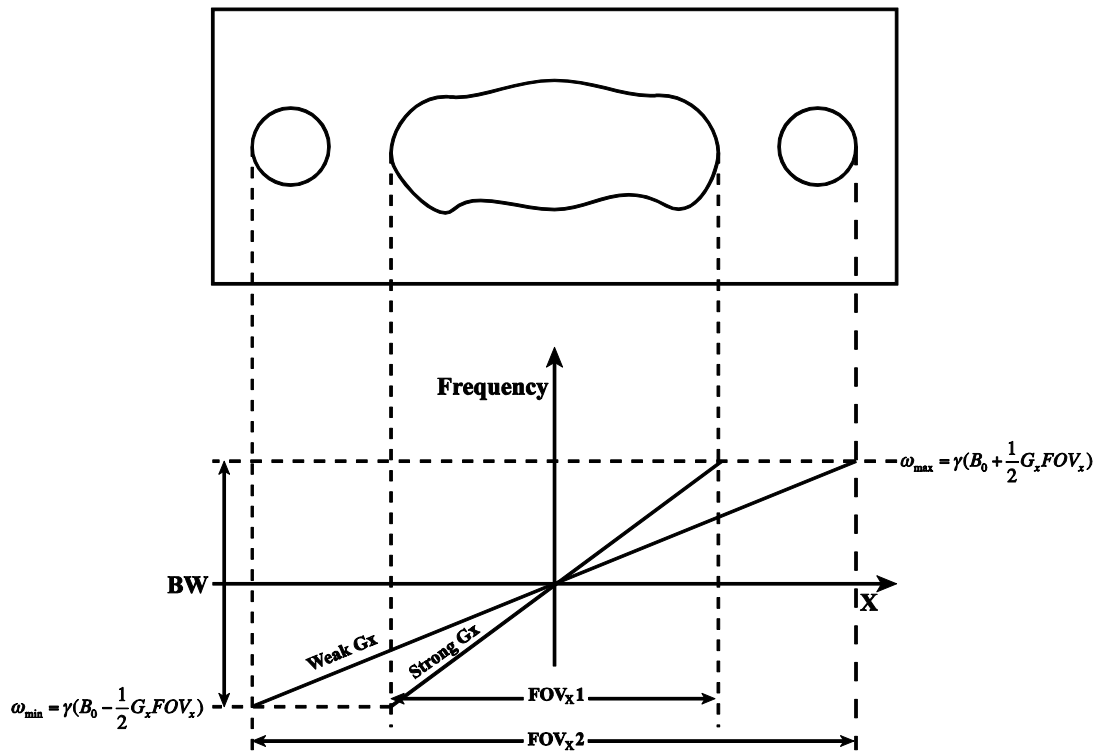
Figure 3-7: The FOV and its relationship with BW and gradient amplitude. With the same BW, a larger gradient results in smaller FOV.

The spread of frequencies from sampling is named bandwidth (BW). If we define the time interval of sampling as Δt, then the BW can be described as:

$$BW = \frac{1}{\Delta t} = \frac{\omega_{max} - \omega_{min}}{2\pi} = \frac{\gamma}{2\pi}G_x \cdot FOV_x$$

[3-19]

From Equation[3-4], the sampling step in k-space is:

$$\Delta k_x = \gamma G_x \Delta t \quad [3\text{-}20]$$

The FOV_x of the image is then related to the sampling interval in k-space, Δk_x by:

$$FOV_x = \frac{2\pi}{\gamma G_x \Delta t} = \frac{2\pi}{\Delta k_x} \quad [3\text{-}21]$$

Once the FOV is fixed, the sampling interval in k-space, Δk_x, is fixed too. If N_x voxels are collected within the FOV_x the resolution is $\Delta x = FOV_x / N_x$, so for a given number of sampling points, one can choose either to have high resolution and a small FOV (large Δk_x) or coarse resolution with a large FOV_x (small Δk_x). A large FOV_x requires less strength of the frequency encoding gradient or a smaller sampling interval. By transforming Equation [3-21] into k-space, the required coverage of k-space along the x axis in order to reconstruct the image with resolution Δx is:

$$k_x^{max} = 2\pi/\Delta x \quad [3\text{-}22]$$

The FOV_x is determined by Δk_x and the resolution of an image is determined by k_x^{max}, meaning that high resolution images require sampling of a large region of k-space. Similarly, for the phase encoding direction along y axis:

$$FOV_y = \frac{2\pi}{\gamma G_y \Delta t} = \frac{2\pi}{\Delta k_y} \quad [3\text{-}23]$$
$$k_y^{max} = 2\pi / \Delta y$$

3.2.4 Signal to Noise Ratio

The MR signal contains thermal noise, which could disturb the reconstruction of the image. To obtain images with better quality, we want to measure the signal from tissue whilst

minimising the contribution from the noise. The signal to noise ratio (SNR) measures the degree to which the noise affects the signal we record. For a 2D Fourier method, the SNR is given by [11] :

$$SNR \propto \Delta x \Delta y \Delta z \sqrt{\frac{N_y NEX}{BW}} \qquad [3\text{-}24]$$

The Δx Δy Δz is the volume of each voxel, N_y is the number of phase encoding steps, NEX is number of averaged experiments and BW is bandwidth. As the thermal noise is proportional to the square root of BW, the SNR is inversely proportional to the square root of BW. The SNR of an image can therefore be improved by averaging, but this will result in longer scanning times. To generate images with good SNR, other factors such as acquisition time and hardware limitations have to be taken into account. For example, SNR can be increased by imaging at high magnetic fields. For a 3D imaging method, similarly we have:

$$SNR \propto \Delta x \Delta y \Delta z \sqrt{\frac{N_y N_z NEX}{BW}} \qquad [3\text{-}25]$$

In a 3D imaging method, slice-selection is not used and the whole slab is excited every time an RF pulse applied. As SNR is now also dependent on the number of phase encoding steps in the z-direction, N_z, SNR is dependent on the coverage in the z-direction, with larger coverage resulting in increased SNR.

3.3 *Fast imaging*

The vast majority of functional MRI (fMRI) experiments are performed using BOLD (Blood Oxygenation Level Dependent) contrast. There are two kinds of paradigm used in fMRI:

block and single-event. Block paradigms are designed to measure BOLD signal changes between periods of activation and rest (typically in the range of 20-30s), whilst single-event paradigms measure the haemodynamic changes in response to stimulation. In the single-event paradigms, which are used for the experiments described in this thesis, the stimuli are of short duration; the haemodynamic changes reach a maximum at about 6s after the stimulus onset. Therefore, fast imaging methods are required.

Echo Planar Imaging (EPI), developed by Sir Peter Mansfield in 1977 [12], represents a crucial improvement in fast imaging. EPI allows a complete 2D image to be acquired after one RF pulse, reducing the acquisition time to only a few tens of milliseconds. EPI is widely used in BOLD fMRI and for other applications such as cardiac, perfusion and diffusion imaging. The first sequence adopted by Mansfield employed a zigzag trajectory through k-space areas. Nowadays k-space is sampled in a rectilinear fashion [13]. There are multiple variations of the conventional EPI method, such as spiral EPI and multi-shot EPI [14-16].

3.3.1 Single-shot GE-EPI

The basic EPI sequence shown in Figure 3-8 is a single-shot, gradient echo 2D EPI sequence.
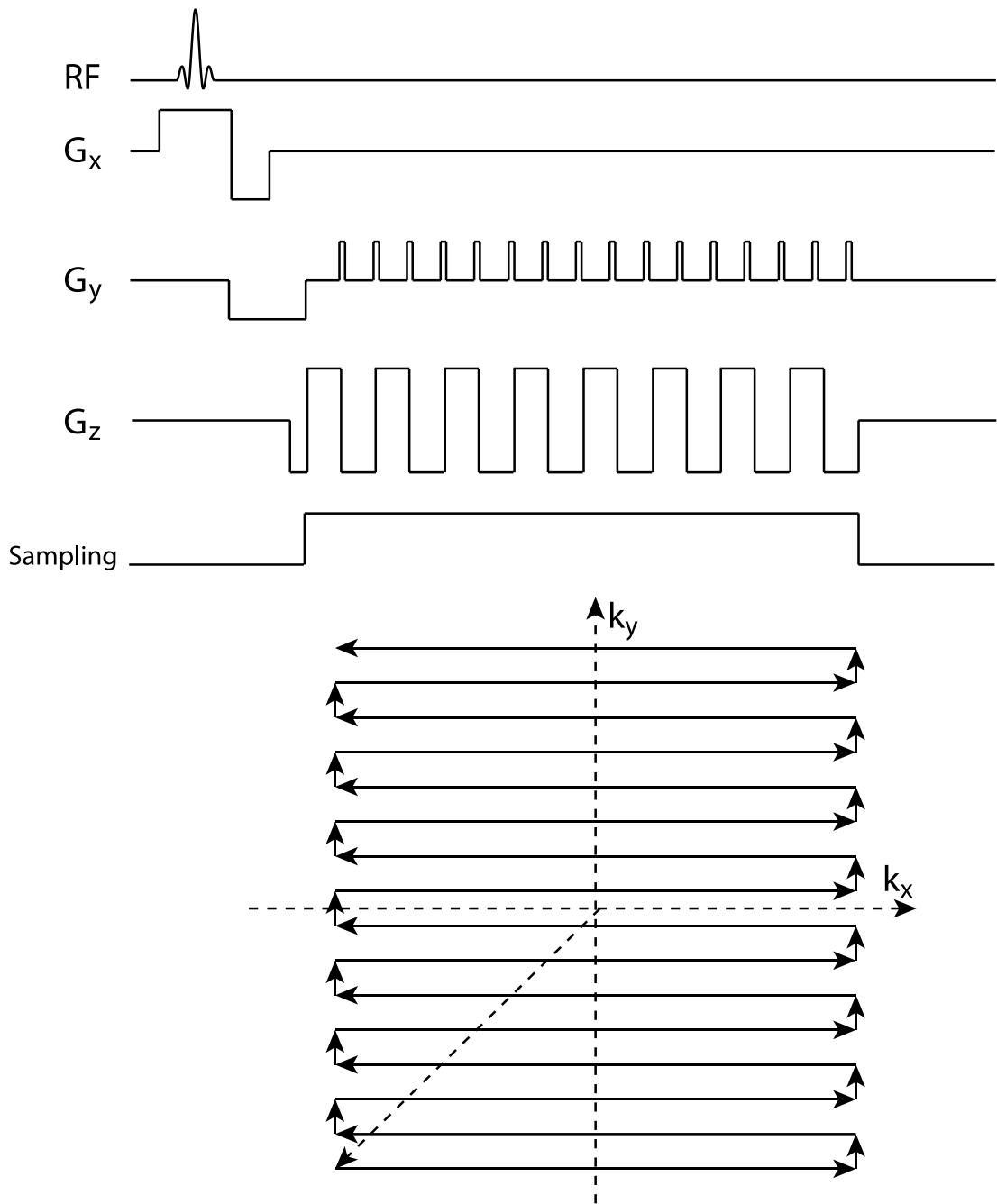
Figure 3-8: The EPI pulse sequence is shown in the upper panel whilst the trajectory through k-space is shown in the lower panel.

The main difference between EPI and conventional MRI methods is the application of a fast switching readout gradient and accompanying phase encoding gradient. The bipolar readout gradient waveform generates multiple echoes, which are k-space lines collected in

alternating directions. The first lobe is applied to move the start point to $-k_x^{max}$. Its area is half that of the following readout gradient lobes. The second lobe moves the point through k-space from $-k_x^{max}$ to k_x^{max}, the next back from k_x^{max} to $-k_x^{max}$, thereafter alternating throughout the echo train. The phase encoding gradient applied before the read out gradient ensures the trajectory of k-space data acquisition starts at $-k_y^{max}$. The following short phase encoding lobes have identical area and polarity and cause the locations of k-space lines to move from $-k_y^{max}$ to k_y^{max} in discrete steps at the end of acquisition of each k_x line.

In EPI, the data are collected whilst the transverse magnetisation decays due to T_2^*. However, because of the dephasing effects of gradient applied, the exponential decay could only describe the signal of the central echo. The TE of the central echo at $k_y=0$ determines the effective contrast for the whole image. From previous discussions and Equation 2-54, the T_2^* decay of the central lobe can be described as:

$$M_{xy}(TE) = M_{xy}(0)e^{-TE/T_2^*} \quad \text{[3-26]}$$

3.3.2 Limitations and artefacts of EPI

EPI allows ultra-fast imaging with a reasonable contrast but it also has disadvantages and limitations. EPI requires a homogeneous main field and a fast switching gradient, neither of which is easily achieved. As k-space is traversed relatively slow in the phase encoding (y) direction, susceptibility differences, chemical shift and other effects lead to artefacts in the images. The main artefacts which affect EPI are described below. These artefacts can be minimised with improved hardware and careful selection of imaging parameters.

3.3.2.1 Nyquist ghost

The Nyquist ghost, which is also called the N/2 ghost, is one of the most common artefacts in EPI [17]. The reason why EPI is sensitive to this artefact is that the MR signal is collected using a bipolar readout gradient. As the data lines in k-space are filled in opposite directions, imperfections of the MR system will result in errors that alternate between neighbouring lines and the interval of mismatch is $2\Delta k_y$. Thus the modulation of signal will result in a ghost artefact that is half of the Nyquist frequency (N/2). A number of factors, such as phase inconsistency, field inhomogeneities, imperfection of gradient waveform, high-order eddy currents etc contribute to this ghost artefact. When the image is reconstructed, it will appear as a low density "ghost" along the phase encoding direction, and shifted by half of the field of view. Figure 3-9 illustrates the errors in k-space and the image of this ghost.
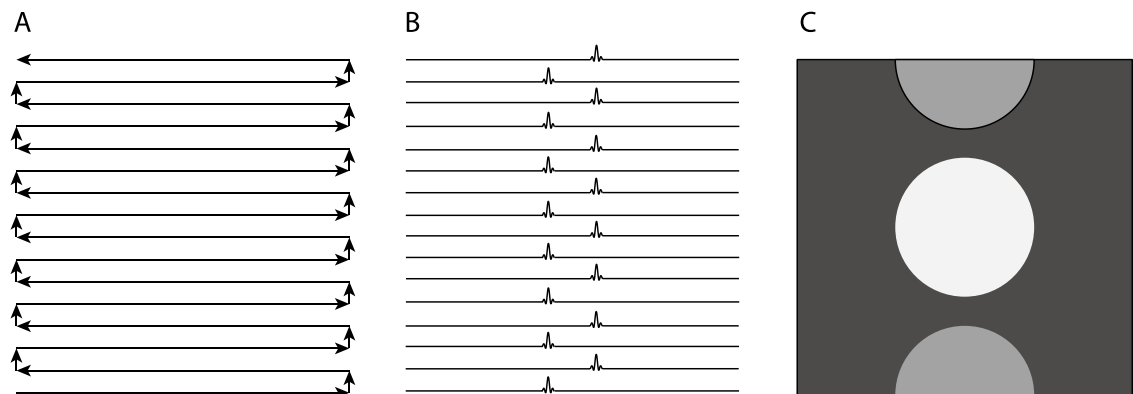
Figure 3-9: The trajectory through k-space for a conventional EPI sequence [A]. Adjacent lines are filled in opposite directions. Mismatches between adjacent lines [B]. Nyquist Ghost [C].

There are several ways to reduce or eliminate the Nyquist Ghost. Usually, a non-phase encoded data set is collected prior to the EPI scan as reference data. The shift of the echo can be calculated from these data and corrected before reconstruction. [18]. Alternatively, the reference scan could be embedded in the phase encoding scan. One phase encoding step is

not applied and the data line (usually the middle line) is collected twice in opposite directions and used as a reference. Other strategies such as improvement of gradient waveforms and high-order phase correction are also sometimes adopted [19-20].

3.3.2.2 Chemical shift

The principle underlying chemical shift is that the resonance frequency of protons depends on their local environment. The precession frequencies of hydrogen nuclei, which are most commonly imaged in MRI, are slightly different in water and fat. The difference is about 3.5ppm, which correspond to about 448Hz at 3T and 1050Hz at 7T. Since the frequency of protons in fat is shifted, in conventional gradient echo and spin echo methods, the chemical shift artefacts will manifest along the frequency encoding or slice selection directions. But the situation is different in EPI sequence. As the readout bandwidth is large, the chemical shift artefact along the frequency encoding direction is effectively suppressed. On the other hand, as the whole k-space is collected after a single excitation, the bandwidth in the phase encoding direction is quite narrow and chemical shift will cause a large artefact along this direction. Short TI inversion recovery (STIR) is a widely used method to suppress this artefact [21]. It applies a 180° pulse, flipping both water and fat spins into the −z direction. At the time that the longitudinal magnetisation of the fat spins crosses the zero point, the RF excitation pulse is applied and the influence from fat is suppressed. In high field MRI, this extra 180° pulse could lead to problems with Specific Absorption Rate (SAR), which represents the absorption of RF power, and alternative methods are sometimes preferred. For example, the chemical shift selective (CHESS) method uses a spectrally selective pulse to excite only the water spins, leaving the spins in fat unaffected [22].

3.3.2.3 Image distortion

The image distortion comes from regions with off-resonance effects. Field inhomogeneities, which may result from magnet imperfection, eddy currents and susceptibility differences (which originates from different magnetic susceptibility χ_m between different tissues or tissue and air) are the main source of image distortion. In EPI, as a narrow bandwidth is applied along the phase encoding direction, it manifests itself mainly in this direction. Better shimming methods could also reduce distortion by minimising field homogeneities. At 7T, this artefact is more prominent as susceptibility effects are increased with field strength. A B_0 map can be acquired and used to improve shimming. Post-processing methods such as phase correction based on B_0 mapping can also be used to reduce image distortion [23].

Besides the artefacts above, there are many other kinds of artefacts. Intra-voxel dephasing, which is caused by susceptibility effects, gives rise to signal loss and T_2^* induced blurring, which means different k-space lines are differently weighted because of T_2^* effects. These artefacts should also be considered in actual experiments [24].

3.3.3 Parallel imaging

Parallel imaging methods, which are applied to decrease imaging time, can also alleviate susceptibility induced artefacts. Parallel imaging methods require the use of multiple receiver coils. Because each channel in the phased array system only maps part of the subject, the imaging time can be significantly reduced. After parallel imaging was developed, it was used in fMRI to achieve ultra-fast imaging [25-26]. The use of parallel imaging allows the number of phase-encoding steps to be reduced whilst maintaining the same k-space coverage (and therefore same spatial resolution). The distances between k-

space lines are increased by a factor R, leading to a reduction of factor R in the acquisition time. R is called the reduction or acceleration factor. As the acquisition time is reduced, compared with conventional EPI, the cumulative effect of field inhomogeneity is also reduced, reducing susceptibility induced image artefacts. However, as there are fewer k-space lines, the FOV will be reduced and will lead to aliasing and wrap-round artefacts. As phased array coils are used, the spatial sensitivity profiles of the coils are used to solve this problem. There are two strategies commonly used, Sensitive Encoding (SENSE) [27] and Simultaneous Acquisition of Spatial Harmonics (SMASH) [28]. In Philips scanners used in the SPMMRC, the SENSE algorithm is implemented. In SENSE reconstruction, k-space data acquired from each channel are reconstructed separately, generating multiple images of the same subject. Images from individual coils are aliased, but they are weighted with the sensitivity of their coils and can be combined to generate images without aliasing artefacts. The SENSE method reduces the acquisition time by the reduction factor R, but also results in a SNR decrease by $\sqrt{R}$. For fMRI using GE-EPI and SENSE, R is usually between 2 and 4. In our work, a 16-channel SENSE coil was used at 7T for fMRI and a reduction factor R of 2 was used to reduce the number of phase encoding steps.

3.4 *Hardware of MRI system*

3.4.1 Overview of MRI system

All the work presented in this thesis, unless otherwise stated, was carried out on the Philips Achieva 7T and 3T systems at the Sir Peter Mansfield Magnetic Resonance Centre at the University of Nottingham. Most of the functional scans were acquired using the 7T system

whereas whole head anatomical scans were acquired using the 3T. A diagram showing the relationship of the component parts of the 7T system is shown in Figure 3-10. The superconducting magnetic with 90cm bore diameter, shim coil, gradient coil, transmit and receive coils are located within a screened room. The computers, waveform generator, gradient, RF and pre-amplifiers and other accessories are outside the screened room.
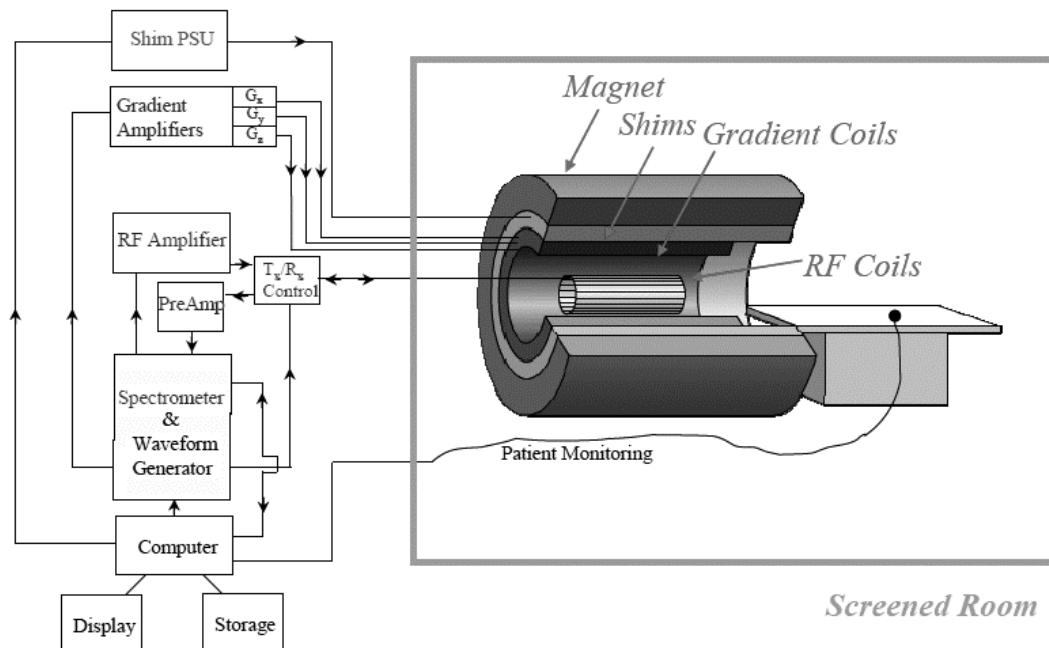
Figure 3-10: Over view of MRI system. The hardware, which drives the system, is shown in the left half. The right half illustrates the magnet and coils in a cutaway version.

3.4.2 Magnet

The magnet is the main part of an MRI system; it supplies the static magnetic field B_0, which ranges from 0.1T to 7T or even higher. Most clinical MR scanners operate at 1.5T though increasingly they are being replaced by 3T systems. The scanners for research are usually at 3T, 7T and even higher.

There are three types of magnet: permanent magnet, electromagnet (iron-cored or air-cored) and superconducting magnet. Typically, permanent magnets are made of ferromagnetic materials, horseshoe shaped to generate a magnetic field between the two poles. The commonly used material is neodymium, iron, boron (NdFeB), which is made into small bricks and then assembled into a yoke. No additional electrical power or cooling system is required and the limited fringe field largely eliminates the missile effect. The fields of permanent magnets are usually less than 0.45T due to weight considerations. The field homogeneity is also an on-going problem as it varies with changing temperature, aging of magnet etc. The electromagnets, which were quite popular in the early days of MRI, require a strong current to generate the field. For a typical 0.2T magnet, the current is 300A and consumption of electricity is over 60kW, so a cooling system is essential and the field strength is usually limited.

Nowadays, superconducting magnets are most often used for MRI scanners both in the clinic and for research. The superconducting material of most magnets including the 3T and 7T is niobium-titanium (NbTi), which is a Type-II superconductor with a critical temperature of 10K and critical field of 15T [29]. Although both values are lower than some other materials such as niobium-tin (Nb_3Tn), NbTi is still the best choice as it has good mechanical properties. NbTi is machined into fine filaments with diameter less than 1mm, embedded in a copper matrix. Superconducting magnets can generate fields more than 10T and have good homogeneity. To reduce the effect of the fringe field, shielding is always needed. There are three kinds of shielding used in practice. The first is a traditional passive shield. A large iron yoke is placed around the magnet, proving a return path for fringe magnetic flux, containing the field and bringing the 5 Gauss (0.5mT) safety line close to the magnet. The second is active shielding: a secondary coil is used to generate a field to cancel the main magnetic field in the region where it is not desired [30]. This type of magnet is also referred to as self-shielded and is widely used in scanners with fields lower than 4T. The last type is room

shielding. High permeable material such as iron is place on the wall, floor and ceiling of the room where the magnet is located, forming a shield to limit the fringe field within it. The magnet from Varian used in the Philips 7T system is shielded in this way.

3.4.3 Shimming

In MRI systems, shimming is the correction of the inhomogeneity of the main magnetic field due to imperfections of the magnet, existence of external ferromagnetic objects or the susceptibility effect. There are two types of shimming used. One type is passive shimming: several pieces of iron are placed at well calculated positions on 24-36 rails, which are mounted on the inner surface of the magnet bore. Magnetic flux is bent by these pieces of the iron and the homogeneity of main magnetic field is improved. Passive shimming is installed during the commissioning of a scanner and it is inadaptable. The other type is active shimming. A shim coil is placed in the magnet (Figure 3-10). Current in the coils generates an auxiliary magnetic field in order to compensate for inhomogeneities of the main magnetic field. Typically, there are 2-3 orders of shims in multiple shim coils. Active shimming is adjustable and widely used to solve problems arising from susceptibility effects. This effect causes the distortion of field when a subject is placed in the scanner, especially at the boundaries between media with different susceptibility such as air/tissue interfaces. On the Philips 7T scanner, we use B_0-mapping before the acquisition of functional scans. Deviation of the magnetic field from its nominal B_0 value is characterised and the shimming currents which minimise field inhomogeneity are calculated. Currents in the shim coils are then adjusted resulting in reduced susceptibly-induced artefacts and optimal T_2*-weighted functional scans. On most commercial MRI systems, active shimming is usually done automatically.

3.4.4 Gradient coils

At the beginning of this chapter, strategies of spatial encoding in MRI were discussed. Frequency encoding, phase encoding and slice selection all require spatially varying magnetic field gradients. Some other applications, such as encoding motion information, in perfusion MRI for example, also require gradient fields. The purpose of a gradient coil set is to produce magnetic fields that vary linearly in three orthogonal directions (G_x, G_y and G_z). Passing currents through three gradient coils usually wound on a cylindrical surface produces these fields.

There are several requirements for the gradient coil. The maximum gradient amplitude G_{max} (mT/m) and homogeneities of gradient over the sample volume are important parameters. Slew rate (T/m/s), which indicates the rapidity of gradient switching and duty cycle, which indicates the percentage of time during which the gradient system can be run, are also considered. The 3T we use has G_{max} 40mT/m and SR 200 T/m/s, whilst the 7T has G_{max} 33mT/m and SR 166 T/m/s. Both are sufficient for EPI and other fast imaging methods. Usually the duty cycle is 50% when both gradient amplitude and slew rate are maximum, but it could be higher when only one reaches a maximum. Power dissipation, which causes heating of the coil and sample, should be reduced by restricting the duty cycle. Eddy currents induced in the magnet and other equipment generate opposing fields, which disturb the gradient and degrade the images. Active shield coils are placed outside the gradient coils to confine the gradient field to the subject. However, this shielding requires additional currents which reduces the efficiency of the coils. In order to maintain the same slew rate, a higher current is required for shielded gradient system. The currents in the gradient coils are controlled by the computer, which stores the waveforms in a waveform generator and output them to the gradient amplifiers. Acoustic noise from switching gradients and peripheral nerve stimulation from currents induced in the body should also be taken into consideration.

3.4.5 Radiofrequency coils

RF coils are used in MRI mainly for two purposes: exciting the magnetisation, which is referred to as transmit coil and receiving the resonance signal from excited spins, which is referred to as the receive coil. Although we can use one coil to perform both transmitting and receiving, usually we use separate coils, as they require different properties to optimize the images.

3.4.5.1   Transmit coil

The transmit coil is used to generate RF pulses. Spins which have a Larmor frequency within the bandwidth of these RF pulses will be excited. Quadrature coils are driven by two signals with a phase difference of 90° from the amplifier. A circularly polarised RF field is generated. It provides a factor of two reduction in transmit power over a linear transmit coil. Transmit coils could also be used for receiving as well. In this case, it would be known as transmit/receive (T/R) coil.

3.4.5.2   Receive coil

There are several kinds of receive coils used in MRI for different purposes [31]. For the work in this thesis, SENSE receive only array coils are used [27]. An 8-channel SENSE coil and a 16-channel SENSE coil were used for anatomical and functional scans at 3T and 7T respectively. For these SENSE coils, a number of surface coils are placed at different locations and orientations to receive signals from different channels in parallel. Details about the SENSE strategies have been discussed in Section 3.3.3.

3.5 *MR safety*

Generally, MRI is thought to be a safe non-invasive imaging technique. Compared to ionising imaging methods such as X-ray, the energy of RF radiation is much lower and dosimetric limitation is much less. However, potential hazards still arise from static magnetic fields, gradient fields, RF fields and acoustic noise. Bioeffects of these factors should be considered to ensure the safety of subjects in the experiment.

3.5.1 Static magnetic field

The static magnetic field required for MRI is quite strong and presents several risks. As the field is not completely shielded and grows rapidly when approaching the bore, any ferromagnetic objects near the scanner could be dangerous, as they can become a lethal projectile due to the attraction of the magnet. Subjects who have a pacemaker or aneurysm clip shouldn't be scanned, as the strong magnetic field could cause the device to malfunction or move its position. People who operate the scanner should check all subjects carefully before they get into the scanner room to confirm that they meet the security for scanning. Other items, which may cause dangerous problems, such as inplants and tattoos, should also be checked and taken into consideration. As for the bioeffects of the static field, it is believed that exposure to static magnetic fields produces no long-term substantial effects. Some short-term bioeffects have been reported, including vertigo, nausea and a metallic taste in the mouth, but analysis of the effects indicate that they are below the threshold to be considered harmful. The guidelines from U.S. Food and Drug Administration (FDA) indicate that for clinical MR systems, main magnetic fields up to 8T for adults, children, infants> 1 month and 4T for neonates are considered as a non-significant risk.

3.5.2 Magnetic field gradients

In MRI scanning, gradient or time-varying magnetic fields may induce electrical currents in the nerve or muscle. As the stimulation threshold is large for cardiac muscle and skeletal muscle, the bioeffect usually expected is peripheral nerve stimulation (PNS). It is perceived as tingling or tapping sensations and if the amplitude reaches 50%-100% over threshold, the subjects may feel uncomfortable or be in pain. This effect is dependent on the direction of the gradient field; different parts of body are sensitive to different orientations of field change. The threshold for PNS is about 60T/s and the limitation of the UK National Radiological Protection Board is 20T/s.

3.5.3 Radiofrequency fields

The majority of the RF power transmitted for an MRI scan is transformed into heat within the patient's tissue. Thermogenic aspects of this RF field could generate bioeffects. The dosimetric term SAR is applied to measure the absorption of RF power, typically in units of W/kg. The SAR in a MRI scan is determined by multiple parameters including frequency, type of pulse, repetition time, flip angles, type of coils and so on. The limitations to SAR under EU regulations are listed in Table 3-1

Table 3-1 SAR limits within the EU (IEC 60601-2-33)

	Whole body	Partial body	Head
SAR measurement	W/kg, averaged over 6 min		
Normal	**2**	**2-10**	**3.2**
1st level control	**4**	**4-10**	**3.2**
2rd level control	**>4**	**>4-10**	**3.2**

In our experiments, the limit of 3.2W/kg averaged over 6 min for a head scan of a normal patient is used.

3.5.4 Acoustic noise

The acoustic noise from the MRI system could be a problem and cause harmful bio-effects if the patient is not well protected. The magnetic field gradient is the main source of the noise. The currents in the static field produce a strong Lorentz force upon the coils. When the direction of currents change, so does the direction of the force, causing vibration and motion of the coils and generating the noise. The noise limitation of FDA for MRI systems is 140dB for the peak sound pressure. However, exposure to noise over 99dB without proper protection could result in temporary or permanent hearing impairment. Both noise control methods for the scanner and protection equipment for patients are applied in the clinic and research scanners.

3.6 *Blood Oxygenation Level Dependent contrast*

In functional MRI, the objective is to measure a signal which reflects dynamic brain activity. In this thesis we will mainly focus on fMRI based on Blood Oxygenation Level Dependent (BOLD) contrast, which originate from the changes in magnetic properties of haemoglobin between oxygenic and deoxygenic states. The ratio of oxy- to deoxyhaemoglobin in local capillaries, venules and veins is affected by the consumption of oxygen in the tissues around them and this depends on neuronal activity. Hence, an image with contrast related to this

ratio should reflect the functional activity. Besides BOLD contrast, there are other fMRI methods based on mapping Cerebral Blood Flow (CBF) changes and Cerebral Blood Volume (CBV) changes [32-33].

3.6.1 Physical basis of BOLD

Most oxygen in blood is bound to haemoglobin in the red blood cells. As illustrated in Figure 3-11, haemoglobin is an iron-containing metalloprotein with four heme groups. Each heme group consists of an iron (Fe) ion held in porphyrin. The magnetic properties of haemoglobin rely on its status of oxygenation [34]. In deoxygenated haemoglobin, each iron in the heme group is in the high spin state (Fe^{2+}), having four of its six outer electrons unpaired. As the electron has a very large magnetic moment, if an unpaired electron is present in the sample, e.g. in the form of a free radical or paramagnetic ion, it will have a large effect on the magnetic properties. Deoxyhaemoglobin, therefore, shows a pronounced paramagnetic property. In contrast to deoxyhaemoglobin, when oxygen is added, one of these electrons is partially transferred to an oxygen molecule and the iron state becomes a low-spin state. In this case, the molecule of oxyhaemoglobin is found to have very subtle (near zero) diamagnetic magnetism. This can be interpreted as each iron atom being attached to an oxygen molecule by a covalent bond.
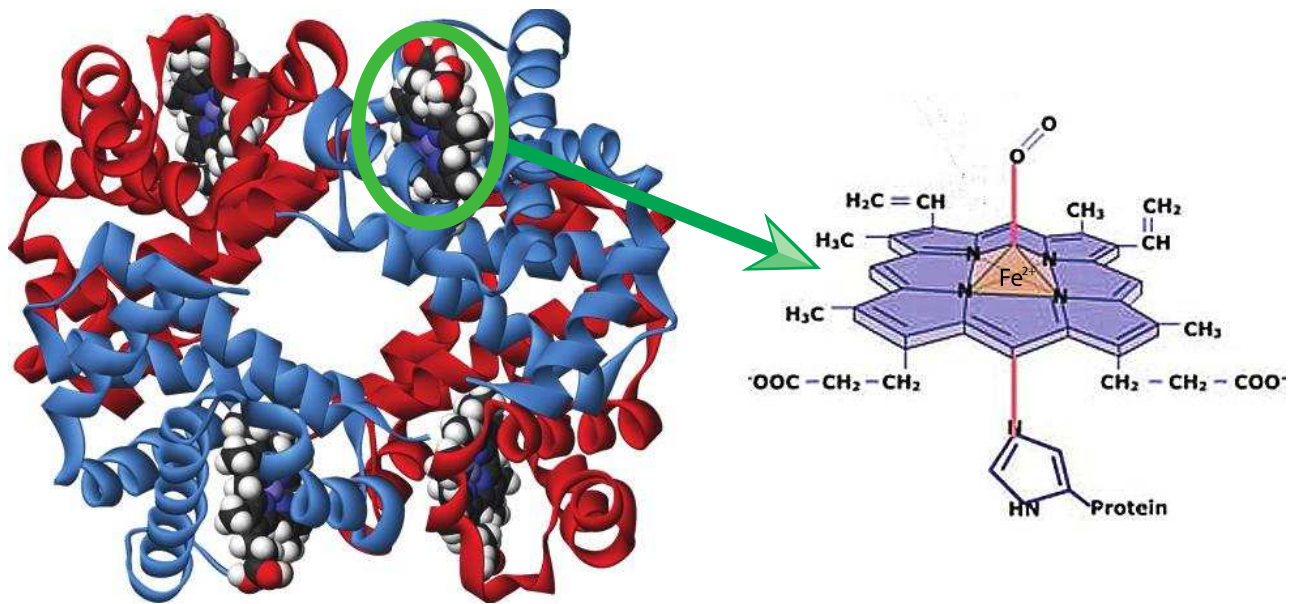
Figure 3-11: The structure of haemoglobin is shown in the left panel. It contains four heme groups, which are illustrated in the right panel. The oxygen is connected to the heme through the Fe^{2+}.

The physical basis of the BOLD effect is that the magnetic susceptibility effect from deoxyhaemoglobin in the blood influences the dispersion of T_2^* relaxation [35]. In conventional MRI, this is the same mechanism which causes susceptibility artefacts near the air and tissue interfaces. Under resting conditions, the susceptibility difference between deoxygenated blood, which is paramagnetic, and surrounding tissue, which is diamagnetic, induce large field gradients around vessels. This results in an increased phase dispersion which shortens the T_2^* and therefore reduces the MR signal in the vicinity from vessels. On activation, with less deoxyhaemoglobin present, the susceptibility of blood becomes closer to that of tissue, reducing the susceptibility difference and the phase dispersion, thus T_2^* lengthens compared to rest and the MR signal increases. BOLD contrast arises therefore from changes in the T_2^* relaxation upon activation. For small changes in R_2^* ($1/T_2^*$), written as ΔR_2^*, the BOLD signal for active (S_a) and rest (S_r) states can be written as:

$$S_r = S_0 e^{-TE \cdot R_2^*}$$
$$S_a = S_0 e^{-TE(R_2^* - \Delta R_2^*)}$$

[3-27]

The signal changes between active and rest state (ΔS) can be written as:

$$\frac{\Delta S}{S} = \frac{S_a - S_r}{S_r} = e^{TE \cdot \Delta R_2^*} - 1 \approx TE \cdot \Delta R_2^*$$

[3-28]

This equation describes BOLD contrast using the Gradient Echo method, which is most widely used in fMRI. BOLD contrast depends on TE and ΔR_2^*. The optimum BOLD contrast is obtained when imaging at a TE corresponding to the T_2^* of grey matter. ΔR_2^* increases with field strength [36]. The BOLD Contrast to Noise Ratio (CNR), which is crucial for fMRI, depends on both BOLD contrast and SNR. As SNR and BOLD contrast increase with field strength, ultra-high-field fMRI benefits from improved BOLD CNR. However, as field strength increases, the physiological noise (respiratory, cardiac) also increases. It has been shown that by using high resolution fMRI, the physiological noise can be reduced to the same level of thermal noise [37]. Therefore, the benefit of ultra-high field fMRI is better realised when imaging with small voxels.

Another benefit from using ultra-high-field systems is the increased specificity due to the reduction of signals originating from blood. Although the intravascular component only occupies a small fraction of the total volume (about 4%), experiments with diffusion weighting methods have shown that the contribution from the intravascular blood is comparable to extravascular tissues at low field strengths [38]. However, as the T_2^* of blood dramatically shortens compared to tissue T_2^* at higher field, the intravascular component is significantly reduced when imaging at echo times optimal for grey matter [39]. The BOLD signal at high field mainly reflects the changes in the tissues rather than the vessel.

3.6.2 Physiological basis of BOLD

The BOLD response measured in the study of brain function is not a direct measurement of neural activity but rather reflects metabolic activity and the blood flow changes that accompany neural activity. Neural activity in the brain requires energy, which is usually supplied as Adenosine-5'-triphosphate (ATP). The post-synaptic activity has been suggested to be the most costly compared to all the other neuronal activities. The Na^+-K^+ pump using ATP as power consumes at least half of the ATP used in brain activity. This finding should be considered when interpreting functional images. The energy metabolism changes are not associated with the location where the spike is originated, but mainly with the downstream synaptic terminals where the signal is conducted and processed. Although in the brain, considering the spatial resolution of fMRI, most dendrites are too short to distinguish the locations of metabolic changes to different voxels, some research on neurons from the hypothalamus, with long-range projections, has proved that the changes in energy metabolism are most strongly correlated with the increased synaptic activity, rather than the increased spiking activity.

The haemodynamic parameters which influence BOLD contrast are illustrated in Fig Figure 3-12.
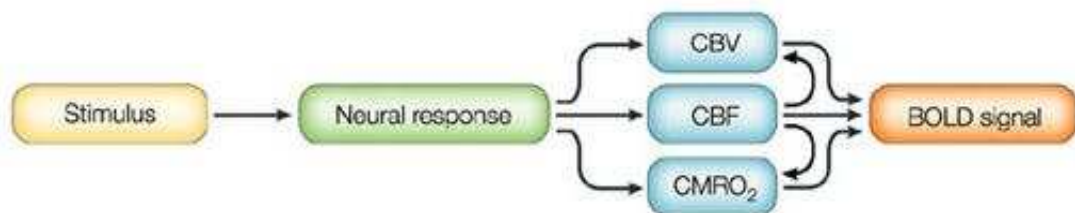
Figure 3-12: Neural activity alters BOLD by influencing several factors including cerebral blood flow (CBF), cerebral blood volume (CBV) and cerebral blood metabolic rate of oxygen consumption ($CMRO_2$) [40].
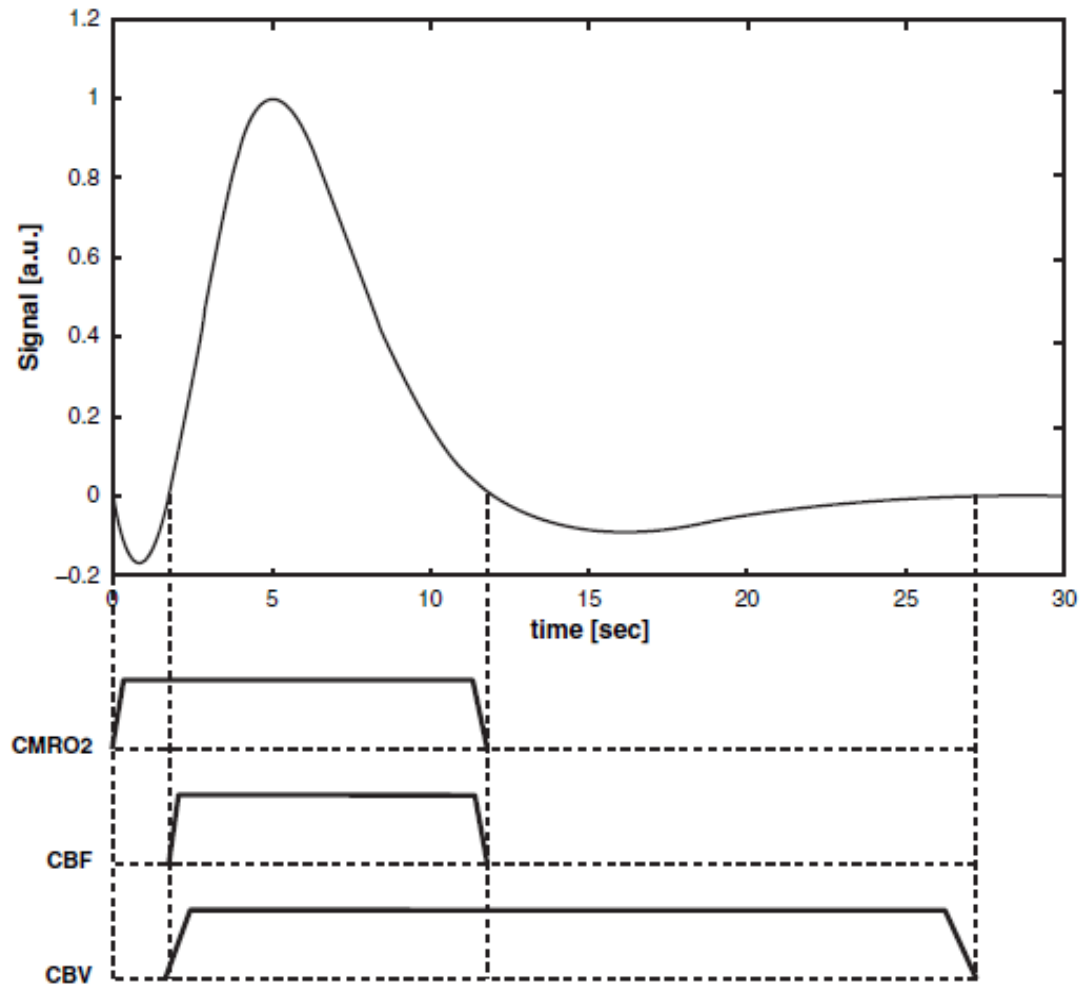
Figure 3-13: Schematic of a typical haemodynamic response following a stimulus, showing a negative initial dip, a strong positive BOLD response, and a subsequent negative undershoot. These phenomena can be explained with the different time constants of the underlying physiological parameters of CBV CBF and $CMRO_2$ [41].

Cerebral Blood Flow (CBF), Cerebral Blood Volume (CBV) and Cerebral Metabolic Rate of Oxygen consumption ($CMRO_2$) are the main components that directly contribute to the BOLD response. The expected changes in these components with brain activation have different effects on the BOLD response, making the result difficult to predict. In the

activated states, as neural activity requires energy from glucose metabolism, $CMRO_2$ in the tissue increases. The brain reacts by increasing the regional CBF to the active tissue in order to supply glucose and oxygen, and CBV increases correspondingly. The increase of CBF produces positive BOLD signals (increase of MR signal) whilst the increase of $CMRO_2$ produces a negative BOLD signal, which is much smaller. The increase in CBF brings oxygenate blood which overcompensates for the oxygen consumption ($CMRO_2$) and results in a positive BOLD change. The largest increase in BOLD response appears ~6s following the stimulus onset.

A typical BOLD timecourse is shown in Figure 3-13. Besides the main positive BOLD response, it also contains an initial dip at the beginning and an undershoot after the termination of the stimulus. The initial dip is a transient signal drop which happens about 0.5s after stimulus onset and reaches a maximum at about 2-3s. The amplitude of the initial dip is quite small, compared to the main BOLD response but more stable with the length of stimulus duration. This effect is due to a rapid increase in $CMRO_2$ before the blood flow is able to change [42]. Because of this, the initial dip may be better localized to the neuronal activity which leads to the changes in $CMRO_2$. The post stimulus undershoot, which is a negative BOLD change following the positive BOLD change, has been a source of speculation for a long time. Research using a combination of fMRI and Arterial Spin Labelling (ASL) has demonstrated that undershoot of BOLD exists without any change of CBF [43]. It has also been found that $CMRO_2$ is well correlated with CBF change whilst CBV recovery lags behind that of CBF[44]. When the activation is terminated, CBF, which has a positive effect on BOLD recovers to the baseline quickly. After it has recovered, CBV is still larger than in the resting state, generating a small negative signal, known as undershoot.

Previous research using PET suggested that the increased glucose metabolism is associated with functional activity [45]. The metabolic rate in grey matter is about 3-4 times that in white matter. High-resolution studies show that the layer IV of the cortex which also has the largest density of synapses has the highest metabolic rate [46]. This confirms that the metabolic rate is mainly connected to the synapse [47]. As glucose metabolism requires oxygen as well, the $CMRO_2$ should also change with the functional activity. However, the measured balance of CBF and $CMRO_2$ shows that the increase of O_2 metabolism is much less than that of glucose (CMRGlc), suggesting that transiently a large fraction of energy required for brain activity is from the pathway of glycolysis which generates ATP without oxygen [48].

3.6.3 Spatial and temporal resolution of BOLD fMRI

In order to optimize the spatial and temporal resolution of fMRI experiments, many factors need to be considered, including the limitations in spatial and temporal resolution posed by the physiological origin of the BOLD response. A trade-off between CNR, coverage, spatial and temporal resolution is usually required in the determination of scanning protocols.

3.6.3.1   Spatial resolution

The spatial scales of neuronal activity vary across different types of brain function. The scale of these areas is typically tens of millimetres and they could be further divided to multiple specialized areas which have scales of several millimetres. In some well-studied cortices, e.g. visual cortex, a sub-unit which participates in the early sensory processing has been found and has a size less than 1 mm (ocular dominance columns). Somatosensory function is

mainly organized in the somatosensory cortex, which could be further separated into primary and secondary somatosensory cortexes. The sub-units of the somatosensory cortex are the columns reflecting the sensory input from different parts of the body.

The spatial resolution of a BOLD fMRI experiment depends on both the voxel size and the volume over which haemodynamic regulation occurs. The vascular origin of the BOLD response poses a limit to the achievable resolution due to the contamination from veins which drain large areas of the cortex, which may result in a mismatch between the measured BOLD response and real locations of neural activities perhaps by as much as millimetres [49]. This suggests that the mapping of cortical layers may not be possible with fMRI methods based on GE BOLD contrast.

The spatial resolution of fMRI affects the SNR significantly. As SNR increases with voxel volume, increasing spatial resolution results in reduced SNR but also reduced partial volume effect because signals from vessels and tissues which are averaged within the voxel can be better separated. Therefore the optimal voxel size should be equal to the volume of active tissue, just small enough to resolve the activated areas and reduce partial volume effect but not any smaller in order to get the maximum SNR.

The implementation of high spatial resolution requires a trade-off in SNR, scanning time and image coverage. To achieve higher spatial resolution, the scanning time needs to be prolonged if the same coverage is required, or the image coverage can be reduced with no time penalty.

3.6.3.2   Temporal resolution

The temporal dynamic of the human brain has undergone much investigation in neuronal electrical physiology and psychology. The low level processes in the brain (e.g. visual) are usually within 200ms, whilst higher order processes could last up to several seconds after the termination of the task. In some self-paced experiments, pre-stimulus activation is also found prior to the beginning of the task. The BOLD response which is related to haemodynamic activities could be delayed even longer as mentioned above. Usually it starts about 2s after the onset of stimulus and reaches the peak at about 6s or even later. It takes over 20s to return to the baseline, making the necessary trial length in an fMRI study much longer than required for MEG and EEG.

The TR selected in the fMRI experiment determines the temporal resolution of the study. TR is an important parameter because it limits the number of slices that can be acquired in the 2D GE-EPI method used in this thesis. Besides the limitation of scanning protocols, a change in experiment design could also improve the temporal resolution. This can be done by using jittered stimuli with respect to image acquisition sampling. The haemodynamic response will be sampled from different points on each trial. Hence the interpolation of these data could result in a timecourse with higher temporal resolution for the activity of our interest.

3.7 *References*

[1]   Ljunggren, S., A simple graphical representation of Fourier-based imaging methods. Journal of Magnetic Resonance, 1983. **54**(2): p. 338-343.

[2]   Twieg, D.B., The k-trajectory formulation of the NMR imaging process with applications in analysis and synthesis of imaging methods. Medical Physics, 1983. **10**(5): p. 610-621.

[3]   Edelstein, W., Hutchison, J., Johnson, G. and Redpath, T., Spin warp NMR imaging and applications to human whole-body imaging. Physics in Medicine and Biology, 1980. **25**: p. 751-756.

[4]   Kumar, A., Welti, D. and Ernst, R.R., NMR Fourier zeugmatography. Journal of Magnetic Resonance, 1975. **18**(1): p. 69-83.

[5]   Garroway, A., Grannell, P. and Mansfield, P., Image formation in NMR by a selective irradiative process. Journal of Physics C: Solid State Physics, 1974. **7**: p. 457-462.

[6]   Mansfield, P., Maudsley, A. and Bains, T., Fast scan proton density imaging by NMR. Journal of Physics E: Scientific Instruments, 1976. **9**: p. 271-278.

[7]   MacFall, J., Charles, H. and Prost, R., Truncated sinc slice excitation for 31P spectroscopic imaging. Magnetic Resonance Imaging, 1990. **8**(5): p. 619-624.

[8]   Frahm, J., Haase, A. and Matthaei, D., Rapid NMR imaging of dynamic processes using the FLASII technique. Magnetic Resonance in Medicine, 1986. **3**(2): p. 321-327.

[9]   Constable, R.T. and Henkelman, R.M., Contrast, resolution, and detectability in MR imaging. Journal of computer assisted tomography, 1991. **15**(2): p. 297-303.

[10]   Ernst, R. and Anderson, W., Application of Fourier transform spectroscopy to magnetic resonance. Review of Scientific Instruments, 1966. **37**(1): p. 93-102.

[11]   Edelstein, W., Glover, G., Hardy, C. and Redington, R., The intrinsic signal to noise ratio in NMR imaging. Magnetic Resonance in Medicine, 1986. **3**(4): p. 604-618.

[12]   Mansfield, P., Multi-planar image formation using NMR spin echoes. Journal of Physics C: Solid State Physics, 1977. **10**: p. 55-58.

[13]   Chapman, B., Turner, R., Ordidge, R., Doyle, M., Cawley, M., Coxon, R., Glover, P. and Mansfield, P., Real time movie imaging from a single cardiac cycle by NMR. Magnetic Resonance in Medicine, 1987. **5**(3): p. 246-254.

[14]   Ahn, C., Kim, J. and Cho, Z., High-speed spiral-scan echo planar NMR imaging. Medical Imaging, IEEE Transactions on, 1986. **5**(1): p. 2-7.

[15]   McKinnon, G., Ultrafast interleaved gradient echo planar imaging on a standard scanner. Magnetic Resonance in Medicine, 1993. **30**(5): p. 609-616.

[16]   Schmitt, F., Stehling, M.K. and Turner, R., Echo-planar imaging: theory, technique and application. 1998: Springer.

[17]   Zakhor, A., Weisskoff, R. and Rzedzian, R., Optimal sampling and reconstruction of MRI signals resulting from sinusoidal gradients. Signal Processing, IEEE Transactions on, 1991. **39**(9): p. 2056-2065.

[18]   Bruder, H., Fischer, H., Reinfelder, H.E. and Schmitt, F., Image reconstruction for echo planar imaging with nonequidistant k space sampling. Magnetic Resonance in Medicine, 1992. **23**(2): p. 311-323.

[19]   Zhou, X., Maier, J.K. and Epstein, F.H., Reduction of Nyquist ghost artifacts in oblique echo planar imaging. United States Patent and Trademark Office, 1997. **5672969**.

[20]   Du, Y.P., Joe Zhou, X. and Bernstein, M.A., Correction of concomitant magnetic field induced image artifacts in nonaxial echo planar imaging. Magnetic Resonance in Medicine, 2002. **48**(3): p. 509-515.

[21]   Bydder, G., Pennock, J., Steiner, R., Khenia, S., Payne, J. and Young, I., The short TI inversion recovery sequence--an approach to MR imaging of the abdomen. Magnetic Resonance Imaging, 1985. **3**(3): p. 251-254.

[22]   Haase, A., Frahm, J., Hanicke, W. and Matthaei, D., 1H NMR chemical shift selective (CHESS) imaging. Physics in Medicine and Biology, 1985. **30**: p. 341-344.

[23]   Jezzard, P. and Balaban, R.S., Correction for geometric distortion in echo planar images from B0 field variations. Magnetic Resonance in Medicine, 1995. **34**(1): p. 65-73.

[24]   Yang, Q.X., Williams, G.D., Demeure, R.J., Mosher, T.J. and Smith, M.B., Removal of local field gradient artifacts in T2* weighted images at high fields by gradient echo slice excitation profile imaging. Magnetic Resonance in Medicine, 1998. **39**(3): p. 402-409.

[25]   Hutchinson, M. and Raff, U., Fast MRI data acquisition using multiple detectors. Magnetic Resonance in Medicine, 1988. **6**(1): p. 87-91.

[26]   Ra, J. and Rim, C., Fast imaging using subencoding data sets from multiple detectors. Magnetic Resonance in Medicine, 1993. **30**(1): p. 142-145.

[27]   Pruessmann, K.P., Weiger, M., Scheidegger, M.B. and Boesiger, P., SENSE: sensitivity encoding for fast MRI. Magnetic Resonance in Medicine, 1999. **42**(5): p. 952-962.

[28]   Sodickson, D.K. and Manning, W.J., Simultaneous acquisition of spatial harmonics (SMASH): fast imaging with radiofrequency coil arrays. Magnetic Resonance in Medicine, 1997. **38**(4): p. 591-603.

[29]   Blatt, F.J., Modern physics. 1992: McGraw-Hill.

[30]   Mansfield, P. and Chapman, B., Active magnetic screening of coils for static and time-dependent magnetic field generation in NMR imaging. Journal of Physics E: Scientific Instruments, 1986. **19**: p. 540-545.

[31]   Morris, P.G., Nuclear magnetic resonance imaging in medicine and biology. 1986: Oxford.

[32]   Le Bihan, D., Urayama, S., Aso, T., Hanakawa, T. and Fukuyama, H., Direct and fast detection of neuronal activation in the human brain with diffusion MRI. PNAS, 2006. **103**(21): p. 8263-8268.

[33]   Wang, J., Aguirre, G.K., Kimberg, D.Y., Roc, A.C., Li, L. and Detre, J.A., Arterial spin labeling perfusion fMRI with very low task frequency. Magnetic Resonance in Medicine, 2003. **49**(5): p. 796-802.

[34]   Pauling, L. and Coryell, C.D., The magnetic properties and structure of hemoglobin, oxyhemoglobin and carbonmonoxyhemoglobin. Proceedings of the National Academy of Sciences of the United States of America, 1936. **22**(4): p. 210-216.

[35]   Ogawa, S., Lee, T., Kay, A. and Tank, D., Brain magnetic resonance imaging with contrast dependent on blood oxygenation. Proceedings of the National Academy of Sciences, 1990. **87**(24): p. 9868-9872.

[36]   Peters, A.M., Brookes, M.J., Hoogenraad, F.G., Gowland, P.A., Francis, S.T., Morris, P.G. and Bowtell, R., T2* measurements in human brain at 1.5, 3 and 7T. Magnetic Resonance Imaging, 2007. **25**(6): p. 748-753.

[37]   Triantafyllou, C., Hoge, R., Krueger, G., Wiggins, C., Potthast, A., Wiggins, G. and Wald, L., Comparison of physiological noise at 1.5 T, 3 T and 7 T and optimization of fMRI acquisition parameters. Neuroimage, 2005. **26**(1): p. 243-250.

[38]   Boxerman, J.L., Hamberg, L.M., Rosen, B.R. and Weisskoff, R.M., MR contrast due to intravascular magnetic susceptibility perturbations. Magnetic Resonance in Medicine, 1995. **34**(4): p. 555-566.

[39]   Boxerman, J.L., Bandettini, P.A., Kwong, K.K., Baker, J.R., Davis, T.L., Rosen, B.R. and Weisskoff, R.M., The intravascular contribution to fmri signal change: monte carlo modeling and diffusion weighted studies in vivo. Magnetic Resonance in Medicine, 1995. **34**(1): p. 4-10.

[40]   D'Esposito, M., Deouell, L.Y. and Gazzaley, A., Alterations in the BOLD fMRI signal with ageing and disease: a challenge for neuroimaging. Nature Reviews Neuroscience, 2003. **4**(11): p. 863-872.

[41]   Deichmann, R., Nöth, U. and Weiskopf, N., The basics of functional magnetic resonance imaging, in EEG-fMRI. 2010, Springer.

[42]   Devor, A., Dunn, A.K., Andermann, M.L., Ulbert, I., Boas, D.A. and Dale, A.M., Coupling of total hemoglobin concentration, oxygenation, and neural activity in rat somatosensory cortex. Neuron, 2003. **39**(2): p. 353-359.

[43]   Buxton, R.B., Luh, W.M., Wong, E.C., Frank, L.R. and Bandettini, P.A. Diffusion weighting attenuates the BOLD peak signal change but not the post-stimulus undershoot. Proceedings in ISMRM. Sydney 1998: p. 7.

[44]   Mandeville, J.B., Marota, J.J.A., Kosofsky, B.E., Keltner, J.R., Weissleder, R., Rosen, B.R. and Weisskoff, R.M., Dynamic functional imaging of relative cerebral blood volume during rat forepaw stimulation. Magnetic Resonance in Medicine, 1998. **39**(4): p. 615-624.

[45]   Sokoloff, L., Relation between physiological function and energy metabolism in the central nervous system. Journal of Neurochemistry, 1977. **29**(1): p. 13-26.

[46]   Kennedy, C., Des Rosiers, M., Sakurada, O., Shinohara, M., Reivich, M., Jehle, J. and Sokoloff, L., Metabolic mapping of the primary visual system of the monkey by means of the autoradiographic [14C] deoxyglucose technique. Proceedings of the National Academy of Sciences, 1976. **73**(11): p. 4230-4234.

[47]   Sokoloff, L., Relationship between functional activity and energy metabolism in the nervous system: whether, where and why?, in Brain Work and Mental Activity, N.A. Lassen, D.H. Ingvar, M.E. Raichle, and L. Friberg, Editors. 1991, Munksgaard: p. 52-64.

[48]   Prichard, J., Rothman, D., Novotny, E., Petroff, O., Kuwabara, T., Avison, M., Howseman, A., Hanstock, C. and Shulman, R., Lactate rise detected by 1H NMR in human visual cortex during physiologic stimulation. Proceedings of the National Academy of Sciences, 1991. **88**(13): p. 5829-5831.

[49]   Turner, R., How much cortex can a vein drain? Downstream dilution of activation-related cerebral blood oxygenation changes. Neuroimage, 2002. **16**(4): p. 1062-1067.

Chapter 4

Magnetoencephalography

Overview: In this third theory Chapter, the basic principles, instrumentation and applications of Magnetoencephalography (MEG) are introduced. MEG is a technique that maps brain activity by recording magnetic fields produced by electrical currents in the brain, which was originally developed by David Cohen in the 1960's [1-3]. Firstly, in Section 4.1, the neurophysiological basis of MEG, including the types of neuronal cells within the brain, their electromagnetic properties and contribution to the extracranial magnetic field, is discussed. Secondly, in Section 4.2, different types of neuroelectrical effects recorded in MEG are discussed. Thirdly, the instrumentation used to record MEG signals, including the principles of Superconducting Quantum Interference Devices (SQUID), noise reduction strategies and 3D digitizer systems for co-registration, is discussed in Section 4.3. In Section 4.4, the forward problem and inverse problem are introduced and beamformer spatial filtering, the inverse method mainly used in the later experimental chapters, is discussed. Finally, Section 4.5 discusses the MEG analysis using beamformer.

4.1 *The neurophysiological basis of MEG*

4.1.1 Neurons

In the brain, there are two main classes of cells: neurons and glial cells. Neurons are the basic signalling units of the nervous system. They are electrically excitable cells which play an import role in the processing and transmission of neuronal information. A typical neuron consists of four morphologically defined regions: the cell body (soma), the dendrites, the axon and the presynaptic terminals (Figure 4-1). The soma is the metabolic centre of the cell, containing the nucleus and endoplasmic reticulum. Dendrites branch out in tree-like fashion and receive the incoming signal from other cells. The axon is a long fibre which conveys electrical signals from the soma. Near the end of the axon, it divides into fine branches, forming communication sites, which are known as synapses, with other neurons. These branches are the presynaptic terminals.
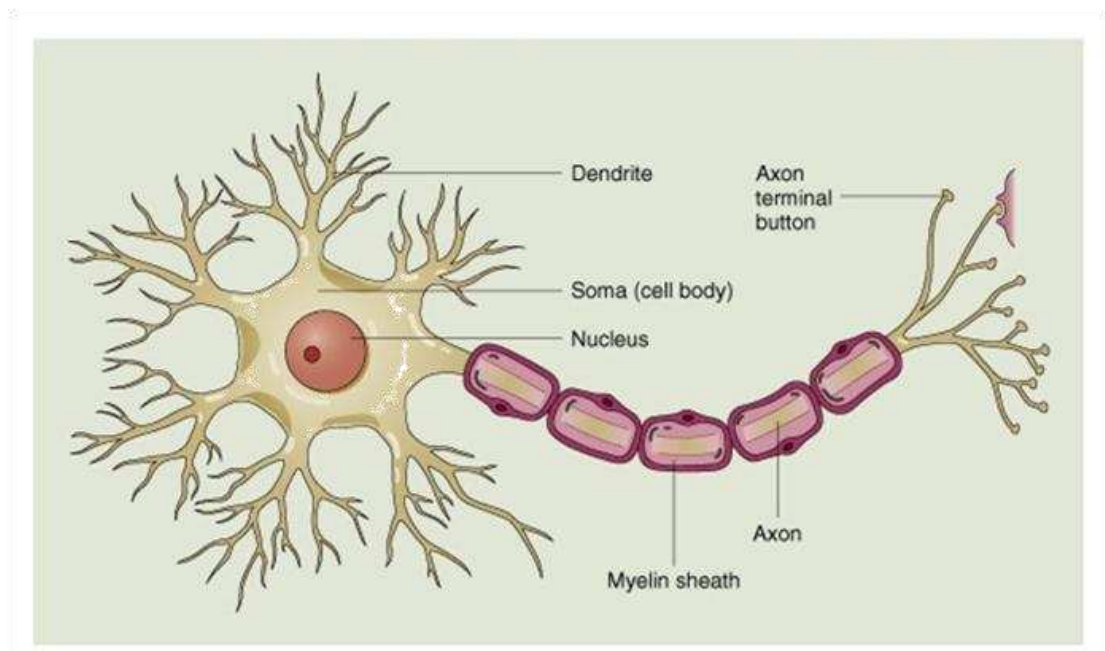
Figure 4-1: The structure of a typical neuron. [4]

Glial cells are supporting cells in the brain, which surround and support neurons and insulate between them. Glial cells also supply nutrients and oxygen to neurons, destroy dead neurons and remove their carcasses.

There are two main forms of neuronal activity: the fast depolarization of the axon, which results in action potentials and the more protracted change of membrane potentials due to postsynaptic activations. The contribution of these activities to extracranial MEG signals will be discussed in the following subsections.

For postsynaptic events associated with simple excitatory synapses, the neurotransmitter released from a presynaptic axon binds with the receptor molecules embedded within the postsynaptic dendrite membrane. This results in an increase in the membrane's permeability to positively charged ions. As the positive ions enter the cell and cause repulsion of positive ions already present, an axial intracellular current is directed away from the synaptic region of a dendrite. Then the ion pumps generate outward transmembrane currents and positive ions are repelled to the extracellular space, producing volume currents. The transmembrane currents and volume currents contribute little to the extracranial field, because they exhibit symmetry in terms of their direction of flow, however the primary current flow can result in measurable MEG signals [5]. The primary and volume currents of a neuron are illustrated in Figure 4-2.
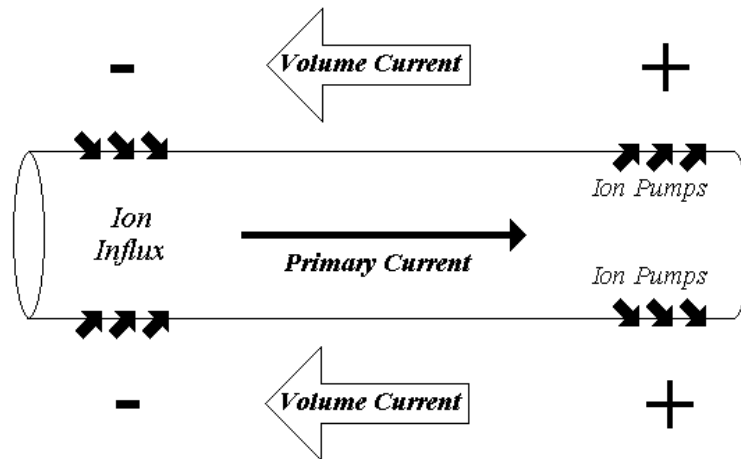
Figure 4-2: The primary current inside the dendrite is balanced by an equal but opposite volume current in the surrounding extracellular tissue. [6]

A current dipole model is used to simulate the primary dendritic currents. The dipole is defined by a positive and a negative charge with a current flowing in a straight line between them and a return current flowing in a dipolar pattern through the conductive medium. The magnitude of the magnetic field generated by a current dipole decreases as a function of the square of the distance from the source. Many (~100,000) small dipole currents must synchronise to generate the magnetic field that can be detected by MEG.

Action potentials flow in the axon is characterised by a leading edge of depolarization and a trailing edge of repolarization as they move down the axon. A dipole oriented away from the cell body is generated by the depolarization whilst an opposite dipole is generated by the repolarization [7]. Thus, the action potential could be conceived as a current quadrupole, which is illustrated in Figure 4-3. The magnitude of the magnetic field generated by a quadrupole decreases with the cube of distance. Compared to the current diploes of post synaptic currents which decrease with the square of the distance, the magnetic field recorded at a distance from an action potential attenuates much more quickly. The duration of a post synaptic current is over 10ms whilst action potentials last about 1ms. The short duration and

restricted spatial extent of the magnetic field due to an action potential make it extremely unlikely to make a significant contribution to extracranial signals [8].
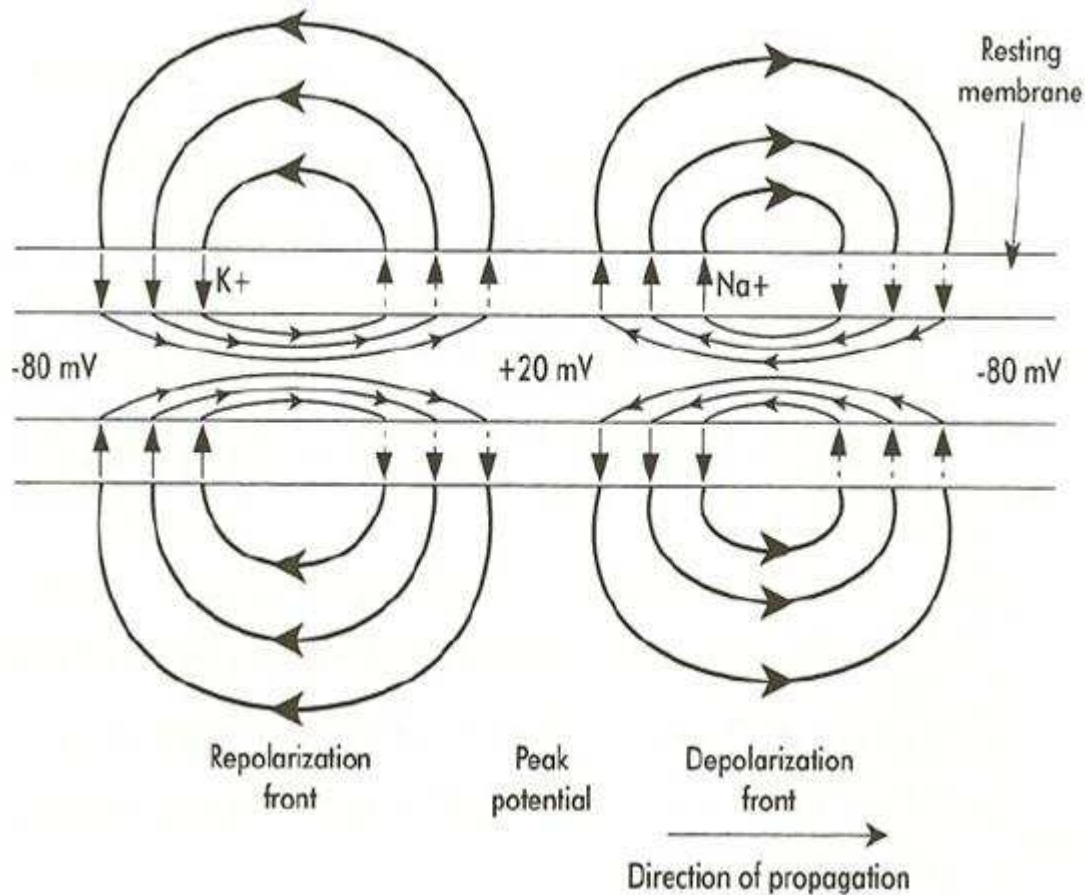
Figure 4-3: Schematic of a current quadrupole generated by action potential.

4.1.2 Morphology and organization of neurons

When considering the extracranial magnetic field, which is the summed field generated by neuronal ensembles, it is important to take into account both the morphology of a single neuron and the spatial organization (geometry) of neuronal clusters. There are two types of

neurons in the human cortex: pyramidal neurons and stellate neurons. As shown in Figure 4-4, pyramidal neurons have highly asymmetric dendrites, which are orientated perpendicular to the surface of the cortex. Since dendrite orientation directs primary current flow, pyramidal neurons offer the best chance to generate large magnetic field at a distance (open field). Conversely, the stellate neurons have symmetrically organized dendrites and the field generated is mostly limited to within the region of the cell, producing no signal at a distance (closed field) [9].
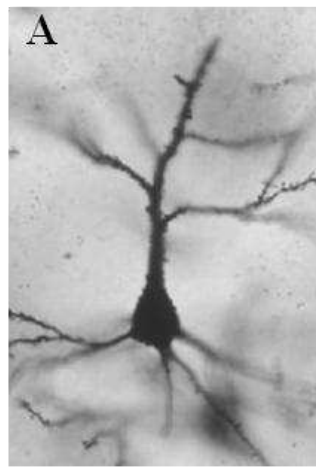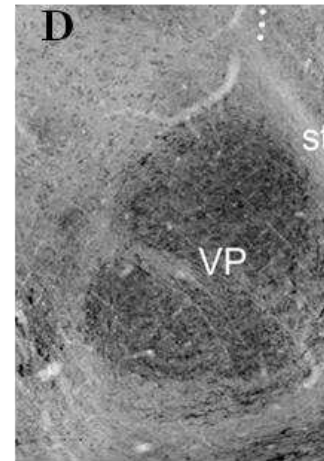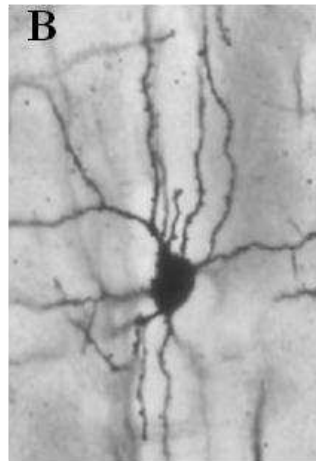
Figure 4-4: The morphology of neurons and organization of neurons. Pyramidal cells [A] are open field and stellate neurons [B] are closed field. The neocortex [C] has a largely open field configuration and the ventral posterior nucleus [D] has a closed field configuration.

In the neocortex, pyramidal neurons are arranged in cortical columns. Inside the columns, neurons are mostly parallel and arranged in laminae which are orthogonal to the surface of cortex. The synchronous activation in this open field structure could generate strong magnetic fields in the extracranial spaces. However, even for pyramidal neurons, if they are organized into a symmetric structure, as for example in some sub-cortical nuclei, because of the cancellation of magnetic fields no significant contribution to the extra cranial magnetic field will be measured [10].

4.1.3 Orientations of currents

If the conductive medium in which the neurons are embedded is of infinite dimensions and uniform conductivity, only the primary current flow within the cells produces a measurable magnetic field. This is because the return current pattern is symmetric in such a way that the magnetic field generated by each return current is cancelled out by other elements. In the actual brain, we have to consider the effect the boundary. The conductivity boundary can be mathematically replaced by surface currents that have an equivalent effect. These secondary current sources must be placed at and oriented perpendicular to the original boundary, regardless of the orientation of the primary source. Superposition of the primary and secondary currents is exactly equivalent to that generated by the dipole and its volume currents in the original boundary case. Because of the orientation of the secondary currents, if one were to measure only the magnetic field perpendicular to the boundary, as in MEG, the secondary source would make no contribution [11].

The orientations of cortical currents have significant influences on the measureable magnetic field outside of the head, which is illustrated in Figure 4-5. If the pyramidal neurons are perpendicular to the scalp, there is no extracranial magnetic field. If these neurons are parallel to the scalp, the maximum extracranial field is generated. Contributions to extracranial fields from neurons with other orientations are determined by their components in the parallel direction. In the neocortex, the pyramidal neurons are perpendicular to the cortical surface; the contribution to the MEG signal from different cortical areas is thus dependent on cortical folding. Activation in gyri and at the bottom of sulci have little effect on measured MEG signals whilst the walls of sulci, which are perpendicular to the scalp, generate most of the extracranial signals.
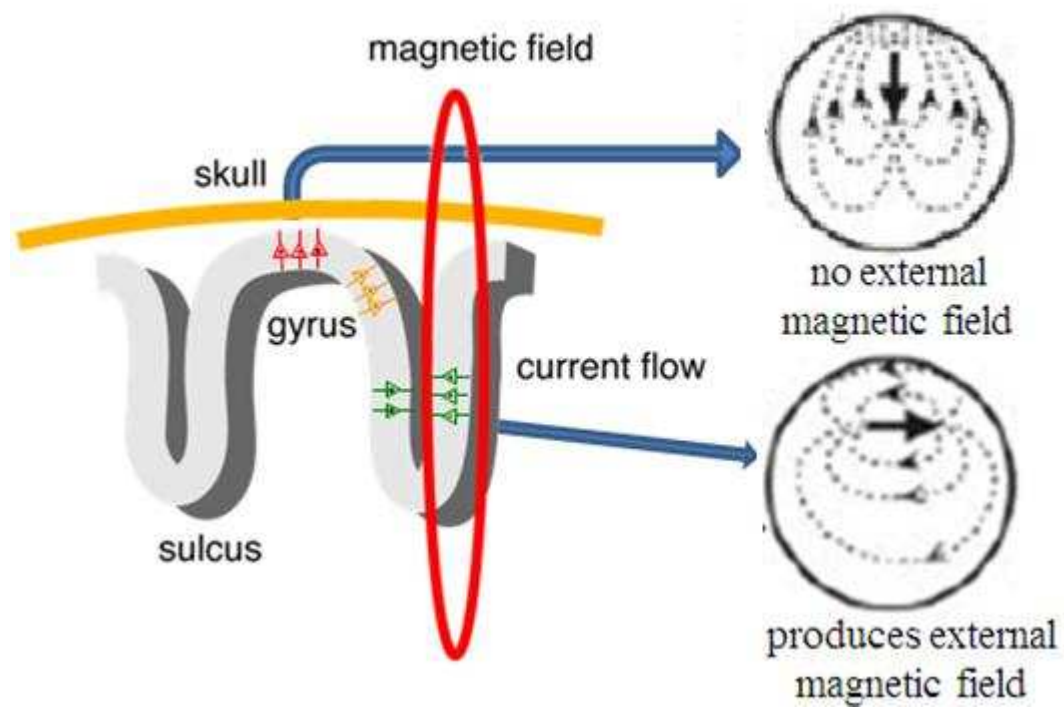
Figure 4-5: Contributions to the external magnetic field from pyramidal neurons with different orientations. The neurons parallel to the scalp (Green) generate external field whilst the neurons perpendicular to the scalp (Red) have no contribution to the external magnetic field.

4.2 *Neuroelectrical effects*

The EEG/MEG signals recorded are rich in information and contain a large number of different effects. However, these effects can be broadly classified into three categories: spontaneous rhythms, evoked responses and induced effects.

4.2.1 Spontaneous rhythms

Spontaneous rhythms are oscillatory signals observed in the absence of explicit tasks such as sensory inputs or motor outputs. They are also referred to as on-going brain activity. In 1929, Hans Berger first detected spontaneous rhythms in humans by using his newly developed EEG [12]. This finding agreed with the previous invasive animal studies under taken by Richard Caton in 1875 [13].
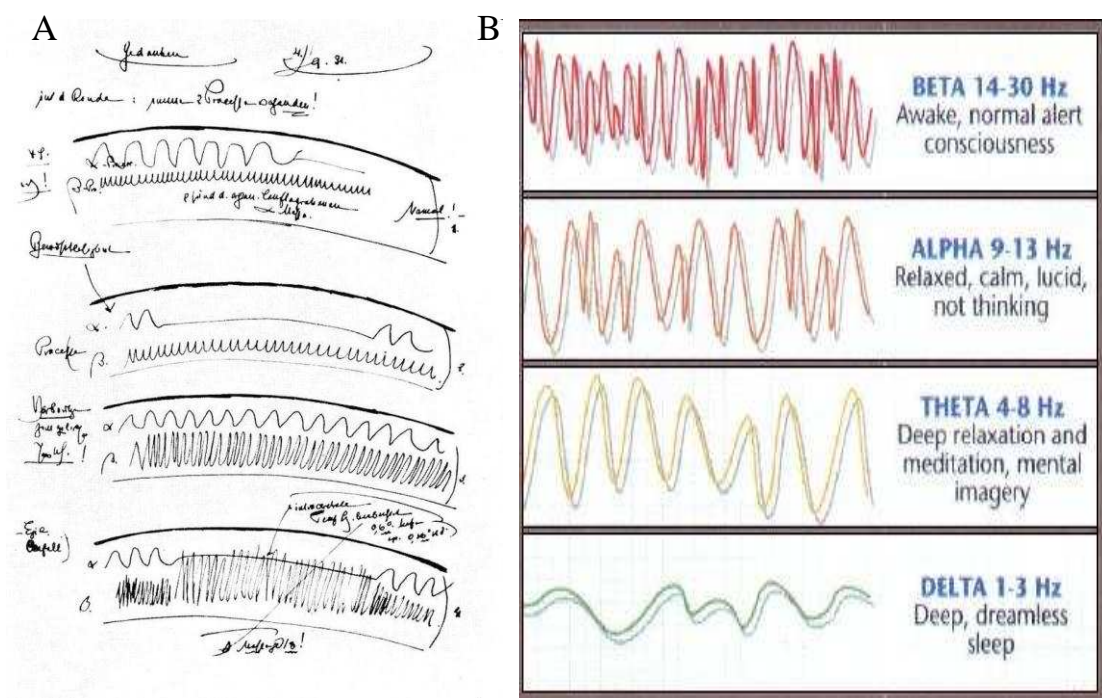
Figure 4-6: Original recording of spontaneous rhythms [A] by Hans Berger [12] and the function of spontaneous rhythms within different characteristic frequencies [B].

These spontaneous rhythms are measurable in both EEG/MEG and invasive recordings. The most prominent rhythm is found around 10Hz and is known as the alpha rhythm. It predominantly originates from the brain of a healthy subject during wakeful relaxation with closed eyes and is reduced when the eyes are open. It is thought to be representative of a thalamo-cortical communication network and plays an important role in attention and consciousness [14-15]. Since Berger's first discovery of the alpha rhythm, spontaneous activity in a number of other frequency bands has been observed. The functions related to these in other frequency bands are summarized in Figure 4-6 [B].

4.2.2 Evoked responses

Evoked responses are electromagnetic signals recorded from the brain following the presentation of some stimuli to the subject. They are both time locked and phase locked to the stimulus onset. By applying the same stimuli (i.e. visual, auditory, motor etc.) to the subject multiple times (usually 20-100), EEG/MEG data can be averaged across trials to reduce noise and to generate the evoked response timecourse. Evoked responses usually occur shortly after stimulus onset and offset and are typically transient in nature.

4.2.3 Induced effects

Induced effects are time locked but non phase locked changes in spontaneous rhythms induced by stimulation. The increases and decreases in spontaneous rhythms are often referred to as event-related synchronization (ERS) and desynchronization (ERD). After presenting stimuli to a subject, modulation can be observed in a number of frequency bands. As induced effects have different onset phase across trials, they would cancel out with signal

averaging. They can only be observed by averaging power or instantaneous amplitude envelopes across trials. The differences between evoked responses and induced effects are shown schematically in Figure 4-7.
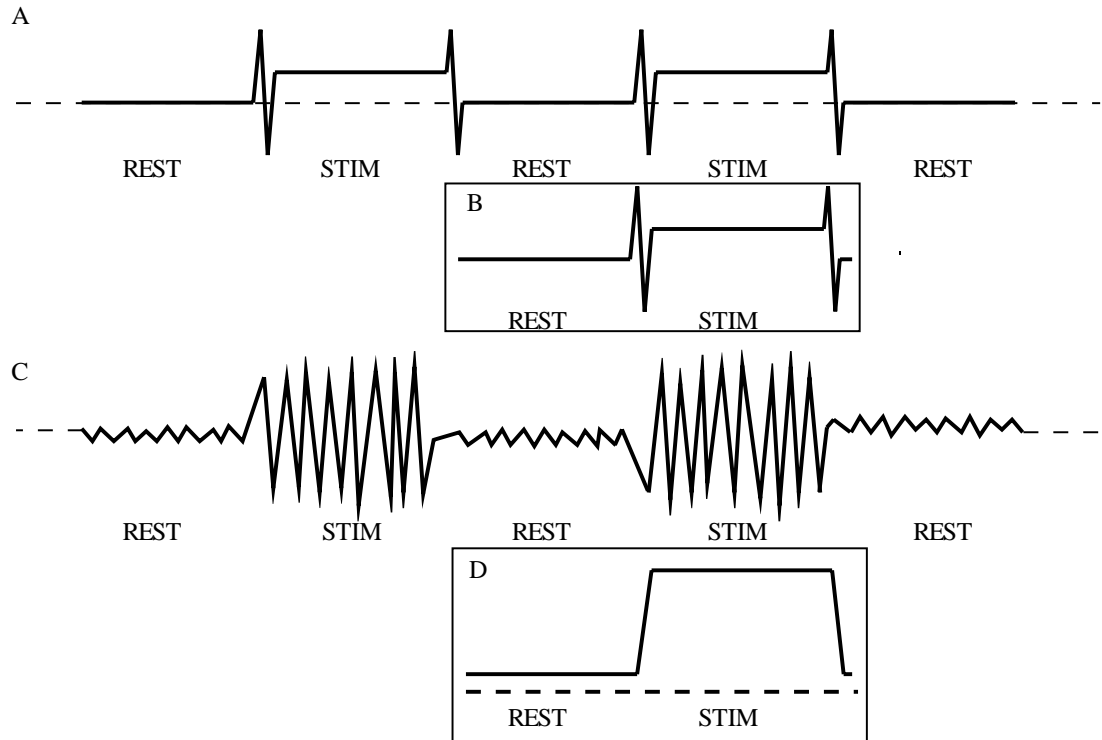
Figure 4-7: Differences between evoked response [A] and induced effects [C]. REST and STIM indicate rest and stimulus presentation. Time locked and phase locked evoked responses can be respectively averaged across trials [B]. However, time locked but non phase locked induced effects[C] require computation of oscillatory power prior to averaging [D].

4.3 *The MEG system*

The whole-cortex MEG system used throughout this thesis is a 275-channel Omega MEG system manufactured by CTF Systems Inc. A schematic diagram of CTF's MEG system is

shown in Figure 4-8. The brain's magnetic field, generated from neuronal activity is about 50-500 fT and is considerably smaller than the environmental magnetic noise (of order of 10^8 fT) and earth's magnetic field (0.5×10^{-4} T). Therefore, the MEG system is required to be sited within a magnetically shielded room (MSR). The MEG system and the patient couch operate with the patient either seated or supine. Other accessories such as the head position indicators (HPIs), patient communication system (intercom and camera), and stimulation equipment are also housed in the MSR.
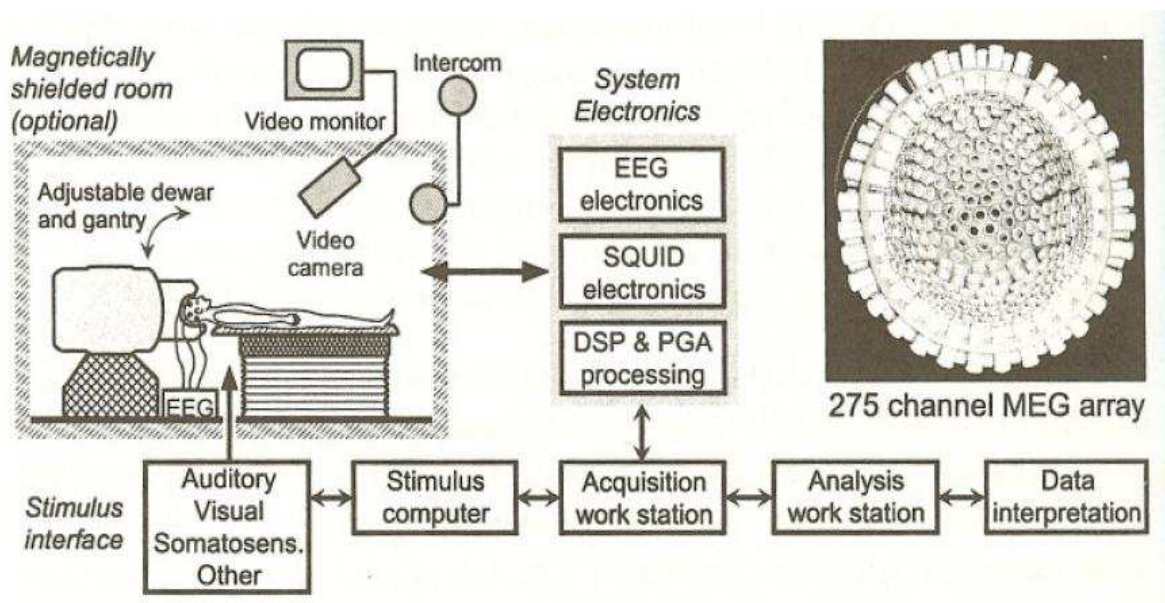
Figure 4-8: A Schematic Diagram of the CTF MEG system. A MEG sensor array with 275 channels is shown in the insert. [16]

4.3.1 SQUIDs

The small magnitude of the neuronal magnetic field necessitates very sensitive magnetic field sensors. The sensors employed for this purpose comprise superconducting coils and SQUIDs. The superconducting coils facilitate flux transfer from the scalp surface to the

SQUIDs which are located above the head. The coils will be discussed below. Here we focus on the operation of the SQUID sensor.
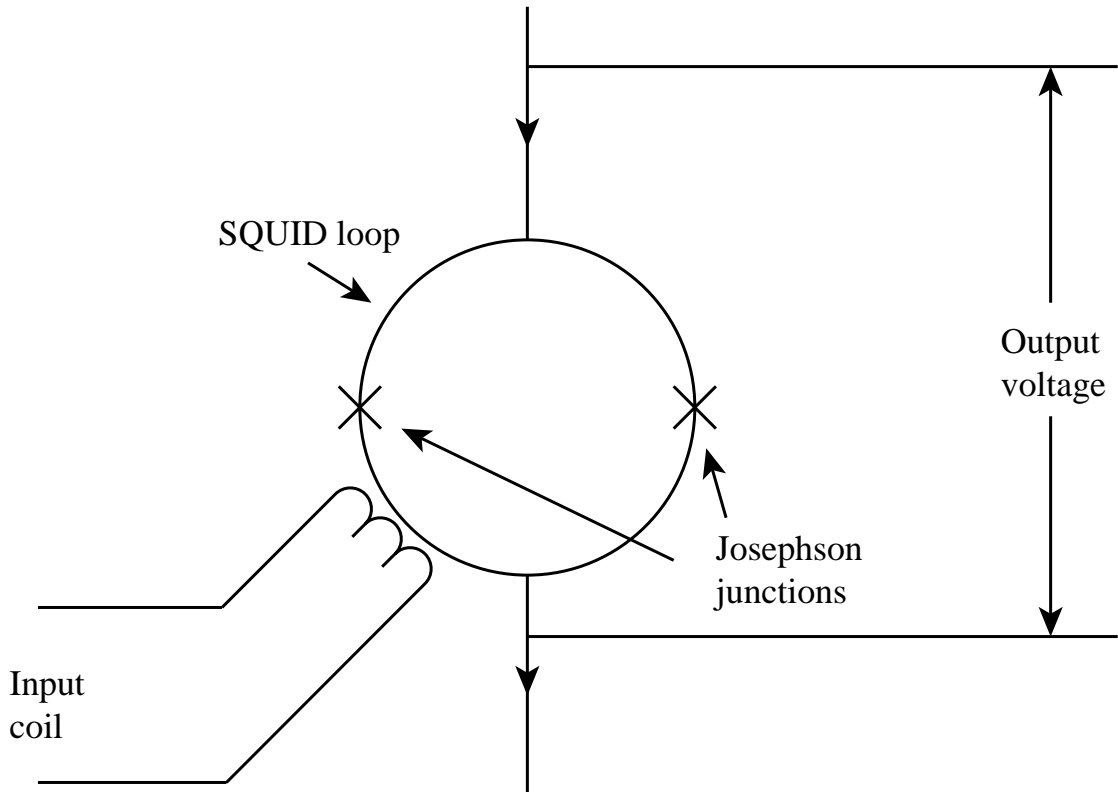
Figure 4-9: A schematic illustration of the SQUID. The changing magnetic field is transmitted from the input coil to the SQUID loop and the voltage across the loop is measured as the output signals.

At temperatures approaching absolute zero, certain materials undergo a transition to what is known as a superconducting state, losing resistance to the flow of electrical current. This transition from normal to superconducting behaviour takes place at the transition temperature (T_c), usually about 5K. The superconducting property allows small changes in magnetic flux to cause significant changes in the amount of current flow. The SQUID consists of a loop of superconducting wire interrupted by layers of normal, resistive materials, forming Josephson junctions (Figure 4-9). For currents less than the critical current (I_c), this loop acts as a

superconductor, because electrons can "tunnel" through thin resistive segments without loss of energy [17]. If the level of current in the ring is kept just below I_c, a small change in the magnetic field can cause the currents to exceed the I_c, resulting in a significant voltage drop across the Josephson junction. In this way, the SQUID acts as a high-gain current-to-voltage converter. It is sensitive only to changing magnetic field (e.g. neuronal magnetic activity), not to the steady magnetic field (e.g. Earth's magnetic field).

4.3.2 Noise reduction

In a laboratory environment, the interference magnetic noise level is several orders of magnetic higher than the signal to be measured. The reduction of environmental magnetic interference is therefore very important. In the CTF MEG system, the noise is reduced to an acceptable level by the combined action of 3 additive methods: hard wired first order gradiometer, passive magnetic shielding and synthesized higher order gradiometers.

4.3.2.1   Hard wired gradiometer

In a first-order axial gradiometer, an oppositely wound coaxial coil is connected in series with the pickup coil. This arrangement is insensitive to a homogeneous magnetic field which imposes an opposite net flux through the lower (pickup) and the upper (compensation) coils. The first-order gradiometer is thus effective in measuring inhomogeneous magnetic fields produced by nearby signal sources, whereas the field from a distant noise source is cancelled. If the distance (baseline) between the two coils is about 4-5 cm, when the detector is placed at the head surface, the output of the gradiometer mostly reflects the magnetic field of nearby neuronal sources and the influences of environmental noise are highly suppressed [18]. This

is shown schematically in Figure 4-10. In the 275-channnel CTF MEG system, the sensors are first-order axial gradiometers, with diameter = 1.8cm and baseline = 5cm [19].
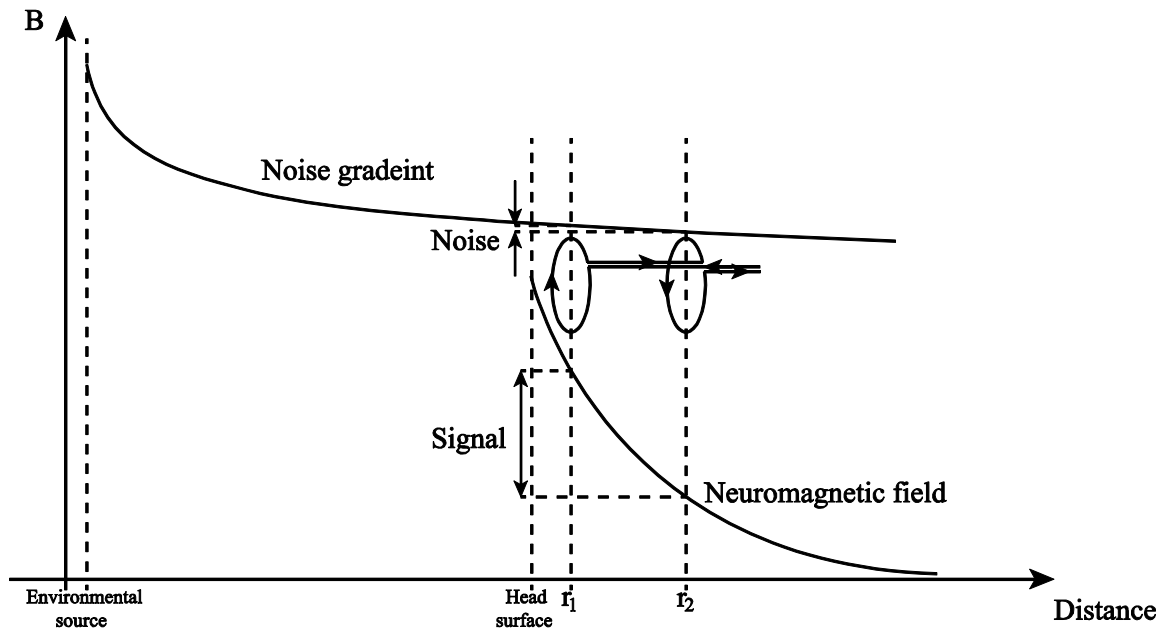
Figure 4-10: Schematic of the first order gradiometer. As only the differences between magnetic field between the lower coil at r_1 and upper coil at r_2 are measured, the contribution of distal sources of magnetic interference and static fields is eliminated.

4.3.2.2   Passive magnetic shielding

The most straightforward and reliable way of reducing the effect of external magnetic fields is to perform the measurement inside a magnetically shielded room. The room is built of high magnetic permeability materials, such as μ-metal (an alloy consisting mostly of nickel and iron). It is mounted on an aluminium plate that serves as an eddy-current and radiofrequency shield. When external magnetic flux impinges on the room, it takes the path of greatest permeability through the walls around the room and away from the MEG system which is located inside. Practical shielded rooms employ multiple shells to increase the

shielding effect [20]. The noise recordings of the environmental magnetic field with the door of shielded room open and closed are shown in Figure 4-11.

4.3.2.3 Synthetic gradiometer

As discussed in Section 4.3.2.1, compensation of the external interference field through using gradiometers is a practical technique in conjunction with shielded rooms to reduce environmental magnetic interference. In the CTF system, the interference is further reduced by the use of a novel synthetic gradiometer system, which is an electronic noise cancellation method applied to the measured signal. This system uses some reference sensors, located distal to the main MEG array, to measure the magnetic field. These reference channels are insensitive to brain signals, since they are located far away from the head, but assuming noise generators are sufficiently far away, they are sensitive to the same environmental noise as the main array. By compensating the interference using the signals from the reference channels, noise in the resulting corrected signal is reduced. In practice, the result is combined with information from several reference sensors in order to allow a higher order gradiometer and better noise cancellation [21]. Noise spectrum with and without the 3rd order Synthetic gradiometer are shown in Figure 4-11.
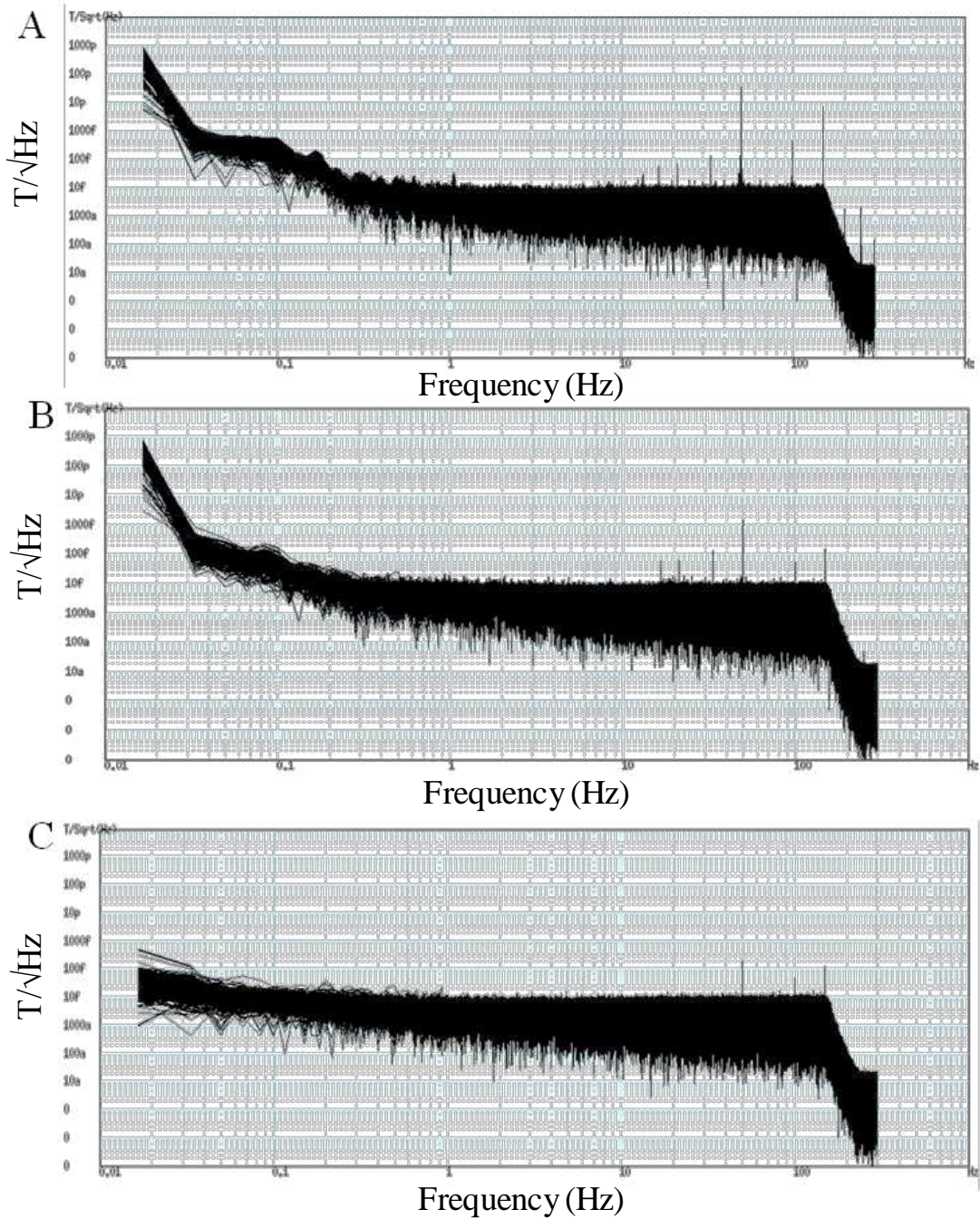
Figure 4-11: Noise spectra plotted on log-log scales from the MEG system acquired with the door of the magnetic shielded room open [A] and closed [B,C]. Third order synthetic gradiometer correction is applied in [C] to further reduce the noise.

91

4.3.3 Co-registration

When studying human brain activity using MEG, a structural image of the brain is often used to construct a model of the head for source localization and for visualization of the active area. In our case, the structural data are obtained using a T_1-weighted Gradient Echo MPRAGE sequence at 3T. Co-registration is required to convert the brain anatomy and the geometry of the MEG system into a single co-ordinate frame. Co-registration is based on a set of anatomical landmarks (fiducial points) and surface-matching.
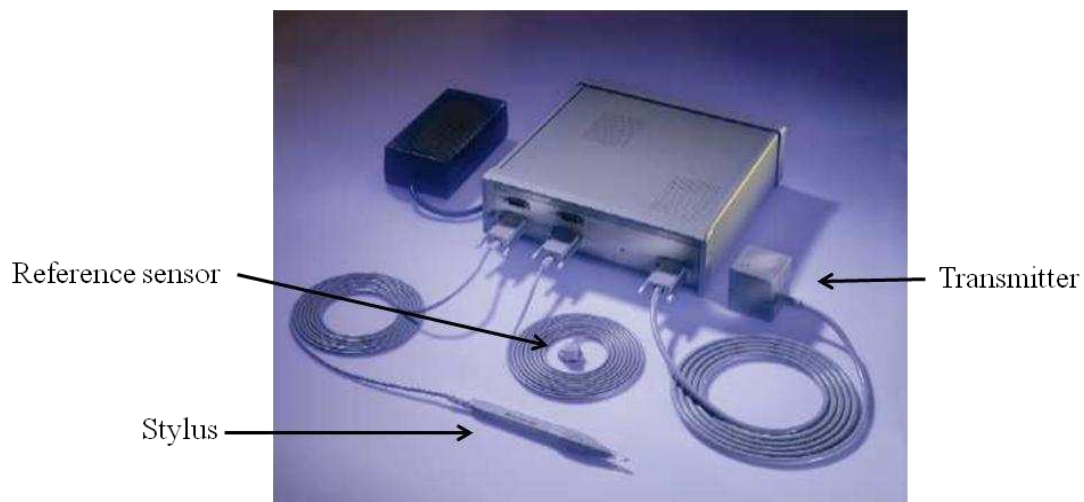
Figure 4-12: The Polhemus FASTRAK 3D digitizer. The large transmitter box is usually placed directly behind the subject's head. The small reference sensor is held firmly on the head.

In the experiments discussed in this thesis, fiducial makers comprising a set of small localization coils have been used to localize the head inside the MEG helmet. These coils are attached to the head at nasion, left preauricular (LPA) and right preauricular (RPA) using adhesive tape. The coil locations are determined by the MEG system before and after each recording session and the final position used for the co-registration procedure is obtained

from the average of these measurements. The coil locations with respect to the subject's head shape are also determined using a Polhemus FASTRAK 3D digitizer (Figure 4-12). A reference sensor is held on the subject's mastoid bone and the location of the tip of a 3D stylus is measured with respect to the location of the reference sensor. In this way, a 3D set of surface points representing the head shape is produced. The coordinate system is based on the 3 fiducial markers and is shown in Figure 4-13. The shape of the head, nose, eye sockets and the position of the three fiducial coils are recorded. Usually more than 300 points across the head surface are required to obtain a good co-registration. The fiducial points are checked after the measurement to ensure that the reference sensor has not moved. These surface points are then co-registered with the segmented scalp surface from the MRI data. This surface matching is achieved by minimising the squared Euclidean distance between the two surfaces. In this way, the locations of the three fiducial points with respect to the MRI image can be found. Further, the location of the MEG sensors with respect to the fiducial points is also known. All of the relevant geometrical information including the brain anatomy, fiducial points, and MEG sensors is then placed in a single co-ordinate system, usually chosen to be that shown in Figure 4-13 [22-23].
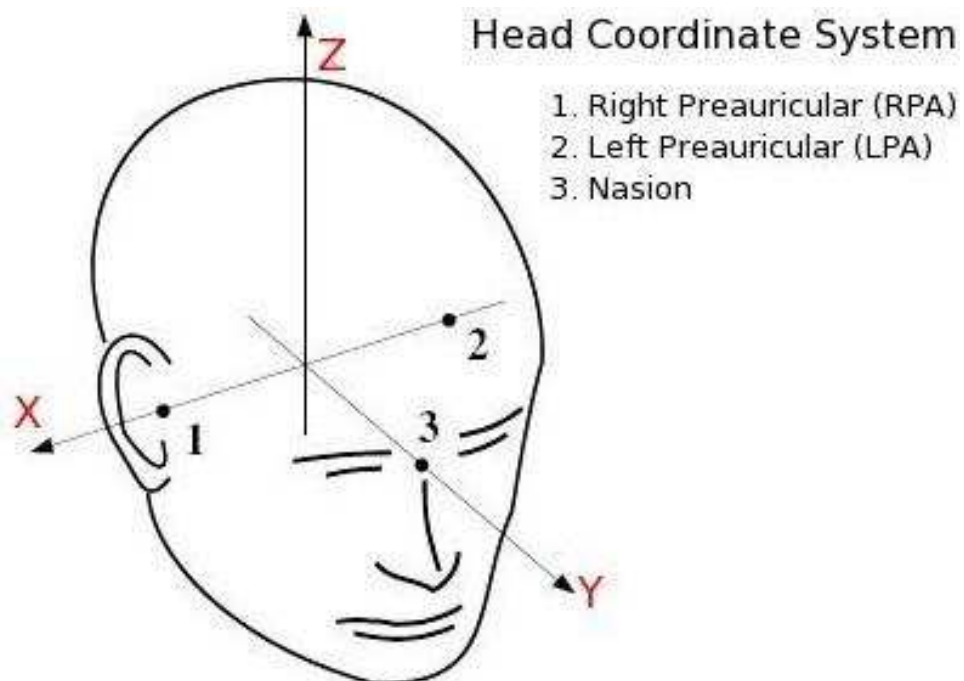
Figure 4-13: The head coordinate system and three fiducial points.

4.4 *Forward and inverse problems*

In MEG the spatiotemporal behaviour of electrodynamic sources inside the brain is sought. To achieve this, two problems, termed the forward and inverse problem, must be solved.

The forward problem states: Given a known current in the head can we compute the distribution of magnetic field outside the head? This is a well posed physics problem and can be solved using the Biot-Savart Law.

The inverse problem states: Given a known magnetic field distribution outside the head can we compute the underlying current distribution? This is a physically ill posed problem since field cancellation means that an infinite number of current distributions could generate a single magnetic field pattern.

4.4.1 Forward problem

In the experiments in this thesis, a spherically symmetric conductor model is applied and the magnetic field **B** outside the source space is calculated using a quasi-static approximation (the time derivative of electric field is negligible compared to the Ohmic term) as:

$$\mathbf{B(r)} = \frac{\mu_0}{4\pi} \frac{F\mathbf{Q} \times \mathbf{r_Q} - (\mathbf{Q} \times \mathbf{r_Q} \square \mathbf{r})\nabla F}{F^2} \quad [4-1]$$

where **Q** is a current dipole located at $\mathbf{r_Q}$ and the magnetic field is calculated at **r**. F = a (ra + r^2 - $\mathbf{r_Q} \cdot \mathbf{r}$), $\nabla F = (r^{-1}a^2 + a^{-1} \mathbf{a \cdot r} + 2a + 2r) \mathbf{r} - (a + 2 r + a^{-1} \mathbf{a \cdot r}) \mathbf{r_Q}$, $\mathbf{a} = \mathbf{r} - \mathbf{r_Q}$, a = |**a**| and r =|**r**|. More details about this equation can be referred to Sarvas' study [24]. This model assumes a current dipole mode of brain electrical effects. For a more realistic head geometry, a sensor weighted overlapping sphere model is used based on Equation[4-1]. Then, the head

is more realistically modelled as a set of overlapping spheres, rather than a single sphere [25-26].

Based on the forward models, the "lead-field", which is also referred to as the "forward field", is calculated. The lead-field is the responses of each sensor to a source of unit amplitude with a particular location and orientation in the head. Lead-fields are key factors for the MEG inverse method.

4.4.2 Inverse problem

The ability to compute the distribution of currents in the brain that underlies the observed extracranial magnetic fields will determine the ultimate usefulness of MEG. This is known as the inverse problem. It was shown by Helmholtz in 1853 that a current distribution inside a conductor cannot be retrieved uniquely from knowledge of the magnetic field outside [27]. Because of field cancellation, there are primary current distributions that are magnetically silent. However, under some assumptions and limitations, the inverse problem can be solved.

Let $\mathbf{b}(t)$ be an M×1 column vector which contains the data from M MEG sensors at a given instant in time t. The source vector $\mathbf{S}(\mathbf{r},t)$ represents source strength at location $\mathbf{r}$ and time t with orientation optimized to maximize the source power. The contribution of a source located at $\mathbf{r}$ to each sensor $b_m(t)$ could be calculated based on the lead-field. Then the sensitivity of the whole sensor array for this source could be represented as a vector $\mathbf{L(r)}$, which is called the lead-field vector. The lead-field vector defines a projection from current sources at discrete locations in the brain to field measurements at discrete recording sites above the scalp. By using this lead-field vector, we can calculate the theoretical response of

any sensor array $\mathbf{b}(t)$ to the sources inside the head and the magnetic field vector is given by the sum over all sources in the brain volume thus:

$$\mathbf{b}(t) = \int_\Omega \mathbf{L}(\mathbf{r})\mathbf{S}(\mathbf{r},t)dv + \mathbf{n}(t) \quad [4\text{-}2]$$

In this equation, dv is the volume element and the integral is performed over the whole source volume Ω. $\mathbf{n}(t)$ is the instrumental noise vector added to the integral. The target of all inverse solutions is to find the source vectors, $\mathbf{S}$, from the measured $\mathbf{b}(t)$.

The inverse problem is essentially a modelling problem. The oldest and simplest model to solve the inverse problem is the Equivalent Current Dipole (ECD) model. It assumes current dipoles are placed at some location inside the brain. A forward solution is used to compute the field from a dipole in the brain at some arbitrary location and with some orientation. The result from this model is compared with the real magnetic field measured. We can change the dipole location until the error between the model and the measurement is minimised and this gives the information on the spatial location and orientation of a current source. The major assumption in this model is that the number of sources of activation is small, making this model more realistic for shorter time windows. Typically time windows of about 10ms are used and there are only one or two dipoles assumed to be active in each block. The mathematical expression for solving inverse problems using the ECD model is:

$$\min_{\mathbf{Q},\mathbf{r}_\mathbf{Q}} \left\| \mathbf{b} - \mathbf{L}_{\mathbf{r}_\mathbf{Q}} \mathbf{Q} \right\| \qquad [4\text{-}3]$$

Where $\mathbf{b}$ is the measured magnetic field and the field from a dipole $\mathbf{Q}$ at location $\mathbf{r}_\mathbf{Q}$ can be modelled and given by $\mathbf{m}_{\text{model}} = \mathbf{L}_{\mathbf{r}_\mathbf{Q}} \mathbf{Q}$.

4.4.3 Beamforming Methods

One method that does not make any assumption about the number of active sources is the MEG beamformer. Beamforming is a spatial filtering method for localizing sources of brain electrical activity from surface recordings. The electrical activity at any one location in the brain is estimated as a weighted sum of the data recorded at the MEG sensors. The weights are chosen to minimise the filter output power, subject to a linear constraint. The linear constraint forces the filter to pass brain electrical activity from the specified location, whilst the power minimisation attenuates activity originating at all other locations. Sequential application will generate brain activation images. This method does not require any prior assumption about the sources because it explores the covariance of the source electrical activity at all brain locations [28-29].

Mathematically, the equation describing the relationship between the estimated source vector $\mathbf{S}(\mathbf{r},t)$ and the measured vector $\mathbf{b}(t)$ is:

$$\mathbf{S}(\mathbf{r},t) = \mathbf{W}^T(\mathbf{r})\mathbf{b}(t) \qquad [4\text{-}4]$$

where $\mathbf{W}(\mathbf{r})$ is the weight vector. The covariance matrix $\mathbf{C}$ is an M×M matrix and the element on the i_{th} column of j_{th} row contains the covariance measured between signal recorded at i_{th} and j_{th} sensors. The covariance matrix can be written as

$$\mathbf{C} = E\left[\mathbf{b}(t)\mathbf{b}^T(t)\right] \quad [4\text{-}5]$$

where E donates the expectation value. The electrical source power of the spatial filter at this site is:

$$\mathbf{S}(\mathbf{r},t)^2 = \mathbf{W}^T(\mathbf{r})\mathbf{b}(t)\mathbf{b}^T(t)\mathbf{W}(\mathbf{r}) \qquad [4\text{-}6]$$
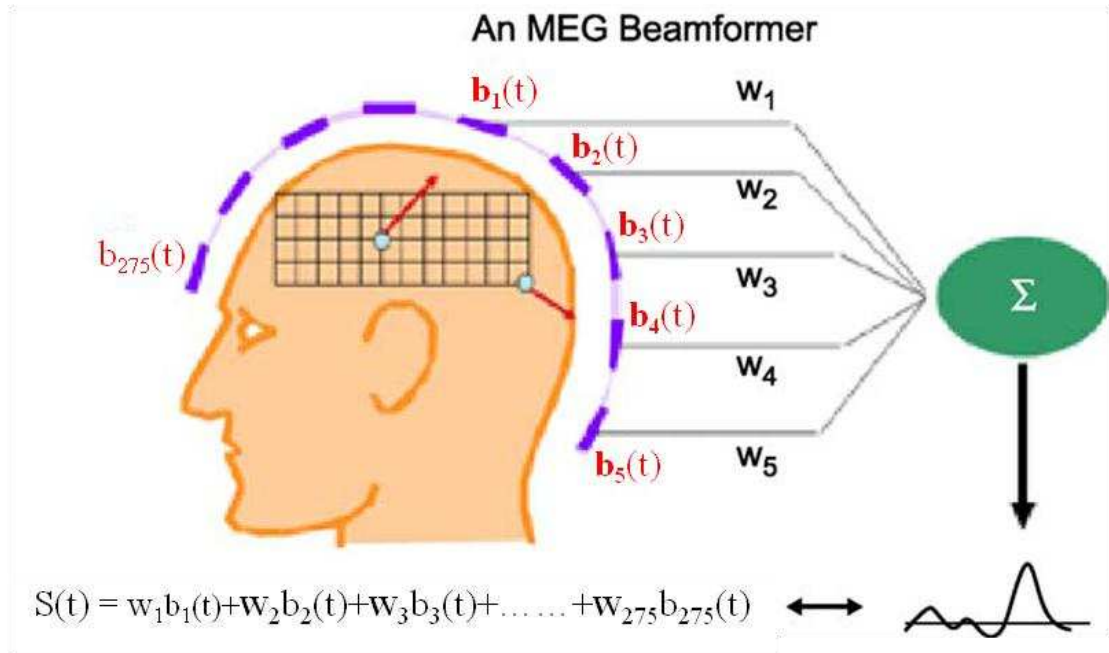
Figure 4-14: Illustration of the beamformer method. The estimated source vector is calculated by weighting signals from all the 275 sensors (b_n) with corresponding weights (W_n).

The weighted sum of sensor measurements described in Equation [4-4] is common to all inverse algorithms. What is different about the beamformer is the way in which weights are derived. Ideally the spatial filter is defined as:

$$\mathbf{W}^T(\mathbf{r}_0)\mathbf{L}(\mathbf{r}) = \begin{cases} 1 & \mathbf{r} = \mathbf{r}_0 \\ 0 & \mathbf{r} \neq \mathbf{r}_0 \end{cases} \qquad [4\text{-}7]$$

The weights obtained with this constraint pass a signal from the location of interest, but suppress the signal from all other locations. Hence this perfect spatial filter is selectively sensitive to the source from the site of interest. However, in reality, it is impossible to null all signals from all other locations. Instead we aim to compute a weight matrix which minimises the output power $\mathbf{S}(\mathbf{r},t)^2$ but with the linear constraint $\mathbf{W}^T(\mathbf{r})\mathbf{L}(\mathbf{r})=1$. This minimises the contribution to estimated current vectors from other sites. Mathematically we formulate the beamformer problem as:

$$\min_{\mathbf{W(r)}} \text{tr}[\mathbf{W}^{\text{T}}(\mathbf{r})\mathbf{CW(r)}] \quad \text{subjected to } \mathbf{W}^{\text{T}}(\mathbf{r})\mathbf{L(r)} = 1 \quad \text{[4-8]}$$

The solution to this equation is [28]:

$$\mathbf{W}^{\text{T}} = \frac{\mathbf{L(r)}[\mathbf{C} + \mu\mathbf{\Sigma}]^{-1}}{\mathbf{L}^{\text{T}}(\mathbf{r})[\mathbf{C} + \mu\mathbf{\Sigma}]^{-1}\mathbf{L(r)}} \quad \text{[4-9]}$$

Here $\mathbf{L(r)}$ is the lead-field, $\mathbf{C}$ is the covariance matrix. $\mathbf{\Sigma}$ is the noise covariance matrix, which assumes the sensor noise as an independent zero-mean Gaussian random quantity, and μ is the regularization parameter which will be further discussed later. Using the weight vectors from Equation[4-9], the estimated power of each location can be found using a voxel by voxel calculation:

$$\mathbf{S(r,t)}^2 = \mathbf{W}^{\text{T}}(\mathbf{r})\mathbf{CW(r)} \quad \text{[4-10]}$$

The contribution of sensor noise to the power of beamformer output is:

$$\sigma(\mathbf{r})^2 = \mathbf{W}^{\text{T}}(\mathbf{r})\mathbf{\Sigma W(r)} \quad \text{[4-11]}$$

In source mapping, the ratio of source power to noise is a better measurement of source distribution than the source power alone and statistical mapping is usually based on [30]:

$$Z(\mathbf{r}) = \sqrt{\frac{\mathbf{S(r)}^2}{\sigma(\mathbf{r})^2}} \quad \text{[4-12]}$$

This accounts for the inhomogeneous noise distribution observed across source space. By mapping the pseudo-Z statistical parameter, baseline activity is imaged. However, source activity related to performance of task is of more interest. To measure such task related change, the output power measured in an "active time window" is compared to the power from "control time window" using a pseudo-T statistical method. Mathematically:

$$\mathrm{F}(\mathbf{r}) = \frac{\mathbf{S(r)}_{\text{active}}^2 - \mathbf{S(r)}_{\text{control}}^2}{\sigma(\mathbf{r})_{\text{active}}^2 + \sigma(\mathbf{r})_{\text{control}}^2} \qquad [4\text{-}13]$$

4.5 *MEG analysis using beamformer*

The solution to the minimisation of variance with a unit gain constraint in Equation [4-8] is the fundamental equation describing the beamformer. As the SNR at the sensor level is determined by the hardware of MEG system, the noise matrix mainly relies on the system itself. However, the covariance matrix, lead-field vector and regularization can be modified by experimental design and post-processing steps. Here we will discuss how they influence the beamformer and how to optimize them in order to achieve maximum accuracy.

4.5.1 Covariance matrix

The covariance matrix, which is constructed from recorded data, plays the most important role in beamforming. The accuracy of covariance estimation influences the errors of beamformer source localization significantly. In experiments, the contribution of the effects of interest to the covariance matrix should be maximized, given the limitation of other parameters (i.e. hardware, scanning time etc). The accuracy of covariance estimation depends on the amount of effective data used in the construction of covariance matrix. Both the signal bandwidth and the total duration of timecourses play a key role in the amount of data. The covariance matrix error is defined as:

$$\Delta \mathbf{C} = \mathbf{C} - \mathbf{C_0} \qquad [4\text{-}14]$$

Where $\mathbf{C}$ is the data-derived covariance matrix and $\mathbf{C_0}$ is the analytically derived covariance matrix calculated using a single dipole source model. The Frobenius norm of the covariance matrix error $\Delta \mathbf{C}$ is given by [31]:

$$\left\| \Delta \mathbf{C} \right\|_F = \sqrt{\sum_i^M \sum_j^M \Delta C_{ij}^2} \qquad [4\text{-}15]$$

Where M is the number of channel and ΔC_{ij} represent the elements of data covariance matrix. In the limit M>>1, it can be shown that

$$\left\| \Delta \mathbf{C} \right\|_F = v^2 M \sqrt{\frac{2SNR+1}{2T_{cov}BW}} \qquad [4\text{-}16]$$

Where υ is the standard deviation of Gaussian distributed noise and is equal in all channels. SNR is the the root mean square (r.m.s.) average of the signal power across all sensors divided by average r.m.s. noise power per sensor, T_{cov} is the duration of the recorded data that is used to construct the covariance estimate and BW is the bandwidth. In this equation, a simple and intuitive relationship between $T_{cov,}$ BW and Frobenius norm, of the covariance matrix error was derived showing covariance error and integration window are related.

Initially, the bandwidth is limited by the sampling rate of data recording. The sampling rate used in this thesis is 600Hz. It means the theoretical bandwidth of the data is 300Hz, ranging from 0-300Hz, according to the Nyquist sampling theorem. However, an anti-aliasing filter of 0-150Hz is applied using a hardware filter for overcompensating. So the data collected for post-processing only has a bandwidth of 150Hz. However, the bandwidth will be further reduced since in most cases we are interested in a particular band of interest (alpha band, beta band, etc.) or a particular time window of interest, usually BW and T_{cov} are reduced. For example, if we only focus on the evoked response which lasts 200ms after the onset of

stimulus, even if trials last several seconds, we can only use the first 200ms for an active time widow as this small window contains the signal of interest. Adding further noise to the active window by increasing BW or T_{cov} will decrease the SNR and thus influence the accuracy of the covariance matrix. It is also noteworthy that a 200ms time window means a 5Hz high-pass filter is applied which reduces the bandwidth to 145Hz, ranging from 5-150Hz.

As a second example take a case where a neural electrical signal within a particular frequency band is of interest. Take the beta band for example; a 13-30Hz band pass filter is applied on the data. If the duration time of contrast windows remains the same, the bandwidth of data used in covariance matrix is reduced from 150Hz to 17Hz. The Frobenius norm of covariance matrix error $\lVert \Delta \mathbf{C} \rVert$ will increase by $\sqrt{150/17}$.

As shown in Equation[4-16], the $\lVert \Delta \mathbf{C} \rVert$ of beamformer is inversely correlated to both the square root of bandwidth and square root of total duration. In order to minimise the error, we need to optimize the parameters for experimental design and post processing. As the duration of a particular neural event is finite, the experiment should contain as many trials as possible. The resting time in each trial should be short, but still long enough to the let the brain activity return to baseline. Active and control windows should also be equal in duration. Frequency windows should be large enough to capture the signal of interest whilst minimise contributions from all other bands.

4.5.2 Lead-field

The lead-field is another key factor in beamforming. The accuracy of a lead-field has been proved to influence beamformer localization significantly. Increasing error in the lead-field results in a rapid decrease of the estimated output power from a spatial filter and a large localization error.

The lead-field can be computed in different ways. One of the most widely used models is the current dipole model. This assumes that each voxel within source space contains a single current dipole with a single orientation and this dipole is small enough to be considered as a point dipole. The cortical field change is then calculated using the forward equations in Section 4.4.1. This dipole model breaks down when the source volume is relative large. The low-frequency oscillations of interest in this thesis happen in a large area in the cortex. However, as they are uncorrelated sources and can be calculated as single point dipoles, the single equivalent point dipole model successfully predicts these sources and the lead-field can be calculated correctly.

4.5.3 Regularization

In beamformer analysis, the inverse covariance matrix needs to be computed. However the measured covariance matrix may be singular or badly conditioned. If the covariance matrix $\mathbf{C}$ is close to a singular matrix, calculation of $\mathbf{C}^{-1}$ will be unstable. This situation occurs for example if there are too few data samples to construct the covariance matrix, or the data have been averaged across trials. In these conditions, the covariance matrix requires regularization.

Regularization is introduced as a method to convert the covariance matrix to a well conditioned matrix. The simplest regularization, as shown in Equation[4-9], involves adding the same number to every element in the leading diagonal of the covariance matrix. The Σ, which is the noise covariance matrix, is controlled by the regularization parameter μ. The parameter μ adjusts the tradeoff between the full-width half-maximum (FWHM) of the point spread function for beamformer image and the magnitude of uncorrelated noise in the timecourse. When $\mu=0$, no regularization is applied. With the increase of μ, larger weights are clustered together in the neighbouring channels. The clustered weights lead to average of similar signals across a number of channels and improve the SNR. When a large μ is applied, since $\|\mu\Sigma\| >> \|C\|$, the Equation[4-9] reduces to:

$$\mathbf{W}^{\mathrm{T}} = \frac{\mathbf{L(r)}}{\mathbf{L}^{\mathrm{T}}\mathbf{(r)L(r)}} \quad [4\text{-}17]$$

This means the beamformer-derived weights become closer to the lead-field with a larger μ. In this case, the spatial filter output will have a better SNR but the spatial resolution is reduced. In practice, regularization therefore adjusts the trade off between high temporal SNR and high spatial resolution. The beamformer images and time-courses of beta ERD with different regularization parameters are shown in Figure 4-15. The regularization parameter used in this thesis is 2 based on previous studies [31-32] .
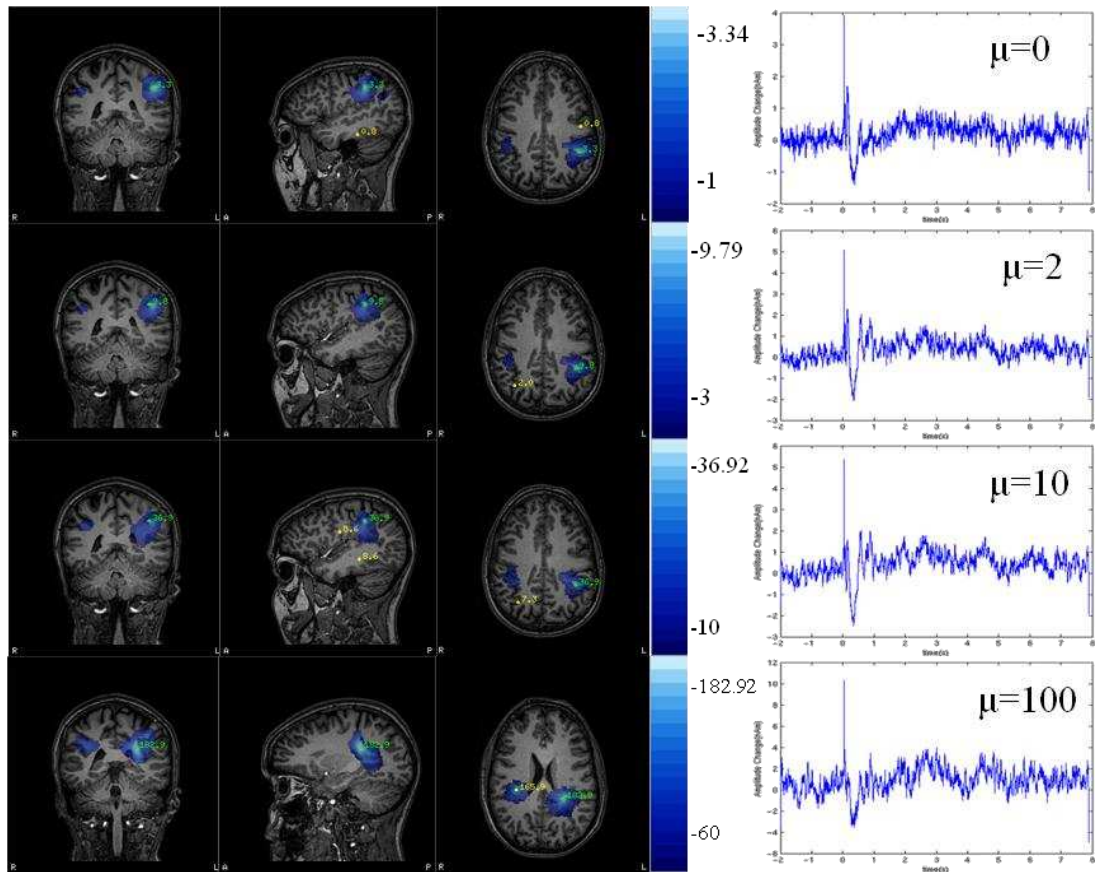
Figure 4-15: SAM beamformer images (left) and virtue sensor timecourses of amplitude changes (right) of beta ERD with regularization parameters (*μ*) of 0,2,10 and 100. [31]

4.6 *References*

[1]   Baule, G. and McFee, R., Detection of the magnetic field of the heart. American Heart Journal, 1963. **66**: p. 95-96.

[2]   Cohen, D., Magnetoencephalography: evidence of magnetic fields produced by alpha-rhythm currents. Science, 1968. **161**(3843): p. 784-786.

[3]   Cohen, D., Edelsack, E.A. and Zimmerman, J.E., Magnetocardiograms taken inside a shielded room with a superconducting point contact magnetometer. Applied Physics Letters, 1970. **16**(7): p. 278-280.

[4]   Huffman, K., Psychology in action. 5 edition. 1999: Wiley.

[5]   Swinney, K.R. and Wikswo Jr, J.P., A calculation of the magnetic field of a nerve action potential. Biophysical Journal, 1980. **32**(2): p. 719-731.

[6]   Brooks, M.J., Functional Imaging An Introduction to Magnetoencephalography (MEG). in Lecture given at University of Nottingham,. 2008.

[7]   Lorente de No, R., Analysis of the distribution of action currents of nerve in volume conductors. Stud Rockefeller Inst Med Res, 1947. **132**: p. 384-482.

[8]   Wikswo, J.P., Cellular action currents, in Biomagnetism, An Interdisciplinary Approach, S.J. Williamson, G.L. Romani, L. Kaufman, and I. Modena, Editors. 1983, Plenum: p. 173-207.

[9]   Lorente De, N.R., Action potential of the motoneurons of the hypoglossus nucleus. Journal of Cellular and Comparative Physiology, 1947. **29**(3): p. 207-287.

[10]   Niedermeyer, E. and Da Silva, F.H.L., Electroencephalography: basic principles, clinical applications, and related fields. 2005: Lippincott Williams & Wilkins.

[11]   Cohen, D. and Hosaka, H., Magnetic field produced by a current dipole. Journal of Electrocardiology, 1976. **9**(4): p. 409-417.

[12]   Berger, H., Uber das elektrenkephalogramm des menschen. Archiv für Psychiatrie und Nervenkrankheiten, 1929. **87**: p. 527-570.

[13]   Caton, R., The electric currents of the brain. British Medical Journal, 1875. **2**(1): p. 278.

[14]   Plotkin, W.B., On the self-regulation of the occipital alpha rhythm: Control strategies, states of consciousness, and the role of physiological feedback. Journal of Experimental Psychology: General, 1976. **105**(1): p. 66-99.

[15]   Steriade, M., Contreras, D., Amzica, F. and Timofeev, I., Synchronization of fast (30-40 Hz) spontaneous oscillations in intrathalamic and thalamocortical networks. The Journal of neuroscience, 1996. **16**(8): p. 2788-2808.

[16]   Vrba, J., Robinson, S.E. and Fife, A.A., Toward Noise-Immune Magnetoencephalography Instrumentation, in Magnetic Source Imaging of the Human Brain, Z.-L. Lu. and L. Kaufman, Editors. 2003, Routledge: p. 203-216.

[17]   Josephson, B.D., Possible new effects in superconductive tunnelling. Physics Letters, 1962. **1**: p. 251-253.

[18]   Vrba, J., Fife, A.A., Burbank, M.B., Weinberg, H. and Brickett, P.A., Spatial discrimination in SQUID gradiometers and 3rd order gradiometer performance. Canadian Journal of Physics, 1982. **60**(7): p. 1060-1073.

[19]   CTF MEG Hardware Manuals, Operation and Technical Reference. , in Technical Description. 2006. p. 17.

[20]   Erne, S.N., Hahlbohm, H.D., Scheer, H. and Trontelj, Z., The Berlin magnetically shielded room (BMSR), Section B: Performances, in Biomagnetism. 1981, Walter de Gruyter.

[21]   Vrba, J. and Robinson, S.E., Signal processing in magnetoencephalography. Methods, 2001. **25**(2): p. 249-271.

[22] Adjamian, P., Barnes, G.R., Hillebrand, A., Holliday, I.E., Singh, K.D., Furlong, P.L., Harrington, E., Barclay, C.W. and Route, P.J.G., Co-registration of magnetoencephalography with magnetic resonance imaging using bite-bar-based fiducials and surface-matching. Clinical Neurophysiology, 2004. **115**(3): p. 691-698.

[23] Munck, J.C., Verbunt, J.P.A., Ent, D. and Dijk, B.W.V., The use of an MEG device as 3D digitizer and motion monitoring system. Physics in Medicine and Biology, 2001. **46**: p. 2041-2052.

[24] Sarvas, J., Basic mathematical and electromagnetic concepts of the biomagnetic inverse problem. Physics in Medicine and Biology, 1987. **32**: p. 11-22.

[25] Huang, M.X., Mosher, J.C. and Leahy, R.M., A sensor-weighted overlapping-sphere head model and exhaustive head model comparison for MEG. Physics in Medicine and Biology, 1999. **44**: p. 423-440.

[26] Miller, C.E. and Henriquez, C.S., Finite element analysis of bioelectric phenomena. Critical reviews in biomedical engineering, 1990. **18**(3): p. 207-233.

[27] Von Helmholtz, H.L.F., Some laws concerning the distribution of electrical currents in conductors. Annalen der Physik, 1853. **89**(6): p. 211-233.

[28] Van Veen, B.D., Van Drongelen, W., Yuchtman, M., and Suzuki, A., Localization of Brain Electrical Activity via Linearly Constrained Minimum Variance Spatial Filtering. IEEE Transaction on Biomedical Engineering, 1997. **44**(9): p. 867-880.

[29] Brookes, M.J., Gibson, A.M., Hall, S.D., Furlong, P.L., Barnes, G.R., Hillebrand, A., Singh, K.D., Holliday, I.E., Francis, S.T. and Morris, P.G., GLM-beamformer method demonstrates stationary field, alpha ERD and gamma ERS co-localisation with fMRI BOLD response in visual cortex. Neuroimage, 2005. **26**(1): p. 302-308.

[30] Robinson, S.E. and Vrba, J., Functional neuroimaging by synthetic aperture magnetometry (SAM), in Recent advances in biomagnetism, Y. T., K. M., K. S., K. H., and N. N., Editors. 1999, Tohoku University Press: p. 302-305.

[31] Brookes, M.J., Vrba, J., Robinson, S.E., Stevenson, C.M., Peters, A.M., Barnes, G.R., Hillebrand, A. and Morris, P.G., Optimising experimental design for MEG beamformer imaging. Neuroimage, 2008. **39**(4): p. 1788-1802.

[32] Stevenson, C.M., Brookes, M.J. and Morris, P.G., β‐Band correlates of the fMRI BOLD response. Human Brain Mapping, 2011. **32**(2): p. 182-197.

Chapter 5

Somatosensory system

Overview: In this chapter, the basic principles of the somatosensory system are introduced. Firstly, in Section 5.1, the anatomical and functional organization of the somatosensory system, including the pathways, somatosensory cortex and thalamus are described. Secondly, in Section 5.2, evoked responses and induced oscillations in the somatosensory cortex are discussed. In Section 5.3, the functional connectivity within the thalamo-cortical loop and the Cortical Activation Model (CAM), which is used to interpret the relation between event-related oscillations and cortical activation state, are discussed. Finally, Section 5.5 describes somatosensory fMRI.

5.1 *Introduction*

5.1.1 The somatosensory pathway

The somatosensory system is a part of the nervous system responsible for receiving and processing sensory information such as touch, pain, body position and temperature. It is composed of huge numbers of neurons organized in a hierarchical system. The groups of neurons at higher levels receive information from lower levels and enhance the important information whilst discarding irrelevant information. To illustrate the organization of the somatosensory system, the well studied sensory modality of touch is taken as an example.

This is also the relevant system for processing median nerve stimuli as used in the work described in this thesis.
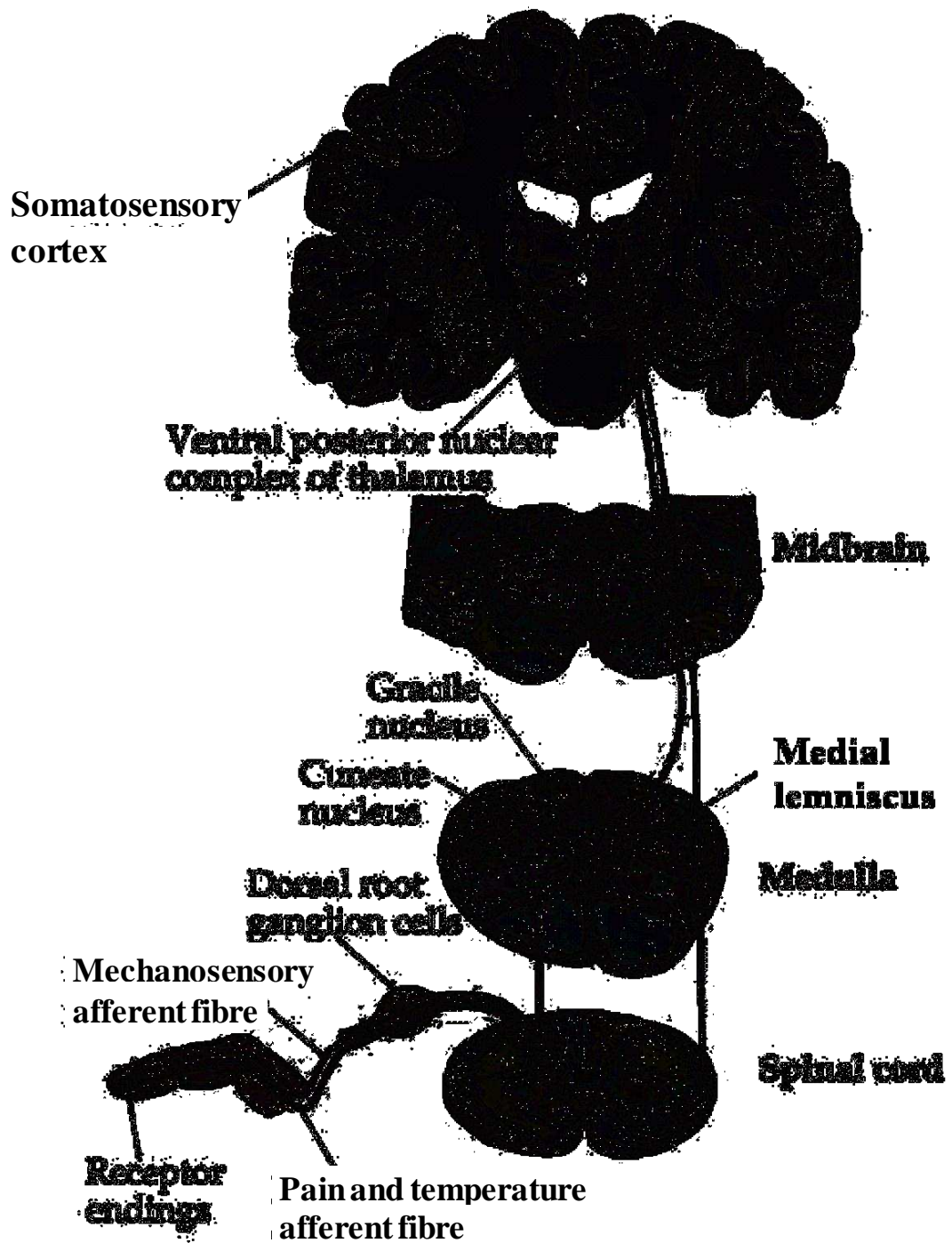
Figure 5-1: The somatosensory ascending pathways for the upper body. Tactile sensation and limb proprioception are transmitted to the thalamus by the dorsal column-medial lemniscal system (red). Painful and thermal sensations are transmitted to the thalamus by the anterolateral system (blue). The picture is from [1].

The somatosensory pathway is illustrated in Figure 5-1. Touch activates the mechanoreceptors within the skin of the trunk and limbs. Through sensory nerves, the information enters the spinal cord. The spinal cord is the main pathway for information flow and connects the brain and body. It is located in the bony spinal column, named the vertebral column, protected by several layers of membranes and composed of central core region of gray matter and surrounding region of white matter. Although all the sensory stimuli enter the spinal cord within the dorsal root of gray matter together, they are transmitted to brain via separated pathways. The axons of sensory neurons in the dorsal horn form fibres and ascend to the brain. In the medulla oblongata, which is the lower part of the brain stem, the fibres from the upper body run in the cuneate funiculus and terminate in the ipsilateral cuneate nucleus. The fibres from the lower body run in the gracile funiculus and terminate in the ipsilateral gracile nucleus. The axons from the cuneate and gracile nuclei then cross to the contralateral side of the brain, forming the sensory decussation. The fibres after this decussation keep ascending along the central core of the brainstem, forming the medial lemniscus. The medial lemniscus is part of the posterior column-medial lemniscus system and terminates in the thalamus. The thalamus receives sensory fibres and in turn sends nerve fibres to the cerebral cortex. The final stages of processing take place in the neocortex of the cerebral cortex, forming sensory perceptions and contributing to cognition.

5.1.2 Somatosensory cortex

The somatosensory cortex contains multiple areas as illustrated in Figure 5-2. Somatosensory information coming from the thalamus is firstly transmitted to the primary somatosensory cortex (SI), and then projected to other parts of the cortex for higher order processing. Somatosensory stimuli from all parts of the body have been found to be represented in the cortex somatotopically, forming a somatosensory map. Although each part

of the whole body is represented in its corresponding area in the cortex, the extent is not in proportion to the size of the body part represented. Rather, it is determined by the degree of innervation. The area of cortex devoted to the fingers, which have dense receptors and highly discriminative feelings, is larger than the area for the arms and legs. The neurons in the somatosensory cortex are functionally organized into columns of similar size, about 300-600μm wide and spanning all the six layers from the white matter to the surface of neocortex. This neural map was first obtained by applying stimuli to the surface of the postcentral gyrus during surgery. More accurate maps were later obtained by recording the evoked potentials from the cortex [2]. The SI can be further divided into Brodmann areas 1, 2, 3a and 3b. There are actually four fairly complete maps in SI, one in each of these areas. These four areas represent different types of information and play different roles in sensory signal processing.
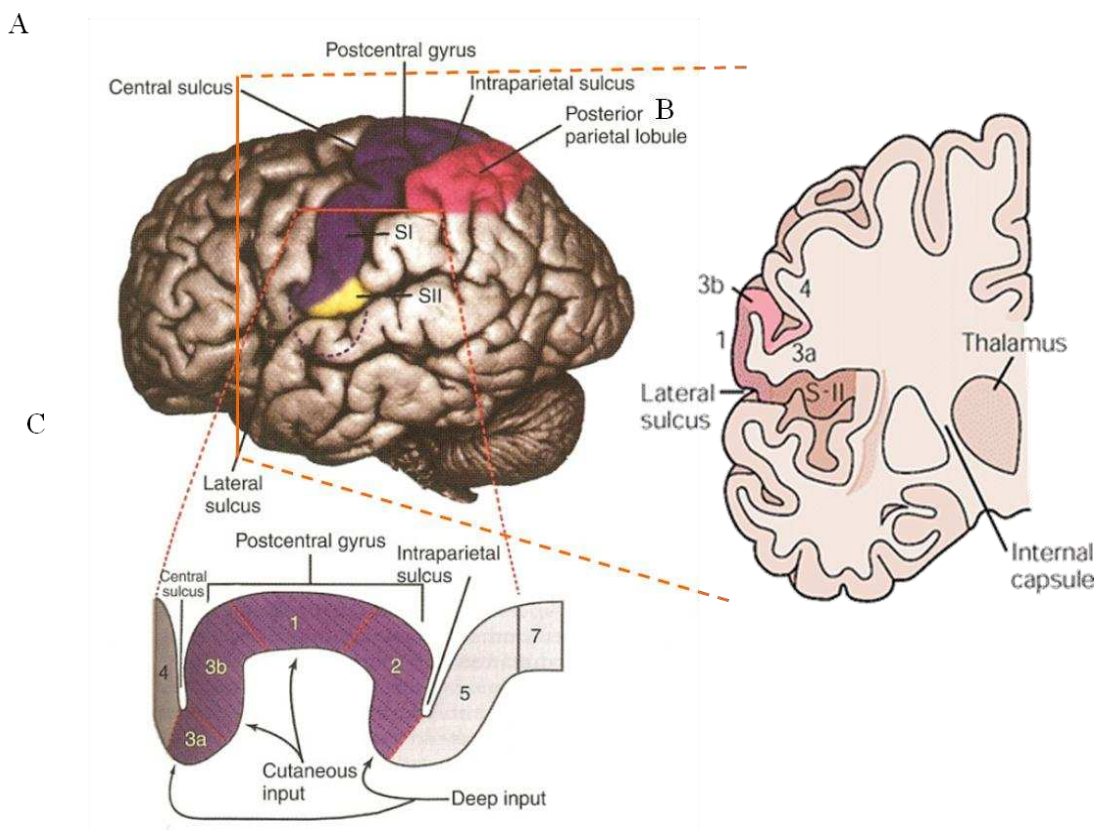
Figure 5-2: Lateral view of the cerebral hemisphere illustrating the location of the somatosensory cortex including the primary (SI) and secondary (SII) somatosensory cortices

and the posterior parietal cortex (PPC) [A]. A section shows the four distinct regions of SI (Brodmann's areas 3a, 3b, 1, and 2) and their spatial relationship to area 4 of the motor cortex and areas 5 and 7 of the posterior parietal cortex [B]. The relationship between SI and SII is illustrated in a coronal section through the cortex. SII cortex lies lateral to S-I, and extends laterally to the insular cortex, forming the superior bank of the lateral sulcus [C]. This picture is modified from [3].

The somatosensory information from skin terminates primarily in Brodmann area 3b. The receptive field of a single neuron in area 3b represents the composition of input from about 300-400 mechanoreceptors in the skin. Proprioceptive information from receptors in muscles and joints terminates in Brodmann area 3a. Neurons in areas 3a and 3b project to areas 1 and 2. Touch information is further processed in area 1 and combined with proprioceptive information from area 3a in area 2. Neurons in areas 1 and 2 are concerned with more abstract properties of incoming stimuli. There are some orientation and direction sensitive neurons in area 2, which play a rather important role in reconstruction of the shape of objects. Direct responses in areas 3a and 3b occur about 20ms after the application of stimulus. The more posterior activities in areas 1 and 2 have longer latencies of 30-100ms.

The somatosensory information from touch stimuli in SI is projected to adjacent areas and to the secondary somatosensory cortex (SII). The posterior parietal cortex (PPC), which is in Broadmann areas 5 and 7, is often referred to as the somatosensory association cortex. Unlike the areas of SI, these areas are organized functionally instead of topographically. Area 5 plays an important role in sensory guidance of movement. Area 7, which also receives input from the visual cortex, participates in the eye-hand coordination. Neurons from SI also project to motor areas (Broadmann area 4), SII and to premotor areas (Broadmann area 6).

5.1.3 Thalamus

The thalamus is the largest structure in the dorsal part of the diencephalon. It is located between the mesencephalon and the telencephalon, on the top of the brainstem, and plays an import role in information transmitting and processing. Anatomically, it is subdivided by bands of white matter into several component parts. The main white matter band that runs within the thalamus is the internal medullary lamina, which is Y shaped and divides the thalamus into a lateral mass, a medial mass, and an anterior group of nuclei in each half. Nowadays, more than 50 nuclei have been identified in the thalamus and are classified as specific relay nuclei, non-specific nuclei and associate nuclei. The major subdivisions of the thalamus are illustrated in Figure 5-3.
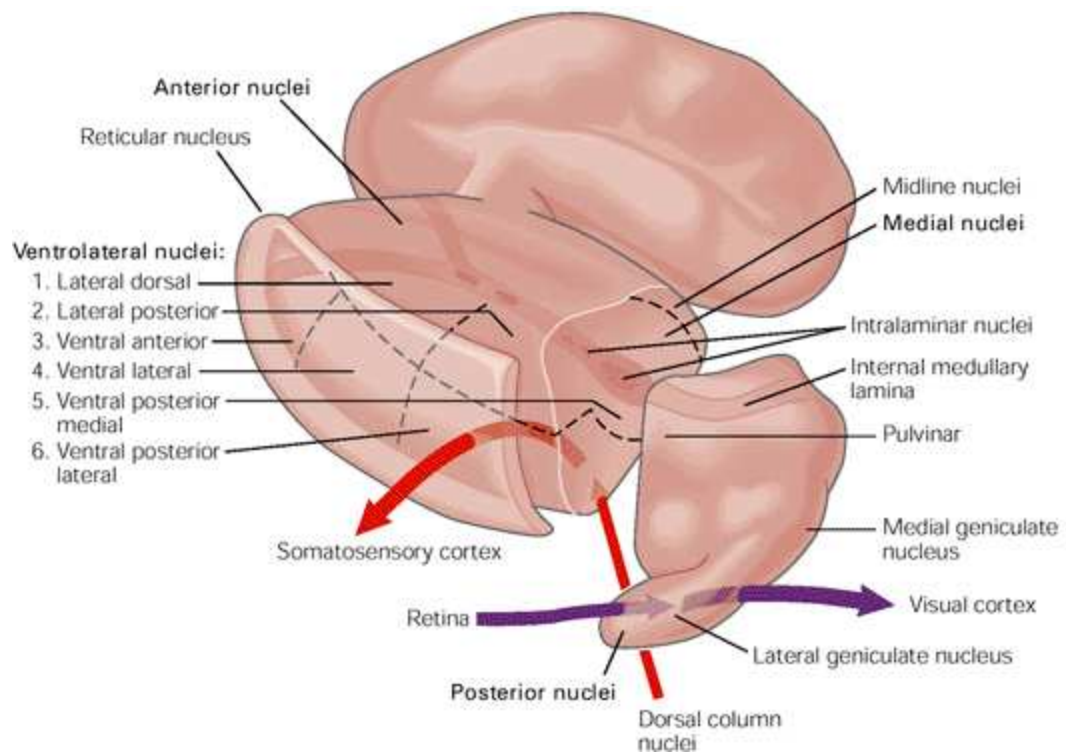
Figure 5-3: The major subdivisions of the thalamus. The thalamus is the critical relay for the flow of sensory information to the neocortex. Somatosensory information from the dorsal root ganglia reaches the ventral posterior lateral nucleus, which relays it to the primary somatosensory cortex [4].

Neurons in specific relay nuclei have axons that project to specific areas of the neocortex, travelling in the internal capsule. Sensory ascending information and motor modulation is carried out through these nuclei. The ventral posterolateral lateral (VPL) nucleus located in the lateral mass of the thalamus receives tactile information of touch from the medial lemniscus and projects it to the primary somatosensory cortex. The associate nuclei have axons connecting broad areas of the cortex, participating in cognitive and attention tasks. The non-specific nuclei, especially the reticular nucleus (RN), which forms the outer shell of the thalamus, do not project to the neocortex directly. However, the RN has multiple connections between other nuclei in the thalamus. It receives inputs from the fibres of other nuclei which project to the neocortex via collaterals of axons when they exit the thalamus thought the RN. The neurons within this nucleus project back to the nuclei within the thalamus such as the VPL, modulating the cortical-thalamical interactions. This feedback loop is included in the non-specific thalamo-cortical projection system. This system plays a rather important role in both spontaneous and event-related brain rhythms. Most of the neurons in the specific relay nuclei make use of excitatory transmitters, which activate the corresponding neocortex. In contrast, the RN is mainly composed of neurons utilizing the inhibitory transmitter γ-aminobutyric acid (GABA).

5.2 *Somatosensory neuroelectrical activity*

5.2.1 Somatosensory evoked magnetic field

Somatosensory evoked magnetic fields (SEFs), obtained from averaged MEG data following somatosensory stimulation, were first reported around 1980 [5-6]. As stated in Chapter 4,

MEG detects only a specific orientation of brain currents tangential to the scalp. Therefore neuroelectrical activity in Brodmann areas 3b and 2 of SI (which are located on the posterior bank of the central sulcus and the anterior bank of the intraparietal sulcus) and area 4 of MI (which is located on the anterior bank of the central sulcus) is easily detected, but activity in areas 1 and 3a (which are located on the crown and the bottom of the postcentral gyrus) is not (Figure 5-2).

The SEFs following somatosensory stimulation include a number of responses with different latencies. The short-latency effects are mainly restricted in contralateral SI. The equivalent current dipoles (ECDs) of P20m, N35m (also referred to as N30m) effects are localized in the hand area of area 3b. The P25m effect with a smaller amplitude is found in area 1 [7]. The mid-latency effects are found in large cortical areas including SI, SII, PPC and MI. The P100m effect is mainly localized in cSI, the N60m is localized in bilateral PPC and P90m is localized in bilateral SII [8]. The long-latency effects such as N160m and P300m are more complex and usually found in widespread areas as they are associated with attention and cognitive functions [9-10]. The mean onset latencies of cortical activity in Brodmann areas 3b 4, 1, 5 and SII are 14.4, 14.5, 18.0, 22.4 and 21.7ms respectively [11]. The differences of onset latency among these activations indicate the serial mode of sensory information processing both through the postcentral gyrus and through SI and SII. SEFs following sensory stimulation have been found to be markedly modified by active/passive movement and tactile stimulation, a phenomenon known as 'gating' [12-13]. Specific gating effects of SEFs have been reported on short-latency responses such as N30m following median nerve stimulation. However, the mechanism and sites responsible for gating are still unclear.

5.2.2 Event-related oscillations

The main oscillatory changes in SI occur in the beta band (13-30Hz). Following a short sensory stimulus, there is an immediate amplitude decrease in beta band power. This appears bilaterally in the primary somatosensory cortex. The peak latency of ERD is about 350ms in the contralateral cortex, with a delay of about 150ms in the ipsilateral cortex. Also, the amplitude of the decrease in the contralateral hemisphere is significantly larger. It has been reported that changes in the amplitude of the ERD are influenced by both repetition and intensity of the stimulus, but the peak latency is quite stable across different conditions [14]. Beta ERS occurs a short while after stimulus cessation with a latency of about 400ms [15-16]. The latency of the ERS peak is at about 800ms [17]. The amplitude change is also similar in both hemispheres, but is larger when shorter intervals or higher intensity of stimuli is applied. Negative correlation of ERS between contralateral and ipsilateral SI has also been reported [18]. No influence of stimulation parameters on the latency of ERS in either hemispheres was found. Both ERD and ERS effects are mainly localized in SI, but high-frequency components of beta band ERS also covers the precentral gyrus primary motor cortex (MI) [19]. The ERD and ERS are also sometimes found in the area overlying the supplementary motor area (SMA) [20].

Unlike SI activity, which has been widely studied, there are few studies of oscillatory changes in SII. Although the SEFs in SII are well recorded, the ERD/ERS have not been localized until very recently. The ERD has been observed in low frequency bands (~10Hz), but is less significant compared to that detected in SI [21]. An increase in phase locked correlation between beta band oscillations in SI and SII has been reported [22], but the non phase locked ERS has not yet been confirmed. There are many possible reasons why ERS has not yet been observed in SII. SII lies much deeper than SI, so the MEG beamformer, which enhances the superficial sources as stated in Chapter 4, is not ideal for localizing SII

116

peak points. Also, because of the complex folding of the frontal and parietal operculum, the fields and potentials from currents in SII cancel out. Another reason is that quite a lot of sources in SII have radial orientations, which are not detected by MEG [23].

Besides the low-frequency ERD/ERS, there are also some high-frequency components. High gamma band (70-90Hz) sychronization appears in contralateral SI and bilateral SII with a very short latency after median nerve stimulation [24]. In SI and MI, high gamma ERS has a much larger amplitude than that in SII and is quite focal, happening only in the contralateral hemisphere. In contrast to the widespread activation areas of beta ERD/ERS, the gamma ERS is localized at discrete points. The temporal latency of high gamma ERS is also shorter, corresponding more to the onset of the stimulus. Non-phase locked activity with a long latency is not found in this band [25].

Based on these studies, models and hypotheses have been set up to explain the ERD and ERS. In the resting state, the thalamus and cortex are engaged in low-frequency background sychronization. It is hypothesized that the low-frequency thalamo-cortical sychronization acts as a low-pass filter for the high-frequency sensory signals, which appear when the stimulus is applied. A recent study has suggested that the wide-spread beta ERD plays a role in suppressing the low-pass filter and opening the channels for high-frequency signals [26]. This ERD facilitates the high frequency signals, which have better spatial and temporal specifications and higher selectivity, to participate in sensory and motor activity more efficiently. The beta ERS after the stimulus cessation suppresses the high frequency component quickly and helps to end the activity. This is considered as a gating theory. When the stimulus is given, beta ERD appears and exists for a short while to open some active neuronal pathways. During this time, the general somatosensory input is reduced by the

diffused ERD at low-frequency, which facilities the more focused high-frequency signals from somatosensory and motor systems during the reaction of the brain. The beta band oscillation then rebounds to block the high-frequency signals, terminating the reaction efficiently and inhibiting the cortex for a while [27]. The high gamma sychronization is also believed to play an important role in making functional connections between SI, SII and other neuronal populations in the somatosensory system. A more detailed model will be introduced in the following subsection.

5.3 *Cortical Activation Model (CAM)*

5.3.1 Thalamo-cortical loop

Based on the detailed electrophysiological investigations of visual alpha rhythms and sensory motor mu rhythms [28], computational models have been built to demonstrate event related oscillations. In these models, which are schematised in Figure 5-4, the ERD/ERS phenomenon is generated from two neuron populations that have functional interactions between each other. One of these populations is thalamo-cortical (TCR) neurons, which receive sensory, cortical and neuromodulatory input; the other is RN neurons, which receive cortical, neuromodulatory and external inhibitory/excitatory inputs.
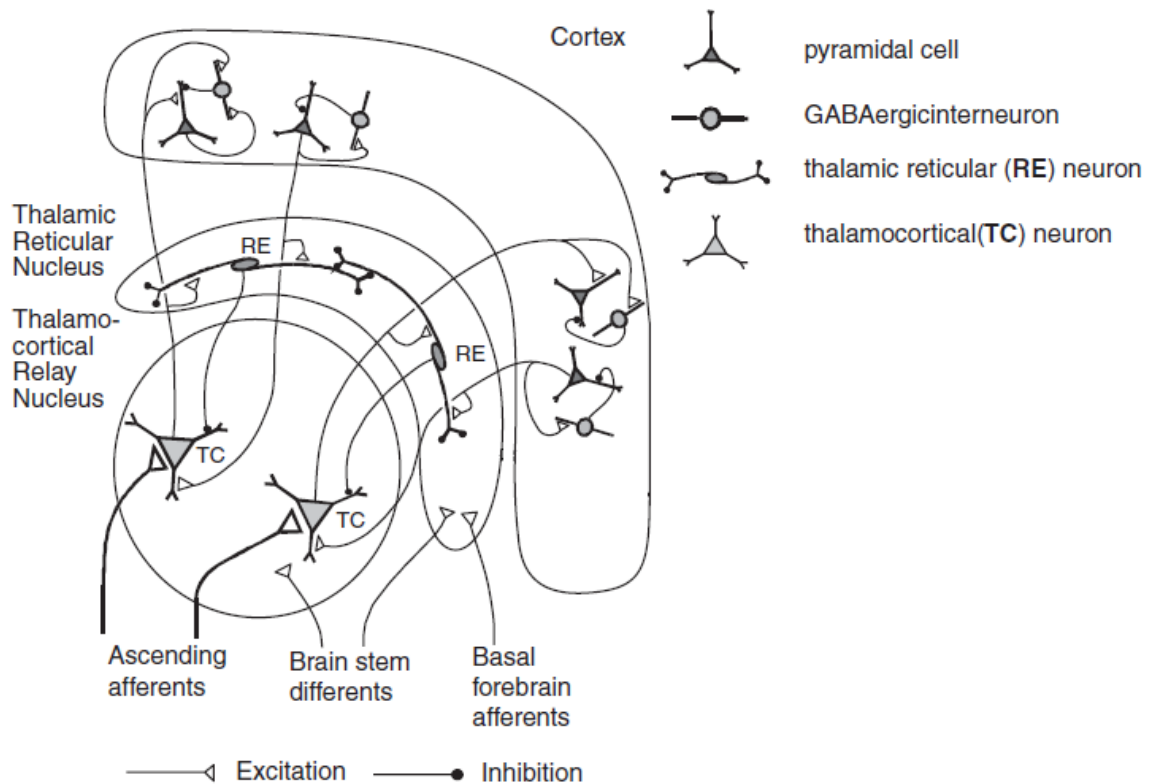
Figure 5-4: The schematic diagram of the model of a thalamo-cortical module. It consists of two interconnected thalamic populations of thalamo-cortical relay (TCR) and reticular nucleus (RE) neurons, and cortical populations. [29]

The TCR neurons, which receive sensory input from the medulla, form excitatory synapses on both the somatosensory cortex and the RN. The RN also forms inhibitory synapses on the TCR whilst the cortex usually forms excitatory synapses [30]. Hence feedback loops are formed between different neuron populations. It is usually assumed that alpha band desynchronization is correlated with the increase of neuronal excitatory state [31]. During desynchronization, the RN neurons are inhibited and the pathway from TCR to cortex is activated, enhancing the evoked responses and other focal activity (e.g. gamma rhythms) in the cortex During synchronization, the activation of the RN, which has negative feedback to TCR, inhibits the neuronal cortical pathways by causing hyperpolarisation on the post-synaptic membranes, which is referred as inhibitory postsynaptic potential (IPSP). In this way, this idling state plays an active 'gating' role, inhibiting the pathways during sensory

119

signal processing. The neuronal transmitter GABA, which mediates IPSP, modulates the input and feedback in this neuronal network as well [29].

5.3.2 Cortical activation curve

Other studies concerning oscillations at different frequency bands, such as the gamma band, and different brain states, have demonstrated a contradictory relationship between ERD/ERS and the activation /deactivation of neuronal pathways to the model discussed above. A more general cortical activation model has, therefore, been applied to explain the ERD/ERS in different frequency bands and brain states. In the thalamo-cortical model which was discussed above, a large number of neurons participate in the ERD/ERS activity. Changes in this large and wide-spread network usually result in low-frequency and high-amplitude oscillations. Feedback loops and neuronal connections which form networks within focal cortical areas also generate ERD/ERS, but this change is usually at high-frequency and of low-amplitude. This ERS usually correlates with the increase of excitatory neural networks. In order to build this general CAM, some factors are key to explain the relationship between ERD/ERS and neuronal excitatory states. Actually a simple general model was developed before the detailed model for alpha rhythms discussed above. In 1973, Speckemans found that the amplitude of a special kind of neuronal response depended on the number of neurons which are not occupied in other activity [32]. The amount of unoccupied neurons available for oscillatory activities and the excitability level of neurons determine the amplitude of oscillations. With the increase of neuronal activity, the number of unoccupied neurons decreases whilst the amplitude of excitation increases. A model based on these two parameters has been built [33]. As illustrated in Figure 5-5, the amplitude of oscillations forms a bell-shaped curve (CAM curve).
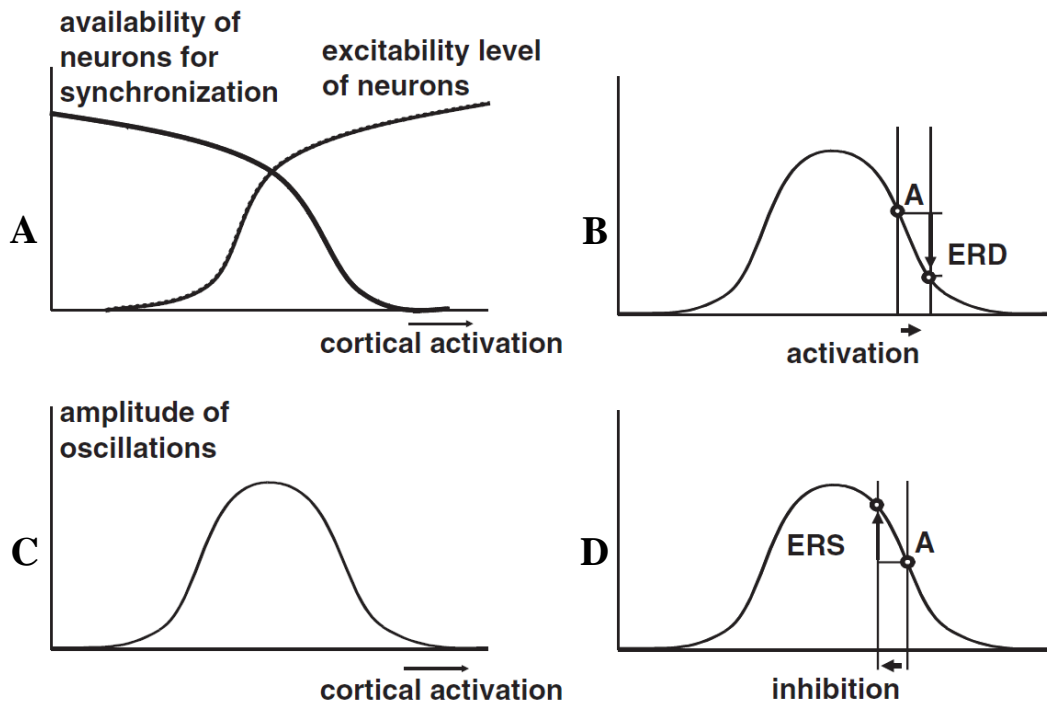
Figure 5-5: The relationship between CA, the excitability level of neurons, and the availability of neurons for synchronization [A]. The bell-shaped CAM curve represents the relationship between CA and the amplitude of oscillations [B]. At a certain baseline level of CA (working point A) an increase of CA results in an ERD [C] whereas a decrease of CA (inhibition) induces ERS [D]. [34]

In the network which generates low-frequency rhythms, quite a large portion of neurons participate in the activity, which accounts for the high-amplitude and wide-spread nature found in different studies. The position of the neuronal network state on this bell-shaped CAM curve, which is called the working point (WP), is on the descending right side. An increase of cortical activation (CA) pulls the WP right, resulting in an ERD, whilst a decrease of CA results in an ERS. If the WP is on the rising left part of the CAM curve, the relationship between changes of activation level and ERD/ERS is opposite.

5.3.3 Relation between ERD/ERS and CA

In this CAM, the WP, which represents the cortical activation level, has impact on the ERD/ERS. Investigation in comatose patients has shown that the level of consciousness influences the oscillatory activity [28]. At the beginning of recovery from coma, visual stimuli induce an ERS in the cortex. During this recovery process, which takes a few days, the Glasgow Coma Scale (GCS) that represents the conscious state of the patient rises from 4 (Deep Coma) to 15 (Near Awake). With the increase of GCS, the ERS amplitude resulting from a visual stimulus increases and then decreases. When the patient is near fully awake (GCS=15), this visual stimulus induces an ERD instead of an ERS. This can be explained if, during this recovery, the WP moves on the CAM curve. In the deep coma state, the WP is close to the left edge of the curve and stimuli only result in a small ERS; in the moderate coma state (GCS=9~12), the activation level of the cortex increases and the WP moves right, resulting in a larger amplitude change with the same level of stimulation. Further recovery moves the WP even more to the right half of this curve. In this near fully awake state, ERD appears during the application of stimuli. The influence of consciousness on ERD/ERS is shown in Figure 5-6.
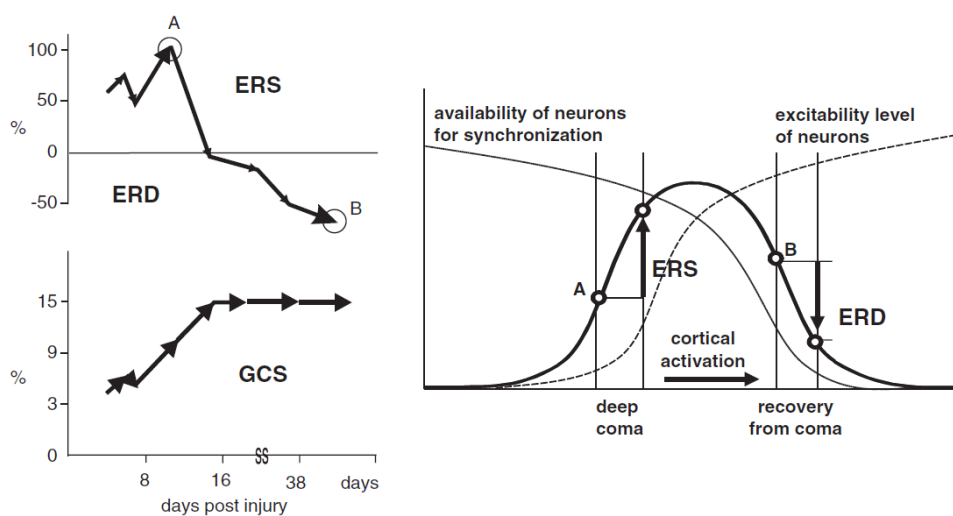
Figure 5-6: ERD/ERS in the 6–14 Hz band during recovery from coma (Left, A to B). The measurements of ERD and ERS are indicated in the CAM curve (Right).

In section 5.2.2, it was noted that low frequency alpha ERD and high frequency gamma ERS can be induced simultaneously in the same cortex. Based on the model discussed, it can be seen that for low-frequency oscillations, the cortical activation level is high and the WP is located on the right part of the CAM curve. The high-frequency components with small amplitude, on the other hand, come from focal inter-cortical networks and represent a low activation level. The WP of the high-frequency oscillations is on the rising left part of the curve. Hence external stimulation which increases the level of cortex activation produces different effects in the same cortex. Simultaneously high-frequency ERS and low frequency ERD can be found within different types of neuronal signal processing. These changes are illustrated in Figure 5-7. Although we present the high-frequency and low-frequency changes in the same curve for demonstration, different frequency components have their own parameters for the CAM curve because they originate from different groups of neurons within the network.
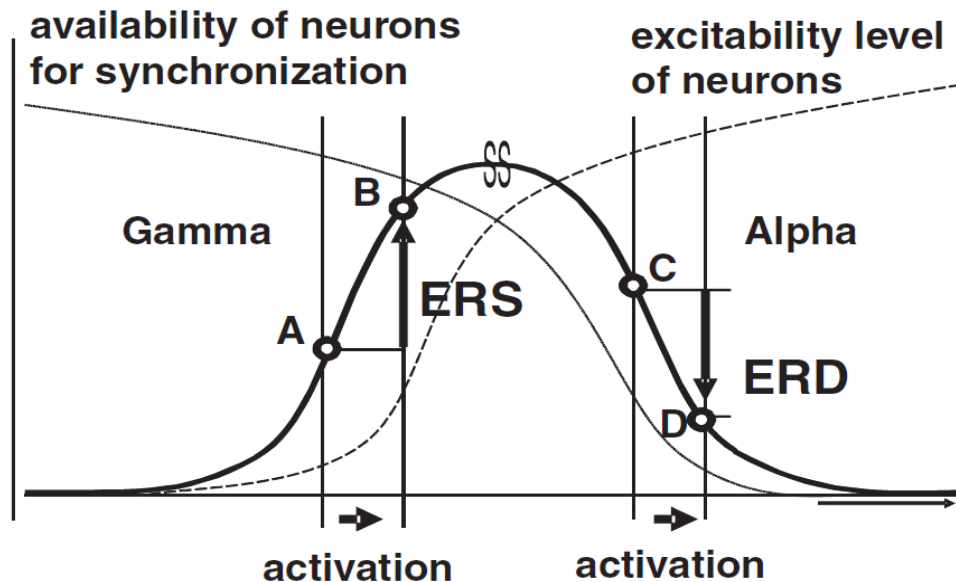
Figure 5-7: The relations between CA states and Alpha ERD/ Gamma ERS indicate the CAM.

The increase in beta band oscillations (Beta-ERS) in somatosensory and motor areas, which is also referred to as post movement beta rebound (PMBR), has been believed to play an important role in the somatosensory system [35]. This beta ERS can be elicited by median nerve stimulation, active or passive motor execution and motor imagery. By using transcranial magnetic stimulation (TMS), depolarization of the neurons in the cortex can be generated noninvasively. During beta ERS after hand movement and median nerve stimulation, the excitability of the motor cortex measured using a TMS method is reduced [36]. It also has been found that beta ERS is significantly attenuated during complex finger movements and imagination of the movements. Based on the CAM model, this beta ERS could be related to a decreased activation level in the cortex. After the termination of a sensory-motor task, the WP returns to its original location. During this inhibitory task on the declining part of CAM curve, an ERS is generated. If motor movement (e.g. cube manipulation) or imagery is applied continuously with other stimulations, the activation level baseline is increased, leading to the reduction of ERS related to these stimulations [37]. As illustrated in Figure 5-8, the amplitudes of the ERS could be used to measure the cortical activation level. A larger beta ERS represents less activated states whilst smaller ERS represents more activated states. This CAM will be tested in Chapter 8.
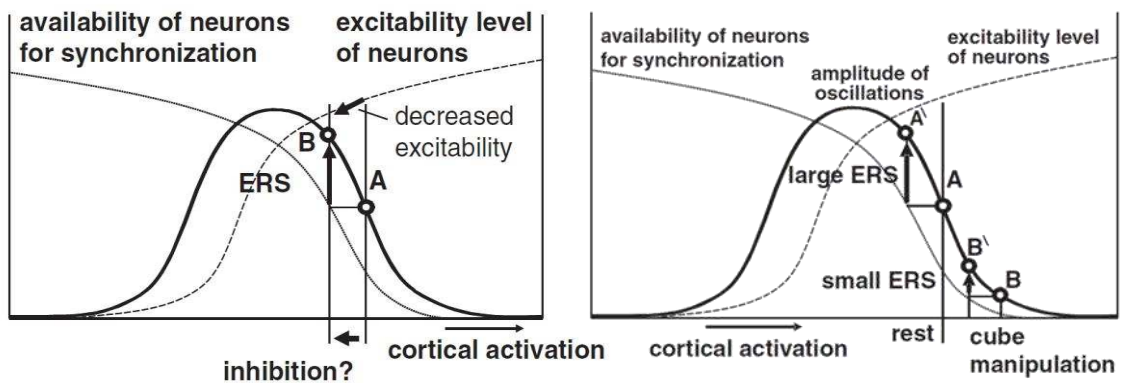
Figure 5-8: The beta ERS, which reflects cortical inhibition (Left), is suppressed during cube manipulation (Right). The two different states are represented by different WPs (A and B) in the CAM curve.

5.4 *Somatosensory fMRI*

In the study of somatosensory activity, fMRI has been applied since the 1990s [38-39]. The early studies mainly focused on the mapping of how the somatosensory cortex is organized and the topographic structure. It has been observed that both SI and SII show positive BOLD changes bilaterally during median nerve stimulation, though negative BOLD changes have also been observed ipsilaterally [40]. Nowadays, high-resolution fMRI at ultra-high-field (7T) offers an opportunity for more detailed mapping of the somatosensory cortex. The amplitude of the BOLD signal is dependent on the frequency of the stimulation [41]. In the area of contralateral SI, an increase in the frequency of median nerve stimulus results in an increase in BOLD signal.

Brain oscillations in primary somatosensory cortex have been found to increase correspondingly with BOLD signals during a finger tapping experiment [42-43]. Both are influenced when the cortex is inhibited using TMS [44]. Also in TMS driven motor tasks, the cortex is facilitated during low frequency band ERD and inhibited on the ERS. Recently it has been reported that the high-gamma band sychronization mainly contributes to the positive changing of BOLD signals [45]. But what the other frequency bands reflect and how they modulate the BOLD signal is still left to be answered. The non-linearity of BOLD, which has been well characterised in other cortices (e.g. visual), is still unclear in the somatosensory cortex. In Chapters 7 and 8, we will characterise somatosensory activity with a combination of 7T fMRI and MEG.

5.5 *References*

[1]   Purves, D., Augustine, G.J., Fitzpatrick, D., Katz, L.C., LaMantia, A., McNamara, J.O. and Williams, S.M., Neuroscience. 2rd edition. 2001: Sinauer Associates.

[2]   Gaetz, W. and Cheyne, D., Localization of sensorimotor cortical rhythms induced by tactile stimulation using spatially filtered MEG. Neuroimage, 2006. **30**(3): p. 899-908.

[3]   Hansen, P.C., Kringelbach, M.L. and Salmelin, R., MEG: An introduction to methods. 2010: Oxford.

[4]   Kandel, E.R., Schwartz, J.H., Jessell, T.M., Siegelbaum, S.A. and Hudspeth, A., Principles of neural science. Vol. 3. 1991: Elsevier New York.

[5]   Brenner, D., Lipton, J., Kaufman, L. and Williamson, S., Somatically evoked magnetic fields of the human brain. Science, 1978. **199**(4324): p. 81-83.

[6]   Kaufman, L., Okada, Y., Brenner, D. and Williamson, S.J., On the relation between somatic evoked potentials and fields. International Journal of Neuroscience, 1981. **15**(4): p. 223-239.

[7]   Kakigi, R., Somatosensory evoked magnetic fields following median nerve stimulation. Neuroscience research, 1994. **20**(2): p. 165-174.

[8]   Kakigi, R., Hoshiyama, M., Shimojo, M., Naka, D., Yamasaki, H., Watanabe, S., Xiang, J., Maeda, K., Lam, K. and Itomi, K., The somatosensory evoked magnetic fields. Progress in Neurobiology, 2000. **61**(5): p. 495-523.

[9]   Legrain, V., Guérit, J.M., Bruyer, R. and Plaghki, L., Attentional modulation of the nociceptive processing into the human brain: selective spatial attention, probability of stimulus occurrence, and target detection effects on laser evoked potentials. Pain, 2002. **99**(1-2): p. 21-39.

[10]   Maeno, T., Kaneko, A., Iramina, K., Eto, F. and Ueno, S., Source modeling of the P300 event-related response using magnetoencephalography and electroencephalography measurements. IEEE Transactions on Magnetics, 2003. **39**(5): p. 3396-3398.

[11]   Inoue, K., Hashimoto, I., Shirai, T., Kawakami, H., Miyachi, T., Mimori, Y. and Matsumoto, M., Disinhibition of the somatosensory cortex in cervical dystonia--decreased amplitudes of high-frequency oscillations. Clinical Neurophysiology, 2004. **115**(7): p. 1624-1630.

[12]   Schnitzler, A., Witte, O.W., Cheyne, D., Haid, G., Vrba, J. and Freund, H.J., Modulation of somatosensory evoked magnetic fields by sensory and motor interferences. Neuroreport, 1995. **21**(6): p. 1653-1658.

[13]   Kakigi, R., Shimojo, M., Hoshiyama, M., Koyama, S., Watanabe, S., Naka, D., Suzuki, H. and Nakamura, A., Effects of movement and movement imagery on somatosensory evoked magnetic fields following posterior tibial nerve stimulation. Cognitive Brain Research, 1997. **5**(3): p. 241-253.

[14]   Stancak, A., Svoboda, J., Rachmanova, R., Vrana, J., Kralik, J. and Tintera, J., Desynchronization of cortical rhythms following cutaneous stimulation: effects of stimulus repetition and intensity, and of the size of corpus callosurn. Clinical Neurophysiology, 2003. **114**(10): p. 1936-1947.

[15]   Salmelin, R. and Hari, R., Spatiotemporal Characteristics Of Sensorimotor Neuromagnetic Rhythms Related To Thumb Movement. Neuroscience, 1994. **60**(2): p. 537-550.

[16]   Schnitzler, A., Salenius, S., Salmelin, R., Jousmaki, V. and Hari, R., Involvement of primary motor cortex in motor imagery: A neuromagnetic study. Neuroimage, 1997. **6**(3): p. 201-208.

[17] Neuper, C. and Pfurtscheller, G., Evidence for distinct beta resonance frequencies in human EEG related to specific sensorimotor cortical areas. Clinical Neurophysiology, 2001. **112**(11): p. 2084-2097.

[18] Stancak, A., Lucking, C.H. and Kristeva-Feige, R., The size of corpus callosum and functional connectivities of cortical regions in finger and shoulder movements. Cognitive Brain Research, 2002. **13**(1): p. 61-74.

[19] Hirata, M., Kato, A., Taniguchi, M., Ninomiya, H., Cheyne, D., Robinson, S.E., Maruno, M., Kumura, E., Ishii, R., Hirabuki, N., Nakamura, H. and Yoshimine, T., Frequency-dependent spatial distribution of human somatosensory evoked neuromagnetic fields. Neuroscience Letters, 2002. **318**(2): p. 73-76.

[20] Brovelli, A., Battaglini, P.P., Naranjo, J.R. and Budai, R., Medium-range oscillatory network and the 20-Hz sensorimotor induced potential. Neuroimage, 2002. **16**(1): p. 130-141.

[21] Ohara, S., Crone, N.E., Weiss, N. and Lenz, F.A., Attention to a painful cutaneous laser stimulus modulates electrocorticographic event-related desynchronization in humans. Clinical Neurophysiology, 2004. **115**(7): p. 1641-1652.

[22] Simões, C., Jensen, O., Parkkonen, L. and Hari, R., Phase locking between human primary and secondary somatosensory cortices. Proceedings of the National Academy of Sciences, 2003. **100**(5): p. 2691-2694.

[23] Stancak, A., Polacek, H., Vrana, J., Rachmanova, R., Hoechstetter, K., Tintera, J. and Scherg, M., EEG source analysis and fMRI reveal two electrical sources in the fronto-parietal operculum during subepidermal finger stimulation. Neuroimage, 2005. **25**(1): p. 8-20.

[24] Ohara, S., Ikeda, A., Kunieda, T., Yazawa, S., Baba, K., Nagamine, T., Taki, W., Hashimoto, N., Mihara, T. and Shibasaki, H., Movement-related change of electrocorticographic activity in human supplementary motor area proper. Brain, 2000. **123**: p. 1203-1215.

[25] Pfurtscheller, G., Graimann, B., Huggins, J.E., Levine, S.P. and Schuh, L.A., Spatiotemporal patterns of beta desynchronization and gamma synchronization in corticographic data during self-paced movement. Clinical Neurophysiology, 2003. **114**(7): p. 1226-1236.

[26] Castro-Alamancos, M.A., Dynamics of sensory thalamocortical synaptic networks during information processing states. Progress in Neurobiology, 2004. **74**(4): p. 213-247.

[27] Prochazka, A., Sensorimotor Gain-Control - A Basic Strategy Of Motor Systems. Progress in Neurobiology, 1989. **33**(4): p. 281-307.

[28] Pfurtscheller, G., Event-related synchornization (ERS) - an electrophysiological correlate of cortical areas at rest. Electroencephalography and Clinical Neurophysiology, 1992. **83**(1): p. 62-69.

[29] Suffczynski, P., Kalitzin, S., Pfurtscheller, G. and Lopes da Silva, F., Computational model of thalamo-cortical networks: dynamical control of alpha rhythms in relation to focal attention. International Journal of Psychophysiology, 2001. **43**(1): p. 25-40.

[30] Lopes da Silva, F., Neural mechanisms underlying brain waves: from neural membranes to networks. Electroencephalography and Clinical Neurophysiology, 1991. **79**(2): p. 81-93.

[31] Steriade, M. and Llinás, R.R., The functional states of the thalamus and the associated neuronal interplay. Physiological Reviews, 1988. **68**(3): p. 649-743.

[32] Speckmann, E. and Caspers, H., Neurophysiologische Grundlagen der Provokationsmethoden in der Elektroenzephalographie. EEG-EMG Zeitschrift fur Elektroenzephalogrphie, Elektromyographie und Verwandte Gebiete, 1973. **4**: p. 157-167.

[33] Pfurtscheller, G. and Lopes da Silva, F., Event-related EEG/MEG synchronization and desynchronization: basic principles. Clinical Neurophysiology, 1999. **110**(11): p. 1842-1857.

[34] Pfurtscheller, G., Event-Related Dynamics of Brain Oscillations, in The cortical activation model (CAM), C. Neuper and W. Klimesch, Editors. 2006, Elsevier: p. 19-27.

[35] Honaga, E., Ishii, R., Kurimoto, R., Canuet, L., Ikezawa, K., Takahashi, H., Nakahachi, T., Iwase, M., Mizuta, I. and Yoshimine, T., Post-movement beta rebound abnormality as indicator of mirror neuron system dysfunction in autistic spectrum disorder: An MEG study. Neuroscience Letters, 2010. **478**(3): p. 141-145.

[36] Chen, R., Yaseen, Z., Cohen, L.G. and Hallett, M., Time course of corticospinal excitability in reaction time and self paced movements. Annals of Neurology, 1998. **44**(3): p. 317-325.

[37] Pfurtscheller, G., Woertz, M., Muller, G., Wriessnegger, S. and Pfurtscheller, K., Contrasting behavior of beta event-related synchronization and somatosensory evoked potential after median nerve stimulation during finger manipulation in man. Neuroscience Letters, 2002. **323**(2): p. 113-116.

[38] Hammeke, T.A., Yetkin, F.Z., Mueller, W.M., Morris, G.L., Haughton, V.M., Rao, S.M. and Binder, J.R., Functional Magnetic-Resonance-Imaging Of Somatosensory Stimulation. Neurosurgery, 1994. **35**(4): p. 677-681.

[39] Sakai, K., Watanabe, E., Onodera, Y., Itagaki, H., Yamamoto, E., Koizumi, H. and Miyashita, Y., Functional Mapping Of The Human Somatosensory Cortex With Echo-Planar MRI. Magnetic Resonance in Medicine, 1995. **33**(5): p. 736-743.

[40] Kastrup, A., Baudewig, J., Schnaudigel, S., Huonker, R., Becker, L., Sohns, J.M., Dechent, P., Klingner, C. and Witte, O.W., Behavioral correlates of negative BOLD signal changes in the primary somatosensory cortex. Neuroimage, 2008. **41**(4): p. 1364-1371.

[41] Stippich, C., Hofmann, R., Kapfer, D., Hempel, E., Heiland, S., Jansen, O. and Sartor, K., Somatotopic mapping of the human primary somatosensory cortex by fully automated tactile stimulation using functional magnetic resonance imaging. Neuroscience Letters, 1999. **277**(1): p. 25-28.

[42] Hummel, F., Andres, F., Altenmuller, E., Dichgans, J. and Gerloff, C., Inhibitory control of acquired motor programmes in the human brain. Brain, 2002. **125**: p. 404-420.

[43] Hummel, F., Kirsammer, R. and Gerloff, C., Ipsilateral cortical activation during finger sequences of increasing complexity: representation of movement difficulty or memory load? Clinical Neurophysiology, 2003. **114**(4): p. 605-613.

[44] Jancke, L., Steinmetz, H., Benilow, S. and Ziemann, U., Slowing fastest finger movements of the dominant hand with low-frequency rTMS of the hand area of the primary motor cortex. Experimental Brain Research, 2004. **155**(2): p. 196-203.

[45] Muthukumaraswamy, S.D., Edden, R.A.E., Jones, D.K., Swettenham, J.B. and Singh, K.D., Resting GABA concentration predicts peak gamma frequency and fMRI amplitude in response to visual stimulation in humans. Proceedings of the National Academy of Sciences of the United States of America, 2009. **106**(20): p. 8356-8361.

Chapter 6

MEG single pulse study of the somatosensory cortex

Overview: This chapter aims to elucidate the most significant neural oscillations found in the somatosensory cortex during electrical median nerve stimulation (MNS). Points to be considered in the experimental design are highlighted and the paradigms for MNS studies are designed. In experiments where a stimulus is presented to the subject at regular intervals, anticipatory effects may confound the neuromagnetic responses directly induced by MNS. For this reason we investigate whether the "temporal regularity" (i.e. whether a stimulus is presented at regular or irregular intervals) impacts the neural activity measured using MEG. Finally, the spatial separation of different neuromagnetic oscillations in the beta band is also discussed.

6.1 *Introduction*

The complex characteristic spatiotemporal patterns of oscillations in the cortex during sensorimotor processing were introduced in Chapter 5. The low frequency oscillations in somatosensory cortex reflect the cortical inhibition and excitation [1] and also appear to play an important role in the modulation of brain networks [2-4]. However, it has been reported in

previous researches [5-7] that, following different types of sensorimotor task (i.e. voluntary and passive movement, somatosensory stimulation, motor imagery etc.) oscillations with various onset time, amplitudes and frequency range can be measured. MNS above the sensory threshold can induce changes in low frequency (~20Hz beta band) oscillations, predominantly in the contralateral primary somatosensory cortex (cSI)[8-9]. In addition, MNS is known to produce phase locked gamma oscillations, and some reports show that these high frequency oscillations persist, even up to the extremely high frequency sigma range (as high as 600Hz). For this reason and for the purpose of this thesis, the most prominent frequency bands in which MNS induces significant changes should be determined, by time-frequency analysis, in some simple studies. The beamformer method, discussed in Chapter 4, has been proven to be ideal for localizing non-phase locked oscillations in the cortex [2]. As beamformers are sensitive to the accuracy of the covariance matrix, a testing study is required to optimize paradigms. Results of this testing study are used to optimize tradeoffs between trial length, number of trials, bandwidth and the total time subjects are kept in the MEG system.

Phase locked somatosensory evoked fields (SEFs) measured during sensorimotor tasks contain a number of effects, inducing the N20m, P35m, N60m, P100m, N160m and P300 [10]. These effects vary during different types of sensorimotor task and the most prominent effect in MNS is P35m. The participation of these effects in the sensorimotor processing and preparation will also be studied in the initial experiments with MNS described in this chapter.

MEG studies usually involve presenting subject with multiple interactions of the same stimulus (trials). However this brings with it the confound that, if trials are spaced evenly in time, anticipatory may affect the measured response. For this reason the "regularity" of onset times across trials, i.e. variation in the inter stimulus interval (ISI), may affect the neural activity. Regularity of sensorimotor tasks has been reported to influence both evoked

potentials and beta band oscillations in a previous study [11] comparing regular alternating hand presentations with jittered hand presentations. This proves that information processing of voluntary focused movement is highly dependent on regularity in the stream of input. Priming or readiness of the cortex through top-down modulation could be hypothesized as the process by which a stimulus is anticipated and basic sensory response altered. [12] However, for somatosensory studies with MNS, although event related oscillations are modulated by cortical excitability, whether the regularity of stimuli has impacts on oscillations and evoked responses remains unclear.

Previous studies have shown beta band stimulus induced ERD and post-stimulus ERS (or post-movement beta rebound, PMBR) can be separated spatially [13]. As ERD and ERS can be related to activation and inhibition of cortex [14-15], this spatial separation may suggest that these two effects are generated from different neural networks or generators in the thalamo-cortical system. However, the precise mechanisms underlying these effects are still unclear.

In this chapter, we first use non-painful MNS in a study with far more trials than usually required to compare the accuracies of source localization using different amounts of data. In this way, we sought to optimize the paradigm used in the following studies (Chapters 6, 7 and 8) based on this comparison. Then, using a regular and jittered MNS protocol, we undertake time-frequency analysis in the 1-150Hz region to characterise the most significant non-phase locked oscillatory effects. Precise bands and contrast time windows are determined for the experiments described in the following chapters. We also examine whether the regularity of stimuli affects the induced oscillations and evoked responses. Finally, possible spatial separations of beta ERD and ERS are also examined.

More specifically in this chapter, the following hypotheses are tested:

1) Low frequency oscillations in somatosensory cortex can be localized correctly with a relatively small number of trials.

2) Beta band ERD and ERS are the most significant oscillatory changes in MNS studies and have advantages over other low frequency bands in both source localization and timecourse analysis.

3) The regularity of MNS with long inter stimulus intervals (ISIs>5s) does not impact on the induced activities and evoked responses.

4) Beta ERD and ERS can be spatially separated using group averaged SAM images.

6.2 *Methods*

6.2.1 Subjects and paradigms

Six healthy right-handed subjects (4 males, 2 females) took part in the study (1 to test the number of trials required and 5 to test the influence of a jittered paradigm); handedness was assessed using a modified version of the Edinburgh handedness inventory. All these subjects also took part in the 3T anatomical MRI reference scanning. Both the MEG and MRI recordings were approved by the Medical School Ethics Committee of the University of Nottingham.

Electrical non-painful MNS of the right median nerve was applied using a Digitizer Constant Current Stimulator (DS7A, Welwyn Garden City, England). Two surface electrodes (diameter 10mm) fixed in a plastic holder with a distance between them of 30mm were used to deliver the median nerve pulse to the subjects. These electrodes were placed on the right wrist of the subjects, after cleaning the skin and placing conducting gel under each electrode to ensure good electrical connection with the skin. The polarity of the electrodes was chosen to generate the largest effect with lowest current. A 0.5 ms square wave pulse was used and the current amplitude was set at the motor threshold to stimulate the third digit of the hand.

One subject (female) participated in a paradigm which comprised a total of 200 trials. In each trial a single electrical pulse was delivered with 1s pre-stimulus time and 4s trial length. This paradigm was used to study the influence of the total number of trials on source localization. Based on this study, the regular and jittered pulse paradigm was developed.

Five subjects (4 male, 1 female) participated in the regular and jittered pulse paradigm. In all cases a single MNS pulse was applied per trial; the pre-stimulus time was 2s for the regular condition. For the jittered condition, pre-stimulus times were chosen pseudorandomly from 2s, 3s, 4s, 5s and 6s using a pseudo-random programme; the total trial length was 10s and there were 100 trials in both conditions.

6.2.2 Data acquisition

Anatomical magnetic resonance images were acquired using a 3.0T Philips Intera Achieva system (Philips Healthcare, Best, Netherland) with a whole body RF coil for excitation and

an 8-channel SENSE receive coil. A set of T_1-weighted images covering the whole head (FOV= $256\times256\times256mm^3$; matrix $256\times256\times256voxels$) were collected with a 3D-MPRAGE (magnetisation prepared rapid gradient echo) sequence, TR = 8.3ms, TE = 3.8ms, resolution $1\times1\times1mm^3$. These anatomical images were used for co-registration of the brain anatomy to the MEG sensor geometry.

The 275 channel whole head MEG system introduced in Chapter 4 was used to record the neuromagnetic signal from the head in response to the stimulus. The subjects were scanned while supine in the system. A noise recording (60s) was carried out before each experiment to ensure all possible external sources of interference were minimised.

Prior to MEG data acquisition, three head localisation coils (HLCs) were attached to the subjects, at the nasion and left and right preauricular points. Digitised representations of the scalp which consisted of more than 300 points distributed uniformly on the head surface were obtained using the Polhemus digitiser. These Polhemus data were then co-registered to the head shape extracted from the anatomical MR imaging using surface matching software as described in Section 4.3.3.

MEG data were acquired in third order synthetic gradiometer configuration, with a sample rate of 600 Hz and a 150 Hz anti-aliasing filter. The head position was localized both before and after recording. A subject motion tolerance of 5mm throughout the experiment was implemented and any data exceeding this tolerance was disregarded. During data acquisition, subjects were asked to keep their eyes as still as possible and to remain awake. At intervals between scans, the subjects were checked to confirm they were comfortable and still awake via a microphone. The recording time of a whole experiment was designed to be less than 45minutes, in order that the subjects maintained concentration.

6.2.3 Data analysis

The raw MEG data were processed using "DataEditor" (MEGService Ltd., Vancouver, Canada). A high pass filter at 1Hz and a low pass filter at 150Hz were also applied. Bad trials containing excessive noise were removed.

6.2.3.1 Source localization

Source localization of induced oscillatory activity was performed using the adaptive beamforming technique Synthetic Aperture Magnetometry (SAM), discussed in Section 4.4.3. In the 200 trial study, source localization was based on beta (13-30Hz) power change and on all trials (that is 199 trials after the exclusion of bad trials). In addition, separate source localizations were based on 150 trials, 100 trials, 50 trials and 25 trials. Contrast windows were selected with 'active' periods spanning 0.5s immediately following the stimuli and 'control' periods spanning $1 \leq t \leq 0.5s$ before the end of trials. Data covariance matrices were regularised using a regularization parameter of 2 in order to ensure the matrices were well conditioned (see Section 4.5.3). Functional images showing the spatial distribution of power change between active and control windows were created using a Pseudo Student's T comparison. The Pseudo-T-Statistical images were constructed on a $2mm^3$ isotropic grid. Results were compared across trial numbers to find the minimum number of trials required in order to generate a reasonable functional image.

In the regular and jittered study with 100 trials for each condition, source localizations of beta ERD and beta ERS were performed on all trials. For beta ERD, 'active' periods were selected as $0 \leq t \leq 0.5s$ following the stimuli with 'control' periods spanning 0.5s ($-1.25 \leq t \leq -0.75s$) before the stimuli. For beta ERS, 'active' periods were chosen to begin 0.7s following

the stimuli, spanning 1s, and 'control' periods spanning 1s (-1.25≤t≤-0.25s) before the stimuli. The time windows were equal in the regular and jittered conditions.

6.2.3.2   Time-frequency analysis

The SAM beamformer uses a spatial filter to estimate the temporal course of electrical neural activity at a particular site (voxel) in the brain. The output of such a spatial filter is termed SAM virtual sensor, which works like a sensor placed within the voxel. Virtual sensor traces were extracted from peak points in the SAM images. The timecourses of the envelope of electrical oscillatory were obtained by applying a Hilbert transform to the virtual sensor data to derive the analytic signal. The absolute values of the analytic signal then yielded the 'Hilbert envelope'. To calculate the spectrograms which show how the spectral density of a signal varies, 147 band pass filters from 1 to 150Hz were applied to the data extracted from peaks in the SAM images with Nutmeg (http://nutmeg.berkeley.edu/). The bandwidth of each filter was 3Hz and the step was 1Hz. Timecourses of the Hilbert envelopes were generated from the filtered virtual sensor data. To obtain the average non-phase locked oscillatory spectrograms, the Hilbert envelopes were averaged across trials. To obtain the averaged phase locked spectrograms, Hilbert envelopes of the virtual sensor timecourses averaged across trials were calculated. The averaged Hilbert envelopes were concatenated in frequency space to get a Time-frequency spectrogram. By subtracting the phased locked spectrograms from the non-phase locked spectrograms, the non-phase locked only spectrogram was generated. This time-frequency analysis was taken for the regular condition and all the three kinds of spectrogram were averaged across subjects.

Hilbert envelopes computed in individual bands were also calculated in the same way. Virtual sensor traces from peak points in SAM images were filtered into the delta (1-4Hz), theta (4-8Hz), alpha (8-13Hz), beta (13-30Hz), low gamma (30-48Hz), mid gamma (52-90Hz) and high gamma (90-150Hz) bands. Hilbert envelopes were averaged across trials for each frequency range. An average of 1s pre-stimuli data ($-1.25 \leq t \leq 0.25$s) was taken from the Hilbert envelope and assumed to be the baseline for each frequency band. Baseline mean corrected timecourses were then plotted. For the regular condition, the envelopes were calculated across whole trials. For the jittered condition, the envelopes were calculated from 1.9s before the stimulus to 3.6s following the stimulus. Peak percentage changes of ERD and ERS were plotted with error bars.

To obtain the averaged evoked responses, the virtual sensor timecourses without Hilbert transform were averaged across trials for both conditions using the timing stated above. Peak amplitude changes of N20m, P35m, P100m N160m and P300m were plotted with error bars. Paired Wilcoxon Signed Rank tests were used to test for significant differences in both the evoked responses and the ERD/ERS between regular and jittered condition.

6.2.3.3   Group averaged SAM images

In order to generate the group averaged images of oscillatory power change, SAM images were normalized to the T_1 weighted template brain in SPM5 (http://www.fil.ion.ucl.ac.uk/spm/) and then averaged across individual using Matlab. The averaged functional images of both beta ERD and ERS were overlaid onto the same template brain in FSL (www.fmrib.ox.ac.uk/fsl/).

6.3 *Results*

The MEG raw data averaged across trials for the 200 trial subject is shown in with a single

bad trial eliminated. Data from all 275 channels are overlaid in different groups.
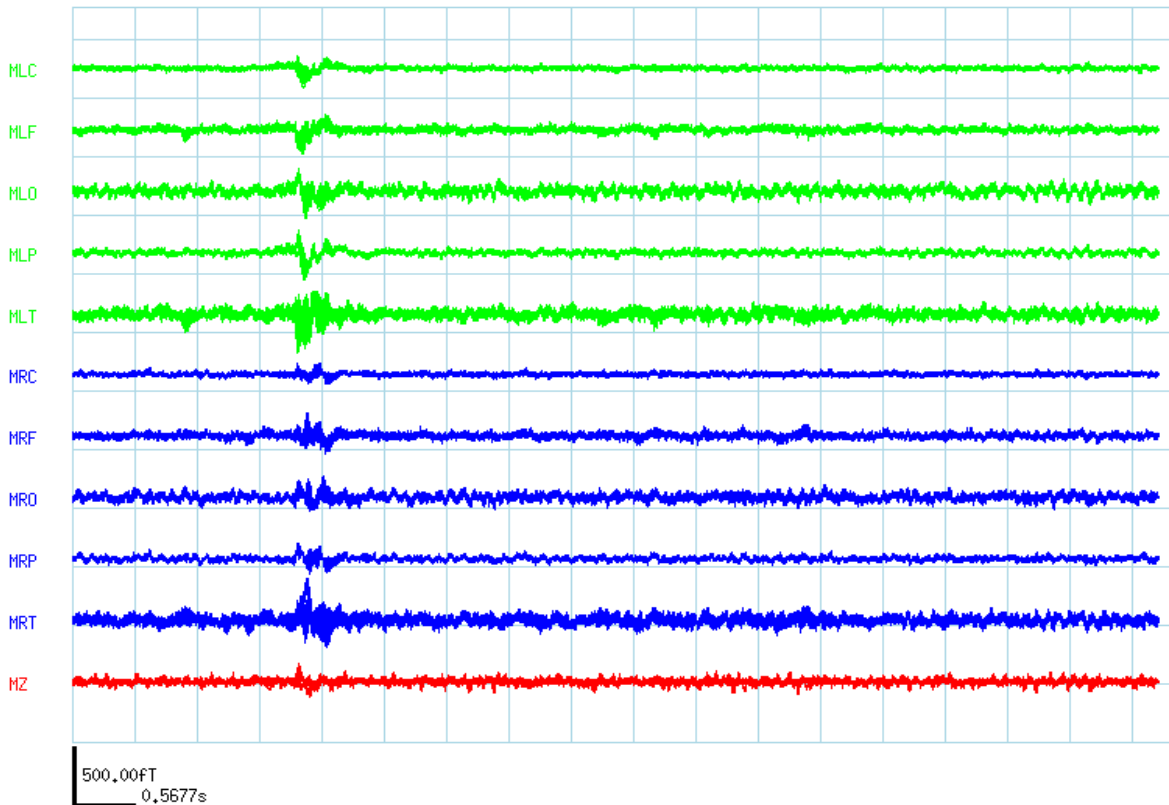
Figure 6-1: The MEG raw data averaged across 199 trials (1 bad trial was eliminated) are

overlaid in different groups. The green lines represent the data from the sensors covering left

hemisphere of brain, MLC for MEG_left_central, MLF for MEG_left_frontal, MLO for

MEG_left_occipital, MLP for MEG_left_parietal and MLT for MEG_left_temporal. The blue

lines represent the data from the sensors covering right hemisphere of brain. The red line

MZ are from the sensor over the central line of brain.

6.3.1 Optimising trial number and length

199 Trials

150 Trials

100 Trials
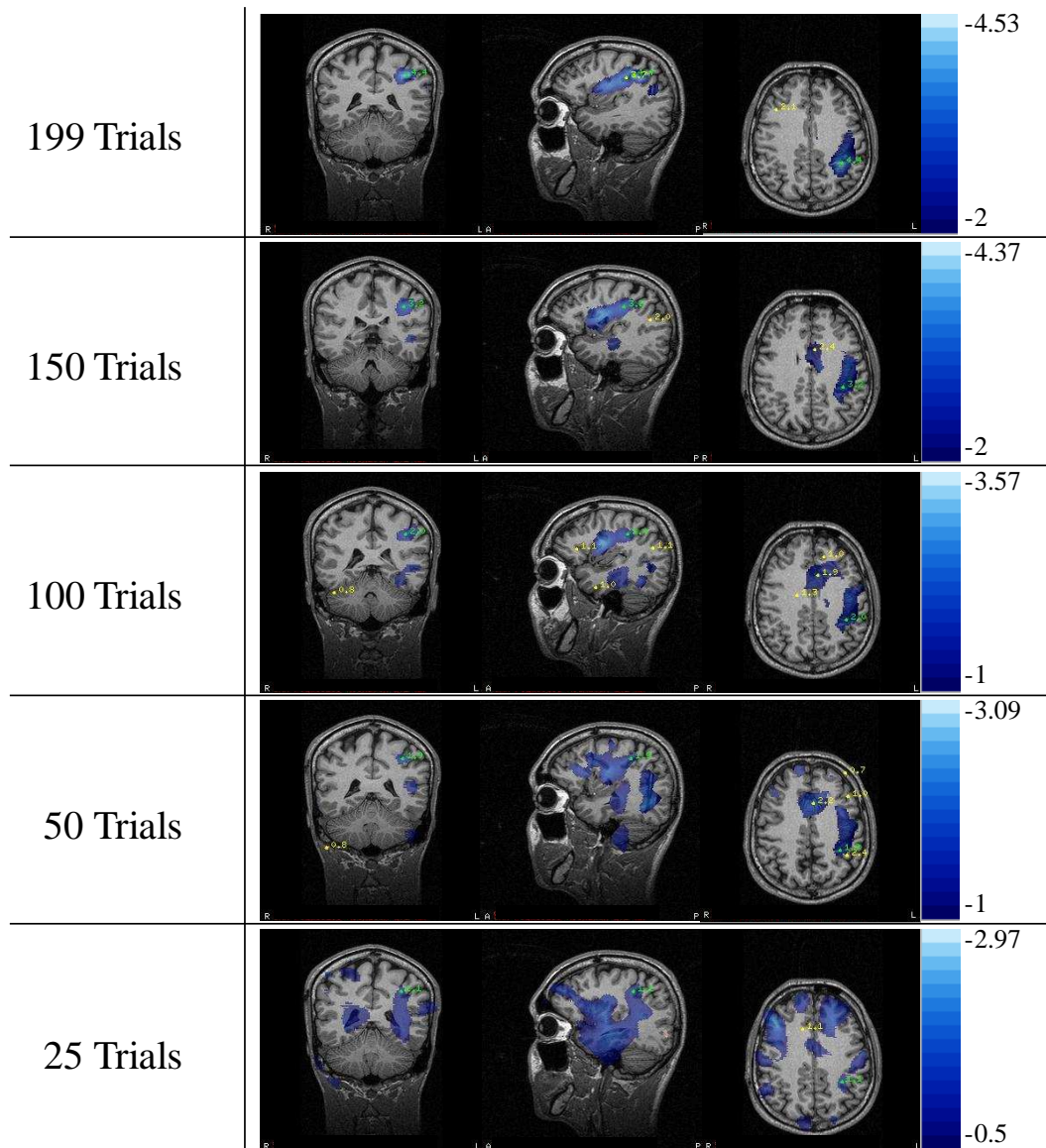
50 Trials

25 Trials

Figure 6-2: SAM images showing the distribution of beta ERD generated using different numbers of trials. Pesuedo T values are shown on the right.

The spatial localization of beta ERD with different numbers of trials is shown in Figure 6-2. By using all trials (199 trials), 150 trials, 100 trials 50 trials and 25 trials, five different SAM images have been generated. The total durations of the covariance window are 99.5s, 75s, 50s, 25s and 12.5s respectively. As discussed in Chapter 4, with a pre-determined

bandwidth, decreasing the length of the total covariance window leads to an increase in error in the beamformer method. With all 199 trials, the total duration was 99.5s. The SAM images in the top row show a large decrease in beta band power in the contralateral primary somatosensory cortex (cSI), close to the posterior bank of the central sulcus. A peak point with a maximum Pseudo-T-value 4.4 is found. Using 150 trials, the image is similar but an artificial peak is found inferior in the brain, which is not in the sensorimotor cortex. However, a peak point with (Pseudo-T-value 3.2) is again found in cSI and its location is close to the peak localized using all trials. The peak points, found within cSI, their locations and Pseudo-T-values are shown in Table 6-1. The regularization parameter is 2.

Table 6-1: Pesudo T values and locations of ERD peak points found in cSI using different number of trials.

	Number of peak	Pesudo-T-Value	Location x (mm)	Location y (mm)	Location z (mm)
199 trials	1 of 58	4.4	2.8	4.0	10.0
150 trials	2 of 60	3.2	3.2	4	9.2
100 trials	4 of 90	2.0	3.2	4.2	9.6
50 trials	16 of 92	1.9	3.2	3.8	10.2
25 trials	53 of 126	1.1	2.8	3.6	10

It can be seen using only 150 or 100 trials that the peak points of beta ERD in cSI are reliably found and their locations are close to the peak point localized using all trials. However, if we further reduce the number of trials to 50 or 25 trials, the number of peaks increases dramatically. The peak points of beta ERD in cSI are possibly covered by the large numbers of artificial points. Under these conditions, it is difficult to localize the beta ERD correctly as a lot of artificial peak points in neighbouring areas can easily lead to errors.

A

Frequency(Hz)

Time(s)

B

Frequency(Hz)

Time(s)

C

Frequency(Hz)

Time(s)

Figure 6-3: Spectrograms (Time-frequency plots) of non-phase locked and phase locked [A], phase locked only [B] and non-phased locked only [C] activity, derived using all 199 good trials in a single individual.

Spectrograms showing different neuroelectrical effects in different frequency bands are shown in Figure 6-3. There is a loss in power following stimulus onset in the beta band (13-30Hz). The beta oscillations rebound immediately after the termination of beta ERD and there is no gap between beta ERD and ERS. It is also evident that although beta band ERD

lasts only about 0.5s, it can take about 2 seconds for beta ERS to return to base line. For the alpha rhythm, it takes even longer for recovery and a 4s trial length is insufficient to study low frequency oscillations in somatosensory cortex, since the effects will not return to baseline between trials.

6.3.2 Time-frequency analysis

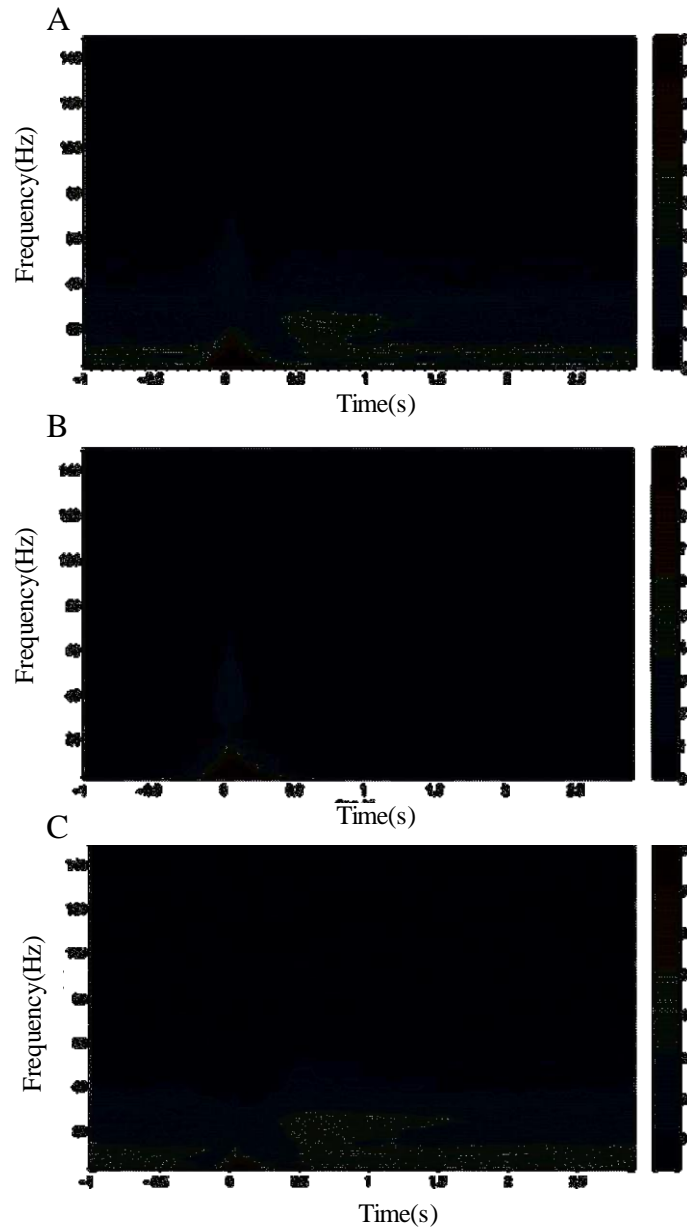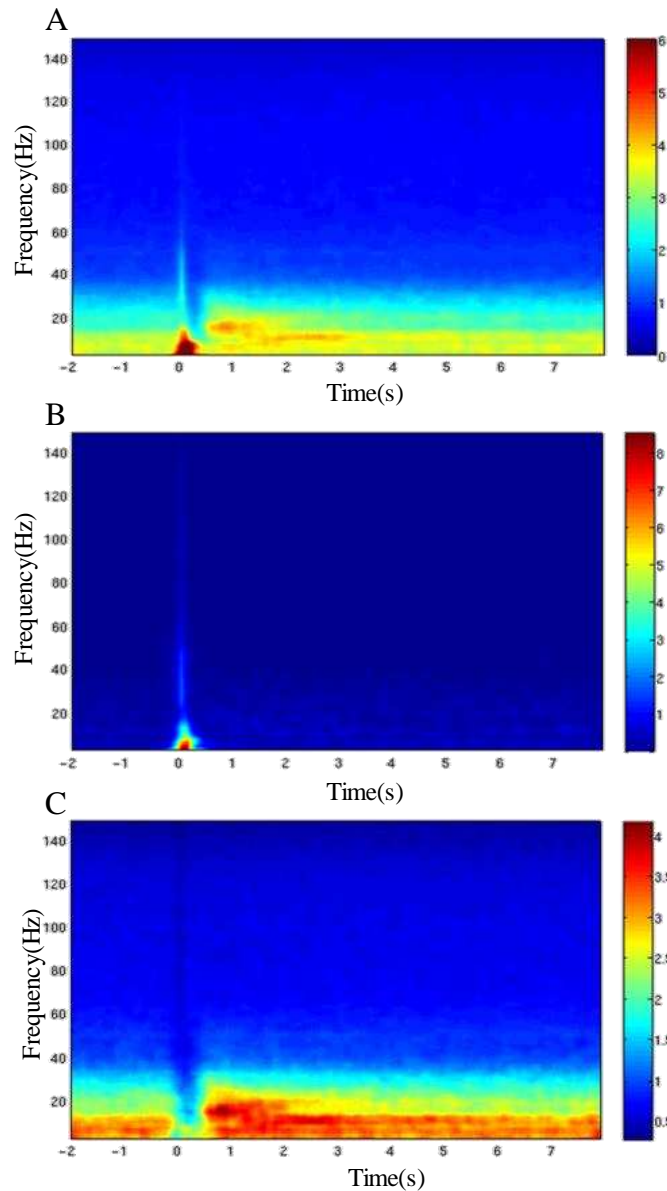Figure 6-4: Group averaged spectrograms of non-phase locked and phase locked [A], phase locked only [B] and non-phased locked only [C] activities in the regular condition of regular and jittered study. Only the case for a regular stimulus is shown.

Figure 6-4 shows the spectrogram of non-phase locked and phase locked [A], phased locked only [B] and non-phased locked only effects [C] averaged across subjects from virtual sensors located in the peak beta ERD locations. These results agree with the beta ERD/ERS changes observed in Figure 6-3. Besides beta band oscillatory activity, in alpha band (8-13Hz), also sometimes referred to as Mu band), a smaller decrease of power is also observed after stimulus onset. The alpha rebound appears 1s following stimulus onset and lasts for approximately 3s. Both the desynchronization and rebound in alpha band are small compared to similar effects in beta band. In theta band (4-8Hz), there is strong phase locked activity after stimulus onset, lasting about 0.2s. The oscillatory power change is tiny compared to other bands. A rebound may exist at the same time as beta ERS, but this effect is masked by low SNR. There are no significant non-phase locked gamma oscillatory effects observed in Figure 6-4[A and C]. But in the spectrogram showing phase locked effects (Figure 6-4[B]), transient gamma oscillations within 0.1s following stimulus onset were observed. The phase locked effects in the lower gamma band exhibit larger amplitude than these observed in the middle and higher gamma bands.
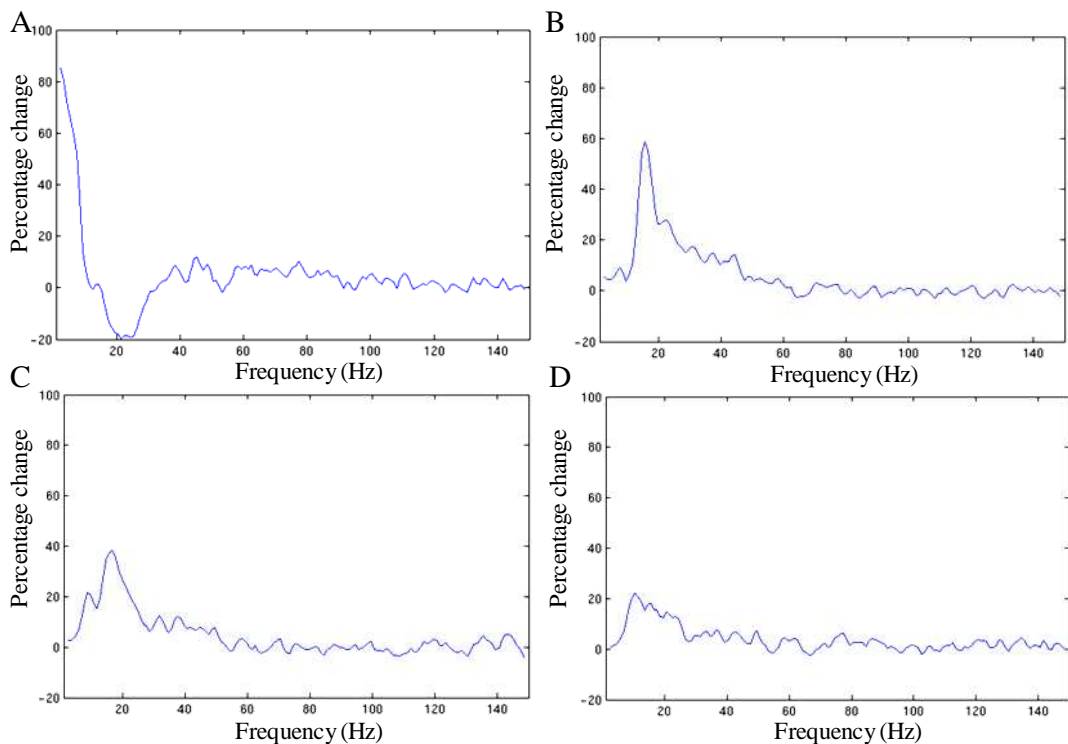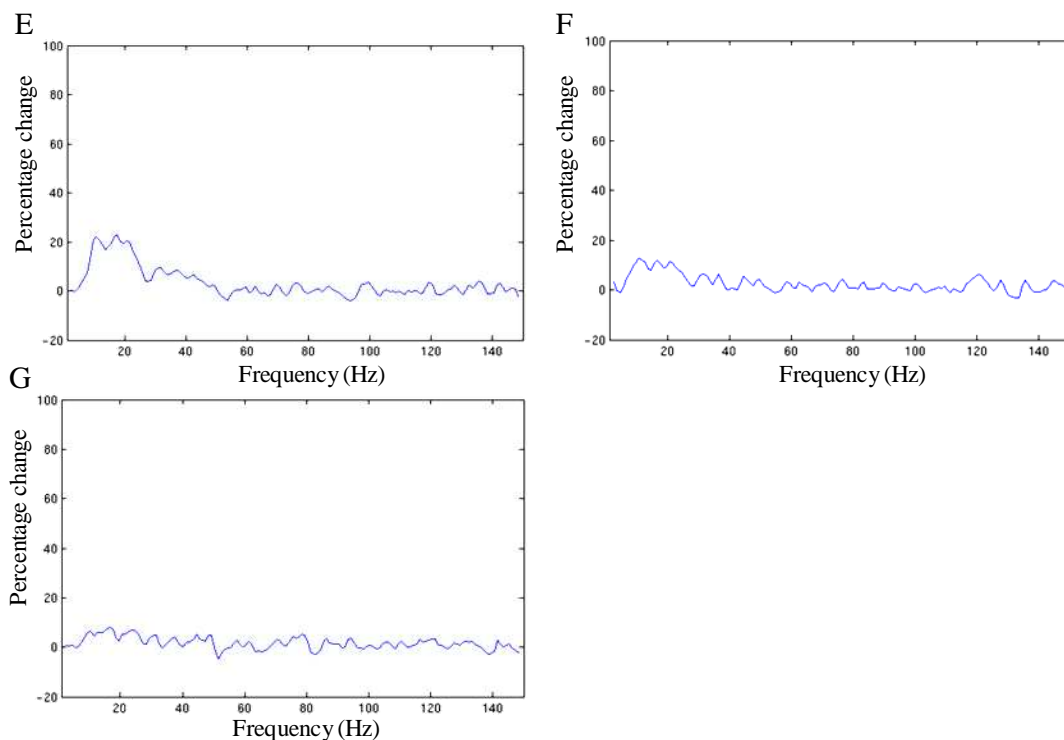
Figure 6-5: Percentage power changes between active windows of 0-0.5s [A], 0.5-1s [B], 1-1.5s [C], 1.5-2s [D], 2-2.5s [E], 2.5-3s [F], 3-3.5s [G] after the stimulus onset and 0.5s pre-stimuli control windows.

The percentage power change between active windows and control windows across all frequency bands are plotted in Figure 6-5. Different active windows are considered. During 0-0.5s after the onset of the stimulus (Figure 6-2 [A]), a large power decrease (~-20%) is found in the beta band. The amplitude of ERD is constant between 13Hz and 30Hz. A small decrease in the alpha band (8-13Hz) is also found. In lower frequency bands (1-8Hz) there is a large increase of power and in the gamma band (30-150Hz) there is no significant change. During 0.5-1s after the onset of stimulus (Figure 6-5 [B]), the largest beta ERS is found. The lower beta band has a peaked in ERS at about 16Hz. In the high beta band, ERS becomes smaller with increasing frequency. The alpha ERS is relatively small compared to that in the beta band. In the 1-2s time window after the onset of stimulus (Figure 6-5 [C] and [D]) the percentage change in beta ERS decreases rapidly in the low beta band whilst the high beta

band component is stable. The alpha ERS increases to about 20%. In the 2-3s time window (Figure 6-5 [E] and [F]) low beta band ERS drops to the same level as high beta band ERS and both keep decreasing with time. The alpha ERS is still stable (~20%) until about 2.5s after the onset of stimulus. After 3s following the stimulus onset (Figure 6-5 [G]), oscillatory power changes across all frequency bands returned to baseline.
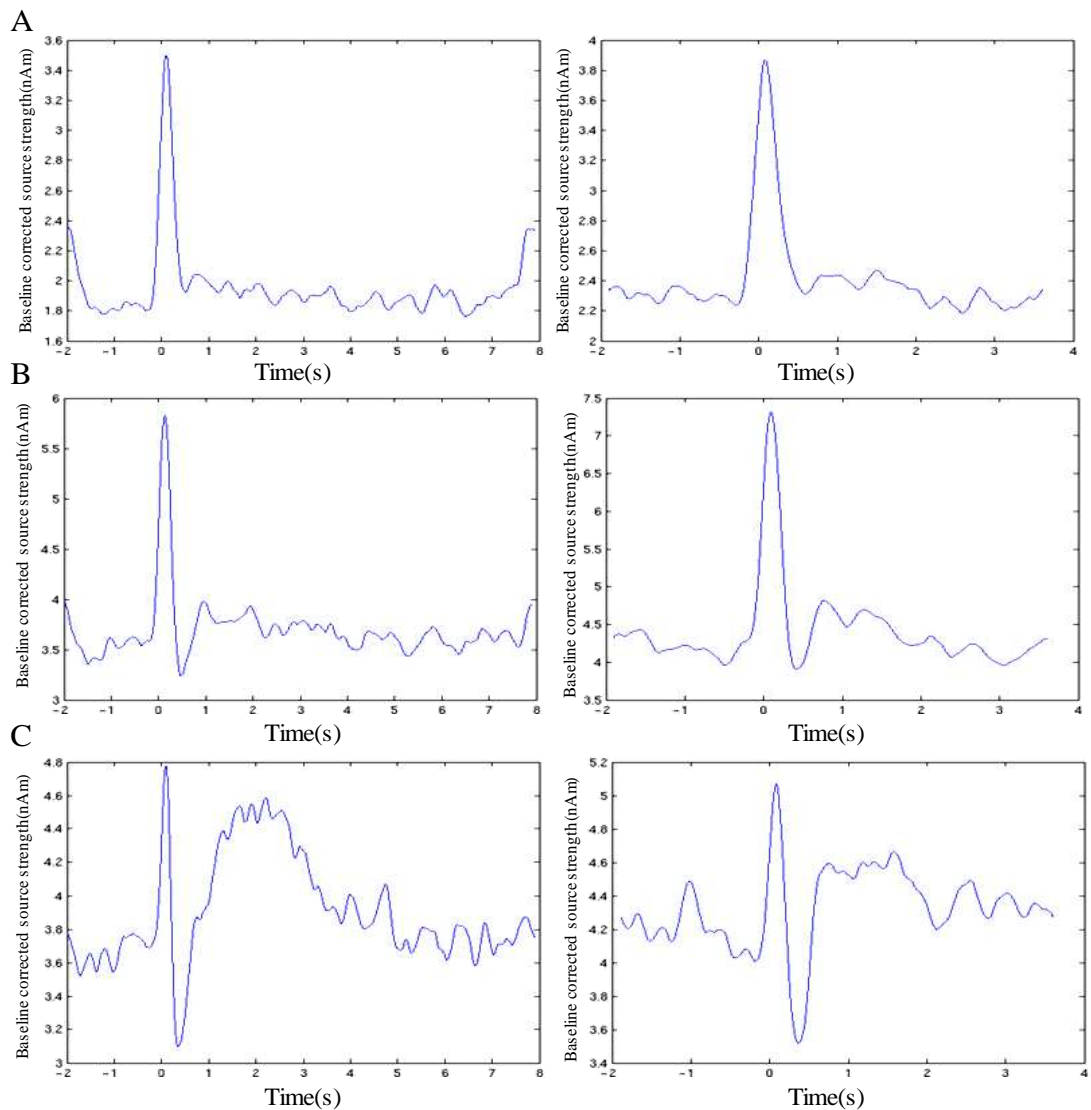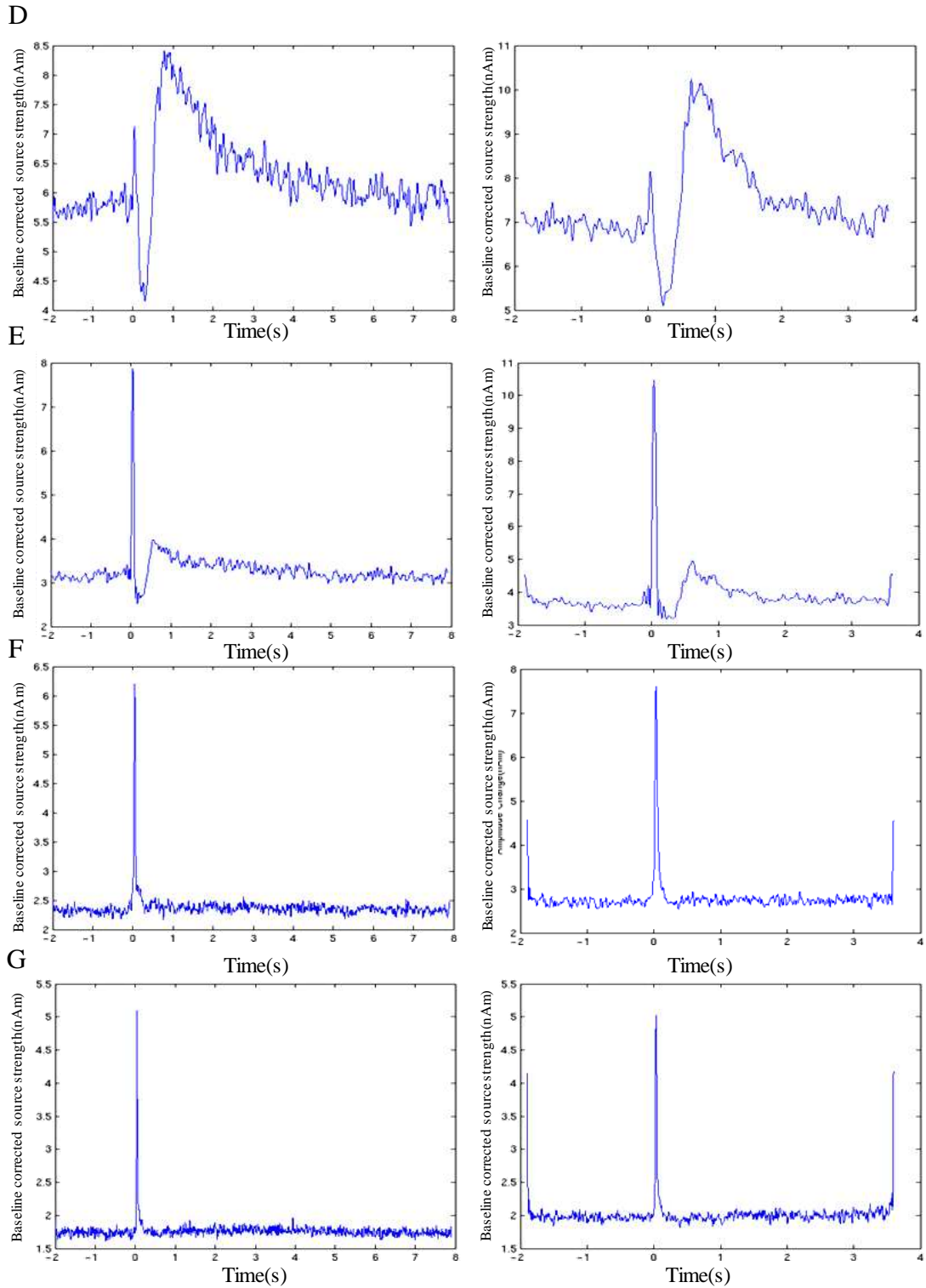
Figure 6-6: Timecourses of delta (1-4Hz)[A], theta (4-8Hz)[B], alpha (8-13Hz)[C], beta(13-30Hz)[D] lower gamma (30-50Hz)[E], middle gamma (50-90)[F] and higher gamma (90-150Hz)[G] band oscillations for both the regular(left column) and jittered (right column) conditions.

In Figure 6-6 the Hilbert envelopes in different frequency bands in both the regular and jittered conditions are plotted. Virtual sensor traces were generated from peak locations in beta ERD located in cSI. It can be seen that most non-phase locked oscillatory effects are in the low frequency band range between 4Hz and 30Hz including theta band (4-8Hz), alpha band (8-13Hz) and beta band(13-30Hz). In even lower delta band (Figure 6-6 [A]), there is no non-phase locked activity. In the theta band, as shown in Figure 6-6[B], a small power decrease following the stimulus onset is found. This desynchronization was relatively small compared to the evoked response and disappeared within 1s after stimulus onset. In the alpha band (Figure 6-6 [C]), the desynchronization was larger and lasted until about 0.5 after the stimulus onset. There was also a significant rebound which started at about 1s following the stimulus onset and returned to baseline at 3s. The largest energy change was in the beta band (Figure 6-6 [D]). The beta ERD appeared immediately after the phased locked evoked response, lasting ~0.5s. The ERS reached a peak quickly, about 1s after the stimulus onset and dropped to baseline in the following 1-2s. The beta ERS had a different shape compared to the alpha ERS. It reached a peak amplitude rapidly after the ERD and drops down slowly. In the gamma band, no significant non-phased locked oscillatory power change was found but transient phased locked evoked responses were found. Although there were some oscillations in the lower gamma band, they were likely due to the influence of the neighbouring beta band having the same timecourse.
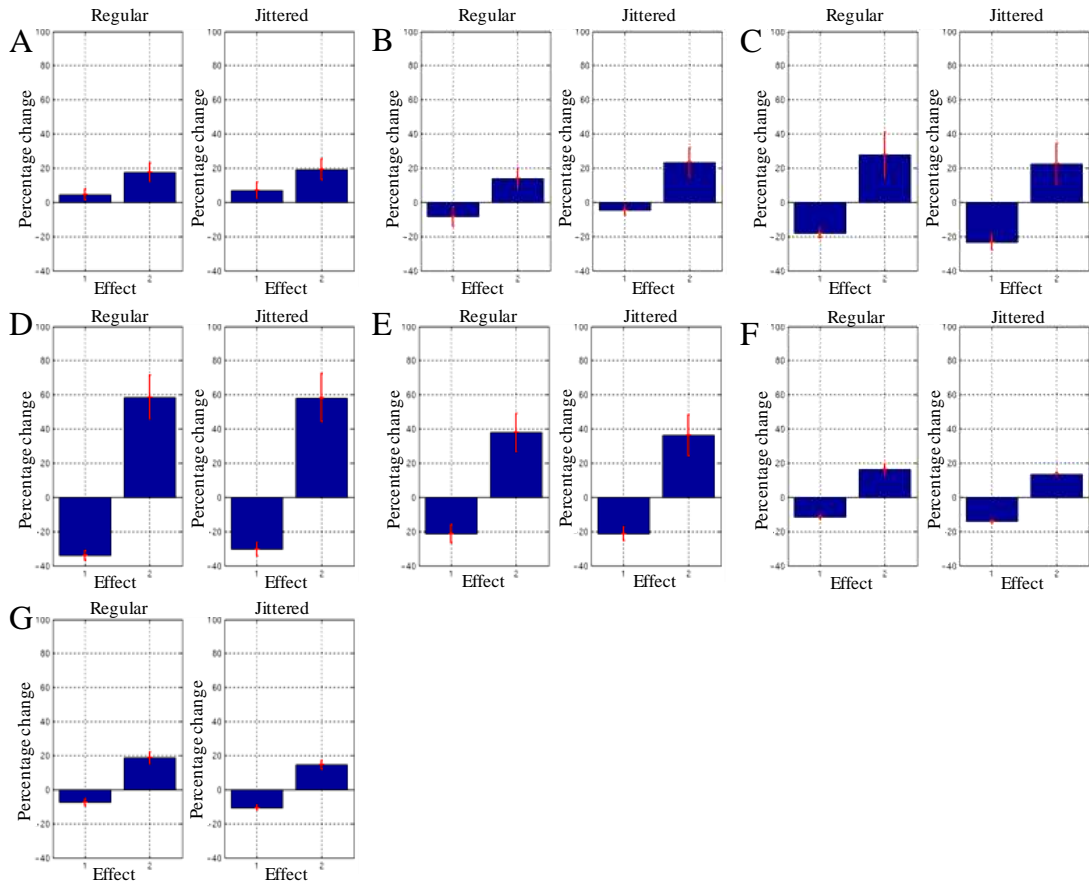
Figure 6-7: Percentage change in delta (1-4Hz) [A], theta (4-8Hz) [B], alpha(8-13Hz) [C], beta(13-30Hz) [D], lower gamma(30-48Hz) [E], middle gamma(52-90) [F] and higher gamma(90-150Hz) [G] band ERD (Effect 1) and ERS (Effect2) in the regular and jittered conditions.

The peak percentage changes of power across all the frequency bands in both the regular and jittered conditions are plotted in Figure 6-7. The largest ERD and ERS were found in the beta band. The percentage change of beta ERD is smaller than the ERS, but had less variance across subjects. The large ERD/ERS changes were also found in alpha and lower gamma band. However, as discussed above, the oscillations in lower gamma band were likely due to influences of beta oscillations. No significant difference (minimal p-value found is p=0.18) was found between regular and jittered condition across all these frequency bands. However, the baseline power varied between the two conditions.
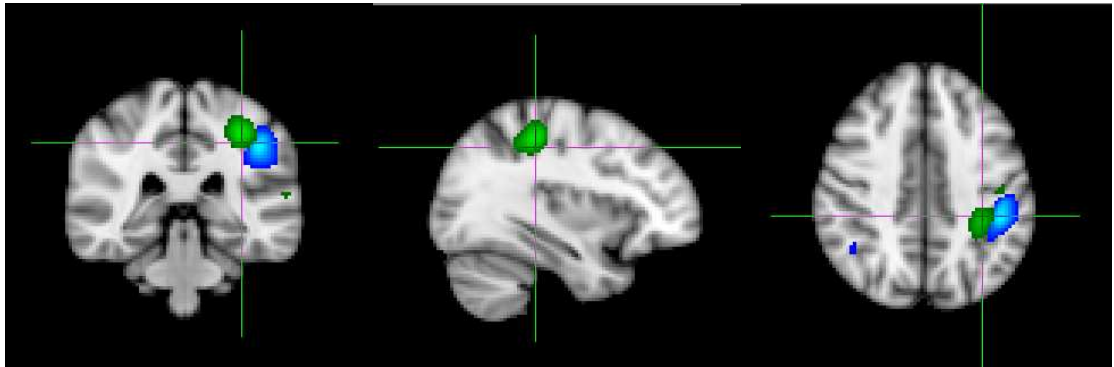
Figure 6-8: Group averaged and normalized SAM images showing the mismatch of alpha ERS (Green) and beta ERD (Blue).

Figure 6-8 shows the mismatch between alpha ERS and beta ERD overlaid onto the template brain. The distance between the alpha ERS peak and beta ERD peak is 1.8±0.7cm. To further confirm the prominence of beta rhythms does not result from source localiztion, alpha ERS was also used as a measurement to localize the peaks in the sensory cortex. The percentage change of beta ERD/ ERS and Alpha ERD/ERS from the peak locations indentified using beta ERD and alpha ERS is shown in Table 6-2.

Table 6-2: Beta ERD/ERS and Alpha ERD/ERS from sources located using Beta ERD and Alpha ERS.

Localization:	Beta ERD	Alpha ERS
Beta ERD (%)	-34±2.8	-15.6±5.7
Beta ERS (%)	59.4±12.1	37.9±10.8
Alpha ERS (%)	-18.1±3.1	-3.7±6.0
Alpha ERS (%)	39.4±10	31.7±10.7

As shown in Table 6-2, even using alpha ERS to localize the sources, the beta rhythms still have a larger percentage change than the alpha rhythm. Compared to the sources localized using beta ERD, the alpha ERD/ERS shows less percentage change.

6.3.3 Temporal signature of evoked responses
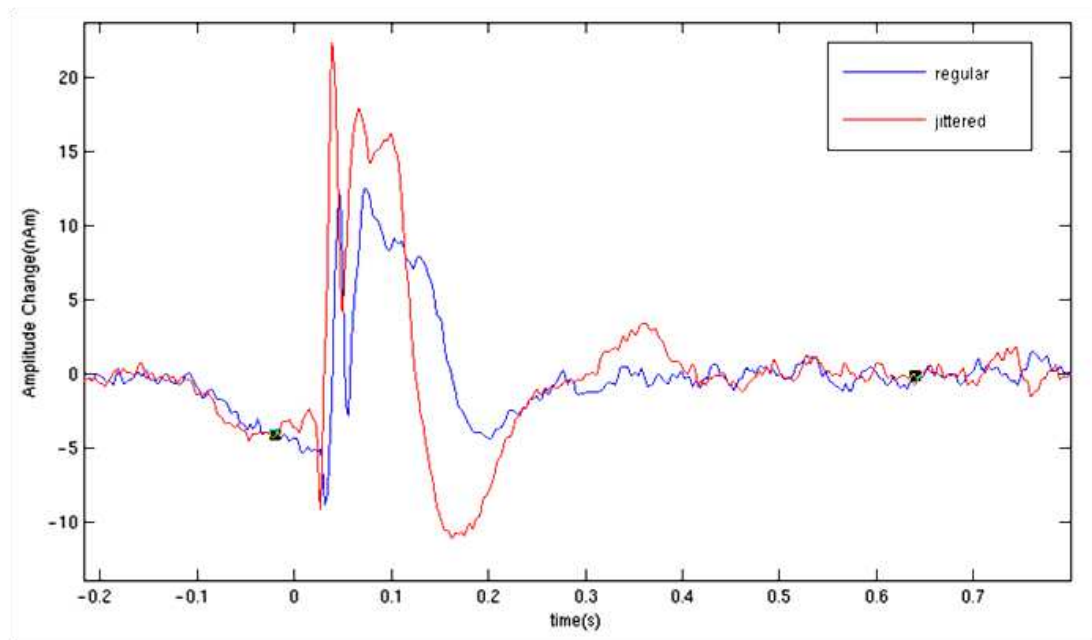
Figure 6-9: Evoked responses of regular (Blue) and jittered (Red) conditions.

It is shown in Figure 6-9 that phase locked evoked responses in the somatosensory cortex last approximately 500ms after the stimuli. In both the regular and jittered studies, SEFs components (N20m, P35m, P100m, N160m, and P300m) were clearly found. P35m represented the most significant change from baseline and the peak to peak amplitude was from N20m-P35m. The comparison of these peak changes between the regular and jittered conditions is shown in Figure 6-10.
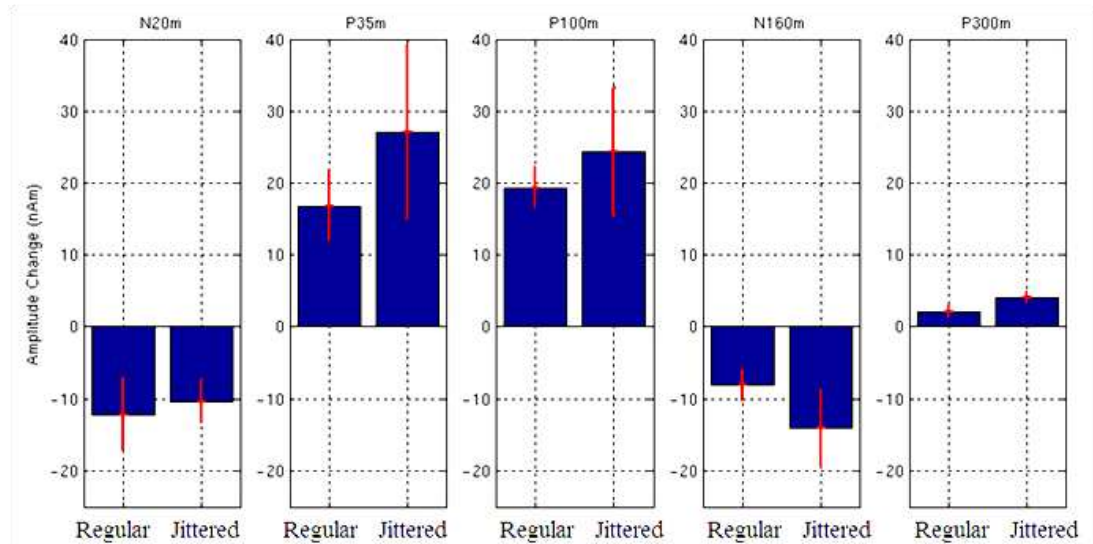
Figure 6-10: Comparison of amplitude changes of N20m, P35m, P100m, N160m and P300m between regular and jittered conditions.

Figure 6-10 shows that there is no significant difference in any of these components between regular and jittered conditions. However, the P300m (p=0.0625) has a trend to be significantly larger in the jittered condition.

6.3.4 Spatial localization of beta ERD and ERS
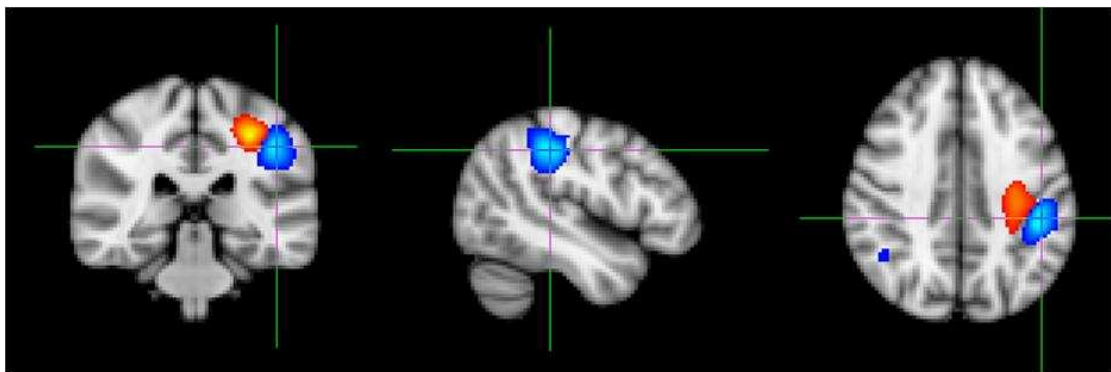
Figure 6-11: Group averaged and normalized SAM images. Activation areas of beta ERD (Blue) and ERS (Red) are overlaid onto the template brain (T_1 weighted, 2mm^3 resolution).

Figure 6-11 shows the locations of beta ERD (Blue) and beta ERS(Red) overlaid onto the standard brain. Normalized Pseudo-T-value images have been averaged. Beta ERD was located posterior to the central sulcus on the primary somatosensory cortex and extended posterior into the parietal region. By reducing the threshold, beta ERD was also found in bilateral somatosensory areas. Compared to contralateral beta ERD, ipsilateral ERD had more limited activation areas around central sulcus but extended more to the posterior parietal cortex. The beta ERS was found in more anterior areas than the beta ERD. It laid anterior to the central sulcus, covering more primary motor cortex than somatosensory cortex. However, beta ERD and ERS were not clearly separated and had overlaid areas.

6.4 *Discussion*

6.4.1 Spatial localization of beta ERD

The spatial localization of neuroelectrical activity in our MEG experiments is achieved using beamformer. As discussed in Chapter 4.5, the accuracy of beamforming is influenced by the covariance matrix, lead-field and regularization. These discussions hold true to the SAM beamformer discussed in Chapter 4 and actually used in this and the following chapters.

In covariance matrix computation, the longer the total duration of the covariance window, the smaller the total error. The duration depends on the length of the contrast window in each trial and on the number of trials. For the beta ERD which occurs 0.5s following the onset of a short stimulus; if the contrast window is set to more than 0.5s, although the beamforming error is reduced, the additional time in which there is no neuronal activity decreases the SNR.

Therefore, in the 200 trial study, an 'active' window spanning 0.5s following the stimulus onset was selected. With these 0.5s contrast windows, the total duration we used to build the covariance matrix is up to 100s.

We cannot simply increase the number of trials as the total experiment time is limited. If the subjects stay in the scanner too long, they cannot stay awake, particularly given that it is very quiet within the shielded room. A low frequency (delta band) ongoing oscillation is usually detected from the subjects after about 45min. This delta wave is a characteristic feature of the human non rapid eye movement (NREM) sleep [16]. It has been previously reported that in NREM sleep activity in somatosensory cortex is highly suppressed [17-18]. Hence, we try to keep the total experiment time less than 45min.

We cannot decrease the trial length too much to increase the number of trials either. The effect sought is limited in time not by experimental design but by neurobiology. The length of each trial should be long enough to let the event related oscillations return to baseline. As depicted in Figure 6-3, it takes up to 3s for the ERD and ERS in the low frequency range to return to baseline completely following stimulus onset. Considering the requirement for some pre-stimulus time, a 4s trial length is insufficient and thus a longer tried length is required.

The trade-off between trial length and number of trials here is made on the basis of results from the 200 trial study. Figure 6-2 and Table 6-1 show that 100 trials (50s total duration) are enough to localize beta ERD induced by MNS reliably. The regular and jittered condition study uses a trial length of 10s with 100 trials. The total experiment time is 33m20s. In the studies with the same MNS in the following chapters, the limit on the total of experimental time is that it should be less than 45min with the total duration of the covariance window about 50s.

6.4.2 Time frequency analysis:

The spectrograms showing power change for phase locked and non phase locked effects across a 1-150Hz range provide valuable information about the processing of somatosensory information in the brain. However, more detailed time frequency analysis for all these activities were carried out to characterise the most significant oscillations.

The group averaged spectrograms (Figure 6-4) have suggested that non-phase locked oscillations were predominantly found in the frequency range between 4Hz and 30Hz. However, although non-phase locked gamma oscillations have been reported in some studies [19-21], only transient phase-locked gamma activities are found here using non-painful MNS. It can be seen in Figure 6-5 that the most significant ERD occurs 0.5s after the stimulus onset in the 13Hz to 30Hz band. The beta ERS also has the largest oscillatory change. In Figure 6-6 and Figure 6-7 it has been further proven that the beta rhythm is the largest non-phase locked oscillation and beta ERD and ERS have the largest peak changes in MNS studies. This suggests that the beta band (13-30Hz) is key for studying the sensorimotor processing and will be investigated in further work in this thesis.

However, it can be argued that the prominence of beta rhythms is just because the beta ERD is pre-selected to be used in the source localization. In other words, had we based the localization on the alpha band, then the alpha band would represent the most prominent effects. In studies using invasive microelectrodes and ECoG methods, the measurements recorded from a single electrode show neuronal electrical activity over a relatively small tissue volume. However, in non-invasive methods, virtual sensor traces from peak points are spread across several millimetres or even centimetres. Previous research using beamformers shows that, the FWHM usually extends to more than 5mm and for some subjects it could be up to 10mm [22-23]. This is a function of location in the brain. The

somatosensory cortex is shallow with high SNR and thus one might expect to get good resolution. This means the measurements made here are actually the summation of neuronal electrical activity across relatively large areas and support the hypothesis that the large and long lasting oscillatory changes in low frequency bands are probably due to extended neuronal networks. Therefore, as the virtual sensor signal contains neuronal activity from a large area in the somatosensory cortex, suggesting it is quite unlikely that the prominence of beta rhythms results from the source localization.

As shown in Table 6-2, if we use alpha ERS to localize the sources, the beta rhythms is still larger than the alpha rhythm and both have smaller changes than using beta ERD for localization. This confirms that the alpha rhythm is weaker than the beta rhythm in this MNS studies and suggests that the alpha rhythm is not appropriate for source localization.

6.4.3 Regularity of stimuli

For the non phased locked oscillation of all frequency bands (1-150Hz), although the baselines are shifted, there is no significant difference in percentage changes (Figure 6-7) between regular and jittered conditions and the timecourses also have similar shapes (Figure 6-6). It suggests that beta band oscillations of interest are unaffected by the regularities of stimuli in MNS studies.

For the phase locked SEFs elicited by MNS, the short latency component N20m shows no difference between regular and jittered conditions. It has been suggested in previous studies that N20m is the primary cortical response generated by excitatory postsynaptic potentials (EPSPs) in cSI (Broadmann 3b) [24-25] which is irrelevant to the regularity and ISIs of stimuli. The P300m components which have a trend to be significantly larger in the jittered

condition with more attention are in general agreement with previous research [26-28]. However, as only five subjects are included in this study, which means the minimal p-value from the Wilcoxon Signed Rank tests is 0.0625, more subjects are required if we want to confirm the significance of this difference. In both active and passive tasks, these long latency peaks have been proved to be facilitated by an increase in attention. The different attentional states between the regular and jittered condition may be the reason for these differences. More details about the complex P35m will be given in the following chapters concerned with paired and linked pulses.

6.4.4 Spatial separation between beta ERD/ERS

Spatial separation of beta ERD and ERS has been previously reported in experiments of voluntary finger movement and brush stimuli using group averaged functional images [13, 29]. Here we show that similar spatial separations can be found in a study of MNS. The more anterior, superior and medial ERS is roughly separated from the ERD along the central sulcus. The separation between ERD and ERS may be an indication that different groups of neurons account for these two phenomena. It could also be explained if the same neuronal network participates in ERD and ERS, but is controlled by different generators in the thalamo-cortical feedback loop. As shown in previous discussion (Chapter 5), the beta oscillations are thought to be due to neuronal networks of certain frequencies in large areas in the cortex. The thalamo-cortical feedback loops plays a rather important role in modulating the sensory signal pathway and controlling the rhythms in sensorimotor cortex. Take the rapid switch from beta ERD to ERS into consideration; it is more likely that the ERD and ERS are related to the same cortical neural networks with different activation states. Different generators in the thalami-cortical loop will active or inhibit the oscillatory networks in different areas.

If a second stimulus applied during the ERS decreases the beta oscillations to the same amplitude below baseline as the initial one, it would suggest that the ERD and ERS are from the same network, not separate ones. Otherwise, if the timecourses reconstructed from the areas covering both ERD and ERS shows a decrease relative to the ERS following the second stimulus applied during ERS, it will in contrast suggest that ERD and ERS are from different networks. This hypothesis will be tested in the following chapter.

6.5   *Conclusions*

We have shown spatially well localized low frequency oscillations in sensorimotor cortex during non-painful MNS. The 'testing study' has shown that a total duration of 100s is required to localize the beta ERD. The largest activities shown in time-frequency analysis are beta ERD and ERS between 13Hz and 30Hz, which will be studied in more detail in the following chapters. No significant difference in the oscillations is found between regular and jittered conditions between 1Hz and 150Hz. However, although the SEFs with short latency (N20m) are relatively stable, mid-latency components P300m show a trend to have significant larger amplitude in the jittered condition than in the regular condition. In the group averaged SAM images, ERD and ERS can be spatially separated along the central gyrus. Beta ERS extends more in the MI than beta ERD which is mainly in SI. beta ERD shows bilateral activations whilst Beta ERS is only contralateral. We will focus on beta band frequency oscillatory activities, especially beta ERD and ERS in the following chapters. By studying the properties of these oscillatory changes together with more complex paradigms such as paired pulse and link pulse MNS and combining MEG with ultra-high-field functional MRI, we are trying to understand how the signals are processed in sensorimotor system.

6.6 *References*

[1]   Stevenson, C.M., Brookes, M.J. and Morris, P.G., Band correlates of the fMRI BOLD response. Human Brain Mapping, 2011. **32**(2): p. 182-197.

[2]   Brookes, M.J., Gibson, A.M., Hall, S.D., Furlong, P.L., Barnes, G.R., Hillebrand, A., Singh, K.D., Holliday, I.E., Francis, S.T. and Morris, P.G., GLM-beamformer method demonstrates stationary field, alpha ERD and gamma ERS co-localisation with fMRI BOLD response in visual cortex. Neuroimage, 2005. **26**(1): p. 302-308.

[3]   de Pasquale, F., Della Penna, S., Snyder, A.Z., Lewis, C., Mantini, D., Marzetti, L., Belardinelli, P., Ciancetta, L., Pizzella, V. and Romani, G.L., Temporal dynamics of spontaneous MEG activity in brain networks. Proceedings of the National Academy of Sciences, 2010. **107**(13): p. 6040-6045.

[4]   Mantini, D., Perrucci, M.G., Del Gratta, C., Romani, G.L. and Corbetta, M., Electrophysiological signatures of resting state networks in the human brain. Proceedings of the National Academy of Sciences, 2007. **104**(32): p. 13170-13175.

[5]   Pfurtscheller, G., Central beta rhythm during sensorimotor activities in man. Electroencephalography and Clinical Neurophysiology, 1981. **51**(3): p. 253-264.

[6]   Hirata, M., Kato, A., Taniguchi, M., Ninomiya, H., Cheyne, D., Robinson, S.E., Maruno, M., Kumura, E., Ishii, R. and Hirabuki, N., Frequency-dependent spatial distribution of human somatosensory evoked neuromagnetic fields. Neuroscience Letters, 2002. **318**(2): p. 73-76.

[7]   Pfurtscheller, G., Brunner, C., Schlogl, A. and Lopes da Silva, F.H., Mu rhythm (de) synchronization and EEG single-trial classification of different motor imagery tasks. Neuroimage, 2006. **31**(1): p. 153-159.

[8]   Neuper, C. and Pfurtscheller, G., Evidence for distinct beta resonance frequencies in human EEG related to specific sensorimotor cortical areas. Clinical Neurophysiology, 2001. **112**(11): p. 2084-2097.

[9]   Brovelli, A., Battaglini, P.P., Naranjo, J.R. and Budai, R., Medium-range oscillatory network and the 20-Hz sensorimotor induced potential. Neuroimage, 2002. **16**(1): p. 130-141.

[10]   Kakigi, R., Somatosensory evoked magnetic fields following median nerve stimulation. Neuroscience research, 1994. **20**(2): p. 165-174.

[11]   Arnfred, S.M., Hansen, L.K., Parnas, J. and Morup, M., Regularity increases middle latency evoked and late induced beta brain response following proprioceptive stimulation. Brain Research, 2008. **1218**: p. 114-131.

[12]   Mattler, U., Van Der Lugt, A. and Münte, T., Combined expectancies: electrophysiological evidence for the adjustment of expectancy effects. BMC Neuroscience, 2006. **7**(37).

[13]   Jurkiewicz, M.T., Gaetz, W.C., Bostan, A.C. and Cheyne, D., Post-movement beta rebound is generated in motor cortex: Evidence from neuromagnetic recordings. Neuroimage, 2006. **32**(3): p. 1281-1289.

[14]   Pfurtscheller, G. and Stancak, A., Event-related synchronization (ERS) in the alpha band--an electrophysiological correlate of cortical idling: a review. International Journal of Psychophysiology, 1996. **24**(1-2): p. 39-46.

[15]   Chen, R., Corwell, B. and Hallett, M., Modulation of motor cortex excitability by median nerve and digit stimulation. Experimental Brain Research, 1999. **129**(1): p. 77-86.

[16]   Hobson, J.A. and Pace-Schott, E.F., The cognitive neuroscience of sleep: neuronal systems, consciousness and learning. Nature Reviews Neuroscience, 2002. **3**(9): p. 679-693.

[17] Yamada, T., Kameyama, S., Fuchigami, Y., Nakazumi, Y., Dickins, Q.S. and Kimura, J., Changes of short latency somatosensory evoked potential in sleep. Electroencephalography and Clinical Neurophysiology, 1988. **70**(2): p. 126-136.

[18] Nakano, S., Tsuji, S., Matsunaga, K. and Murai, Y., Effect of sleep stage on somatosensory evoked potentials by median nerve stimulation. Electroencephalography and Clinical Neurophysiology, 1995. **96**(5): p. 385-389.

[19] Crone, N.E., Miglioretti, D.L., Gordon, B. and Lesser, R.P., Functional mapping of human sensorimotor cortex with electrocorticographic spectral analysis. II. Event-related synchronization in the gamma band. Brain, 1998. **121**(12): p. 2301-2315.

[20] Bauer, M., Oostenveld, R., Peeters, M. and Fries, P., Tactile spatial attention enhances gamma-band activity in somatosensory cortex and reduces low-frequency activity in parieto-occipital areas. The Journal of neuroscience, 2006. **26**(2): p. 490.

[21] Gross, J., Schnitzler, A., Timmermann, L. and Ploner, M., Gamma oscillations in human primary somatosensory cortex reflect pain perception. PLoS biology, 2007. **5**(5): p. e133.

[22] Barnes, G.R. and Hillebrand, A., Statistical flattening of MEG beamformer images. Human Brain Mapping, 2003. **18**(1): p. 1-12.

[23] Barnes, G.R., Hillebrand, A., Fawcett, I.P. and Singh, K.D., Realistic spatial sampling for MEG beamformer images. Human Brain Mapping, 2004. **23**(2): p. 120-127.

[24] Allison, T., McCarthy, G., Wood, C.C. and Jones, S.J., Potentials evoked in human and monkey cerebral cortex by stimulation of the median nerve. Brain, 1991. **114**(6): p. 2465-2503.

[25] Klostermann, F., Nolte, G., Losch, F. and Curio, G., Differential recruitment of high frequency wavelets (600 Hz) and primary cortical response (N20) in human median nerve somatosensory evoked potentials. Neuroscience Letters, 1998. **256**(2): p. 101-104.

[26] Desmedt, J.E. and Tomberg, C., Mapping early somatosensory evoked potentials in selective attention: critical evaluation of control conditions used for titrating by difference the cognitive P30, P40, P100 and N140. Electroencephalography and Clinical Neurophysiology, 1989. **74**(5): p. 321-346.

[27] Picton, T.W., The P300 wave of the human event-related potential. Journal of clinical neurophysiology, 1992. **9**: p. 456-456.

[28] Nakajima, Y. and Imamura, N., Relationships between attention effects and intensity effects on the cognitive N140 and P300 components of somatosensory ERPs. Clinical Neurophysiology, 2000. **111**(10): p. 1711-1718.

[29] Gaetz, W. and Cheyne, D., Localization of sensorimotor cortical rhythms induced by tactile stimulation using spatially filtered MEG. Neuroimage, 2006. **30**(3): p. 899-908.

Chapter 7

The relationship between MEG and fMRI signal in a paired pulse study

Overview:

This chapter aims to characterise the neuronal responses detected using both MEG and 7T fMRI following MNS in a paired pulse paradigm with varying delay between pulses or ISIs. We focus on beta band oscillations and the P35m component of the signal averaged evoked response in the sensorimotor cortex. In agreement with results presented in Chapter 6, spatial separation of beta ERD and ERS is demonstrated suggesting that these two effects arise from separate neural generators, with ERS exhibiting a closer spatial relationship with the BOLD response. The spatial distribution and extent of BOLD activity was unaffected by ISI, but modulations in peak amplitude and latency were observed. Non-linearities in both induced oscillatory activity and in the signal averaged evoked response were found for ISIs of up to 2s, with the P35m component displaying paired pulse depression effects. The beta band ERS magnitude was modulated by ISI, however the ERD magnitude was not. These results support the assumption that BOLD non-linearity arises not only from a non-linear vascular response to neural activity but also a non-linear neural response to the stimulus with ISI up to 2s.

7.1 *Introduction*

A close spatial correspondence has been demonstrated between task specific modulations in the BOLD fMRI response and neuroelectrical effects detectable by MEG [1-2]. The precise relationship between these two measures, however, remains unclear [3]. Despite the disparate nature of the two phenomena, similarities in the spatial distribution and amplitude modulation of haemodynamic and neuroelectrical effects have been attributed to a common source of underlying activity. Synaptically generated Local Field Potentials (LFPs) have been shown to be a good predictor of the BOLD fMRI response [4], and similarly, the MEG detectable signal is thought to arise from post synaptic current flow in apical dendrites as stated in Chapter 4.

Paired pulse stimulus paradigms have been used extensively in invasive electrophysiological studies to systematically manipulate facilitation and inhibition of post synaptic potentials, and consequently may prove informative in understanding what is driving both neuroelectrical and haemodynamic effect [5-6]. Intracellular recordings have shown that Inhibitory Post Synaptic Currents (IPSCs) exhibit a strong sensitivity to ISI in paired pulse paradigms, displaying significant GABA mediated depression of the second pulse for ISIs of 100 ms to 1000 ms [5]. A scalp level correlate of this effect has been reported in MEG [7-8] where increasing the frequency of stimulation of a train of median nerve pulses from 0.2-6.7 Hz resulted in an equivalent reduction in amplitude of the P35m component of the somatosensory signal averaged evoked response in SI, suggesting that the P35m may reflect IPSCs.

In addition to a phase-locked evoked response, which typically lasts ~300 ms, electrical stimulation of the median nerve is also known to induce time locked ERD/ERS in alpha (8-

13Hz) and beta (13-30Hz) oscillations as shown in Chapter 6. The functional role of beta oscillations in the sensorimotor cortex is not fully understood, however recent studies [9-11] suggest that these oscillations are also governed by GABAergic modulation.

There is increasing evidence to suggest that beta ERD and ERS arise from distinct neural generators, although the precise mechanisms giving rise to each of the effects are as yet unclear. In Chapter 6, a spatial distinction between these oscillatory rhythms was demonstrated. The ERD had atrend to be localised to the post central gyrus and the ERS had a trend to be localised to the pre-central gyrus. These results are consistent with previous motor studies[12-13]. Functional differences between the modulations of ERD and ERS have also been reported [10], movement related ERD was shown to be facilitated by increased GABAergic drive following administration of diazepam, whilst no equivalent effect was seen in the post stimulus ERS. As such, one may expect a differential manifestation of the GABA mediated paired pulse depression effect in the amplitudes of beta ERD and ERS respectively.

As stated in Chapter 3, ultra-high-field (7T) fMRI affords high SNR and the BOLD response is weighted to microvasculature with little contribution from the intravascular signal from veins. As such it is expected that at 7T the BOLD response lies closer to the true site of neural activity. It has been shown that both excitatory and inhibitory synaptic processes modulate energy consumption within the brain, and as such both should be detectable with BOLD fMRI [14]. Indeed, an increase in the extent of the BOLD active area in contra-lateral SI with increasing frequency of median nerve stimulation (5-100 Hz) which may be attributed to an increase in underlying inhibitory activity have been reported [15].

In this chapter, MNS in a paired pulse paradigm with varying ISI is used to examine the effects on the phase-locked evoked response (specifically the P35m component), the ongoing

oscillatory activity in the beta (13-30 Hz) band, and the BOLD response. We sought to characterise the spatio-temporal signature of the electrodynamic response to a median nerve pulse and whether ISI related power modulations in MEG detected neural responses were also detectable in the spatio-temporal distribution of the corresponding BOLD haemodynamic data. We also examine how the oscillatory response to a subsequent pulse was affected by the magnitude and shape of the induced decrease and rebound in beta band power induced by the first pulse, to test whether paired pulse depression effects manifest themselves in the oscillatory activity.

The following hypotheses are tested:

1) The spatial localization of beta ERD and beta ERS peak points differ.

2) ISI differentially modulates the amplitude of ERD and ERS.

3) Non-linearity in beta activity and P35m response resulting from variations in ISI will be reflected in both the amplitude and spatial distribution (if ERS and ERD arise from spatially separate neural generators) of the BOLD response.

7.2 *Methods*

Eight subjects (5 males, 3 females) took part in both the fMRI and MEG study; all subjects were classified as right handed [16].

7.2.1 Paradigms

MNS stimulation detailed in Chapter 6 is also applied here in the same manner. The paired pulse paradigm consisted of two MNS pulses at ISIs of 0.25, 0.5, 0.75, 1, 1.5 and 2 s, followed by a rest period; the order of ISIs was presented pseudo-randomly. In MEG, the

total trial length was 8 s and there were 50 trials per condition. In fMRI, the total trial length was increased to 20 s to allow the haemodynamic response to return to baseline between trials, and 10 trials per condition were sufficient due to the increased CNR of the BOLD response compared to the neuro-electric effects measured with MEG.

7.2.2 Data acquisition

MEG data were acquired using the method stated in Chapter 6. fMRI data were collected using a 7T Philips Achieva system with a volume transmit head coil and a 16-channel receiver coil. To reduce distortions due to field inhomogeneity, an image-based shimming procedure was performed prior to the fMRI acquisition. A B_0-field map was generated from the difference in phase of two gradient echo images acquired with echo times of 6 and 6.5 ms. Data were exported and skull-stripped for computation of to second order shim currents which were chosen to minimise the field inhomogeneity inside the shim box. The shim values were then fixed for the functional experiment which comprised the acquisition of gradient echo EPI data spanning 21 transverse slices, covering the sensorimotor cortices bilaterally in a TR of 2.2s (SENSE factor 2, TE=26ms; 2mm isotropic voxels; $192 \times 192 \times 42mm^3$ FOV). Following the functional paradigm, a T_1 weighted anatomical image was acquired (MPRAGE sequence with linear phase encoding order, TE/TR=3.7/ 8.1ms, flip angle = 8°, TI = 960ms, shot interval = 3s, SENSE factor 2, 1.5 mm isotropic resolution, $256 \times 256 \times 160$ matrix).

7.2.3 Data analysis

7.2.3.1 MEG

Source localization of induced oscillatory activity was performed SAM which has been detailed in Chapter 4 and 6. The main focus of this study is the effect of the paired pulse paradigm on the beta oscillations band and its relationship with the BOLD response, the experiment was therefore designed based on the results of Chapter 6. However, to verify that the experimental paradigm was able to noninvasively detect the effects analogous to those previously measured invasively [6], a preliminary signal averaged evoked response analysis was carried out.

7.2.3.2 P35m analysis

Spatial localization of the signal averaged evoked response was carried out using an equivalent current dipole model. Data were bandpass filtered 1–40Hz and analysed using CTF DipoleFit software implementing a least squares analysis [17]. Equivalent current dipole model parameters for the 2 s ISI condition were determined for time windows (3.3 ms width) at ~30 - 35 ms post stimulus for which the magnetic field pattern at the sensor level was dipolar. To maximise signal to noise ratio, sensors covering the regions of greatest magnetic field deflection were used to generate the model parameter estimates. Multiple dipoles were added until the sensor level magnetic field pattern was best explained (the total number of dipoles ranged from 1-3 per subject), dipoles with a fit error of >10 % were excluded.

For comparison with induced beta oscillatory timecourses, virtual sensors using beamformer weights calculated for data filtered 1 - 40 Hz for 0-0.1s following each pulse were used to

extract timecourses of electrical activity from the dipole locations in contra-lateral SI. To obtain the signal averaged evoked response, the virtual sensor timecourses (without Hilbert transformation) were averaged across trials (separately for each ISI and also for first or second pulse of the pair). Peak amplitudes of the phase-locked evoked response (P35m) were recorded following each median nerve pulse. The ratio of the second phase-locked evoked response amplitude relative to the first (amplitude response 2/ amplitude response 1) was calculated to assess modulations in phase-locked evoked amplitude across ISIs. Paired Wilcoxon Signed Rank tests were used to test for significant differences in signal averaged evoked response amplitudes.

7.2.3.3   Induced oscillatory activity analysis

Data were filtered in the 13-30 Hz frequency band. Based on previous studies characterising the beta band response to median nerve stimulation [18] and results in Chapter 6, contrast windows for beta ERD were selected with 'active' periods spanning 0.5s following each of the second pulses and 'control' periods spanning 0.5s of the pre-stimulus rest period ($-1.5 \leq t \leq -1.0s$) prior to stimulus onset of the first pulse. For beta ERS, 'active' periods were chosen to begin 0.7 s following the second pulse and to span a period of 1s. These were contrasted with 'control' periods spanning 1 s ($-1.5 \leq t \leq -0.5s$) of the pre-stimulus rest period. To ensure that the data covariance matrix was well conditioned [19], regularisation of the data covariance matrix was implemented using a regularisation parameter of 2 for both oscillatory and phase-locked evoked data. Pseudo-T-statistical images (1 mm^3 resolution) were created showing the spatial distribution of power change between active and passive windows. These were overlaid onto an anatomical image generated from a 3T T$_1$-weighted MPRAGE MRI. For comparison with fMRI data, the noise normalised power difference images were then normalised to the T$_1$-weighted template brain in SPM5

(), and the same transform applied to the dipole location coordinates. The MNI coordinates were then extracted for each dipole location and global maxima of beta ERD and beta ERS for each condition. The same ROI analysis as used for fMRI was employed for the normalised MEG data (see below).

Hilbert envelopes were generated from virtual sensor traces in the same way as that detailed in Chapter6. An average of the 1s pre-stimulus data was taken from the Hilbert envelope and assumed to represent a baseline amplitude. The average onset time of the beta ERS following the second pulse was calculated by taking the time at which the Hilbert envelope increased above the baseline value. For each median nerve pulse, the time to peak (TTP) of the beta ERS and peak amplitudes of beta ERS and ERD was also calculated. For the beta ERS the TTP and peak amplitude measures for the first two ISI conditions (0.25 and 0.5s) were limited to the effects following the second pulse as the short ISI meant that no rebound effect was seen following the first pulse. Metrics were computed for all subjects and conditions for ERD.

7.2.3.4   fMRI

Data were realigned and spatially smoothed with a Gaussian 5 mm kernel using SPM5. A general linear model (GLM) was employed, in order to identify areas of significant ($p < 0.05$ FWE corrected) BOLD contrast. Individual pulse timings were used to create a box car model design matrix convolved with a canonical HRF and the individual realignment parameters included as covariates of no interest. In order to assess the relationship between BOLD and MEG, MEG metrics (ERD amplitude, ERS peak amplitude and P35m amplitude following each pulse for each individual) were included as parametric modulators in the

GLM. BOLD data were normalized to the T_1-weighted template brain in SPM5 and peak coordinates extracted in MNI space for comparison with MEG.

To assess the linearity of the BOLD response, BOLD timecourses were extracted from volumes of 3x3x3 voxels centered on maxima in contralateral SI from the fMRI maps. These were subsequently averaged across trials and subjects. The maximum BOLD percentage change and power of the BOLD response, by integrating under the BOLD timecourse, for each condition was measured and these results plotted against ISI. Peak latencies for the BOLD timecourse for each condition were also computed. To further interrogate the BOLD response as a function of ISI, a region of interest (ROI) analysis was performed. Masks were created using the wfu-Pick Atlas toolbox in SPM5 and the percentage area of significantly active ($p<0.05$ FWE corrected) voxels, maximum and average T statistic within each ROI computed for all conditions and subjects using the SPM obtained without parametric modulators. ROIs included left and right inferior parietal lobes and left and right pre and post central gyri.

7.3 *Results*

7.3.1 Spatial localization of MEG and BOLD responses

One subject was omitted from MEG data analysis due to excessive noise; results are reported for the remaining 7 subjects.
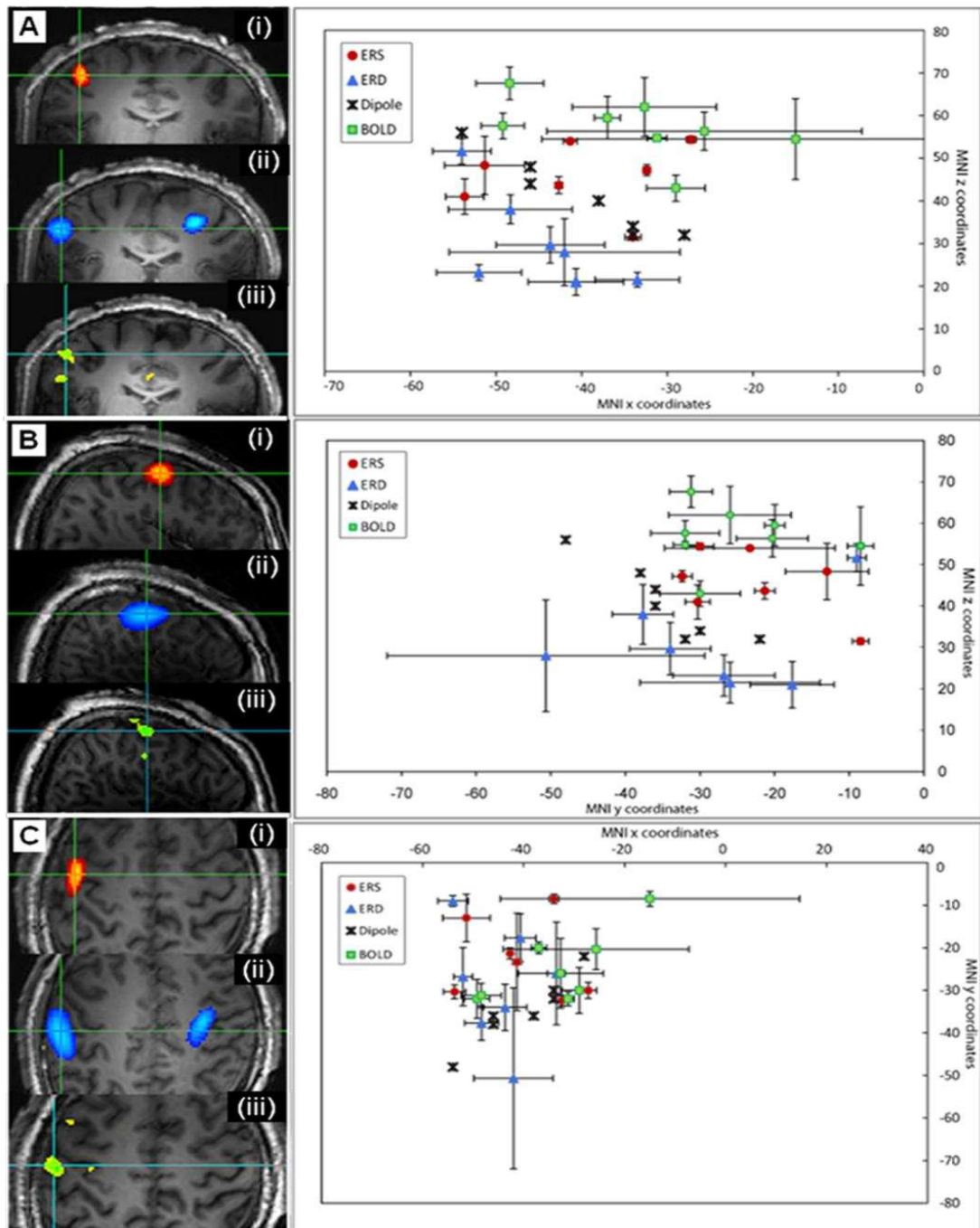
Figure 7-1: Spatial localization in the coronal [A], axial [B] and sagittal [C] planes of *significant beta ERS ($\bar{T}$>5)* (i)*, beta ERD ($\bar{T}$<-5)* (ii) and BOLD activity (p<0.05 FWE corrected) (iii). The results in the left hand column are shown in a single representative subject and were elicited by 2 median nerve pulses with an ISI of 0.25s. Cross hairs indicate the global maxima of effects. The right hand column shows the corresponding spatial location of global maxima of MEG and BOLD fMRI effects in MNI coordinates. Data are

shown for the 7 subjects showing significant task-related activity, with data points giving the average peak location across conditions with error bars depicting the standard error of peak location across conditions for each subject.

The spatial localization of phase-locked evoked activity, induced oscillatory activity in the beta band beta ERS (i) and beta ERD (ii) and the BOLD fMRI response (iii) is shown in Figure 7-1 for coronal [A], axial [B] and sagittal [C] planes. Significant beta ERS and BOLD response was observed in contra-lateral primary sensorimotor cortex, and significant beta ERD in contra-lateral primary sensorimotor cortex and extending to parietal regions (Figure 7-1 [A-C] (ii)). Lower threshold beta ERD was also seen in ipsilateral primary and secondary somatosensory cortex and parietal regions. In all subjects P35 dipoles were localised to contra-lateral primary sensorimotor regions and their respective locations for each subject are shown in Figure 7-1. Additional dipoles at later timepoints were localized to contra-lateral SII and ipsilateral primary sensory regions in 4 subjects. Average global maxima of MEG and BOLD fMRI effects are reported in Table 1.

It can be seen in the right hand column of Figure 7-1[A] that ERS peaks were significantly shifted in their z MNI coordinate (p<0.028) relative to the ERD peaks, although there was no significant difference in the x,y plane coordinates (Figure 7-1[C]). Increased inter- and intra-subject variability in the location of beta ERD peaks compared to ERS locations was observed.

As seen in Figure 7-1 [A-C] (iii), significant BOLD activity (p<0.05 FWE corrected) was predominantly observed in contra-lateral primary sensorimotor cortex encompassing both pre- and post- central gyri. The average MNI coordinates of the BOLD global maxima are shown in Table 7-1. Also visible in the BOLD data, was a small activation focus in the medial frontal cortex, on the upper bank of the cingulate sulcus (1,-15,53) ± (2,3,2), (x,y,z

MNI coordinates averaged across conditions and subjects ± stdev). This has previously been reported in fMRI studies and has been identified as the supplementary motor area [20-21].

Inclusion of the MEG derived parametric modulators showed no significant modulation by ERS to the BOLD signal. Beta ERD yielded significant modulation in all subjects in contra-lateral primary sensorimotor cortex and extending to parietal regions (no different to those areas found to show significant activation to the box car alone). Inclusion of the P35m amplitude revealed significant modulation in 3 subjects in contralateral somatosensory regions. The global maxima for each of the models is reported in Table 7-1. However, due to the lack of consistency across subjects for the parametric modulation analysis, further analysis was confined to active areas in those SPMs generated without parametric modulation.

	Average MNI coordinates of global maxima (x,y,z)± stdev mm
beta ERS	(-40, -23, 46) ± (9, 9, 8)
beta ERD	(-45, 29, 30) ± (7, 14, 11)
Dipole	(-40, -35, 41) ± (9, 8, 9)
BOLD alone	(-34, -24, 56) ± (6, 6, 9)
BOLD (beta ERS amplitude parametric modulator)	No significant activity
BOLD (beta ERD amplitude parametric modulator)	(-33, -24, 56) ± (6, 6, 9)
BOLD (P35m amplitude parametric modulator)	(-28, -27, 56) ± (10, 11, 10)

Table 7-1: Global maxima of beta ERS, beta ERD and signal averaged evoked response dipole location in contra-lateral SI, together with global maxima of significant BOLD activity identified using traditional boxcar design alone, and with MEG derived parametric modulators. (MNI coordinates are shown averaged across both subjects and conditions with associated standard deviation)

The global maxima of BOLD data were on average a Euclidean distance of 13 ± 2 mm from ERS global maxima, 29 ± 6 mm from ERD global maxima, and 19 ± 6 mm from dipole locations in contra-lateral SI. No significant differences in any direction were found between the BOLD global maxima coordinates and the ERS maxima coordinates, with the distance between them being within previously reported ranges of BOLD and MEG correspondence [3] [22]. Significant differences were found between the BOLD maxima and the ERD maxima in the x (p=0.0312) and z (p=0.0312) coordinates, and between BOLD maxima and dipole locations in the z (p=0.0255) coordinates.

Voxels exhibiting significant BOLD activity were also found bilaterally in pre- and post-central gyri and the inferior parietal lobes as reported in Table 7-2 with maximum T statistics on average higher in contra-lateral pre- and post- central gyrus than in contra-lateral inferior parietal lobes. All contra-lateral responses had on average higher maximum T statistics than their ipsilateral counterparts. No significant differences across varying ISIs were found in either the percentage of significantly active voxels or the maximum T statistic within any of the ROIs examined. Table 7-2 also shows the distribution of MEG activity in the same ROIs interrogated with BOLD fMRI. It can be seen that the beta ERS is closely related to BOLD with activity being predominantly contra-lateral and maximum Pseudo-T-statistics on average higher contra-laterally than ipsilaterally. In contrast, little difference was found between the average maximum Pseudo T statistics of beta ERD in contra-lateral compared to ipsilateral regions.

Region of Interest	Maximum T stat: BOLD ± stderr	Maximum T stat: beta ERS ± stderr	Maximum absolute T stat: beta ERD ± stderr
Left Inferior Parietal Lobe	4.28 ± 1.20	5.57 ± 1.05	4.73 ± 0.76
Left Post- Central Gyrus	6.87 ± 1.50	6.51 ± 1.02	4.79 ± 0.72
Left Pre- Central Gyrus	6.65 ± 1.70	6.55 ± 1.10	4.82 ± 0.73
Right Inferior Parietal Lobe	3.10 ± 0.50	1.70 ± 0.63	4.13 ± 0.93
Right Post- Central Gyrus	3.13 ± 1.50	2.24 ± 0.56	4.18 ± 0.82
Right Pre- Central Gyrus	4.43 ± 1.71	2.42 ± 0.53	3.89 ± 0.62

Table 7-2: The spatial distribution and intensity of significant ($p < 0.05$ FWE corrected) BOLD activity in the region of interest analysis. Shown is the maximum BOLD T value and the corresponding maximum Pseudo-T-Statistical of MEG effects in the same region. Data are averaged across conditions and subjects and shown with associated standard error.

7.3.2 Temporal signature of neuroelectrical effects
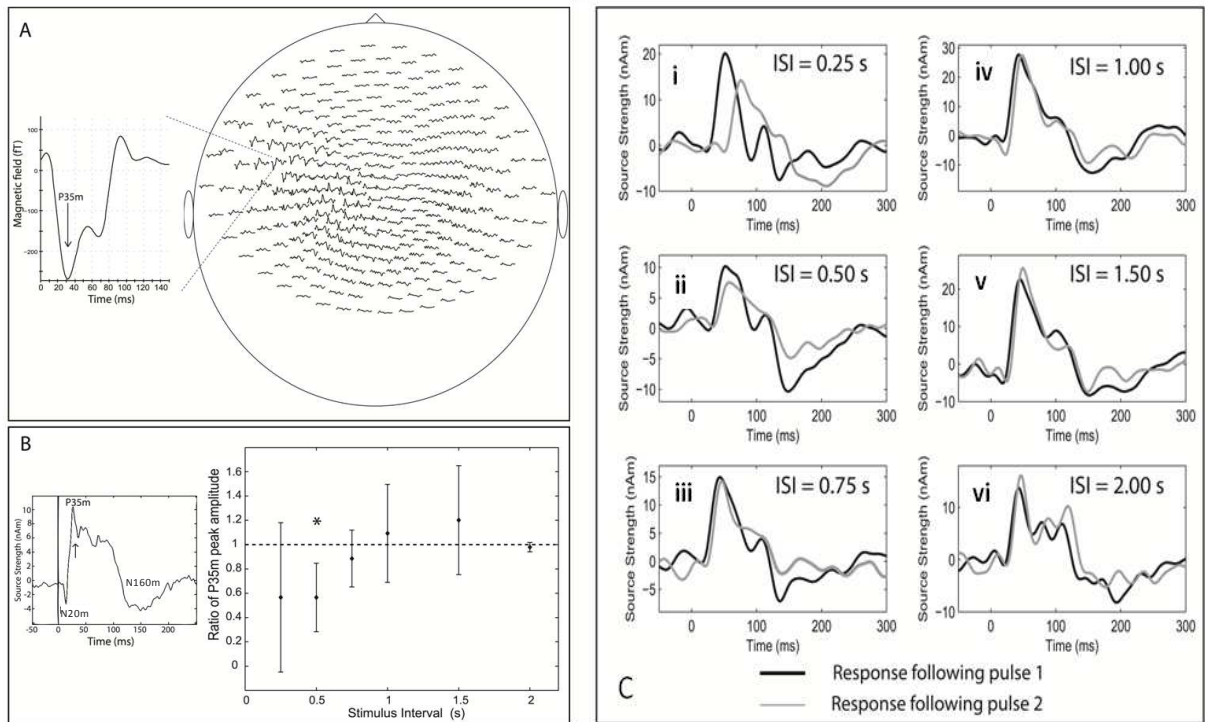
Figure 7-2: [A] Sensor level plot for a single representative subject showing the average phase-locked evoked response to a single median pulse. The timecourse from a single sensor depicts the component of interest (P35m). [B] The equivalent source waveform extracted from the dipole location showing deflections at characteristic time points. The ratio of signal averaged evoked response P35m amplitude for the paired pulses in each condition is also shown. * indicate conditions in which the second SEF was significantly smaller than the first (p=0.018 determined by a Paired Wilcoxon Signed Rank Test). Data are given as an average across subjects with standard error. [C] (i-vi) Average phase locked evoked response following pulses 1 and 2 respectively for each of the ISI conditions in a single representative subject.

Figure 7-2[A] shows the sensor level MEG data for a single representative subject and 2B shows the equivalent source waveform extracted from the dipole location. The signal averaged evoked responses in contralateral SI to median nerve stimulation were consistent with previously reported responses [7, 23], with significant N20m, P35m and later N160m deflections (Figure 7-2[B]).

Figure 7-2[B] (right hand panel) shows the ratio of the amplitude of the P35m component of the second signal averaged evoked response with respect to that of the first. It can be seen that with decreasing ISI (i.e for ISIs 0.25s, 0.5s and 0.75s) the amplitude of the 2nd signal averaged evoked response is reduced, with the P35m amplitude being significantly smaller for an ISI of 0.5s (p=0.018). There were no significant differences between signal averaged evoked response amplitudes for ISIs $\geq$ 0.75s. This effect can also be seen in Figure 2C, which shows the average phase locked evoked response following pulses 1 and 2 respectively for each of the ISI conditions in a single representative subject. It can be seen in Figure 7-2[C](i) that the P35m of the second pulse is delayed as well as being of reduced amplitude when the second pulse is presented within a very short (0.25s) timeframe of the first pulse.
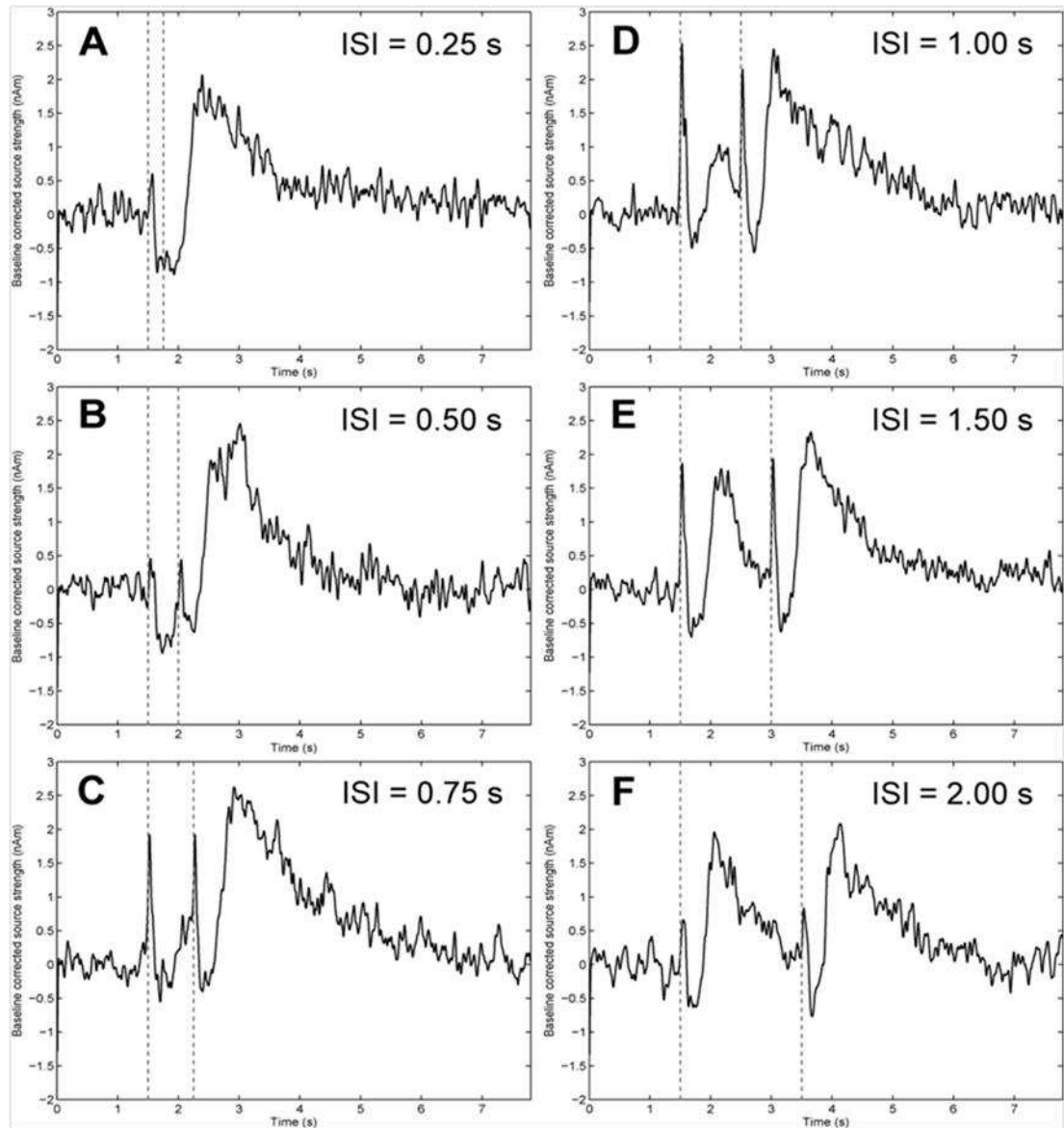
Figure 7-3: Average Hilbert envelopes across subjects from peak in beta ERS data for ISIs 0.25s [A], 0.5s [B], 0.75s [C], 1.0s [D], 1.5s [E] and 2.0s[F]. Grey dashed vertical lines show median nerve stimulation.

Figure 7-3 shows the timecourses of beta (13-30Hz) activity extracted for stimuli of varying ISI. The characteristic temporal signature of beta decrease followed by a rebound can be seen in all conditions. Also visible in Figure 7-3 is a spike in power at the onset of each median nerve pulse which can be attributed to the 13-30Hz component of the signal

averaged evoked response. This effect was not investigated further in terms of task related

amplitude modulation as the P35m provides a well established metric for characterisation of

task related signal averaged evoked effects.
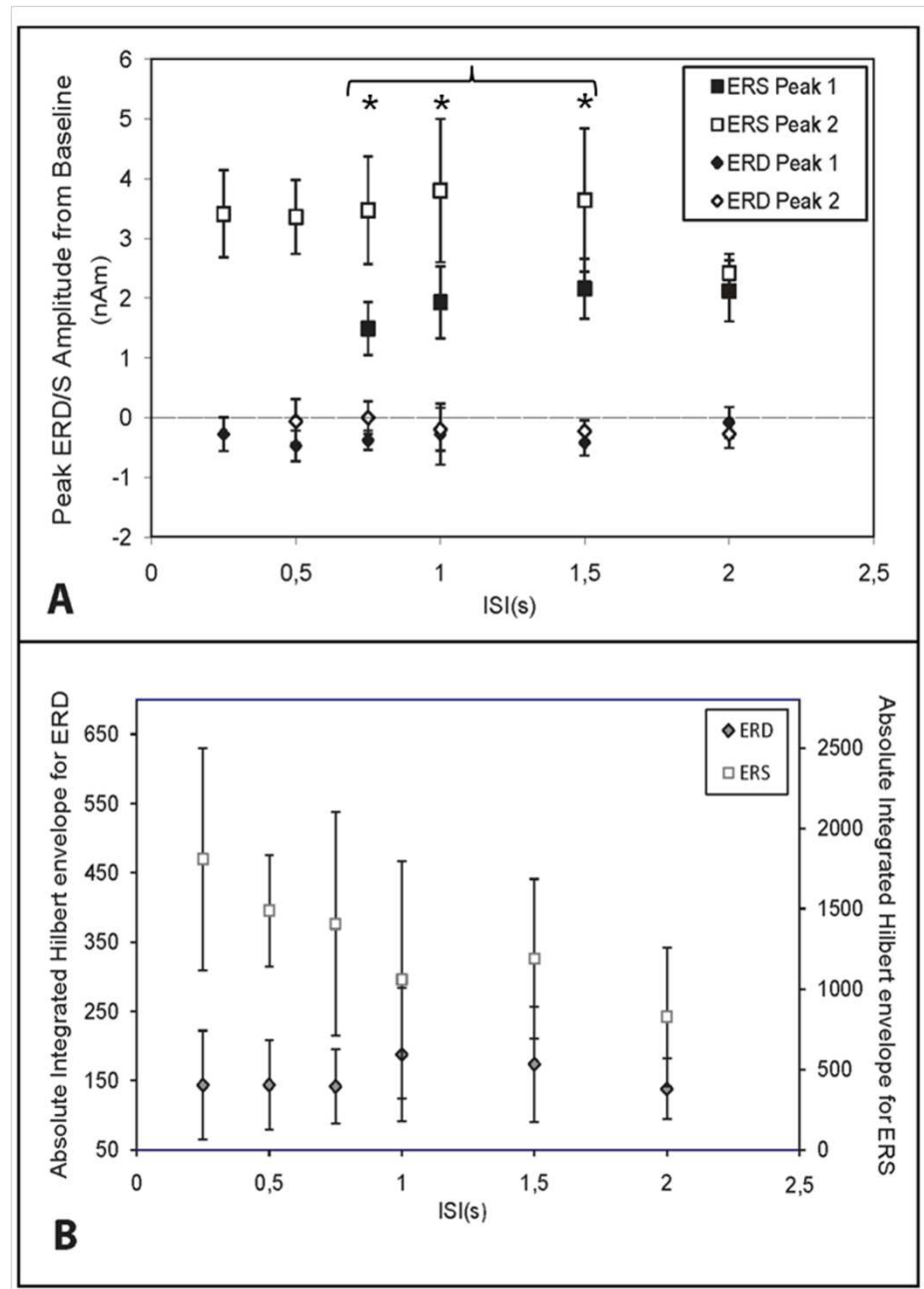
Figure 7-4: [A] Peak amplitudes of ERD/S following pulse 1 (filled) and pulse 2 (open).

Shown is average across subjects with standard error. * indicates second ERS peak

amplitude being significantly larger than 1st ERS peak amplitude (determined by a non-

The percentage change of beta ERD from baseline is consistent (-19 ± 6% across subjects and conditions). The average onset time of ERS was not changed with varying ISI and was found to be 0.38 ± 0.01s following stimulation for ISI of 0.75s or greater. The average TTP of the beta ERS was also unchanged at 0.78 ± 0.09s following stimulation. Despite no significant differences in the time to peak or onset time, the amplitude of the beta ERS (30 ± 12% across subjects and conditions) showed more variability than that of the ERD. Figure 7-4[A] shows that for an ISI of 2 s, no significant difference was found between the peak amplitudes of ERS 1 and ERS 2, suggesting that full recovery had occurred before the second pulse was applied. When the second pulse was applied at an ISI for which beta band activity was not at baseline, i.e. for ISIs < 2s, the peak amplitude of the second beta ERS was significantly larger than that of the first (p=0.028 matched Wilcoxon signed rank test, for ISIs 0.75s, 1s and 1.5s, with peak amplitudes for each ISI tested independently). The peak amplitudes of the beta ERD following the 2 median nerve pulses are also shown in Figure 7-4[A]; no significant modulations in amplitude with varying ISI were found.

The total power change of beta oscillatory activity (i.e the integrated Hilbert envelope), is shown in Figure 7-4[B]. beta ERD is similar across all conditions. However, despite constant peak amplitude of ERS following the second stimulation of ISIs≤1.5s (Figure 7-4[A]), Figure 7-4[B] shows a reduction in total beta ERS power in response to 2 pulses as the stimulus interval is increased.

7.3.3 Temporal signature of BOLD responses
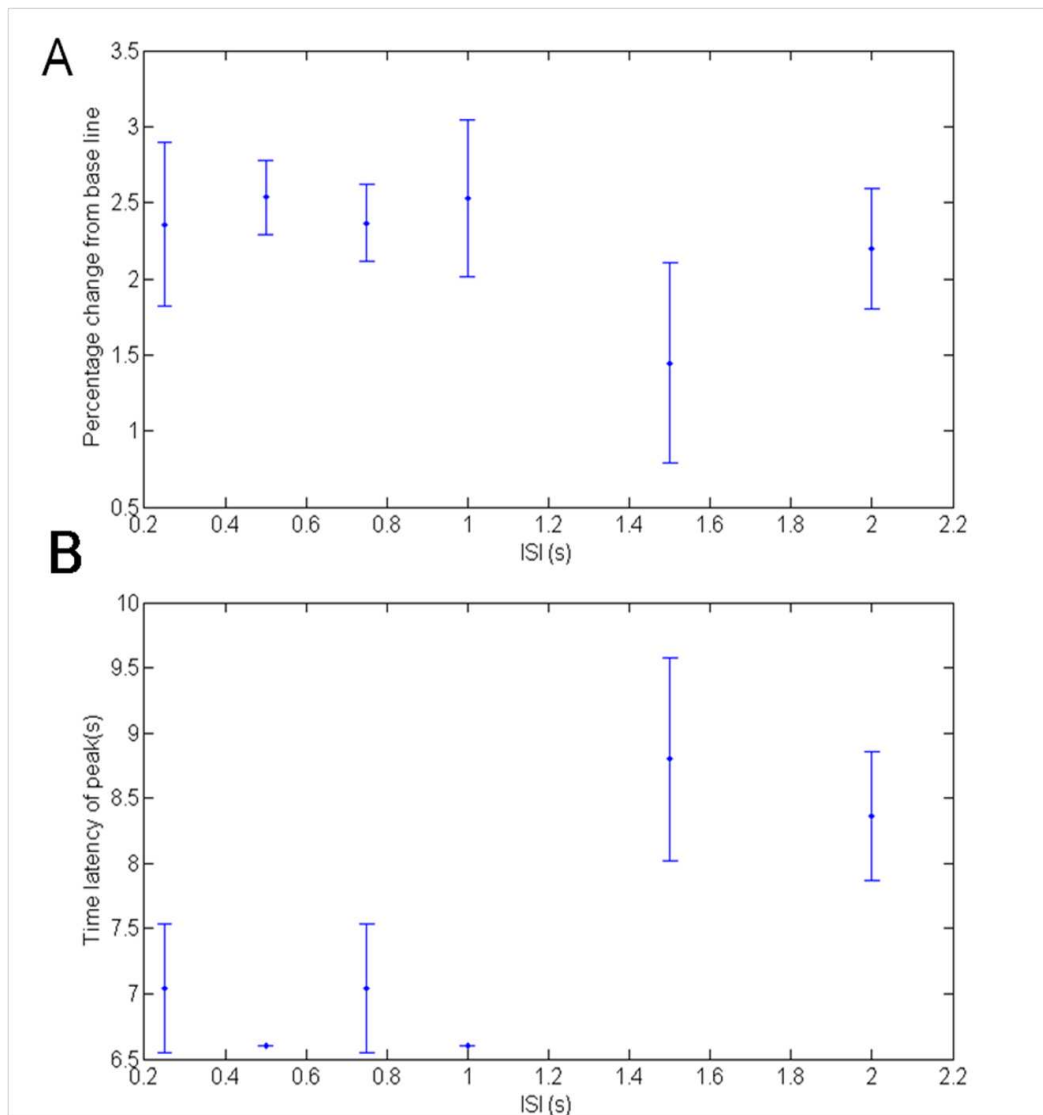
Figure 7-5: [A] Peak amplitudes and [B] peak latencies for BOLD responses in each condition extracted from an ROI centered on the global maximum. Data shown are averaged across trials and subjects, error bars represent standard error across subjects.

Figure 7-5 shows the peak amplitude from the global maximum of BOLD data expressed as a percentage change from baseline. The peak amplitudes were on average reduced for the ISIs of 1.5 and 2s compared to those for shorter ISIs; however this effect did not reach significance. The ISIs generating smaller peak amplitudes (1.5 and 2s) also displayed

increased peak latency, although this did not reach significance. There was no significant difference across conditions in the total integrated area of the BOLD response.

7.4 *Discussion*

In this chapter both signal averaged evoked and induced neuro-electric effects and the haemodynamic BOLD fMRI response are investigated using a paired pulse median nerve paradigm to assess the effects of paired pulse depression.

7.4.1 Spatial signature of effects

Spatial separation of beta ERD and ERS has been previously reported in data acquired during voluntary finger movement [13]. Here we show that this spatial separation also occurs during median nerve stimulation. Beta ERD was observed bilaterally, in the post central gyrus, and extended posterior into parietal regions. ERS was predominantly contra-lateral, focal and with activity extending to the pre-central gyrus. A significant difference in the global maxima of ERD and ERS responses was seen in the superior/inferior direction, which suggests spatially separate neural generators for the two phenomena. Such a finding could be explained by the difference in signal-to-noise of the two effects, with ERS being more robustly localized near to the cortical surface due its higher SNR. Intra-cerebral recordings of cortical activity related to finger movement report a widespread topography of ERD/ERS in temporal and higher–order motor regions [24]. Such extended sources are poorly modeled by dipolar lead-field estimates used for beamformer source localization and therefore may also give rise to inaccuracies in peak locations. However, it is highly likely,

given the consistency in separation of the ERD/ERS across both subjects and conditions, that they are indeed both arising from spatially separate neural generators.

The spatial localization of both MEG activity and significant BOLD activity reported here is consistent with locations reported following median nerve and somatosensory stimulation in previous studies and is somatotopically concordant with right hand stimulation [25-27]. A good spatial correspondence was found between haemodynamic fMRI data and the spatial location of induced oscillatory activity as detected by MEG, particularly post stimulus increases in beta band power. The spatial correspondence between BOLD and beta ERS peaks is consistent with previous studies investigating the correspondence between oscillatory activity detectable by MEG and fMRI BOLD data [2, 22, 28] and within the co-registration error of the two techniques.

A degree of intra-subject variabililty in peak locations in all modalities is evident in Figure 7-1. A common source of spatial localisation error for MEG [29-30] and fMRI [31] data is in the co-registration of functional data to the structural anatomical image and subsequent warping of the co-registered image to a standard brain in the normalisation process. Previous studies [29-30] have reported that for MEG data, inaccuracies in digitisation of fiducial coils of ~1mm can result in co-registration errors in posterior brain regions of ~1-2 cm. In this study, as described in Section 7.2.2, in an attempt to minimise such errors, representations of the scalp surface were obtained for surface matching with MRI data alongside digitisation of anatomical landmarks. Although efforts were made to minimise co-registration errors, it is impossible to remove their effects completely. MEG spatial localization is also limited by the accuracy of the source model used. For both the phase-locked evoked response dipole fit analysis and the beamformer analyses of induced oscillatory activity, sources were modelled as point dipoles. As previously described, if the task stimulation elicited activity in extended

patches of cortex, such extended sources are poorly modeled by dipolar lead-field estimates and therefore may give rise to inaccuracies in peak locations.

The close spatial correspondence of BOLD and ERS global maxima would suggest that the two are linked. The amplitude of beta oscillatory activity has been related to the levels of GABAergic inhibition [11], which has also been shown to affect the BOLD fMRI response with basal GABA levels being inversely related to the amplitude of the BOLD fMRI response. Recent work [9] has shown a correlation between basal GABA concentrations in the motor cortex and post movement ERS amplitude, one may therefore expect to see regional amplitude modulations in BOLD activity related to the non-linear modulations in beta ERS power. However, despite a close spatial relationship (both with regards to the distance between global maxima and the ROI analysis) between the beta ERS and BOLD response, this was not reflected in terms of a correspondence between task related modulations in power of the oscillatory activity and the BOLD response. Consistent with ERS responses, for BOLD data, both the number of significantly active voxels and maximum T score were on average higher in the pre and post central gyri when compared to the inferior parietal lobes; however in contrast to the MEG derived ERS which showed amplitude modulations with ISI, no regions displayed any significant modulation either in spatial extent or in regional maximum T score across conditions. Indeed using the peak amplitude of the ERS as a parametric modulator in the SPM analysis yielded no significant activity in the sensorimotor cortices. Despite the global maxima of BOLD being located closest to peaks in ERS, significant BOLD activity was also seen to extend anteriorly into inferior parietal lobes, consistent with reported locations of beta ERD. It is therefore difficult to comment on the relationship between the BOLD response and post stimulus ERS, it may be the case here that the changes in the ERS amplitude resulting from the paired pulse stimulus were too subtle to be detected in the BOLD response in the same region.

A previous study using vibrotactile stimulation [32] reported a close spatial correspondence between significant BOLD activity and dipole location determined from MEG data, but no consistent modulation in response amplitude. Both the close spatial correspondence between BOLD and MEG responses and the dissociation in signal averaged evoked amplitude modulation is consistent with the results presented here, where we extend this to show a correspondence with induced oscillatory activity. However, they also reported an increase in the spatial extent of significant BOLD activity with increasing ISI. The difference between the results reported here and those reported by Tuunanen et al. [32] may be explained by the difference in stimulus rates, and increased signal to noise afforded by 7T; at 1.5T increased activity in a given region may serve to push some voxels above the noise limit which would then be detected as an increase in spatial extent, whereas at 7T there may be sufficient SNR that for all conditions all active voxels are above the noise floor.

7.4.2 Modulation of the beta-ERD/ERS and P35m by varying ISIs

The phase-locked evoked response analysis was carried out to verify that with this paradigm we were able to detect analogous paired pulse effects to those measured invasively, and that the data reported is also consistent with previous studies. As a result of epicortical [33] and invasive imaging of rat cortex [34], it is believed that a larger area of cortex is activated during the P35m than during the N20m, which is consistent with the increased amplitude of the response that we see in our data. The ISI dependency of the P35m that we show, a decrease in P35 amplitude for ISIs of 0.25, 0.5 and 0.75s, is in general agreement with previous reports. Tiihonen et al. [35] reported a decrease in P35 amplitude with shortening ISI from 0.5 to 0.2s, whilst only a slight reduction was noted in N20m. Karhu et al. [8] describe a reduction in P35m amplitude between ISIs of 2 and 0.4s. Intracellular recordings have demonstrated that inhibitory postsynaptic potentials (IPSPs) also exhibit a strong

sensitivity to frequency of stimulation and as such it is thought that the P35m represents inhibitory postsynaptic currents, with the source orientation suggesting origination in layer IV of the somatosensory cortex, with current flow directed towards the white matter [7]. Deisz and Prince [6] reported a reduction of IPSCs when the ISI was changed from 10s to 1s. Our results show many similarities with data obtained in rat hippocampal neurons, where GABA mediated IPSCs were seen to undergo a paired pulse depression by the second of two pulses, with ISIs of 100-2000ms and were significantly suppressed when the ISIs were between 100 and 1000ms [5]. Since paired pulse depression effects were evident in the signal averaged evoked response data, we went on to investigate if a similar effect was visible in the induced oscillatory activity.

The temporal signature of the beta band oscillatory activity shown here following median nerve stimulation is also in good agreement with previous studies [36], with a power loss for ~0.4s after stimulation followed by a sharp increase in power peaking at ~0.78s. No significant modulations in beta power were apparent during the baseline 1.5s period prior to stimulation. Since no difference in beta band oscillations was found between the regular and jittered conditions discussed in Chapter 6, anticipatory effects on the power modulations following stimulation can be excluded.

The amplitude of the ERD was unaffected by ISI and was consistent across subjects and conditions. It can be seen in Figure 7-3 and Figure 7-4 that the application of a pulse during the ERD period of the previous stimulation did not result in a further reduction of baseline; rather the same amplitude was maintained. What is more, the application of a pulse during the ERS of the previous stimulation resulted in a loss of power to the same level. That is to say the level of ERD reached following stimulation remained constant, irrespective of the level of beta power at the time of stimulation. This is consistent with previous work [2] and supports a hypothesis that beta (ERD) oscillations behave as a cortical 'gate'.

The ERS on the other hand was much less consistent. The peak amplitude of the rebound appeared to increase with the number of pulses received within a recent timeframe (i.e. for ISI < 2s) the width of the rebound curve was affected by the ISI. This led to a cumulative effect on power, with a large total ERS power when the second pulse was applied early in the refractory period of the beta oscillatory activity and a reduction in total power across conditions with increasing ISI, reflecting a non-linearity in the response dependent upon stimulus frequency.

The functional implications of these results are not entirely obvious. The spatial and functional dissociation between modulations in beta ERD and ERS with ISI is consistent with previous work and suggests separate neural generators for the two effects. However, the neuropharmacological basis of these mechanisms requires further investigation. Invasive data suggests that paired pulse depression effects, visible in the signal averaged evoked response here, may be partly attributed to a desensitization of the GABA-A receptor [37]. However, work by Hall et al. [10] show movement related beta ERD to be GABA-A dependent, with post movement beta ERS being GABA-A independent. At first sight our results seem to be in contrast with this which may be due to the paradigm differences, however it may also be that any modulations in the beta ERD amplitude resulting from paired pulse depression effects are simply too subtle to be detected with the current paradigm. In the current study, timecourses were extracted from beta ERS peaks, due to their small inter-subject variability in spatial location when compared to beta ERD peak locations. The regularization of the data covariance matrix used to derive the beamformer weights for the virtual sensor timecourses results in a spatially smoothed MEG source space. This ensures contribution from both ERD and ERS effects and minimises a sensitivity bias towards beta ERS effects, however there may have been a slight reduction in sensitivity to modulations in beta ERD as a result of this approach.

The precise mechanisms underlying generation of beta oscillatory activity and ERD/S phenomena may however be far more complex than alluded to above. Evidence for multiple co-existent beta oscillations in somatosensory cortex has been proven, meaning that a single virtual sensor timecourse may well represent many different underlying processes [38]. The co-existent beta oscillations were shown to differ in their GABA dependence, with one being GABAergically modulated and the other not. Post stimulus beta ERS has previously been attributed to somatosensory re-afference [39] and it may be that this is a separate, non-GABA mediated effect that displays sensitivity to ISI within a relatively short timeframe. Despite not being directly influenced by GABAergic modulation it has been demonstrated that beta ERS is dependent upon the spontaneous beta oscillatory power, which is GABAergically mediated [10, 40]. As such, further studies are required to properly characterise these phenomena and the relationship between the two effects.

7.4.3 Non-linearity of the BOLD response

Most importantly for BOLD studies, here we show that the neuro-electric responses to median nerve stimulation has only recovered at an ISI of 2s (Figure 7-3 [F]). Traditionally, models of neural activity for input into BOLD models only consider signal averaged evoked responses which have recovered after a few hundred milliseconds whereas this study demonstrates significant non-linear modulations of induced oscillatory activity and in signal averaged evoked response amplitude for up to 2s following stimulation. Further, despite being on the same timescale, the modulation in oscillatory beta ERS with ISI is somewhat different from the paired pulse depression effect seen in the P35m component of the signal averaged evoked response. Much work has been done in order to determine the basis of well characterised non-linearities in BOLD [41]. Both non-linear neural responses to stimuli and

non-linear vascular effects may contribute to BOLD non-linearity and the relative contribution of these two effects remains poorly understood. Recent work [42] has reported that in the visual cortex, non-linear phase locked evoked neural activity only exists at ISIs of less than 200ms, and beyond this, BOLD non-linearities are attributed to vascular origins. The direct measures of neural activity made using MEG in this study show non-linearities exist in both phase locked evoked responses and induced oscillatory activity with ISIs on the order of up to 2s. This is of great importance for BOLD models and highlights the need to take both signal averaged evoked and induced activity into account when creating neural input functions to a BOLD model.

Importantly the temporal characteristics of the BOLD response suggest a deviation from a truly linear system. The spatial correspondence of the peaks in BOLD activity dipoles and induced oscillatory activity (beta ERS) intimate that the effects are originating from the same cortical location, as such non-linearities apparent in the signal averaged evoked response and beta ERS response may be contributing to non-linearities in the BOLD response.

In assessing the modulation of BOLD timecourses extracted from the global maxima regions, near to peaks in beta ERS, they showed on average reduced peak amplitude and increased peak latency increased for ISIs > 1s. The trends seen in Figure 7-5 [A] and [B] for peak amplitude and latency deviate from what one would expect from a truly linear BOLD response in an ideal system with short ISIs however neither of these effects reached significance. The fMRI scan parameters for this study were set up for maximum bilateral coverage at high resolution to assess the spatial distribution of BOLD with respect to MEG phenomena. Future work using a short TR would improve assessment of the temporal non-linearities of the BOLD response.

7.5 *Conclusions*

We have shown a good spatial correspondence of BOLD activity and induced oscillatory activity suggesting a relationship between the two phenomena. A statistically significant spatial separation of beta ERD and ERS has been demonstrated suggesting that the two effects arise from separate neural generators. The spatial distribution and extent of BOLD activity was unaffected by ISI, but modulation in peak amplitude and latency were observed. Non-linearities both in induced oscillatory activity and in components of the signal averaged evoked response have been reported for ISIs of up to 2s showing that effects of the paired pulse design manifest themselves in both forms of activity. The beta band ERD magnitude is always equivalent, irrespective of the starting point, which suggests a gating role for this response as no effects of the paired pulse design were evident. The ERS on the other hand was both spatially distinct from the ERD and modulated with ISI, although in a different manner to the signal averaged evoked response. The reported dissociations in amplitude of BOLD and MEG data reflect the rich, complementary information afforded by the two techniques which requires further investigation if we are to understand the relationship between these two disparate phenomena. We have shown that neural activity exhibits a significantly non-linear response to stimulation, implying that BOLD non-linearity comes not only from a non-linear vascular response to neural activity, but also a non-linear neural response to the stimulus. This is the case even when the ISI between stimuli is relatively long (on the order of 2s) and the signal averaged evoked response has returned to baseline.

7.6 *References*

[1]   Muthukumaraswamy, S.D., Edden, R.A.E., Jones, D.K., Swettenham, J.B. and Singh, K.D., Resting GABA concentration predicts peak gamma frequency and fMRI amplitude in response to visual stimulation in humans. Proceedings of the National Academy of Sciences, 2009. **106**(20): p. 8356-8361.

[2]   Stevenson, C.M., Brookes, M.J. and Morris, P.G., Band correlates of the fMRI BOLD response. Human Brain Mapping, 2011. **32**(2): p. 182-197.

[3]   Winterer, G., Carver, F.W., Musso, F., Mattay, V., Weinberger, D.R. and Coppola, R., Complex relationship between BOLD signal and synchronization/desynchronization of human brain MEG oscillations. Human Brain Mapping, 2007. **28**(9): p. 805-816.

[4]   Logothetis, N.K., Pauls, J., Augath, M., Trinath, T. and Oeltermann, A., Neurophysiological investigation of the basis of the fMRI signal. Nature, 2001. **412**(6843): p. 150-157.

[5]   Xu, J., Yang, B. and Sastry, B., The involvement of GABA-C receptors in paired-pulse depression of inhibitory postsynaptic currents in rat hippocampal CA1 pyramidal neurons. Experimental neurology, 2009. **216**(1): p. 243-246.

[6]   Deisz, R. and Prince, D., Frequency-dependent depression of inhibition in guinea-pig neocortex in vitro by GABAB receptor feed-back on GABA release. The Journal of Physiology, 1989. **412**(1): p. 513-541.

[7]   Wikström, H., Huttunen, J., Korvenoja, A., Virtanen, J., Salonen, O., Aronen, H. and Ilmoniemi, R., Effects of interstimulus interval on somatosensory evoked magnetic fields (SEFs): a hypothesis concerning SEF generation at the primary sensorimotor cortex. Electroencephalography and Clinical Neurophysiology, 1996. **100**(6): p. 479-487.

[8]   Karhu, J., Hari, R., Paetau, R., Kajola, M. and Mervaala, E., Cortical reactivity in progressive myoclonus epilepsy. Electroencephalography and Clinical Neurophysiology, 1994. **90**(2): p. 93-102.

[9]   Gaetz, W., Edgar, J., Wang, D. and Roberts, T., Relating MEG Measured Motor Cortical Oscillations to resting [gamma]-Aminobutyric acid (GABA) Concentration. Neuroimage, 2011. **55**(2): p. 616-621.

[10]   Hall, S.D., Stanford, I.M., Yamawaki, N., McAllister, C., Ronnqvist, K., Woodhall, G.L. and Furlong, P.L., The role of GABAergic modulation in motor function related neuronal network activity. Neuroimage, 2011. **56**(2): p. 1506-1510.

[11]   Jensen, O., Goel, P., Kopell, N., Pohja, M., Hari, R. and Ermentrout, B., On the human sensorimotor-cortex beta rhythm: sources and modeling. Neuroimage, 2005. **26**(2): p. 347-355.

[12]   Della Penna, S., Torquati, K., Pizzella, V., Babiloni, C., Franciotti, R. and Rossini, P., Temporal dynamics of alpha and beta rhythms in human SI and SII after galvanic median nerve stimulation. A MEG study. Neuroimage, 2004. **22**(4): p. 1438-1446.

[13]   Jurkiewicz, M.T., Gaetz, W.C., Bostan, A.C. and Cheyne, D., Post-movement beta rebound is generated in motor cortex: Evidence from neuromagnetic recordings. Neuroimage, 2006. **32**(3): p. 1281-1289.

[14]   Jueptner, M. and Weiller, C., Review: does measurement of regional cerebral blood flow reflect synaptic activity?--implications for PET and fMRI. Neuroimage, 1995. **2**(2): p. 148-156.

[15]   Kampe, K.K.W., Jones, R.A. and Auer, D.P., Frequency dependence of the functional MRI response after electrical median nerve stimulation. Human Brain Mapping, 2000. **9**(2): p. 106-114.

[16]   Annett, M., A classification of hand preference by association analysis. British journal of psychology, 1970. **61**(3): p. 303-321.

[17]   Vrba, J., Betts, K., Burbank, M., Cheung, T., Fife, A., Haid, G., Kubik, P., Lee, S., McCubbin, J. and McKay, J., Whole cortex, 64 channel SQUID biomagnetometer system. IEEE Transactions on Applied Superconductivity, 1993. **3**(1): p. 1878-1882.

[18]   Wang, F., Stevenson, C.M., Brookes, M.J., Zumer, J.M., White, T.P. and Morris, P.G. . Role of beta band oscillations in somatosensory cortex. . Proceedings in Organization for Human Brain Mapping (OHBM). San Francisco 2009.

[19]   Backus, G.E. and Gilbert, F., Philosophical Transactions of the Royal Society of London. Vol. 266. 1970. 123-192.

[20]   Boecker, H., Khorram Sefat, D., Kleinschmidt, A., Merboldt, K.D., Hänicke, W., Requardt, M. and Frahm, J., High resolution functional magnetic resonance imaging of cortical activation during tactile exploration. Human Brain Mapping, 1995. **3**(3): p. 236-244.

[21]   Lin, W., Kuppusamy, K., Haacke, E.M. and Burton, H., Functional MRI in human somatosensory cortex activated by touching textured surfaces. Journal of Magnetic Resonance Imaging, 1996. **6**(4): p. 565-572.

[22]   Singh, K.D., Barnes, G.R., Hillebrand, A., Forde, E.M.E. and Williams, A.L., Task-related changes in cortical synchronization are spatially coincident with the hemodynamic response. Neuroimage, 2002. **16**(1): p. 103-114.

[23]   Huttunen, J., Komssi, S. and Lauronen, L., Spatial dynamics of population activities at S1 after median and ulnar nerve stimulation revisited: An MEG study. Neuroimage, 2006. **32**(3): p. 1024-1031.

[24]   Rektor, I., Sochurkova, D. and Bockova, M., Intracerebral ERD/ERS in voluntary movement and in cognitive visuomotor task. Progress in brain research, 2006. **159**: p. 311-330.

[25]   Baudewig, J., Kunkel, M. and Paulus, W. Distribution of cortical activity in motor and sensory tasks focusing on the median nerve: a fMRI study. Proceedings in ISMRM. Vancouver 1997.

[26]   Korvenoja, A., Huttunen, J., Salli, E., Pohjonen, H., Martinkauppi, S., Palva, J.M., Lauronen, L. and Virtanen, J., Activation of multiple cortical areas in response to somatosensory stimulation: combined magnetoencephalographic and functional magnetic resonance imaging. Human Brain Mapping, 1999. **8**(1): p. 13-27.

[27]   Polonara, G., Fabri, M., Manzoni, T. and Salvolini, U., Localization of the first and second somatosensory areas in the human cerebral cortex with functional MR imaging. American Journal of Neuroradiology, 1999. **20**(2): p. 199-205.

[28]   Brookes, M.J., Gibson, A.M., Hall, S.D., Furlong, P.L., Barnes, G.R., Hillebrand, A., Singh, K.D., Holliday, I.E., Francis, S.T. and Morris, P.G., GLM-beamformer method demonstrates stationary field, alpha ERD and gamma ERS co-localisation with fMRI BOLD response in visual cortex. Neuroimage, 2005. **26**(1): p. 302-308.

[29]   Adjamian, P., Barnes, G.R., Hillebrand, A., Holliday, I.E., Singh, K.D., Furlong, P.L., Harrington, E., Barclay, C. and Route, P., Co-registration of magnetoencephalography with magnetic resonance imaging using bite-bar-based fiducials and surface-matching. Clinical Neurophysiology, 2004. **115**(3): p. 691-698.

[30]   Singh, K., Holliday, I., Furlong, P. and Harding, G., Evaluation of MRI-MEG/EEG co-registration strategies using Monte Carlo simulation. Electroencephalography and Clinical Neurophysiology, 1997. **102**(2): p. 81-85.

[31]   Villain, N., Landeau, B., Groussard, M., Mevel, K., Fouquet, M., Dayan, J., Eustache, F., Desgranges, B. and Chételat, G., A simple way to improve anatomical mapping of functional brain imaging. Journal of Neuroimaging, 2010. **20**(4): p. 324-333.

[32]   Tuunanen, P.I., Kavec, M., Jousmäki, V., Usenius, J.P., Hari, R., Salmelin, R. and Kauppinen, R.A., Comparison of BOLD fMRI and MEG characteristics to vibrotactile stimulation. Neuroimage, 2003. **19**(4): p. 1778-1786.

[33] Woolsey, C.N., Erickson, T.C. and Gilson, W.E., Localization in somatic sensory and motor areas of human cerebral cortex as determined by direct recording of evoked potentials and electrical stimulation. Journal of Neurosurgery, 1979. **51**(4): p. 476-506.

[34] Derdikman, D., Hildesheim, R., Ahissar, E., Arieli, A. and Grinvald, A., Imaging spatiotemporal dynamics of surround inhibition in the barrels somatosensory cortex. The Journal of neuroscience, 2003. **23**(8): p. 3100-3105.

[35] Tiihonen, J., Hari, R. and Hämäläinen, M., Early deflections of cerebral magnetic responses to median nerve stimulation. Electroencephalography and Clinical Neurophysiology, 1989. **74**(4): p. 290-296.

[36] Pfurtscheller, G. and Lopes da Silva, F., Event-related EEG/MEG synchronization and desynchronization: basic principles. Clinical Neurophysiology, 1999. **110**(11): p. 1842-1857.

[37] Thompson, S.M. and Gahwiler, B.H., Activity-dependent disinhibition. III. Desensitization and GABAB receptor-mediated presynaptic inhibition in the hippocampus in vitro. Journal of neurophysiology, 1989. **61**(3): p. 524-533.

[38] Roopun, A.K., Middleton, S.J., Cunningham, M.O., LeBeau, F.E.N., Bibbig, A., Whittington, M.A. and Traub, R.D., A beta2-frequency (20–30 Hz) oscillation in nonsynaptic networks of somatosensory cortex. Proceedings of the National Academy of Sciences, 2006. **103**(42): p. 15646-15650.

[39] Cassim, F., Szurhaj, W., Sediri, H., Devos, D., Bourriez, J.L., Poirot, I., Derambure, P., Defebvre, L. and Guieu, J.D., Brief and sustained movements: differences in event-related (de) synchronization (ERD/ERS) patterns. Clinical Neurophysiology, 2000. **111**(11): p. 2032-2039.

[40] Yamawaki, N., Stanford, I., Hall, S. and Woodhall, G., Pharmacologically induced and stimulus evoked rhythmic neuronal oscillatory activity in the primary motor cortex in vitro. Neuroscience, 2008. **151**(2): p. 386-395.

[41] Zhang, N., Zhu, X.H. and Chen, W., Investigating the source of BOLD nonlinearity in human visual cortex in response to paired visual stimuli. Neuroimage, 2008. **43**(2): p. 204-212.

[42] Liu, Z., Rios, C., Zhang, N., Yang, L., Chen, W. and He, B., Linear and nonlinear relationships between visual stimuli, EEG and BOLD fMRI signals. Neuroimage, 2010. **50**(3): p. 1054-1066.

Chapter 8

Electrical and haemodynamic responses to MNS pulse trains

Overview: This chapter aims to investigate the neuronal responses following a train of median nerve stimuli. Beta band oscillations, SEFs (N20m, P35m and N160m) and BOLD responses are measured for pulse trains of varying length and frequency. The gating hypothesis discussed in Chapter 7 is further confirmed with multiple pulse paradigms. The CAM introduced in Chapter 5 is also tested and some amendments are made to allow this model to fit our results. Although some conflicts between the results of our paired pulse study and previous studies have been discussed in Chapter 7, they can be interpreted by the CAM together. Finally, the temporal signature of beta ERS/ERD is used to attempt to separate the cortical areas associated with ERD/ERS effects in fMRI.

8.1 *Introduction*

The modulation of beta band oscillations in the somatosensory cortex has been discussed in Chapter 7. The paired pulse study suggests that the beta ERD plays a gating role in cortical processing. If a second pulse is applied within the 'gating interval' (a 0.5s window following the first pulse), the ERD will be maintained at the same amplitude apart from the evoked components; if the second pulse is applied outside this window, a loss of power to the same level is generated. However, in the paired pulse study, as the maximum length of

beta ERD is only about 1s, whether the amplitudes of ERD following longer stimulus trains is maintained at the same level remains unclear.

The P35m effect has been previously reported to decrease with ISI from 0.5 to 0.2s [1]. This has been confirmed by our paired pulse study. The P35m is suggested to represent the GABA mediated IPSPs [2] and is modulated by paired pulse depression effects. Although the beta ERD is also GABA mediated, whether the P35m is modulated under this gating role remains uncertain. If the P35m is not influenced by the 'cortical gate', there may be other evoked responses modulated by these beta band effects.

As shown in Chapter 7, the peak amplitude of the beta ERS, which has larger variance than the ERD, appears to increase with the number of pulses received within a recent timeframe and have a cumulative effect. However, whether the increase of beta ERS is due to the cumulative effect or the decrease of ISI is still questionable. As discussed in Chapter 7, the precise mechanism underlying beta ERD/ERS remains unclear. It has been reported in previous studies that beta ERD is directly mediated by the GABA level whilst the ERS is indirectly influenced by the spontaneous beta oscillations [3]. As stated in Chapter 5, the thalamo-cortical loops, which contain both GABA mediated and non-GABA mediated neurons, are involved in the modulation of cortical beta oscillations. The CAM which relates the beta ERD/ERS to the changes of the CA level has been developed by previous research. Whether this model holds true with our results and can be used to interpret the beta ERD/ERS following MNS will be tested in this chapter.

In Chapters 6 and 7, studies presented have employed MEG beamforming in order to find the spatial separation between beta ERD and ERS. However, the limited spatial resolution of this method makes precise measurement of spatial separation and extent problematic. Previous research using EEG-fMRI has shown that, by including the timecourse of beta ERS

(PMBR) as a regressor in the fMRI analysis, the source of the ERS effect can be identified by associated BOLD signal increase [4]. We therefore examine the spatial distribution of the BOLD signal using models based on the temporal signature of beta ERD and ERS.

In this chapter, MNS with different pulse train lengths is used to study the modulation of beta ERD/ERS. Then using a fixed length pulse train with different ISIs, the influence of stimulus frequency on the beta ERD/ERS is studied. The gating role of beta ERD and the CAM are tested. Finally, the spatial separation of ERD and ERS is examined by including the temporal signature of beta ERD and ERS in regressor in BOLD fMRI analysis.

Both MEG and ultra-high-field fMRI are used in this chapter to test the following hypothesis.

The gating role:

1) The beta ERD behaves as a cortical gate and the amplitude of ERD is maintained if multiple pulses are applied within the gating interval.

2) There is some evoked responses moderated by the beta band effects under this gating role

In the CAM, the WP can only moves on the bell-shaped curve and the ERD/ERS is limited by this curve. Based on this model:

3) The ERD/ERS can be interpreted by the CAM, no linear independency or accumulative effect is found in ERS with increasing pulse number.

4) The ERS is modulated by changing stimulus frequency in the pulse train frequency study with ISI outside the gating interval, but the amplitudes of ERS following each pulse are the same.

The spatial separation:

5) By including the temporal signature of beta ERD and ERS into the regression model, a delayed BOLD signal, which may be associated with the beta ERS, can be found and is spatially separated from the standard BOLD response.

8.2 *Methods*

Eight healthy right-handed volunteers (6 males, 2 females) took part in the pulse train length study (where pulse number was varied). Eight right-handed volunteers (7 males, 1 female) took part in the MEG and 7T fMRI study where pulse frequency was varied. All volunteers provided written informed consent. Handedness was assessed using a modified version of the Edinburgh handedness inventory.

8.2.1 Paradigms

8.2.1.1 Investigating pulse train length

In order to investigate pulse train length, median nerve stimulation with the same ISI of 0.5s but with four different pulse train lengths was applied to all 8 subjects. The numbers of stimuli applied in each trial were 2, 4, 6, and 10 for the four different conditions. The pre-stimulus time was 1.5s and the trial lengths were 9s, 10s, 11s and 13s respectively. There were 40 trials collected in each condition and blocks containing different conditions were pseudo-randomly ordered.

8.2.1.2   Investigating pulse train frequency

To investigate pulse train frequency, a train of 10 pulses with two different ISIs was applied to the eight subjects. An ISI of 0.5s (2Hz) was used in an effort to maintain the ERD (since pulses were applied within the gating interval) and whereas an ISI of 2s (0.5Hz) allowed the ERS to appear between stimuli. The pre-stimulus time was 1.5s and trial length was 13s for 2Hz and 28s for 0.5Hz; a total of 50 trials was used in the MEG experiment. An fMRI study with the same protocol was undertaken on the same subjects. However, the number of trials was reduced to 10 in fMRI due to the higher SNR of the BOLD response at 7T. The length of each trial was increased to 44s for both ISIs to allow for full recovery of the haemodynamic response between trials.

8.2.2 Data acquisition

MEG data were acquired using the method outlined in Chapter 6. fMRI data were acquired using the method outlined in Chapter 7.

8.2.3 Data analysis

8.2.3.1   Source localization

Source localization of induced changes in oscillatory activity was performed using the adaptive beamforming technique Synthetic Aperture Magnetometry (SAM) as detailed in Chapter 6. In both multiple pulse and link pulse studies, contrast windows for beta ERD

were selected with 'active' periods spanning $0 \leq t \leq 0.5s$ following each of the pulses and 'control' periods spanning the same time near the end of trials. In the pulse train length study, the control periods for 2, 4, 6 and 10 pulses are $6 \leq t \leq 7s$, $6 \leq t \leq 8s$, $6 \leq t \leq 9s$ and $6 \leq t \leq 11s$ respectively. In the frequency study, the control periods for 2Hz and 0.5Hz conditions are $6 \leq t \leq 11s$ and $11 \leq t \leq 16s$ respectively. A regularisation parameter of 2 was applied to ensure that the data covariance matrix was well conditioned in both studies. Pseudo-T-statistical images were reconstructed on a 2mm^3 grid, showing the spatial distribution of power change between active and control windows.

8.2.3.2   Time-frequency analysis

Hilbert envelopes were generated from virtual sensor timecourses extracted from ERD peak points. An average of the 1s pre-stimulus data ($-1.25 \leq t \leq -0.25s$) was taken from the Hilbert envelope and assumed to be baseline. The ERS onset and TTP time was calculated using the method stated in Chapter 7. The evoked responses were generated from the same virtual sensor traces as stated in Chapter 6. Peak amplitude changes of the N20m, P35m and N160m effects were plotted with error bars showing standard error across subjects and compared across different pulses and conditions. Paired Wilcoxon Signed Rank tests were used to test for significant differences in both the evoked responses and the ERD/ERS between pulses and conditions. The Bonferroni correction was used to counteract the problem of multiple comparisons between pulses.

8.2.3.3   fMRI

In the frequency study, the BOLD images and timecourses were generated using the same method as stated in Chapter 7.

However, for testing for BOLD components associated with beta ERS, a GLM containing two separate columns in the design matrix was defined in SPM: the first column represented the stimulus (block design with duration 5s corresponding to ERD); the second column represented a 5s delayed temporal response with 3s duration (corresponding to ERS), based on the MEG beta band timecourse measures. Voxels exhibiting significant correlation (p<0.05 FWE corrected) with the two columns were derived (we shall term these the standard and the delayed BOLD responses), BOLD timecourses were then extracted from 6x6x6mm^3 clusters Centred on the global maxima. fMRI data were also processed using ANOVA [5]. This method detects pixels in which the timecourse shows a repeatable response to each stimulus. The ratio of the variance of the averaged data set (aross trials) to the variance of the unaveraged data set is calculated for each pixel in the image. The ANOVA technique does not make any assumptions about the shape of the activation timecourse, and relies solely on the timing of the start of each trial as input. This model free analysis allowed elucidation of voxels exhibiting a significant BOLD response at any latency. A 'time to peak' map was then generated by measuring the time between stimulus onset and the peak in the haemodynamic response for all activated voxels defined by ANOVA.

8.3 *Results*

8.3.1 Pulse train length study

Timecourses of beta band oscillations with different pulse train lengths are shown in Figure 8-1. For median nerve stimuli with a 0.5s ISI, the characteristic temporal signature of beta

ERD followed by an ERS can be seen in all conditions. The average onset time of ERS was not changed with varying train length and was found to be 0.45±0.02s following the final stimulus. The averaged TTP of the beta ERS was 0.91±0.03s.
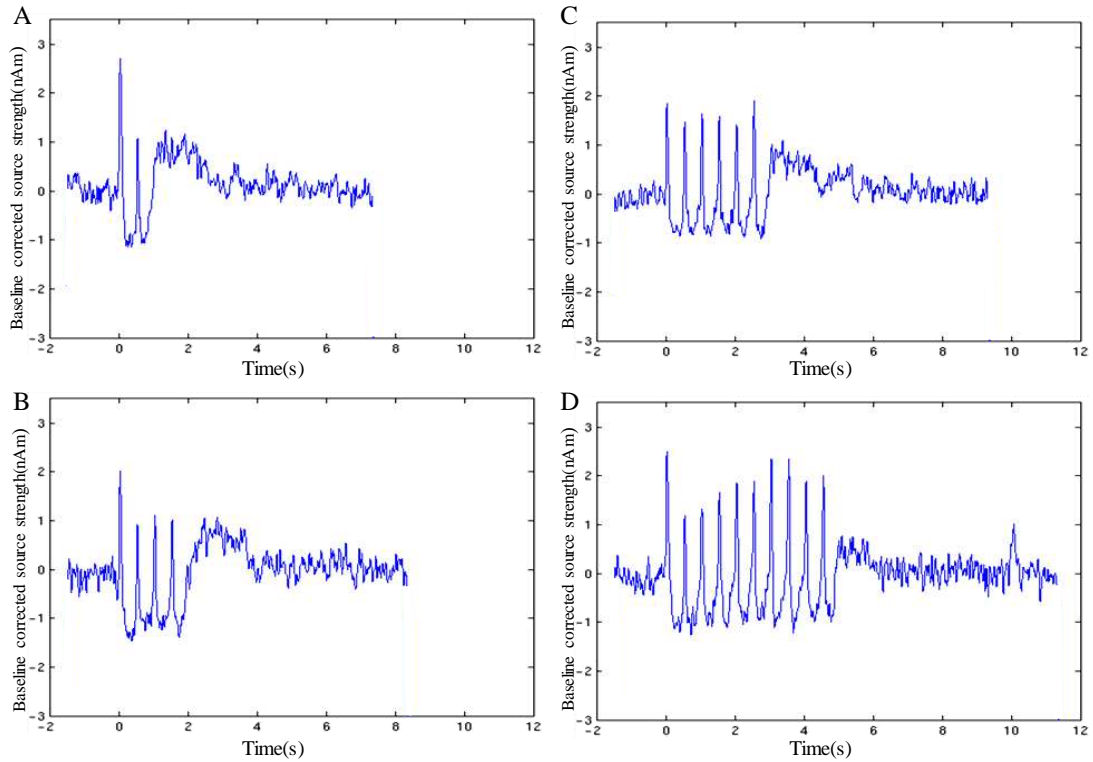

Figure 8-1: Timecourse averaged across subjects for 2 pulses [A] , 4 pulse [B], 6 pulses [C] and 10 pulses [D] conditions.

The percentage change of beta ERD after each pulse for the four different conditions are shown in Figure 8-2. These amplitudes are averaged across all eight subjects and the variance across subjects is indicated by the error bars. No significant (p<0.05) modulations in percentage ERD with different numbers of pulses were found.
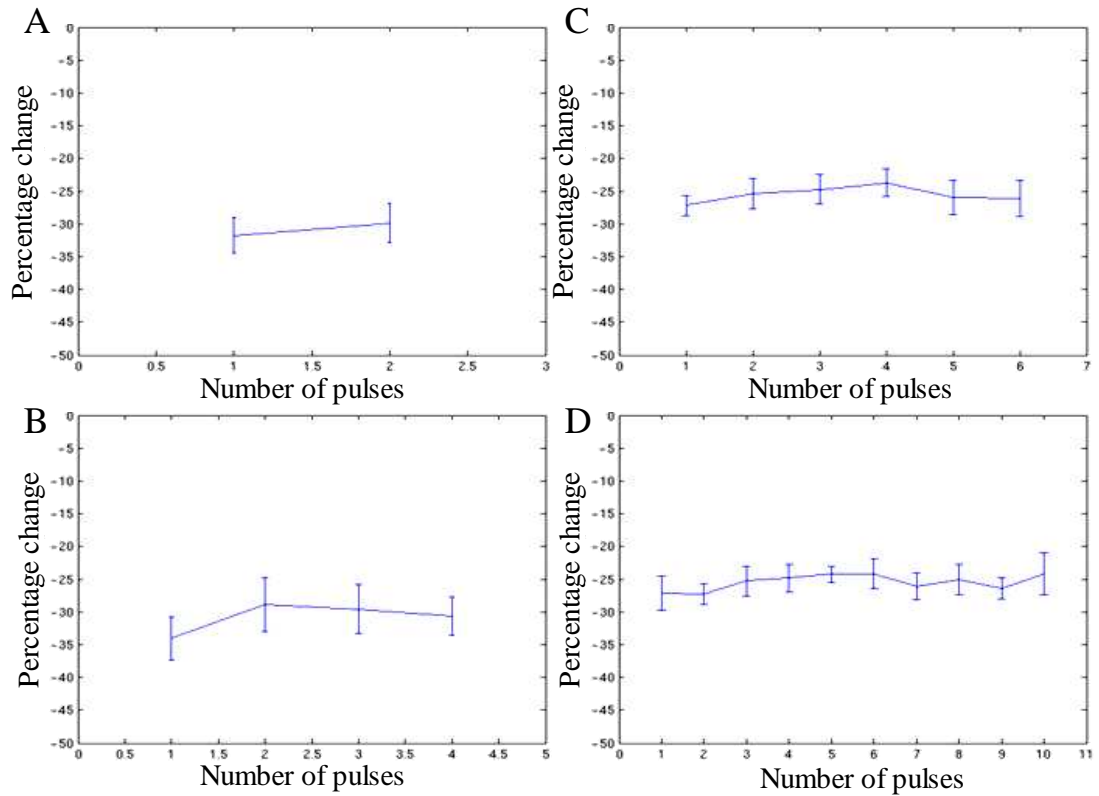
Figure 8-2: Percentage change of peak ERD following each pulse for the conditions of 2 pulses [A] , 4 pulse [B], 6 pulses [C] and 10 pulses [D] with ISI of 0.5s.

Figure 8-3 shows the peak amplitudes of ERD and ERS for the four different conditions of train length study and the variance across subjects is shown in the error bars. If peak amplitudes in ERD and ERS are measured as percentage change from baseline (A), ERS shows large variance across subjects whereas the ERD is stable. If the raw peak amplitudes (nAm) are used, the ERD shows larger variability across subjects. However, in both measurements, there is no significant ($p<0.05$) modulation in either ERD or ERS with varying pulse train length.
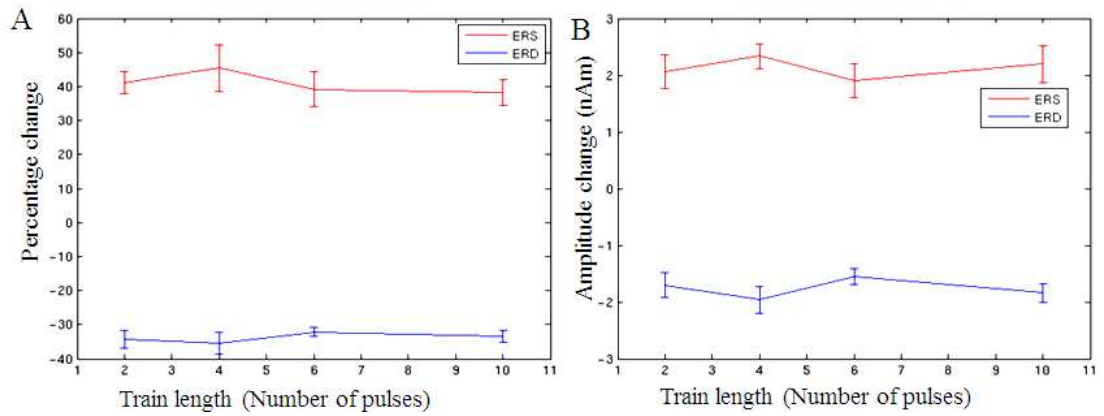
Figure 8-3: Percentage and raw peak amplitude of beta ERD/ERS with different pulse train length.

Figure 8-4 shows the timecourses of trial averaged evoked response. Timecourse from the virtual sensor in each subject were mean corrected and averaged together. In all conditions, ERF components N20m, P35m and N160m were clearly observed.
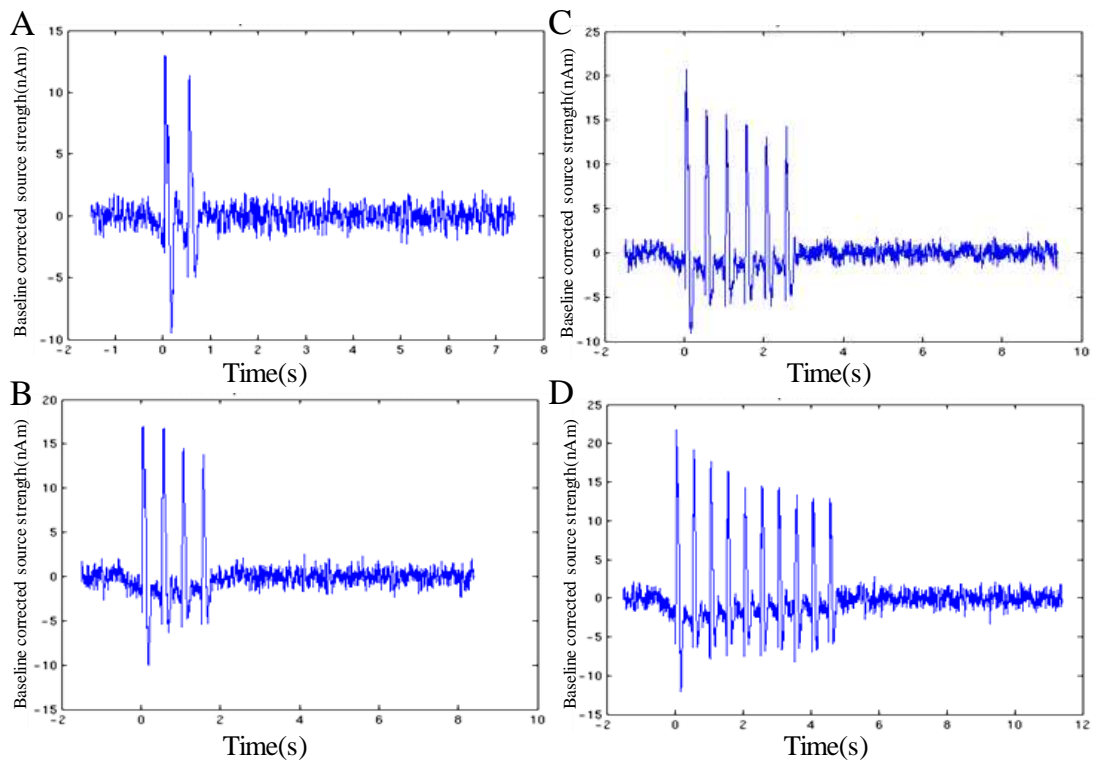

Figure 8-4: Evoked responses for the conditions of 2 pulses [A] , 4 pulse [B], 6 pulses [C] and 10 pulses [D].

Figure 8-5 shows the amplitude of the N20m, P35m and N160m components of all pulses in all four conditions. It can be seen that the N20m is small but stable for all pulses under all conditions. When multiple pulses are applied within a 0.5s ISI, the P35m component, which is the largest peak in SEFs, decreases with increasing number of pulses. But these differences do not achieve significance ($p<0.005$) due to the large variance. The N160m following the first pulses are significantly larger than the ones following subsequent pulses in all four conditions ($p=0.015$ for 2 pulse condition, $p=0.0078$ for 4 pulse condition, $p=0.0453$ for 6 pulse condition, and $p=0.0027$ for 10 pulse condition). The change in amplitude of the N160m from the second pulse to the last pulse was not significant.
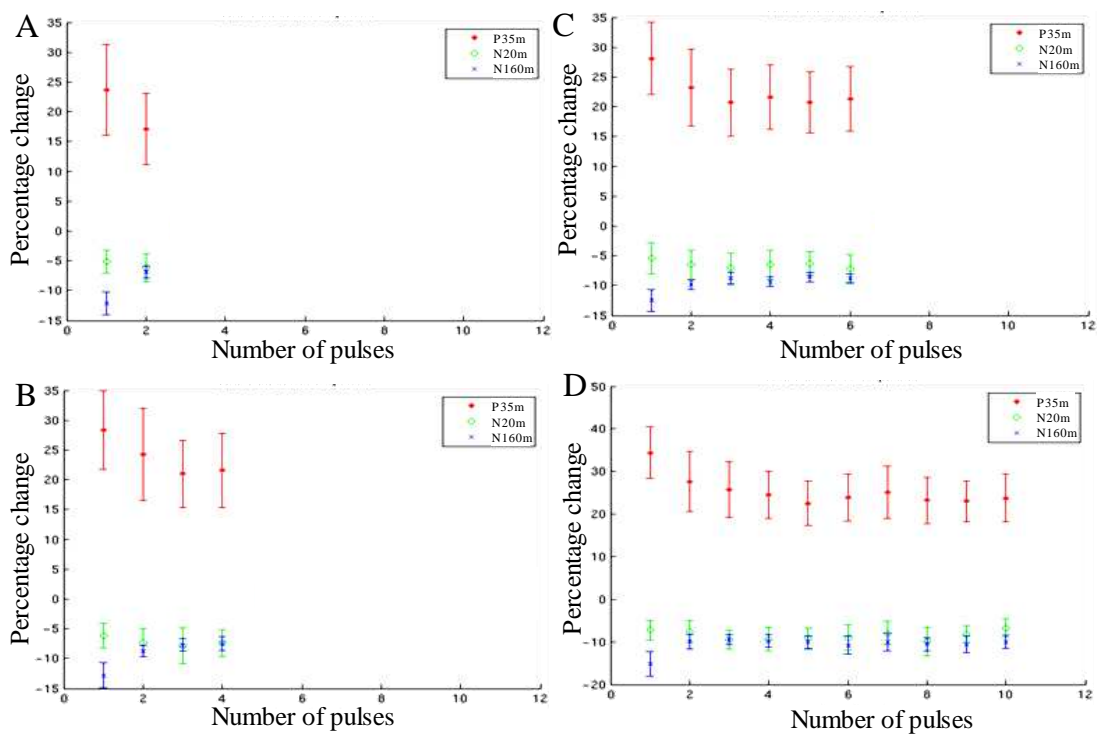

Figure 8-5: Comparison of amplitude change for N20m, P35m, and N160m between different pulses for the 2 pulse [A], 4 pulse [B], 6 pulse [C] and 10 pulse [D] conditions.

8.3.2 Pulse train frequency study

Beta band timecourses for the pulse train frequency study with 10 pulses at 2Hz (A) and 0.5Hz (B) are depicted in Figure 8-6. In the 2Hz condition the ERD is maintained until the last pulse after which the ERS appears. In the 0.5Hz condition (ISI=2s), the ERS appears after each pulse.
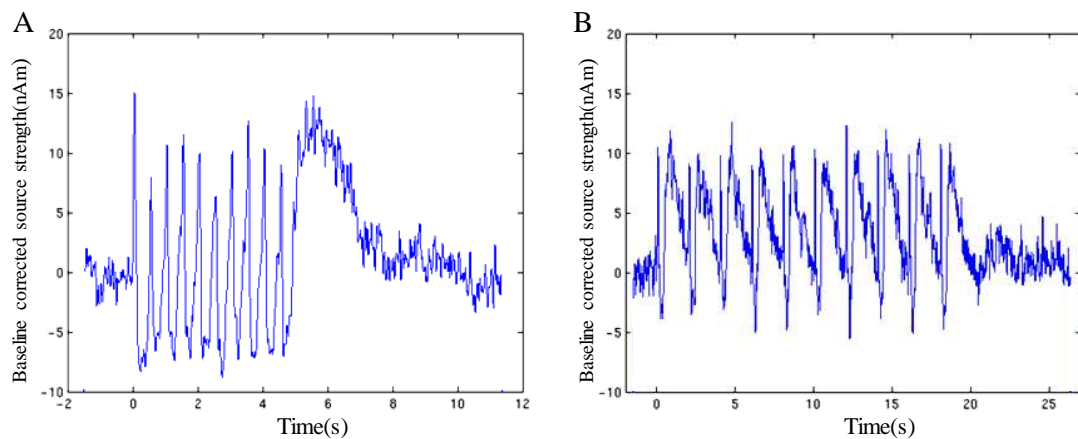
Figure 8-6: Timecourse averaged across subjects for 2Hz [A] and 0.5Hz [B] conditions.

Figure 8-7 shows the percentage changes of ERD and ERS following each pulse in the frequency study and the variance across subjects is shown in the error bars. Neither the ERD nor ERS show significant differences across pulses applied at 0.5Hz and 2Hz. Compared to the ERS of 2Hz condition ($70.12 \pm 10.19\%$), the ERS at 0.5Hz is smaller ($48.51 \pm 11.69\%$).
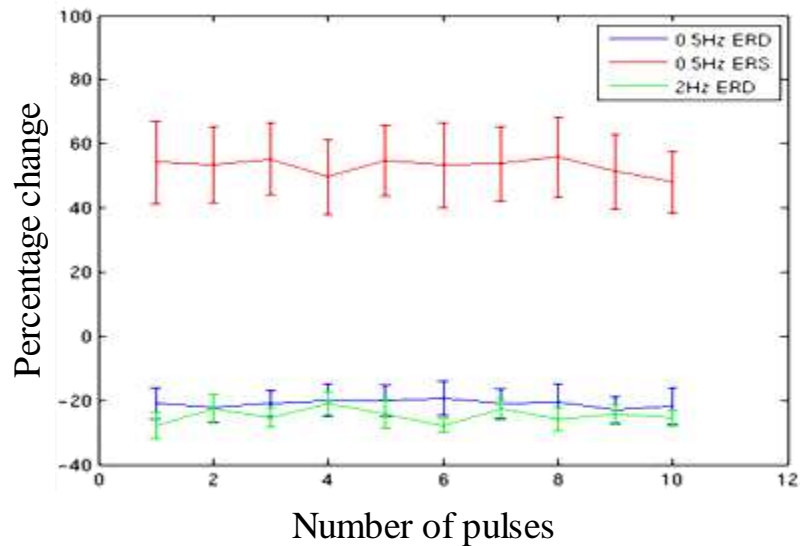
Figure 8-7: Percentage changes of 0.5Hz ERD (Blue), 0.5Hz ERS (Red) and 2Hz ERD (Green) following each pulse in the link pulse conditions.
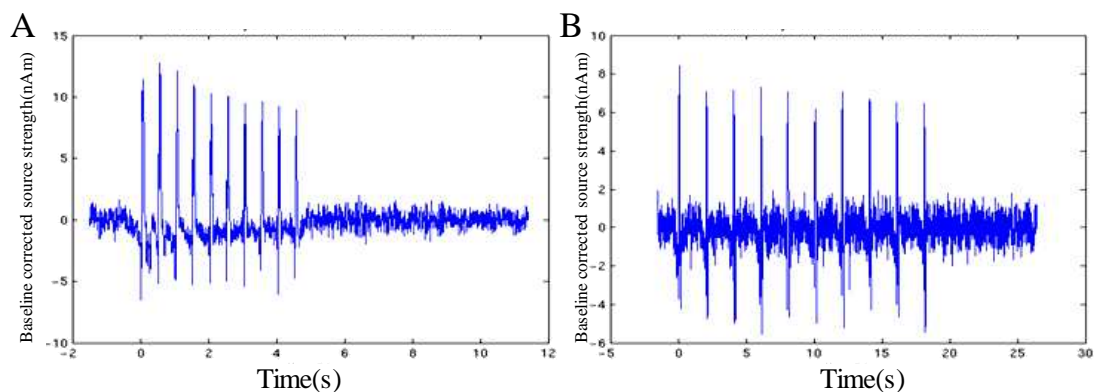
Figure 8-8: Evoked responses for the conditions of 2Hz [A] and 0.5Hz [B].

Figure 8-8 shows the evoked responses and Figure 8-9 shows the amplitudes of the N20m P35m and N160m components for the frequency study. In both cases, the 2Hz condition is on the left and the 0.5Hz condition is on the right. For the 2Hz condition, the amplitude of N160m coincides with the results of multiple pulse study. For the 0.5Hz condition, the N160m does not show significant differences between the first pulse and the subsequent pulses. The N20m is also stable. However, although the ISIs was 2s and the ERS nearly completed between stimuli with ISI of 2s, the P35m still decline slightly with the increase in pulse number. This decline is not significant.
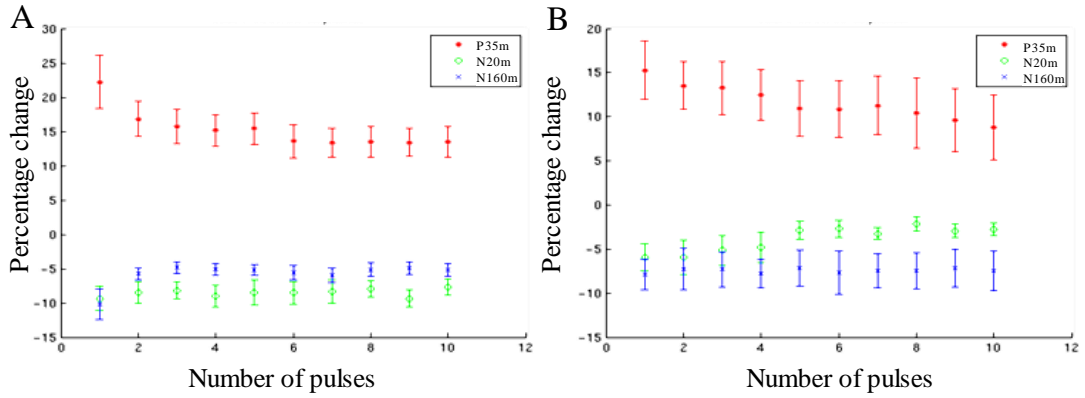
Figure 8-9: Amplitude changes of N20m, P35m, and N160m and between different pulses for the conditions of 2Hz [A] and 10.5Hz pulses [B].

8.3.3 Spatial temporal signature of BOLD responses

The BOLD fMRI timecourse from clusters around the global maximum for the frequency study are shown in Figure 8-10. The peak amplitude for the 2Hz condition was larger than that for the 0.5Hz condition. In the 0.5Hz condition, after reaching a peak, the BOLD signal plateaued at a stable level.
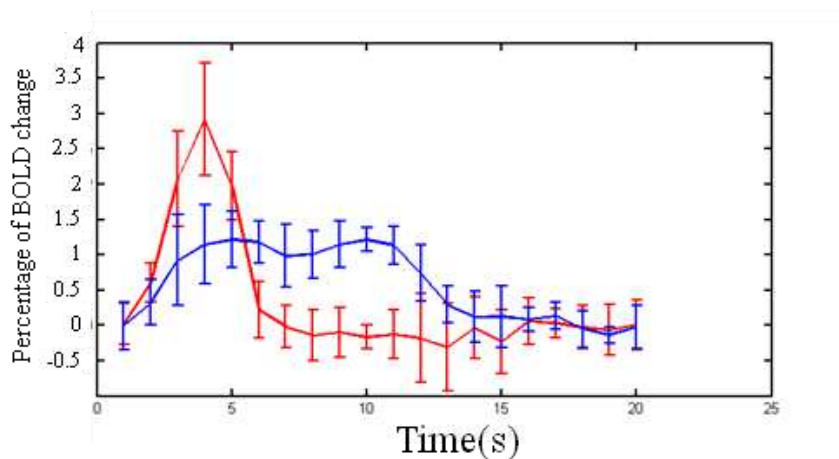
Figure 8-10: Timecourses of BOLD signal changes for the 2Hz (red) and 0.5Hz (blue) conditions.

All 8 subjects in the frequency study showed significant standard BOLD responses in sensory cortex and 5 of the 8 subjects exhibited significant delayed BOLD using the two columns design matrix. Results presented subsequently in this chapter are limited to these 5 subjects. Figure 8-11 [A] shows the spatial distribution of beta ERD. Figure 8-11 [B] shows the associated timecourse extracted from cSI with beta ERD, ERS and the evoked response to the 10 individual median nerve stimuli all apparent.
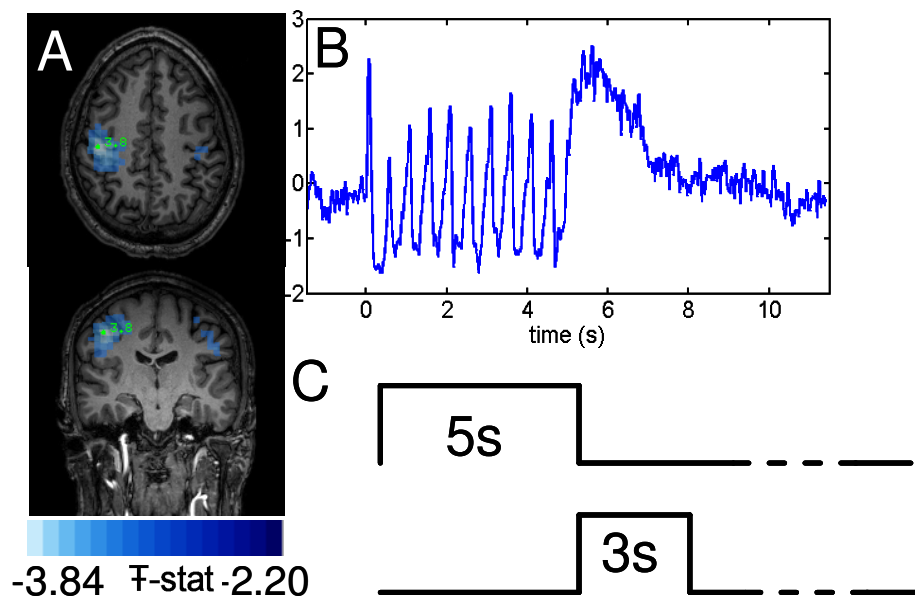
Figure 8-11: Spatial localization of beta ERD [A], timecourse of beta band ERD/ERS [B] and columns in design matrices [C].

Figure 8-12 [A] shows the T-statistical images for both standard (red overlay) and delayed (blue overlay) BOLD. Both effects appear bilaterally in SI; the activated area representing standard BOLD is larger in the contralateral cortex as would be expected with delayed BOLD appearing in neighbouring regions.
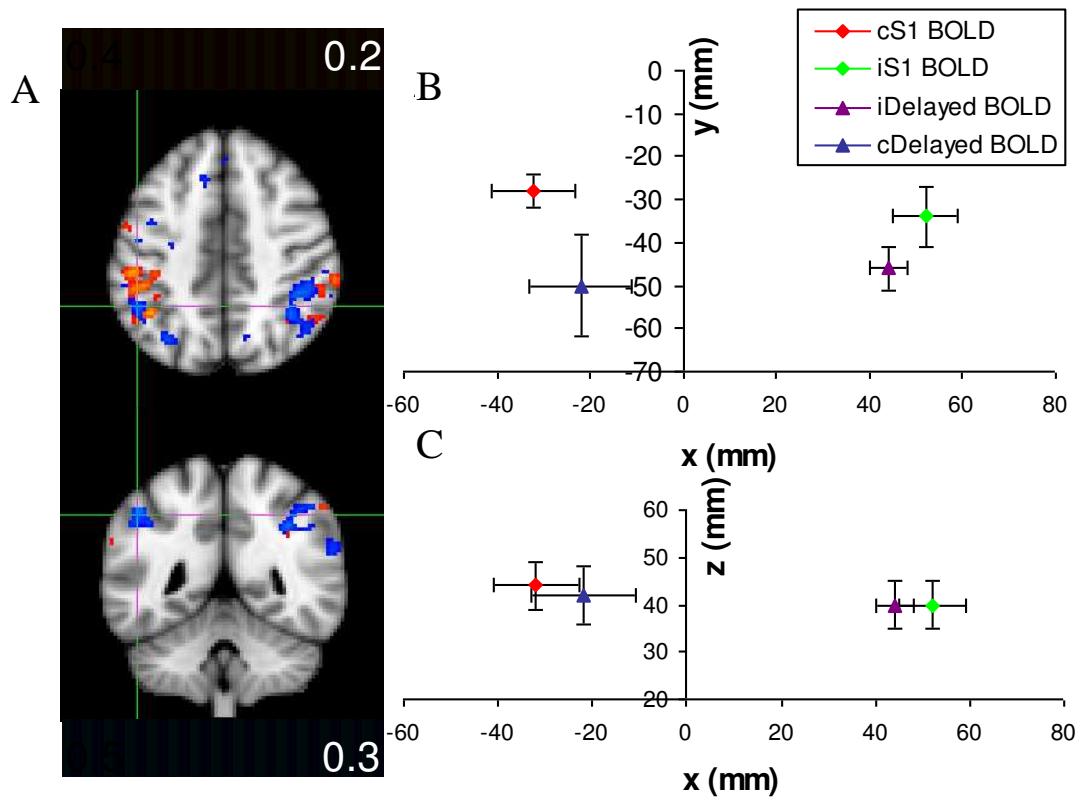
Figure 8-12: Normalized and averaged T score images for standard (Red) and delayed (Blue) BOLD overlaid onto the template brain [A]. Averaged local maximum locations in MNI coordinates, with standard error across subjects in transverse [B] and coronal [C] plane

Figure 8-12 [B,C] shows the locations of the average maxima for standard and delayed BOLD. The x axis is left-right, the y axis is posterior-anterior and the z axis is inferior-superior. Note that the delayed response is posterior and medial to the standard response; both are in approximately the same axial plane.

Figure 8-13 shows the timecourses extracted from 6x6x6mm^3 clusters in contralateral and ipsilateral cortices. Both standard and delayed BOLD responses are shown averaged across subjects.
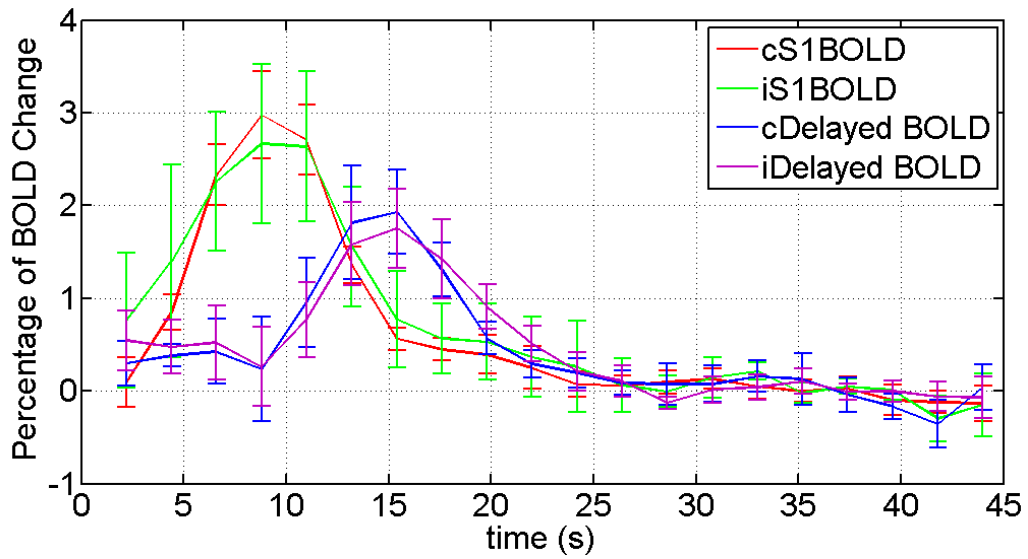
Figure 8-13: timecourses for bilateral natural and delayed BOLD for the 2Hz link pulse condition.

Finally, Figure 8-14 shows the results of our ANOVA analysis. The activated voxel with peak latency of 9.5-11s for natural BOLD (red) and 13-15.5s for delayed BOLD(Blue) are overlaid onto the template brain. The areas of natural and delayed BOLD are discrete and their locations are similar to the T score images based on different models. The distribution of significantly active voxels is plotted as a function of their peak latency. Here the x axis represents time to peak whilst the y-axis represents the fraction of voxels with a specific delay time. Note again that the model free ANOVA is not confounded since voxels exhibiting a BOLD response, at any latency, are included. Discrete 'bimodel' nature suggests that there really are two separate responses which could be associated to ERD and ERS.
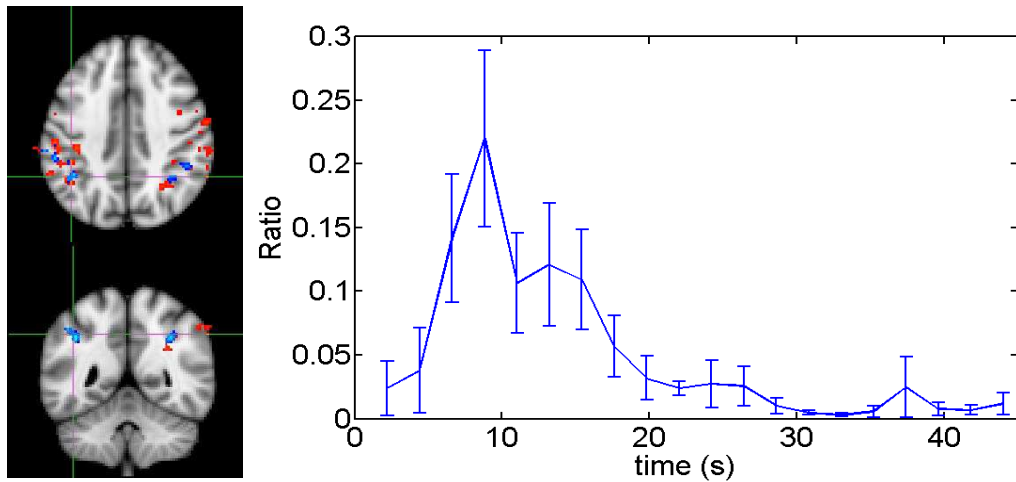
Figure 8-14: Peak latency map for natural (Red) and delayed (Blue) BOLD (left) and ratio of voxels have different latency peaks to all activated voxels (right).

8.4 *Discussion*

8.4.1 The gating role

In Chapter 7, we have found a gating phenomenon in beta band oscillations with different ISIs. With ISIs of 0.5s, a second median nerve pulse was found to maintain the ERD at the same amplitude for a further ~0.5s and the appearance of ERS was postponed for ~0.5s. The beta band oscillation drops down to a stable level for a certain time no matter when the stimulus is applied. Previous research has also reported a gating phenomenon of SEFs during sensorimotor tasks [6-7]. However, whether this simple beta ERD gating role still applies for multiple pulses and whether there is any modulation of the amplitude of ERD under these conditions was unclear. Here we undertook a multiple pulse study, which applied different numbers of pulses with ISI of 0.5s. It was shown that ERD amplitudes after all stimuli do

not differ significantly. This confirms our previous finding that beta oscillations behave as a cortical 'gate'. Even with multiple stimuli, no matter when the median nerve pulse is applied, the amplitude of ERD and the onset time of ERS are stable.

As shown in chapter 7, the amplitude of beta ERS varies in a non-linear fashion with varying ISIs. This suggested that the effect of beta band oscillations appeared to be cumulative. However, in the multiple pulse study, we find that with an ISI of 0.5s, the peak amplitude of beta ERS does not differ significantly between different pulse train lengths. With a fixed ISI, the amplitudes of beta ERS are not influenced by the number of pulses. Although in the paired pulsed study with different ISIs, the peak amplitude of beta ERS changed with varying ISI, this modulation is not sensitive to pulse train length.

In the pulse train frequency study, 10 pulses were applied in each trial at whether 2Hz or 0.5Hz. The beta ERD was also stable for all pulses in both conditions. This finding further reinforces the gating role for beta ERD. The beta ERS after each pulse in the 0.5Hz condition is stable, suggesting that whether the following stimuli are applied within or out of gating interval, there is no accumulative effect on the amplitudes of beta ERS. However, in the 0.5Hz condition the beta ERS is small compared to the 2Hz condition. Overall evidence suggests that the interval between pulses, not the amount of pulses, plays the most important role in the modulation of beta ERS. However, due to the large variance across subjects and conditions in the ERS, this difference does not archive significance in the Wilcoxon Signed Rank Test. If the stimuli are applied at different frequencies, the beta ERS is modulated under different conditions. But when multiple ERS effects are generated in each trial, their amplitudes are stable.

Our results for the evoked responses are consistent with previous reports that the N20m, P35m and N160m components are found in cSI after each pulse. The N20m is stable across

all pulses and all conditions for both the pulse train length and frequency studies. The N20m component is related to the primary stages of processing after the information has been projected to cSI through the sensory signal pathway [8-9]. The P35m is modulated continuously in with multiple pulses, which may reflect inhibitory postsynaptic currents as stated in chapter 7. However, it is not only modulated by the ISI, but also by number of stimuli applied before as shown in Figure 8-5and Figure 8-9.

During application of a train of median nerve pulses, the amplitude of the P35m decreases. The rate of modulation of the P35m decreases and the amplitude of the P35m saturates at a stable level after about 6-7 with an ISI of 0.5s.

There are few previous reports for the N160m component. Some studies have suggested that the amplitude of the N160m does not modulate with either stimulus intensity or attention. These findings agree with our results where, during ERD, the N160m is switched to a lower level. There is no continuous modulation or interim level. This reinforces our previous hypothesis that the beta oscillations play a gating role and the N160m components are modulated by beta band effects.

This is further reinforced in the frequency study. In the 0.5Hz condition, the brain reaches a steady state. The BOLD amplitude stays at a high level during the stimuli and the inter stimulus ERS is small compared to the 2Hz condition. In this condition, as beta oscillations have fully recovered to baseline between stimuli, the N160m is rather stable across all the stimuli. These results show that, if applied out of the gating interval, N160m is switched back to the same level, whereas the resting time required to allow the fully recovery of brain states is as long as 8-10s.

8.4.2 CAM

The Cortical Activation Model was introduced in Chapter 5. Our results from the multiple and link pulse studies can be tested against this model. In the CAM model, the cortical activation level is present on a bell shape CAM curve as working points (WP). In the resting state, with no external stimulation, the cortex still has baseline oscillations, which are also referred to as 'idling rhythms'. For beta band oscillations, the cortical neuronal network is at a high activation level during the resting state and generates beta band idling rhythms over large areas. Hence the WPs for beta band oscillatory activities are on the right descending half of the curve.

Figure 8-15: The CA curve and the relation between beta ERD/ERS and the CA level [A]. Different subjects have CA curves with similar shapes but different amplitudes [B].

As shown in Figure 8-15[A], in the resting state, the WP is at location A. When a median nerve stimulus is applied, the WP moves toward the right end of the curve, forming the ERD. As the beta band ERD has a gating role, the WP is actually switched to the right end of this

curve (B), turning the cortical activation level to 'fully on'. The WP will stay near the right end of the curve for the duration of the gating interval. If the following pulse is applied within the gating interval, it will keep the WP near the right end of the CAM curve, maintaining the ERD at the same amplitude. If it is applied out of the interval, it will switch the WP to the right end again. If this model is correct, no matter how many pulses are applied before and where the location of WP is, the ERD shouldn't show any modulation. This agrees with what we found in the results of this chapter. We have also found that for different subjects, the raw amplitude of beta band oscillations has large variance with respect to each other. But if the beta ERD is calculated as a percentage change from baseline, it is quite stable across subjects. Here we claim that all the subjects may share CAM curves of similar shapes, but the amplitudes of these curves may be different to each other. This is illustrated in Figure 8-15. The baseline and raw amplitude of ERD vary a lot, but the percentage changes of ERD don't.

The beta ERS is more complex compared to the ERD. After the WP has been switched to right end of the CAM curve for about 0.5s (the length of the gating interval) with no further stimulus, the WP moves back left due to the reducing cortical activation. But instead of just returning to the resting state location, the WP moves to a far left position (C), forming the ERS. Then the WP moves back to the start position slowly in the following seconds. If during this process, another stimulus is applied, it will switch the WP back to the right head point (B) again rapidly. This is shown in Figure 8-15 [B]. This ERS plays an inhibition role in the somatosensory cortex and is modulated by the ISIs as stated before.

As WPs only move along the CAM curve, the upward overshoot due to movement to the left side of the start position is limited by the curve. If this CAM model is correct, there shouldn't be significant accumulation of the ERS when multiple pulses are applied. Modulation may still exist, as the point for ERS (C) is quite variable. If there is a linear

correlation or significant accumulation of ERS with the number of stimuli applied within the gating interval, this model fails. The multiple pulse study with 2-10 pulses has shown that with ISI of 0.5s, the amplitude of the ERS does not show a significant difference across all the four conditions. These studies support the CAM model we have introduced [10-12].

In Chapter 7, we have discussed the paired pulse result and the fact that it seems to be in contrast to the previous study by Hall et al. [3] which shows movement related beta ERD to be GABA-A dependent, with post movement beta ERS being GABA-A independent. However, this conflict can be explained by the CAM. For the beta ERD, the GABA-A mainly modulates the start point (A) rather than the right end point (B). Although, beta ERS is also modulated by the movement of the start point on the CA curve, the large amplitude and variance of the left end point (C) makes this modulation insignificant when measured in percentage change. Previous animal research [13] and some recent human studies [14-15] also suggest that the baseline oscillations are associated with the GABA level in the cortex.

Although the ERS is stable in the multiple pulse study with different number of stimuli, the end point of the WP for the ERS is unstable, across both conditions with different ISIs and subjects as shown in Chapter 7. The amplitude is mainly modulated by the frequency of the stimuli. In the 0.5Hz condition, the end point of the WP on the curve is shifted right. Hence the WP oscillates between the right end and the left end on the CAM curve. As the BOLD signal, which reflects the change of blood flow, is related to the total brain activity, the averaged cortical activation level represented by the BOLD change is modulated with different pulse frequencies.

8.4.3 The delayed BOLD response

In Chapters 6 and 7, averaged SAM images and global maximum locations of beta ERD/ERS were computed in order to spatially separate these two effects. The ERS appears to be anterior and to the ERD along the central gyrus. However, significant differences in the global maxima were only found in the superior-inferior direction between peak ERS and ERS. This difference could however been due to the difference in the SNR of these two effects.

Using the 2Hz paradigm, we investigated temporal delays in the fMRI BOLD response, with a view to investigate whether a post stimulus electrophysiological effect, beta ERS, induces a temporally delayed BOLD response and whether this effect can be spatially separated from the natural BOLD response. Previous work has suggested that beta band ERD and ERS may arise from spatially separate neural generators. However, MEG lacks the spatial resolution to investigate whether the two effects indeed arise from different cortical areas assuredly. By basing BOLD models on MEG timecourses of ERD and ERS we did find significantly delayed BOLD responses, apparent in contralateral and ipsilateral somatosensory cortices. However, the beta ERS, which is used to build the GLM model for localizing delayed BOLD, was only found in the contralateral hemisphere of the brain. The location of delayed BOLD is posterior and inferior to the standard BOLD in the posterior parietal cortex. This is in contrast to our previous findings on spatial separations between ERD and ERS. As stated above, the ERS represents inhibition of the cortex, the delayed BOLD, which is positive, may be associated with activation of posterior parietal areas during the inhibition of SI and MI. It is possible that the ERS is associated with negative BOLD and can be localized to the pre-central gyrus. A previous study [4], which claims that the PMBR can be seperated by applying the timecourse of beta ERS (PMBR) as a regressor in the fMRI analysis, is unlikely

to localize the beta ERS effect correctly. The relation between ERD and ERS is complex and the model used to spatially separate their generators requires further work.

Although we cannot definitively link the standard and delayed BOLD response with the beta ERD and ERS respectively, the ANOVA method confirms the existence of a bimodal distribution of BOLD responses, rather than a continuous distribution (Figure 8-14). This delayed BOLD is interesting. What effects it reflects and whether it can give us more information about cortical processing in the somatosensory cortex will be studied in future works.

8.5 *Conclusions*

The median nerve study with multiple pulses goes some way to confirming the gating role of beta effects in the somatosensory cortex. For the beta band oscillations in cSI, the gating hypothesis has been confirmed since the beta ERD always falls to the same level regardless of starting point. There is no additional modulation when multiple pulses are applied. The beta ERS is more complex; it is independent of the number of stimuli, but is modulated by the frequencies of stimulation. It was also been found that the N160m component reflects a similar gating role. Applied within and outside gating interval, it is switched between two discrete levels. The CAM model introduced in Chapter 5 can be fitted to our results as well. The left end point for WP, which determines the peak amplitude of the ERS, is modulated by the frequency of stimuli whilst the right end point is always the same, which may be the right end of the CA curve. When low frequency (ISI > gating interval) train pulses are applied, the WP oscillates between these two points. We also suggest that the CAM curves from different subjects share similar shapes, but have different scales. In fMRI, by using the models based on the temporal signature of beta ERD and ERS, spatially separated delayed

BOLD response can be clearly found posterior to the standard BOLD. However, the relationship between this delayed BOLD and the ERS effects remains unclear.

8.6 *References*

[1]   Karhu, J., Hari, R., Paetau, R., Kajola, M. and Mervaala, E., Cortical reactivity in progressive myoclonus epilepsy. Electroencephalography and Clinical Neurophysiology, 1994. **90**(2): p. 93-102.

[2]   Deisz, R. and Prince, D., Frequency-dependent depression of inhibition in guinea-pig neocortex in vitro by GABAB receptor feed-back on GABA release. The Journal of Physiology, 1989. **412**(1): p. 513-541.

[3]   Hall, S.D., Stanford, I.M., Yamawaki, N., McAllister, C., Ronnqvist, K., Woodhall, G.L. and Furlong, P.L., The role of GABAergic modulation in motor function related neuronal network activity. Neuroimage, 2011. **56**(2): p. 1506-1510.

[4]   Parkes, L.M., Bastiaansen, M. and Norris, D.G., Combining EEG and fMRI to investigate the post-movement beta rebound. Neuroimage, 2006. **29**(3): p. 685-696.

[5]   Clare, S., Humberstone, M., Hykin, J., D Blumhardt, L., Bowtell, R. and Morris, P., Detecting activations in event-related fMRI using analysis of variance. Magnetic Resonance in Medicine, 1999. **42**(6): p. 1117-1122.

[6]   Kakigi, R., Shimojo, M., Hoshiyama, M., Koyama, S., Watanabe, S., Naka, D., Suzuki, H. and Nakamura, A., Effects of movement and movement imagery on somatosensory evoked magnetic fields following posterior tibial nerve stimulation. Cognitive Brain Research, 1997. **5**(3): p. 241-253.

[7]   Schnitzler, A., Witte, O.W., Cheyne, D., Haid, G., Vrba, J. and Freund, H.J., Modulation of somatosensory evoked magnetic fields by sensory and motor interferences. Neuroreport, 1995. **21**(6): p. 1653-1658.

[8]   Hashimoto, I., Kimura, T., Fukushima, T., Iguchi, Y., Saito, Y., Terasaki, O. and Sakuma, K., Reciprocal modulation of somatosensory evoked N20m primary response and high-frequency oscillations by interference stimulation. Clinical Neurophysiology, 1999. **110**(8): p. 1445-1451.

[9]   Allison, T., McCarthy, G., Wood, C.C. and Jones, S.J., Potentials-Evoked In Human And Monkey Cerebral-Cortex By Stimulation Of The Median Nerve - A Review Of Scalp And Intracranial Recordings. Brain, 1991. **114**: p. 2465-2503.

[10]   Pfurtscheller, G., Event-Related Dynamics of Brain Oscillations, in The cortical activation model (CAM), C. Neuper and W. Klimesch, Editors. 2006, Elsevier: p. 19-27.

[11]   Pfurtscheller, G., Woertz, M., Muller, G., Wriessnegger, S. and Pfurtscheller, K., Contrasting behavior of beta event-related synchronization and somatosensory evoked potential after median nerve stimulation during finger manipulation in man. Neuroscience Letters, 2002. **323**(2): p. 113-116.

[12]   Pfurtscheller, G. and Lopes da Silva, F., Event-related EEG/MEG synchronization and desynchronization: basic principles. Clinical Neurophysiology, 1999. **110**(11): p. 1842-1857.

[13]   Faulkner, H., Traub, R. and Whittington, M., Anaesthetic/amnesic agents disrupt beta frequency oscillations associated with potentiation of excitatory synaptic potentials in the rat hippocampal slice. British journal of pharmacology, 1999. **128**(8): p. 1813-1825.

[14]   Gaetz, W., MacDonald, M., Cheyne, D. and Snead, O., Neuromagnetic imaging of movement-related cortical oscillations in children and adults: age predicts post-movement beta rebound. Neuroimage, 2010. **51**(2): p. 792-807.

[15]   Hamandi, K., Singh, K.D. and Muthukumaraswamy, S., Reduced movement-related beta desynchronisation in juvenile myoclonic epilepsy: A MEG study of task specific cortical modulation. Clinical Neurophysiology, 2011. **122**(11): p. 2128-2138.

Chapter 9

Conclusions and future works

9.1 *Summary of the thesis*

In this thesis, we use the combination of MEG and ultra-high-field fMRI to investigate the neuroelectircal activity and BOLD response in the somatosensory cortex. The aim of these studies is to gain greater understanding into the complex neuronal networks underlying the sensory information process.

The background of the studies in this thesis was reviewed in Chapter 5. Previous research has already offered an overview of the signal pathway in the somatosensory system and indicates that the thalamo-cortical loops play key roles in the signal process. However the low frequency non-phase lock oscillations have not attracted a lot of interest until recent years. Our studies in the following experimental chapters focused on the modulation of these oscillations and their relationship with SEFs and BOLD responses. The CAM based on previous studies was also tested with our results.

A single pulse MNS paradigm, with far more trials than usually reported, was applied to find the amount of data required for source localization and time-frequency analysis. This finding was also used to optimise the paradigms used in the following chapters. Single pulse MNS was also applied at regular and jittered intervals to test the influence of temporal regularity. The beta band oscillations between 13-30Hz showed the largest changes following the

stimulus onset in the low frequency band and were not impacted by the regularity of MNS. Efforts using group averaged SAM images were made to separate the beta ERD/ERS spatially.

The paired pulse MNS paradigm with varying ISIs was applied in Chapter 7 in order to characterise the modulation of beta band oscillations, the P35m effect and their contributions to the non-linearity of BOLD responses. The beta ERD was associated with a gating role and the ERS was modulated with different ISIs. A non-linear neuronal response was found with ISIs up to 2s. The beta ERD/ERS effects were separated using the peak locations normalized in MNI coordinates and were suggested to have different generators.

The multiple pulse study with varying train length and the link pulse study with varying frequency is described in Chapter 8. The gating role of beta ERD found in Chapter 7 was further confirmed with longer pulse trains and the N160m effect was controlled under this cortical gate. The CAM introduced in Chapter 5 held true for the multiple and link pulse results and provided a framework for interpretation of our previous findings. By including the temporal signature of beta ERD/ERS as regressor, delayed BOLD responses were found in the posterior parietal cortex but the relation between the delayed BOLD and beta ERS remains unclear and will require more study.

9.2 *Future works*

Combination of MEG and fMRI has been proved to be useful in studying the neuronal activity in the somatosensory cortex. However, there are still questions left to be answered during the sensory information process, such as what does the delayed BOLD represent and how are the inter-cortical networks modulated. A MEG-fMRI study with a longer pulse train

length could be taken to determine whether this delayed is related to the onset or offset of the stimulus. If the ERS is postponed, is the delayed BOLD also postponed correspondingly. Zoomed EPI or spin-echo EPI may also be used in the fMRI study to gain better separation of different neuronal effects. With the new 32-Channel SENSE coil which has increased SNR, the negative BOLD response which may be related to the beta ERS could also be studied. In the more distant future, these findings in healthy subjects may contribute to clinical applications in patients with movement disorders such as Parkinson's disease, where changes in neural oscillations have been demonstrated.